CISM International Centre for Mechanical Sciences 580
Courses and Lectures

Herman J.H. Clercx
GertJan F. Van Heijst *Editors*

Mixing and Dispersion in Flows Dominated by Rotation and Buoyancy

International Centre for Mechanical Sciences

Springer

CISM International Centre for Mechanical Sciences

Courses and Lectures

Volume 580

The series presents lecture notes, monographs, edited works and proceedings in the field of Mechanics, Engineering, Computer Science and Applied Mathematics. Purpose of the series is to make known in the international scientific and technical community results obtained in some of the activities organized by CISM, the International Centre for Mechanical Sciences.

More information about this series at http://www.springer.com/series/76

Herman J.H. Clercx · GertJan F. Van Heijst
Editors

Mixing and Dispersion in Flows Dominated by Rotation and Buoyancy

Springer

Editors
Herman J.H. Clercx
Department of Applied Physics
Eindhoven University of Technology
Eindhoven, Noord-Brabant
The Netherlands

GertJan F. Van Heijst
Department of Applied Physics
Eindhoven University of Technology
Eindhoven, Noord-Brabant
The Netherlands

ISSN 0254-1971 ISSN 2309-3706 (electronic)
CISM International Centre for Mechanical Sciences
ISBN 978-3-319-66886-4 ISBN 978-3-319-66887-1 (eBook)
https://doi.org/10.1007/978-3-319-66887-1

Library of Congress Control Number: 2017951146

Printed on acid-free paper

This Springer imprint is published by Springer Nature
The registered company is Springer International Publishing AG
The registered company address is: Gewerbestrasse 11, 6330 Cham, Switzerland

Preface

The chapters contained in this volume correspond to the lectures given during the course "Mixing and Dispersion in Flows Dominated by Rotation and Buoyancy" that was held at the CISM in Udine (Italy), July 6–10, 2015.

Rotation and buoyancy play an essential role in many astrophysical, geophysical, environmental, and industrial flows. They influence the transition to turbulence, strongly affect large-scale (turbulent) flow properties by inducing anisotropy, and also affect boundary-layer dynamics and inertial-range turbulence characteristics. Moreover, rotation and buoyancy may have a strong impact on mixing, and on the dispersion of passive and active tracers and of (inertial) particles and droplets in such flows. The impact of buoyancy or rotation on transport may be direct (gravitational, centrifugal, or Coriolis forces on fluid parcels or particles/droplets) or indirect by the modified flow characteristics. These processes have direct relevance for heat and mass transfer in many natural systems. Examples are (large-scale) convection processes, transport of sediment in coastal flows, dispersion of suspended particulate matter in estuarine flows, in lakes and reservoirs, and dispersion of aerosols and pollutants in the atmospheric boundary layer. Increasing computational capabilities and the rapid development of advanced experimental measurement tools, for example optical diagnostics and particle tracking techniques, provide highly resolved temporal and spatial data sets. This allows the exploration and analysis of more complex flow phenomena and the associated transport processes in more depth.

The aim of this course had been to present an overview of recent developments in this field in a way accessible to participants coming from a variety of fields, including turbulence research, (environmental) fluid mechanics, lake hydrodynamics, or atmospheric physics. Topics to be discussed during the lectures ranged from the fundamentals of rotating and stratified flows, mixing and transport in stratified or rotating turbulence, transport in the atmospheric boundary layer, the dynamics of gravity and turbidity currents, mixing in (stratified) lakes, and the Lagrangian approach to analyze transport processes in geophysical and environmental flows. This goal is not only reflected in this volume and the contributions are aimed at doctoral students and postdoctoral researchers, but also at academic and

industrial researchers and practicing engineers, with a background in mechanical engineering, applied physics, civil engineering, applied mathematics, meteorology, physical oceanography, or physical limnology.

This volume starts with a general introduction on effects of rotation and density stratification on fluid flows by GertJan van Heijst, followed by an overview of the basic phenomena of turbulence and mixing in flows dominated by buoyancy by Paul Linden. Subsequently, the connection is made with certain environmental flow situations, such as mixing in lakes and reservoirs by Damien Bouffard and Alfred Wuëst and energy balances in stably stratified, wall-bounded turbulence by Oscar Flores and James Riley. The Lagrangian approach to unravel transport in turbulence is addressed by Mickaël Bourgoin. Eckart Meiburg and Mohamad Nasr-Azadani give an overview of recent numerical and modeling developments in the field of gravity and turbidity currents. Finally, several aspects of transport processes in rotating turbulence are reviewed by Herman Clercx.

The authors wish to thank all the contributors and the members of CISM for their support and thoughtful suggestions during the course and the preparation of this volume.

Eindhoven, The Netherlands

Herman J.H. Clercx
GertJan F. Van Heijst

Contents

Contributors

Damien Bouffard Physics of Aquatic Systems Laboratory, Ecole Polytechnique Federale de Lausanne, Lausanne, Switzerland

Mickaël Bourgoin Université de Lyon, ENS Lyon, Université Claude Bernard – Lyon 1, CNRS, Laboratoire de Physique, Lyon, France

Herman J.H. Clercx Fluid Dynamics Laboratory, Department of Applied Physics, Eindhoven University of Technology, Eindhoven, The Netherlands; J.M. Burgers Center for Fluid Dynamics, Enschede, The Netherlands

Oscar Flores Departamento de Bioingeniería e Ingeniería Aeroespacial, Universidad Carlos III de Madrid, Madrid, Spain

GertJan F. van Heijst Fluid Dynamics Laboratory, Department of Applied Physics, Eindhoven University of Technology, Eindhoven, The Netherlands; J.M. Burgers Center for Fluid Dynamics, Enschede, The Netherlands

Paul F. Linden Department of Applied Mathematics and Theoretical Physics, Centre for Mathematical Sciences, University of Cambridge, Cambridge, UK

Eckart Meiburg Department of Mechanical Engineering, University of California at Santa Barbara, Santa Barbara, CA, USA

Mohamad M. Nasr-Azadani Department of Mechanical Engineering, University of California at Santa Barbara, Santa Barbara, CA, USA

James J. Riley Department of Mechanical Engineering, University of Washington, Seattle, WA, USA

Alfred Wüest Swiss Federal Institute of Aquatic Science and Technology, Kastanienbaum, Switzerland

Effects of Rotation and Stratification: An Introduction

GertJan F. van Heijst

Abstract Large-scale flows in the natural environment can be influenced by the planetary rotation and also by density differences. This chapter aims to provide an informal introduction into the effects of background rotation and stratification.

1 Effects of Rotation

The relative motion of a fluid in a rotating system is conveniently described by using a co-rotating reference frame. Adopting such a reference system implies the appearance of two additional forces in Newtons second law: the Coriolis and the centrifugal forces. Expressed in a co-rotating coordinate frame the momentum equation takes the following form:

$$\frac{D\mathbf{v}}{Dt} + 2\boldsymbol{\Omega} \times \mathbf{v} = -\frac{1}{\rho}\boldsymbol{\nabla} P + \nu \nabla^2 \mathbf{v} \,, \tag{1}$$

with $\mathbf{v}$ the relative velocity, $\boldsymbol{\Omega}$ the rotation of the system, ρ the density, P the 'reduced' pressure, t the time, ν the kinematic fluid viscosity, and $\frac{D}{Dt} \equiv \frac{\partial}{\partial t} + \mathbf{v} \cdot \boldsymbol{\nabla}$ the material derivative. The Coriolis acceleration is $-2\boldsymbol{\Omega} \times \mathbf{v}$, while the reduced pressure is defined as

$$P = p + \rho \Phi_{grav} - \frac{1}{2}\Omega^2 r^2 \,, \tag{2}$$

where p is the fluid pressure, Φ_{grav} the gravitational potential, $\Omega = |\boldsymbol{\Omega}|$ the angular velocity, and $\frac{1}{2}\Omega^2 r^2$ represents the centrifugal contribution (with r the distance measured with respect to the rotation axis). Note that the Coriolis acceleration $-2\boldsymbol{\Omega} \times \mathbf{v}$ is directed perpendicular to the fluid velocity $\mathbf{v}$. On the northern hemisphere the

G.J.F. van Heijst (✉)
Fluid Dynamics Laboratory, Department of Applied Physics, Eindhoven University of Technology, P.O. Box 513, 5600MB Eindhoven, The Netherlands
e-mail: g.j.f.v.heijst@tue.nl

G.F. van Heijst
J.M. Burgers Center for Fluid Dynamics, Enschede, The Netherlands

H.J.H. Clercx and G.J.F. van Heijst (eds.), *Mixing and Dispersion in Flows Dominated by Rotation and Buoyancy*, CISM International Centre for Mechanical Sciences 580, https://doi.org/10.1007/978-3-319-66887-1_1

Coriolis induces a deflection to the right, while on the southern hemisphere a moving fluid experiences a deflecting force to its left.

By using a typical length scale L, a typical velocity U, and $1/\Omega$ as a time scale, the physical quantities may be non-dimensionalised as:

$$\mathbf{r} = L\tilde{\mathbf{r}} \ , \quad \mathbf{v} = U\tilde{\mathbf{v}} \ , \quad t = \tilde{t}/\Omega \ , \quad P = \rho\Omega U L\tilde{p} \tag{3}$$

with the tilde ($\sim$) denoting nondimensionality. Equation (1) is then written in non-dimensional form:

$$\frac{\partial\tilde{\mathbf{v}}}{\partial\tilde{t}} + Ro(\tilde{\mathbf{v}}\cdot\tilde{\boldsymbol{\nabla}})\tilde{\mathbf{v}} + 2\mathbf{k}\times\tilde{\mathbf{v}} = -\tilde{\boldsymbol{\nabla}}\tilde{p} + E\tilde{\nabla}^2\tilde{\mathbf{v}} \tag{4}$$

with $\mathbf{k} = \boldsymbol{\Omega}/|\boldsymbol{\Omega}|$ the unit rotation vector and $\tilde{\boldsymbol{\nabla}}$ the non-dimensional gradient operator. In this equation Ro and E represent the Rossby number and the Ekman number, respectively, defined as

$$Ro \equiv \frac{U}{\Omega L} \sim \frac{[(\mathbf{v}\cdot\boldsymbol{\nabla})\mathbf{v}]}{[\boldsymbol{\Omega}\times\mathbf{v}]} \ , \tag{5}$$

$$E \equiv \frac{\nu}{\Omega L^2} \sim \frac{[\nu\nabla^2\mathbf{v}]}{[\boldsymbol{\Omega}\times\mathbf{v}]} \ . \tag{6}$$

These nondimensional numbers indicate the relative importance of the advective and viscous terms, respectively, compared to the Coriolis term in the momentum equation. For a large-scale flow in the Earth's atmosphere, with $U \sim 10$ ms^{-1} and $L \sim 1000$ km, with $\Omega = 1$ rev day$^{-1} \sim 10^{-4}$ s^{-1}, the Rossby number is typically $Ro \sim 0.1$. For oceanic flows, with $U \sim 1$ ms^{-1}, on such a scale, $Ro \sim 10^{-2}$. Apparently, the Coriolis force plays a nearly dominant role in such flows. Such large-scale flows are turbulent, implying that the kinematic viscosity ν should be replaced by a turbulent eddy viscosity ν_t. Nevertheless, the Ekman number for such large-scale flows is usually much less than unity, implying that viscous effects are only of very marginal importance (as long as the gradients in the flow field are not too large). For a steady flow with $Ro \ll 1$ and $E \ll 1$, the momentum Eq. (4) reduces to

$$2\mathbf{k}\times\mathbf{v} = -\boldsymbol{\nabla}p \tag{7}$$

(note that from hereon the tildes have been dropped). This expression reveals a balance between the Coriolis force and the pressure gradient, which is referred to as the *geostrophic balance*. Apparently, the velocity $\mathbf{v}$ is directed perpendicular to the pressure gradient, in other words: the flow is directed along isobars. A remarkable property of geostrophically balanced flow is derived by taking the curl of Eq. (7), yielding

$$(\mathbf{k}\cdot\boldsymbol{\nabla})\mathbf{v} = 0 \rightarrow \frac{\partial\mathbf{v}}{\partial z} = 0 \ . \tag{8}$$

This so-called *Taylor-Proudman theorem* expresses that the geostrophic flow is independent of the axial coordinate (z), see Proudman (1916). The validity of this theorem was demonstrated experimentally by Taylor (1917) by slowly towing a cylindrical obstacle through a rotating fluid: the obstacle carried an axially aligned column of stagnant fluid, while moving steadily moving through the rotating fluid tank. Although Eq. (8) is strictly only valid for $Ro \ll 1$, such columnar structures are common features of rotating flows, even under conditions $Ro \sim 1$. They are commonly referred to as 'Taylor columns'.

1.1 Flow on a Spherical Planet

The oceans and atmosphere on our planet can be considered as relatively thin fluid shells on a rotating solid sphere. Due to this geometry, the large-scale oceanic and atmospheric flows can be considered as motions in the locally horizontal plane. This implies that the local vorticity vector ω is directed vertically upwards. For flow not too close to the poles, it is convenient to adopt a Cartesian coordinate system (x, y, z), with the coordinates pointing in eastward, northward, and vertically upward direction, respectively (see Fig. 1). The corresponding velocity components are $\mathbf{v} = (u, v, w)$. Decomposing the rotation vector in these coordinate directions gives

$$\mathbf{\Omega} = (\Omega_x, \Omega_y, \Omega_z) = (0, \Omega \cos\phi, \Omega \sin\phi) \,, \tag{9}$$

with ϕ the geographical latitude. The x, y, z-components of the Coriolis term in Eq. (1) are then easily derived:

$$2\mathbf{\Omega} \times \mathbf{v} = 2\Omega(w \cos\phi - v \sin\phi, u \sin\phi, -u \cos\phi) \,. \tag{10}$$

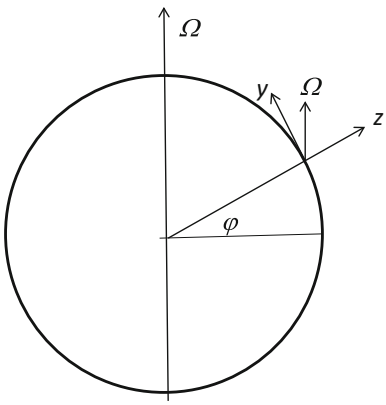

Fig. 1 Definition sketch of coordinates on a rotating sphere

The thin-shell approximation implies $w \ll u, v$, so that expression (10) can be approximated by

$$2\boldsymbol{\Omega} \times \mathbf{v} = (-fv, +fu, -2\Omega u \cos\phi) \tag{11}$$

with

$$f = 2\Omega \sin\phi \tag{12}$$

the so-called *Coriolis parameter*. The x, y, z-components of Eq. (1) can then be written as

$$\frac{Du}{Dt} - \frac{uv\tan\phi}{R} + \frac{uw}{R} - 2\Omega v \sin\phi + 2\Omega w \cos\phi = -\frac{1}{\rho}\frac{\partial p}{\partial x} + F_x \,, \tag{13a}$$

$$\frac{Dv}{Dt} + \frac{u^2\tan\phi}{R} + \frac{vw}{R} + 2\Omega u \sin\phi = -\frac{1}{\rho}\frac{\partial p}{\partial y} + F_y \,, \tag{13b}$$

$$\frac{Dw}{Dt} - \frac{u^2+v^2}{R} - 2\Omega u \cos\phi = -\frac{1}{\rho}\frac{\partial p}{\partial z} - g + F_z \,, \tag{13c}$$

with R the planet's radius and F_x, F_y, F_z representing e.g. viscous forces. For the large-scale flows in the Earth's atmosphere and oceans, a scaling analysis reveals that the curvature-related terms in Eq. (13) are small compared to the others, in such a way that the equations (for the inviscid case) take on the following form:

$$\frac{\partial u}{\partial t} + u\frac{\partial u}{\partial x} + v\frac{\partial u}{\partial y} - fv = -\frac{1}{\rho}\frac{\partial p}{\partial x} \,, \tag{14a}$$

$$\frac{\partial v}{\partial t} + u\frac{\partial v}{\partial x} + v\frac{\partial v}{\partial y} + fu = -\frac{1}{\rho}\frac{\partial p}{\partial y} \,, \tag{14b}$$

$$0 = -\frac{1}{\rho}\frac{\partial p}{\partial z} - g \,, \tag{14c}$$

with f the Coriolis parameter as defined in Eq. (12). Apparently, curvature effects associated with the Earth's spherical shape are negligible, except in the Coriolis terms.

The Coriolis parameter is a nonlinear function of the geographical latitude ϕ. For limited latitudinal scales ($L < 1000\,\text{km}$) we may assume f to be constant:

$$f = f_0 = 2\Omega \sin\phi_0 \,, \tag{15}$$

with ϕ_0 a reference latitude. This is the so-called *f-plane approximation*, which ignores the latitudinal variation of f. In a better approximation, one may expand $f(\phi)$ in a Taylor series:

$$f(\phi) = f(\phi_0 + \delta\phi) = 2\Omega[\sin\phi_0 + \frac{\cos\phi_0}{R}R\delta\phi + O(\delta\phi^2)] \,, \tag{16}$$

where $R\delta\phi = y$, the northward coordinate. For small $\delta\phi$-values, the higher-order terms in the expression are negligibly small, leaving:

$$f = f_0 + \beta y, \text{ with } \beta = \frac{2\Omega \cos \phi_0}{R} . \tag{17}$$

This linear approximation of $f(\phi)$ is the so-called *β-plane approximation*, which is relevant for large-scale flows with a moderate latitudinal extent. In particular, the β-plane approximation is relevant for flows in the equatorial region, for which $f_0 = 0$.

1.2 Some Horizontal Balances

Vortical motions are common features of large-scale flows, both in the atmosphere and in the ocean. Examples are the high- and low-pressure cells in the atmosphere and the vortices shed from ocean currents such as the Gulf Stream. It is instructive to consider a model curvilinear flow around a common centre, for which centripetal accelerations may be important. For steady inviscid flow with velocity V around a circular trajectory with curvature radius R, the basic (dimensional) balance is written as

$$\frac{V^2}{R} + fV = \frac{1}{\rho}\frac{\partial p}{\partial r} , \tag{18}$$

with r the local radial coordinate. In this expression one recognizes the nonlinear centrifugal acceleration, the Coriolis acceleration, and the radial pressure gradient. When written in nondimensional terms, the Rossby number Ro would appear as a prefactor of the centrifugal term. Depending on the Ro-value, different balances are possible, see e.g. Holton (1992).

Ro* ≪ 1 : *geostrophic balance

$$fV = \frac{1}{\rho}\frac{\partial p}{\partial r} . \tag{19}$$

When the centrifugal term is negligibly small, the flow is governed by a balance between the pressure gradient force and the Coriolis force. A low-pressure centre ($\partial p/\partial r > 0$) corresponds with a cyclonic flow, and vice versa a high-pressure centre corresponds with an anticyclonic circulation.

Ro* ≫ 1 : *cyclostrophic balance

$$\frac{V^2}{R} = \frac{1}{\rho}\frac{\partial p}{\partial r} . \tag{20}$$

For $Ro \gg 1$, the centrifugal term dominates the Coriolis term, such that the flow is governed by a balance between the pressure-gradient force and the centrifugal force.

As Eq. (20) reveals, cyclostrophic motion is in all cases around a low-pressure cell ($\partial p/\partial r > 0$). Moreover the flow can be either cyclonic or anticyclonic. This regime corresponds to e.g. tornadoes, but also to the bathtub vortex.

Ro* ∼ *O*(1) : *gradient flow

$$\frac{V^2}{R} + fV = \frac{1}{\rho}\frac{\partial p}{\partial r} \,. \tag{21}$$

For a given pressure gradient the solution for the velocity V is:

$$V = -\frac{1}{2}fR \pm [\frac{1}{4}f^2R^2 + \frac{R}{\rho}\frac{\partial p}{\partial r}]^{1/2} \,. \tag{22}$$

Four cases are possible, depending on the sign of the pressure gradient $\partial p/\partial r$. However, two of these cases are not stable. The two 'regular' cases correspond to a 'regular low', with cyclonic motion ($V > 0$) governed by a balance between the outward centrifugal and Coriolis forces and the inward pointing pressure gradient force. In the other case, the 'regular high', the motion is anticyclonic ($V < 0$) and governed by a balance between the inward Coriolis force and the outward centrifugal and pressure gradient forces.

inertial motion

The balance Eq. (18) for steady motion along circular trajectories also describes a balanced flow for the case of a zero radial pressure gradient. In that case the equation is reduced to

$$\frac{V^2}{R} + fV = 0 \,. \tag{23}$$

Apart from the trivial solution $V = 0$ this balance between centrifugal and Coriolis forces allows inertial motion, with $V = -fR =$ constant. Apparently, this inertial flow corresponds with fluid motion along circular paths in anticyclonic direction. Alternatively, the motion may also be described in Cartesian coordinates, namely by

$$\frac{du}{dt} - fv = 0 \,, \quad \frac{dv}{dt} + fu = 0 \,, \tag{24}$$

with solutions

$$u(t) = V\cos ft, \;\; v(t) = V\sin ft \,. \tag{25}$$

This solution describes harmonic motion along circular paths with frequency f, i.e. with inertial period $T = 2\pi/f$. This type of motion is typically observed in large lakes or semi-enclosed seas like the Baltic after some disturbance (such as the passage of an atmospheric low-pressure cell) has occurred.

1.3 How to Create Vortices in the Lab

Vortex structures may be created in a rotating fluid confined in a container mounted on a turntable in a number of different ways, see e.g. van Heijst and Clercx (2009). One way is by locally stirring the fluid confined in a smaller bottomless cylinder that is placed vertically in the otherwise solidly rotating fluid. By vertically lifting the cylinder out of the fluid the 'stirring vortex' is released. After some adjustment this vortical flow becomes nicely organised in the form of an axially aligned columnar structure. In principle one may thus create both cyclonic and anticyclonic vortices in this way. It was found, however, that the anticyclonic vortices are very unstable: they usually fall apart, eventually resulting in two dipolar structures, see Kloosterziel and van Heijst (1991). An alternative generation method is by having the fluid level inside the generating cylinder initially somewhat lower than outside: upon lifting the cylinder, the 'gravitational collapse' results in a radially inward motion, which—by conservation of angular momentum—is quickly converted into a cyclonic vortex flow. Another generation method is by syphoning fluid through a perforated tube placed vertically in the rotating fluid tank. Again, by conservation of angular momentum the radial flow thus induced is converted into a cyclonic swirl motion around the perforated tube. After carefully lifting the the tube out of the fluid, a stable cyclonic 'sink vortex' is produced.

The vorticity and swirl velocity profiles of the 'sink' and 'stirring' vortices are very well fitted by

$$\omega_{sink}(r) = \omega_0 \exp(-\frac{r^2}{R^2}) \,, \tag{26a}$$

$$v_{sink} = \frac{\omega_0 R^2}{2r}[1 - \exp(-\frac{r^2}{R^2})] \,, \tag{26b}$$

and

$$\omega_{stir}(r) = \omega_0(1 - \frac{r^2}{R^2}) \exp(-\frac{r^2}{R^2}) \,, \tag{27a}$$

$$v_{stir} = \frac{1}{2}\omega_0 r \exp(-\frac{r^2}{R^2}) \,, \tag{27b}$$

with ω_0 a vorticity amplitude and R some radial length scale (see Kloosterziel and Heijst 1992).

These generation techniques have been applied in a variety of experimental studies of barotropic vortices, see e.g. Kloosterziel and van Heijst (1991), Trieling et al. (1998), and Zavala Sansón et al. (2012). Similar techniques may be applied to generate baroclinic two-layer vortices. Additionally, anticyclonic two-layer vortex structures can be created by adding a source of dense fluid (at the bottom) or a source of lighter fluid (at the free surface): the radial spreading of the source fluid results in an

anticyclonic motion of the injected fluid. After removal of the source, an anticyclonic two-layer vortex has been established.

1.4 The Ekman Layer

Although for $E \ll 1$ viscous effects play a minor role in most of the flow domain, near solid domain boundaries—where velocity gradients become large—viscous effects are essential in order to let the geostrophic flow in the bulk of the domain satisfy the boundary conditions (no-slip at solid walls and stress conditions at the free surface). We will here confine ourselves to the Ekman layer, which is the boundary layer at a horizontal (or weakly sloping) solid boundary.

For a steady, small-*Ro* flow the momentum Eq. (4) becomes (after dropping the tildes)

$$2\mathbf{k} \times \mathbf{v} = -\nabla p + E\nabla^2 \mathbf{v} \, . \tag{28}$$

Since $E \ll 1$ the viscous term is generally very small, but it may become important when the normal gradients at a boundary become large. At a horizontal boundary the viscous term becomes equally important as the Coriolis term when

$$E\nabla^2 \sim E\frac{\partial^2}{\partial z^2} \sim \frac{E}{\delta^2} \sim O(1) \, , \tag{29}$$

from which one derives that the nondimensional thickness of the Ekman layer is $\delta \sim E^{1/2}$ and in dimensional form:

$$\delta_E = L\delta = LE^{1/2} = (\frac{\nu}{\Omega})^{1/2} \, . \tag{30}$$

Note that the (constant) thickness of the Ekman layer is independent of the size of the flow configuration. In a laboratory experiment in a water-filled rotating tank with $\nu = 10^{-6}$ m^{2}s^{-1} and $\Omega = 10^{-4}$ s^{-1} (the Earth makes one revolution in 24 h), one derives $\delta_E \simeq 30$ m.

The Ekman layer over a solid horizontal boundary serves to provide the matching of the geostrophic flow in the 'interior' domain to the no-slip boundary condition. If the horizontal velocity in the interior is $\mathbf{v}_I = (u_I, v_I) = O(1)$, with the subscript I referring to 'interior' and u and v the velocity components in a corotating Cartesian x, y-frame, this requires that the velocity in the Ekman layer (subscript E) is $\mathbf{v}_E = (u_E, v_E) = O(1)$. As the Ekman layer is very thin (since $E \ll 1$), this implies $p_I \sim p_E = O(1)$. The x, y-components of Eq. (28) can then be written as

$$-2v_E = -\frac{\partial p_I}{\partial x} + E\frac{\partial^2 u_E}{\partial z^2} , \tag{31a}$$

$$+2u_E = -\frac{\partial p_I}{\partial y} + E\frac{\partial^2 v_E}{\partial z^2} , \tag{31b}$$

while the geostrophic flow in the interior regime is governed by the geostrophic balance (7), or

$$-2v_I = -\frac{\partial p_I}{\partial x} , \qquad +2u_I = -\frac{\partial p_I}{\partial y} . \tag{32}$$

With the bottom at $z = 0$, the boundary conditions for the Ekman-layer solution of the Eqs. (31a) and (31b) are

$$z = 0 : u_E = v_E = 0 \ \text{(no slip)} , \tag{33a}$$

$$z \to \infty : (u_E, v_E) \to (u_I, v_I) . \tag{33b}$$

The solution to this problem is

$$u_E = u_I - [u_I \cos(z/\delta) + v_I \sin(z/\delta)]e^{-z/\delta} , \tag{34a}$$

$$v_E = v_I - [v_I \cos(z/\delta) - u_I \sin(z/\delta)]e^{-z/\delta} . \tag{34b}$$

These solutions show an oscillating behaviour in the z-direction, although damped. Moreover, the horizontal flow in the Ekman layer has a significant component also in the direction perpendicular to the principal direction of the geostrophic flow. This can be nicely seen by taking $\mathbf{v}_I = (u_I, 0)$, for which Eq. (34) become

$$u_E = u_I[1 - e^{-z/\delta}\cos(z/\delta)] , \tag{35a}$$

$$v_E = u_I e^{-z/\delta}\sin(z/\delta) . \tag{35b}$$

Apparently, the Ekman-layer flow contains a y-component, while the geo-strophic flow is purely in the x-direction. By integrating the continuity equation $\nabla \cdot \mathbf{v} = 0$ for incompressible flow over the thickness of the Ekman layer, with the condition $w_E(z = 0) = 0$, one arrives at

$$w_E(z > \delta) = \frac{1}{2}E^{1/2}\omega_I , \tag{36}$$

with ω_I the z-component of the relative vorticity of the geostrophic interior flow. This is the so-called *'Ekman suction condition'*, which the Ekman layer imposes on the geostrophic flow outside the viscous layer. A non-zero suction velocity is directly associated with a horizontal divergence of the flow in the Ekman layer. By integrating the Ekman contributions $(u_E - u_I)$ and $(v_E - v_I)$ over the thickness of the Ekman layer, one derives the following expressions of the Ekman volume fluxes in the x- and y-directions, respectively:

$$M_x = -\frac{1}{2}(u_I + v_I)E^{1/2}\,, \tag{37a}$$

$$M_y = -\frac{1}{2}(v_I - u_I)E^{1/2}\,. \tag{37b}$$

Note that these are two-dimensional fluxes, with dimensions [$m^2 s^{-1}$], so fluxes per unit length in the perpendicular direction.

For the special case $\mathbf{v}_I = (u_I, 0)$ the Ekman transport components are

$$M_x = -M_y = -\frac{1}{2}u_I E^{1/2}\,, \tag{38}$$

so the Ekman layer accommodates a mass flux in a direction perpendicular to that of the principal flow in the interior.

Note that, since $u_E, v_E \sim O(1)$ and $\delta = E^{1/2}$, the horizontal Ekman fluxes are $O(E^{1/2})$. Likewise, the suction velocity is $w_E \sim O(E^{1/2})$. Although this suction velocity is small compared to the principal horizontal velocity components of the geostrophic interior flow, this Ekman suction velocity may play a crucial role in the development of the geostrophic interior flow. For example, in the case of a cyclonic or anticyclonic vortex above a flat horizontal bottom the Ekman layer leads to a 'blowing' or 'suction' flow, which sets up an internal circulation in the vortex that gradually changes its vorticity structure. From Eq. (36) one sees that positive vorticity ($\omega_I > 0$, as in the core of a cyclonic vortex) implies $w_E(z > \delta) > 0$, i.e. Ekman 'blowing', while the opposite takes place for $\omega_I < 0$: Ekman 'suction'. This mechanism is illustrated in Fig. 2.

Spin-up/spin-down Most vortices, such as the 'stirring' vortices produced in a laboratory experiment, see (27), have a double-signed vorticity structure: a cyclonic vortex core is shielded by a region of negative vorticity. In such a case the Ekman layer produces 'blowing' under the vortex core, while 'suction' is produced under the shielding outer band. As a result a (weak) internal circulation is generated with a radial velocity ($u_I > 0$) inside the vortex. Conservation of angular momentum ($rv_\theta =$ constant) implies that the swirl velocity of fluid elements brought to a larger radius

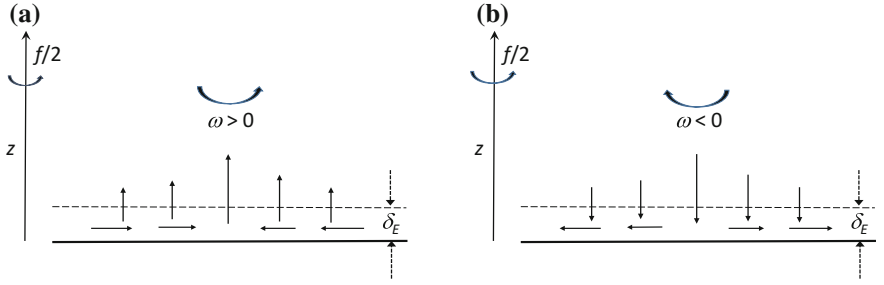

Fig. 2 The *bottom* Ekman layer generates **a** 'blowing' in the core of a cyclonic vortex, and **b** 'suction' in the core of an anticyclonic vortex

decreases. Obviously, this internal circulation driven by the Ekman suction/blowing results in the spin-down of cyclonic vortices. Likewise, anticyclonic vortices will show spin-up by the same mechanism.

Exactly the same mechanism governs the spin-up of fluid in a rotating cylindrical container. Immediately after increasing the container rotation from Ω to $\Omega + \Delta\Omega$ Ekman layers are formed at the bottom and top endplates of the cylinder. As the fluid in the bulk lags behind, it has negative relative vorticity (with respect to the coordinate system corotating with the container): $\omega_I < 0$. As a result Ekman suction will occur at both Ekman layers, thus setting up an internal circulation with $u_I < 0$. The fluid elements thus brought to smaller radii will acquire an increasing azimuthal velocity, until eventually all the fluid rotates with the new rotation speed $\Omega + \Delta\Omega$. The timescale associated with this adjustment process is called the 'Ekman spin-up timescale', which is given by

$$T_E = (\Omega E^{1/2})^{-1} = \frac{H}{(\nu\Omega)^{1/2}} \,. \tag{39}$$

This timescale also applies to more general flow adjustments (spin-up, spin-down) in a fluid layer with depth H.

Wind-Driven Ekman layer Although the above analysis was confined to a geostrophic flow over a solid boundary (such as wind blowing over a ground surface, a sea current flowing over the sea bottom, barotropic vortices in a rotating water-filled laboratory tank with a solid bottom), it may be extended to the case of a stress exerted at the surface of the fluid. This corresponds to the case of a wind stress exerted on the surface of the ocean. An Ekman layer will be formed at the surface, which can be analysed in the same way as for the Ekman at a solid no-slip boundary. Most strikingly, it is then found that the Ekman layer carries a net mass flux *perpendicular* to the direction of the wind stress exerted at the ocean surface: to its right on the northern hemisphere, and to its left on the southern hemisphere. This feature is responsible for so-called 'coastal upwelling', when the prevailing winds in a coastal area induce an Ekman transport directed away from the coast: by mass conservation this flux has to be compensated by upwelling of deeper ocean water.

1.5 The Shallow-Water Approximation

Consider the flow in a layer of fluid over some fixed bottom in a rotating system. For convenience, we adopt a Cartesian coordinate system, with z pointing vertically upwards. Viscous effects are neglected. In view of the background rotation it is assumed that the vertical velocity w is much smaller than the horizontal components, i.e. $u, v \gg w$, and besides that the horizontal flow (u, v) is independent of z. In other words: the fluid moves in the form of vertical columns. These columns may be stretched or squeezed when moving over bottom topography, or due to elevation changes of the free surface, but they do not tilt.

The flow is assumed to be in hydrostatic balance, so that the horizontal pressure gradients are directly linked with the gradients in the free-surface elevation. Writing out the x, y-components of the momentum equation leads, after cross-differentiation and subtraction, to the following relation:

$$\frac{1}{f+\zeta}\frac{D}{Dt}(f+\zeta)+(\frac{\partial u}{\partial x}+\frac{\partial v}{\partial y})=0 \tag{40}$$

with f the Coriolis parameter and

$$\zeta \equiv \omega_z = \frac{\partial v}{\partial x}-\frac{\partial u}{\partial y} \tag{41}$$

the z-component of the relative vorticity. The relation (40) expresses that a horizontal convergence ($\frac{\partial u}{\partial x}+\frac{\partial v}{\partial y}<0$) leads to an increase in the vorticity ($f+\zeta$), while divergence results in a decreasing vorticity. This is directly related to stretching and squeezing of vertical columns in the regions of convergence and divergence, respectively. By integrating the continuity equation in the vertical one derives a relation between the horizontal divergence and the change in the fluid depth:

$$\frac{1}{H}\frac{DH}{Dt}+(\frac{\partial u}{\partial x}+\frac{\partial v}{\partial y})=0\,. \tag{42}$$

Combination of Eqs. (40) and (42) results in

$$\frac{D}{Dt}(\frac{f+\zeta}{H})=0\,, \tag{43}$$

which expresses *conservation of 'potential vorticity'* $(f+\zeta)/H$. This quantity plays an essential role in geophysical fluid dynamics (GFD) theory, and its conservation plays a key role in the understanding of many fundamental phenomena in this field. For example, the north-south motion of a vortex column implies changes in its relative vorticity (even in the case $H=$ constant): according to Eq. (43) a *cyclonic* vortex (with $\zeta>0$) moving northward will become *weaker*, while an *anticyclonic* vortex (with $\zeta<0$) moving in the same direction will *intensify*. Furthermore, the property of conservation of potential vorticity allows for a topographic modelling of the β-effect in the laboratory. Whereas a fluid column (with constant H) in the GFD situation when moving in north/south direction experiences changes in its relative vorticity ζ due to changes in the Coriolis parameter f, a proper bottom topography in a rotating tank (with uniform $f=2\Omega$) may lead to similar changes in ζ when a fluid column moves up or down the topographic slope. Of course, this is all under the assumption of columnar fluid motion and that viscous effects are negligible.

Conservation of potential vorticity also explains the meandering motion of an eastward flow over a topographic ridge. The mechanism works as follows: a fluid column when moving up the mountain ridge is squeezed ($H<H_0$) and thus acquires

negative relative vorticity ($\zeta < \zeta_0 = 0$), implying a deflection of the flow in southward direction. Once it has crossed the mountain ridge the column has obtained its initial length H_0, but it has arrived at a more southern latitude, so that the local f-value has decreased: $f < f_0$. As a consequence the relative vorticity of the flow is then $\zeta > 0$, implying a deflection to the 'left', i.e. in northern direction. The flow (with constant depth H) then sets in a meandering motion in eastern direction, centred around its initial latitude ϕ_0, such that the total vorticity remains conserved. The same mechanism is responsible for the existence of Rossby waves, by virtue of the gradients in the background vorticity.

2 Density Effects

Effects of density differences and gradients play an essential role in environmental and geophysical flows, both on smaller and larger scales. In the atmosphere these density differences may be due to differences in temperature and humidity, while in the ocean, seas, estuaries they are usually due to a combination of temperature and salinity. Additionally, suspended material will also lead to net differences in density.

2.1 Density Currents

Horizontal density differences or gradients usually result in density currents or gravity currents, in which the denser component flows underneath the lighter fluid, or vice versa, in which the lighter fluid flows over the denser fluid. Examples of such density currents are found in the salt-tongue intrusion in a river mouth, where salty sea water flows inland over the river bed, and also in the flow of cold air over the floor of a room when opening a window on a cold winter day. Such flows can be conveniently modelled in the laboratory in a so-called 'lock-exchange' experiment as sketched in Fig. 3.

In this experiment, a vertical barrier initially separates two fluids of different densities ρ and $\rho + \Delta\rho$. When working with water, the density difference is conve-

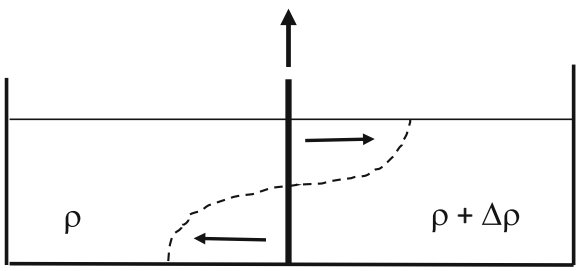

Fig. 3 The lock-exchange experiment

niently obtained by dissolving some amount of salt in one of the fluid compartments). After removing the barrier, a bottom current of denser fluid and a surface current of lighter fluid set in. The gravitational driving force of both currents is of course essentially dependent on the density difference $\Delta\rho$. It is convenient to define the so-called 'reduced gravity' g', which is defined as

$$g' = \frac{\Delta\rho}{\rho} g \,, \tag{44}$$

where g is the magnitude of the gravitational acceleration. In most geophysical or environmental situations $\Delta\rho/\rho$ is very small, implying that $g' \ll g$. For this reason internal gravity currents such as in the lock-exchange experiment (Fig. 3) are much slower than gravitational flows with $\Delta\rho \approx \rho$. Many aspects of gravity currents have been studied by many researchers, see e.g. the review by Simpson (1999). In the early years research on gravity currents was mainly experimental and theoretical modeling was based on the shallow-water approximation. In recent years more sophisticated high-resolution numerical modeling studies became possible, in which even details of the turbulent mixing could be taken into account. See, for example, the work by Härtel et al. (2000).

2.2 *Stability*

Let us now consider the case of a vertical density stratification, as sketched in Fig. 4. Such a configuration, which is easy to realise in the laboratory, can be considered as a model situation of a realistic density distribution, such as encountered in the atmosphere or in oceans, seas and inland waters. In order to analyse possible fluid motion in this density configuration—which is assumed horizontally homogeneous—we perform a hypothetical experiment: we consider a small fluid parcel of density $\rho(z_0)$ at initial level $z = z_0$ and displace it upwards over a small distance ζ. The ambient density in its new position is then equal to $\rho - \delta\rho$, with

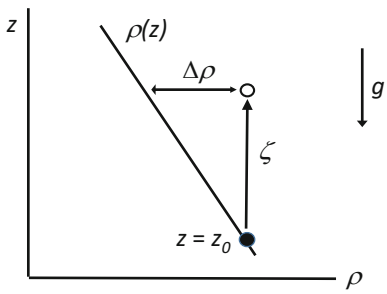

Fig. 4 Schematic configuration of a vertical density stratification

$$\delta\rho = -\frac{d\rho}{dz}\zeta \,. \tag{45}$$

The displaced particle thus experiences a 'restoring' force (per unit mass) equal to $g\delta\rho$, which tends to bring the parcel back to its initial position. Such a stratification is statically stable if $d\rho/dz < 0$. If the density would decrease with depth, the displaced particle would experience a buoyancy force in upward direction, and it would accelerate vertically upwards. Such a stratification with $d\rho/dz > 0$ is thus statically unstable.

As remarked, the restoring gravity force acting on the displaced fluid parcel is equal to $g\delta\rho$, with $\delta\rho$ given by relation (45). As a result, the parcel will experience a vertical acceleration $d^2\zeta/dt^2$, and the equation of motion (excluding viscous effects) is then

$$\rho\frac{d^2\zeta}{dt^2} = g\frac{d\rho}{dz}\zeta \,. \tag{46}$$

This equation can also be written as

$$\frac{d^2\zeta}{dt^2} + N^2\zeta = 0 \,, \tag{47}$$

with N the buoyancy frequency defined as

$$N^2 = -\frac{g}{\rho}\frac{d\rho}{dz} \,. \tag{48}$$

For a statically stable stratification N is real, and the solution of the differential Eq. (47) describes a harmonic oscillation around the equilibrium level $\zeta = 0$: apparently, an initial perturbation in a stably stratified fluid results in wavelike motions. On the other hand, in the case of an unstable stratification the solution has a runaway character: perturbations in an unstably stratified fluid are strongly amplified and result in vigorous overturning motions, and hence mixing.

2.3 Baroclinic Generation of Vorticity

The motion of an incompressible inviscid stratified fluid is governed by the equations of momentum and mass conservation and by the incompressibility condition, respectively:

$$\rho\frac{D\mathbf{v}}{Dt} = \rho[\frac{\partial\mathbf{v}}{\partial t} + (\mathbf{v}\cdot\boldsymbol{\nabla})\mathbf{v}] = -\boldsymbol{\nabla}p + \rho\mathbf{g} \,, \tag{49}$$

$$\rho\frac{D\rho}{Dt} = \frac{\partial\rho}{\partial t} + (\mathbf{v}\cdot\boldsymbol{\nabla})\rho = 0 \,, \tag{50}$$

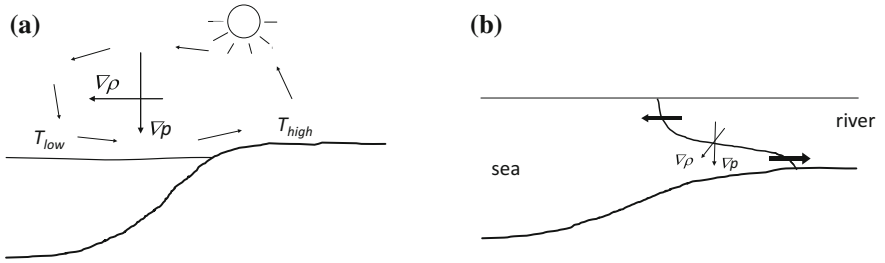

Fig. 5 Baroclinic vorticity generation in two different cases: **a** sea breeze, **b** salt intrusion in a river mouth

$$\nabla \cdot \mathbf{v} = 0 \,. \tag{51}$$

By taking the curl of the momentum equation one derives

$$\frac{D\boldsymbol{\omega}}{Dt} = \frac{\partial \boldsymbol{\omega}}{\partial t} + (\mathbf{v} \cdot \nabla)\boldsymbol{\omega} = (\boldsymbol{\omega} \cdot \nabla)\mathbf{v} + \frac{1}{\rho^2}\nabla\rho \times \nabla p \,, \tag{52}$$

which is usually referred to as the vorticity equation. It describes the change of the vorticity of a fluid element due to stretching/squeezing/tilting of vortex tubes (first term on the r.h.s. of Eq. (52)) and due to baroclinic production (second term on the r.h.s.). The latter effect is present whenever the gradients of density and pressure are not aligned (i.e. $\nabla\rho \times \nabla p \neq \mathbf{0}$). This situation is encountered, for example, in the case of a sea breeze on a sunny day near the coast, and in the case of a salt intrusion into a river mouth (see Fig. 5).

2.4 Boussinesq Approximation

In many geophysical situations the variations in density and pressure may be considered as small perturbations (ρ' and p') with respect to their static equilibrium distributions $\rho_0(z)$ and $p_0(z)$, respectively:

$$\rho(\mathbf{x}, t) = \rho_0(z) + \rho'(\mathbf{x}, t) \;\; , \qquad p(\mathbf{x}, t) = p_0(z) + p'(\mathbf{x}, t) \,. \tag{53}$$

Substitution into Eq. (50) yields

$$(\rho_0 + \rho')\frac{D\mathbf{v}}{Dt} = -\nabla(p_0 + p') + (\rho_0 + \rho')\mathbf{g} \,. \tag{54}$$

Under the assumption of a basic hydrostatic balance, i.e. $0 = -\nabla p_0 + \rho_0 \mathbf{g}$, this equation may be written as

$$(1+\frac{\rho'}{\rho_0})\frac{D\mathbf{v}}{Dt} = -\frac{1}{\rho_0}\nabla p' + \frac{\rho'}{\rho_0}\mathbf{g}\,, \tag{55}$$

For $\rho'/\rho_0 \ll 1$, this equation becomes

$$\frac{D\mathbf{v}}{Dt} = \frac{\partial \mathbf{v}}{\partial t} + (\mathbf{v}\cdot\nabla)\mathbf{v} = -\frac{1}{\rho_0}\nabla p' + \frac{\rho'}{\rho_0}\mathbf{g}\,. \tag{56}$$

In this so-called Boussinesq approximation the density variations only arise in the gravitational term, which is usually referred to as the buoyancy term, which is essentially the reduced gravity.

2.5 *Waves in a Stratified Fluid*

A stratified fluid may support internal waves, as already discussed in Sect. 2.2. In the case of a discrete stratification, for example in the form of two fluid layers separated by a sharp interface, the internal wave motion is easily observed in the motion of the interface. Such internal waves can be analysed in the same fashion as gravity waves at a free fluid surface. In the case of a continuous stratification the analysis of the internal wave motion is more subtle, and one has to start from the Eqs. (49), (50) and (51), expressing conservation of momentum, conservation of mass, and the continuity condition, respectively. In the Boussinesq approximation this set of equations becomes

$$\frac{\partial \mathbf{v}}{\partial t} + (\mathbf{v}\cdot\nabla)\mathbf{v} = -\frac{1}{\rho_0}\nabla p' + \frac{\rho'}{\rho_0}\mathbf{g}\,, \tag{57}$$

$$\frac{\partial \rho}{\partial t} + (\mathbf{v}\cdot\nabla)\rho = 0\,, \tag{58}$$

$$\nabla\cdot\mathbf{v} = 0\,. \tag{59}$$

When additionally restricting the analysis to wave motions with small amplitudes one may linearise the equations of motion. Written in terms of a Cartesian coordinate system (x, y, z), with z vertically upwards, and (u, v, w) the corresponding velocity components, the linearised equations take the following form:

$$\frac{\partial u}{\partial t} = -\frac{1}{\rho_0}\frac{\partial p'}{\partial x}\,, \tag{60}$$

$$\frac{\partial v}{\partial t} = -\frac{1}{\rho_0}\frac{\partial p'}{\partial y}\,, \tag{61}$$

$$\frac{\partial w}{\partial t} = -\frac{1}{\rho_0}\frac{\partial p'}{\partial z} - \frac{\rho' g}{\rho_0}\,, \tag{62}$$

$$\frac{\partial \rho'}{\partial t} - N^2 \frac{\rho_0}{g} w = 0 \,, \tag{63}$$

$$\frac{\partial u}{\partial x} + \frac{\partial v}{\partial y} + \frac{\partial w}{\partial z} = 0 \,. \tag{64}$$

These are five equations for the five variables u, v, w, ρ' and p'. Elimination in favour of w results in

$$\nabla^2 [\frac{\partial^2 w}{\partial t^2}] + N^2 [\frac{\partial^2 w}{\partial x^2} + \frac{\partial^2 w}{\partial y^2}] = 0 \,, \tag{65}$$

with the buoyancy frequency defined as $N^2 = -(g/\rho_0) d\rho_0/dz$. Solution of Eq. (65) for arbitrary $N(z)$ is far from trivial. In order to make the analysis feasible, we consider the most simple case N = constant. For $\Delta\rho \ll \rho_0(z_0)$ this corresponds with a linear stratification of the form $\rho_0(z) = \bar{\rho}\{1 + \alpha(z_0 - z)\}$. We assume wave-like solutions of the following form

$$w(x, y, z, t) = \hat{w} \exp[i(kx + ly + mz - \omega t)] \,, \tag{66}$$

with $\hat{w}$ the constant amplitude, ω the frequency, and $\mathbf{K} = (k, l, m)$ the wave number vector. Substitution of the general solution (66) into (65) yields the following dispersion relationship:

$$\omega^2 = N^2 \frac{(k^2 + l^2)}{(k^2 + l^2 + m^2)} \,. \tag{67}$$

For the most simple case $\mathbf{K} = (k, 0, 0)$ the solution reduces to

$$w(x, t) = \hat{w} \cos(kx - \omega t) \,, \tag{68}$$

which represents waves with frequency $\omega = N$ propagating in the x-direction. The wave period is $T = 2\pi/\omega = 2\pi/N$, while the wavelength is $\lambda = 2\pi/k$. This is a transversal wave: the fluid particles move vertically up and down with velocity w, whereas the wave propagates in the x-direction at phase speed

$$c = \frac{\omega}{k} = \frac{\lambda N}{2\pi} \,. \tag{69}$$

For the general case with $\mathbf{K} = (k, l, m)$ the dispersion relationship (67) can also be written as

$$\frac{\omega}{N} = \pm \frac{(k^2 + l^2)^{1/2}}{(k^2 + l^2 + m^2)^{1/2}} = \pm \cos\theta \,, \tag{70}$$

where θ is the angle between the lines of constant phase and the vertical. Some of the wave characteristics are sketched in Fig. 6.

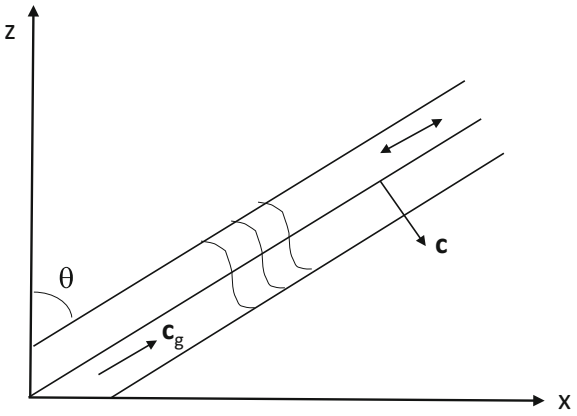

Fig. 6 Schematic illustration of some internal wave characteristics

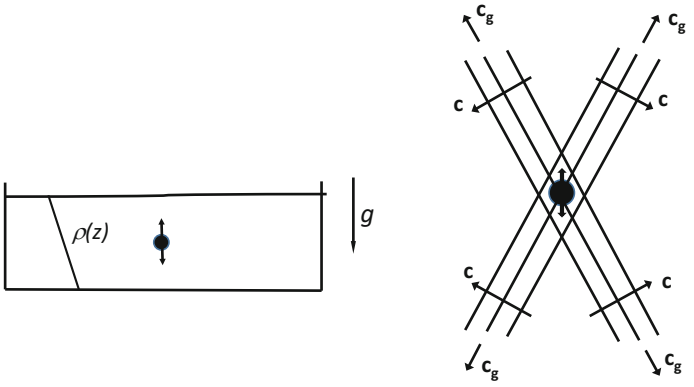

Fig. 7 Internal waves generated by an oscillating cylinder

The discussion can be simplified by choosing the x-axis such that the wave-number vector $\mathbf{K}$ lies in the xz-plane (this can be done without loss of generality), so that in this new coordinate frame we have $\mathbf{K} = (k, 0, m)$. The dispersion relationship (70) then takes the following form:

$$\frac{\omega}{N} = \pm \frac{k}{|\mathbf{K}|} = \pm \cos\theta \,. \tag{71}$$

Waves of this type can be generated in the laboratory by a horizontal cylinder performing vertical oscillatory motions (with frequency ω) in a linearly stratified fluid, see Fig. 7. The internal wave motion, visualised by the shadowgraph technique, is confined to an X-shaped pattern, the legs making an angle θ with the vertical.

2.6 *Vortices in a Stratified Fluid*

Vortex structures are observed both in the atmosphere and in the oceans. These vortices occur on a range of length scales, and often show complicated interactions. In many cases stratification effects play an important role in the dynamical evolution of the vortex structures.

Generation of vortices in the laboratory Vortices in a stratified fluid may be generated in the lab in a number of different ways, some of which are schematically drawn in Fig. 8. Vortices are easily produced by localized stirring with a rotating, bent rod or by using a spinning sphere. In both cases the rotation of the device adds angular momentum to the fluid, which is swept outwards by centrifugal forces. After some time the rotation of the device is stopped, upon which it is lifted carefully out of the fluid. After a short while the turbulence introduced during the forcing has decayed, and a laminar horizontal vortex motion results. The shadowgraph visualizations shown in Fig. 9 clearly reveal the turbulent region during the forcing by the spinning sphere and a more smooth density structure soon after the forcing is stopped. Vortices produced in this way typically have a pancake' shape, with the vertical size of the swirling fluid region being much smaller than its horizontal size. This implies large gradients of the flow in the vertical direction and hence the presence of a radial vorticity component ω_r. Although the swirling motion in these thin vortices is in good approximation planar, the significant vertical gradients imply that the vortex motion is not 2D. Additionally, the strong gradients in z-direction imply a significant effect of diffusion of vorticity in that direction.

Alternatively, a vortex may be generated by tangential injection of fluid in a thin-walled, bottomless cylinder, as also shown in Fig. 9. The swirling fluid volume is released by lifting the cylinder vertically. After some adjustment, again a pancake-like vortex is observed with features quite similar to the vortices produced with the spinning devices.

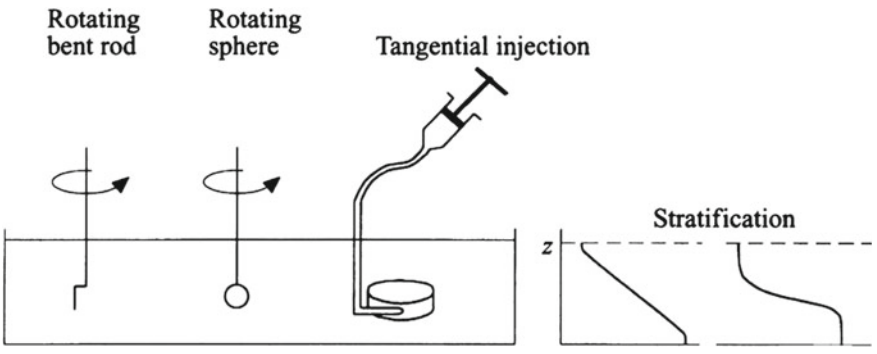

Fig. 8 Generation techniques of vortices in a stratified fluid, see Flór (1994)

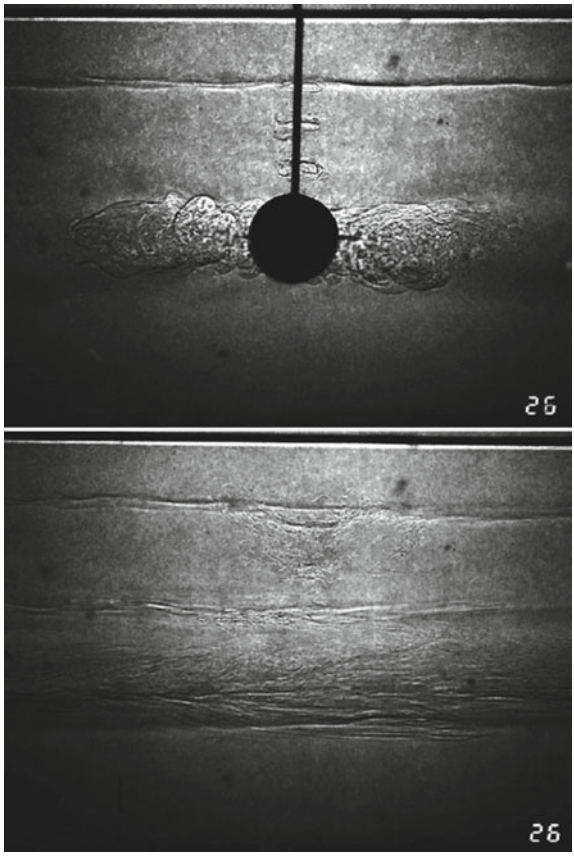

Fig. 9 Shadowgraph visualisation of the flow generated by a rotating sphere **a** during the forcing, and **b** some time after the removal of the sphere. Taken from Flór and van Heijst (1996)

As remarked, due to the large gradients in the vertical direction, diffusion in the vertical is significant and leads to a relatively rapid decay of these planar vortices. In the laboratory experiments by Flór and van Heijst (1996) it was observed that the radial distributions of the swirl velocity v_θ and the vertical vorticity ω_z remained more or less similar during the decay process. This observation triggered the development of a diffusion model by Flór and van Heijst (1996), which was later refined by Trieling and Heijst (1998). These models were rather approximate, as they only considered the time evolution of the vertical vorticity ω_z at the horizontal midplane. Later experiments by Beckers et al. (2001) have revealed the temporal evolution of the vertical and radial density distribution during the vortex decay. Assuming that the vortex motion is dominated by the swirl velocity component v_θ, the non-dimensional r,θ,z-components of the Navier-Stokes equation for an axisymmetric vortex flow are:

$$-\frac{v_\theta^2}{r} = -\frac{\partial p}{\partial r}\,, \tag{72}$$

$$\frac{\partial v_\theta}{\partial t} = \frac{1}{Re}\left(\frac{\partial^2 v_\theta}{\partial r^2} + \frac{1}{r}\frac{\partial v_\theta}{\partial r} - \frac{v_\theta}{r^2} + \frac{\partial^2 v_\theta}{\partial z^2}\right), \tag{73}$$

$$0 = -\frac{\partial p}{\partial z} - \frac{\rho}{F^2}, \tag{74}$$

with $Re = VL/\nu$ the Reynolds number and $F = V/(LN)$ the Froude number, both based on typical horizontal velocity and length scales V and L, respectively. The radial component (72) describes the cyclostrophic balance, see Eq. (20). The azimuthal component (73) describes diffusion of v_θ in the r, z-directions, while the z-component (74) represents the hydrostatic balance. Elimination of the pressure yields the following relation

$$F^2 \frac{2v_\theta}{r}\frac{\partial v_\theta}{\partial z} + \frac{\partial \rho}{\partial r} = 0. \tag{75}$$

This equation describes the 'thermal wind' balance, which relates horizontal density gradients ($\frac{\partial \rho}{\partial r}$) with vertical shear in the cyclostrophic velocity field ($\frac{\partial v_\theta}{\partial z}$). Apparently, the vortex flow field v_θ requires a specific density field to be in a cyclostrophically balanced state. The numerical simulations by Beckers et al. (2001) have confirmed this behaviour. These authors have investigated the adjustment process of vortices initialised in different ways, for an initial state corresponding with

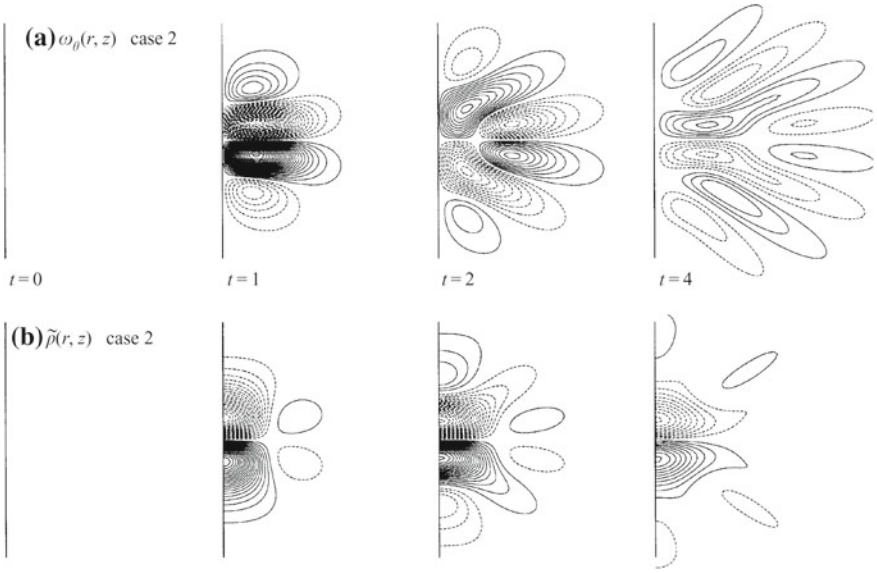

Fig. 10 Contour plots in the r, z-plane of **a** the azimuthal vorticity ω_θ and **b** the density perturbation during the evolution from an initial state with a certain swirl field v_θ without any density perturbation. Numerical simulation by Beckers et al. (2001)

a density perturbation, but without the swirl flow required to satisfy the cyclostrophic balance (72) or for a given swirl flow but without the proper density distribution. In either case, a circulation is set up in the r, z-plane and internal waves are clearly observed. This is nicely illustrated by the simulation results presented in Fig. 10, showing the evolution of (a) the azimuthal vorticity ω_θ and (b) the density perturbation for an initial v_θ distribution without the proper density structure.

The internal waves are generated during adjustment from an initially unbalanced state. During their viscous decay, the dynamical balance of the vortex structure also changes, requiring an adjustment in its density structure. Since that adjustment process is taking place much more gradually, no internal waves are generated in that case.

3 Concluding Remarks

This introduction has shown that background rotation and/or density stratification may lead to remarkable flow behaviour that is often somewhat counter-intuitive. Think of the Taylor-column effect and the transport in the Ekman layers in a rotating fluid, and the dynamics of internal waves in a continuously stratified fluid. In view of the scope of this chapter, this introduction was bound to be very limited, implying that many interesting and important properties of rotating and stratified flows were left untouched. For a more extensive introduction and overview of the dynamics of rotating and stratified flows, the reader may consult the book by Cushman-Roisin and Beckers (2011).

References

M. Beckers, R. Verzicco, H.J.H. Clercx, G.J.F. van Heijst, Dynamics of pancake-like vortices in a stratified fluid: experiments, model and numerical simulations. J. Fluid Mech. **433**, 1–27 (2001)

B. Cushman-Roisin, J.-M. Beckers, *Introduction to Geophysical Fluid Dynamics*, 2nd edn. (Academic Press, 2011)

J.B. Flór, Coherent vortex structures in stratified fluids. Ph.D. Thesis, Eindhoven University of Technology, 1994

J.B. Flór, G.J.F. van Heijst, Stable and unstable monopolar vortices in a stratified fluid. J. Fluid Mech. **311**, 257–287 (1996)

C. Härtel, E. Meiburg, F. Necker, Analysis and direct numerical simulation of the flow at a gravity current head. Part 1. J. Fluid Mech. **418**, 189–212 (2000)

G.J.F. van Heijst, H.J.H. Clercx, Laboratory modeling of geophysical vortices. Annu. Rev. Fluid Mech. **41**, 143–164 (2009)

J.R. Holton, *An Introduction to Dynamical Meteorology* (Academic Press, San Diego, 1992)

R.C. Kloosterziel, G.J.F. van Heijst, An experimental study of unstable barotropic vortices in a rotating fluid. J. Fluid Mech. **223**, 1–24 (1991)

R.C. Kloosterziel, G.J.F. van Heijst, The evolution of stable barotropic vortices in a rotating free-surface fluid. J. Fluid Mech. **239**, 607–629 (1992)

J. Proudman, On the motion of solids in a liquid possessing vorticity. Proc. R. Soc. A Math. Phy. Eng. Sci. **92**(642), 408–424 (1916)
J.E. Simpson, *Gravity Currents in the Environment and the Laboratory* (Cambridge University Press, 1999)
G.I. Taylor, Motions of solids in fluids when the flow is not irrotational. Proc. R. Soc. A Math. Phy. Eng. Sci. **93**(648), 99–113 (1917)
R.R. Trieling, A.H. Linssen, G.J.F. van Heijst, Monopolar vortices in an irrotational annular shear flow. J. Fluid Mech. **360**, 273–294 (1998)
R.R. Trieling, G.J.F. van Heijst, Decay of monopolar vortices in a stratified fluid. Fluid Dyn. Res. **23**, 27–43 (1998)
L. Zavala Sansón, A.C. Barbosa Aguiar G.J.F. van Heijst, Horizontal and vertical motions of barotropic vortices over a submarine mountain. J. Fluid Mech. **661**, 32–44 (2012)

Turbulence and Mixing in Flows Dominated by Buoyancy

Paul F. Linden

Abstract This chapter discusses the physics underlying mixing caused by turbulent flow in a stratified fluid. The ability of the oceans to absorb and redistribute heat from the atmosphere at low latitudes is a crucial aspect of the climate system and accurate quantitative estimates of the mixing rates are critical to the development of reliable climate models. However, mixing occurs at very small scales where molecular diffusion is active and these processes cannot be calculated explicitly in climate models. Thus it is necessary to represent these rates in terms of the larger scale fields and this requires an understanding of the links between these large and small scales. We focus here on laboratory experiments that attempt to make these links and, in particular, represent transport rates in terms of a mixing efficiency. We show that insights can be obtained in this way that point to reasonable representations of mixing in geophysical flows.

1 Introduction

In these lectures we discuss the dynamics of turbulence and mixing in stably stratified fluids. To start we begin by considering what happens when a completely full (spherical) bottle of water is shaken. Shaking a bottle of water dimension L with a speed U inputs energy per unit mass at a rate U^3/L. Shaking at a steady rate implies that the turbulent flow is in a statistically steady state, with eddies ranging in scales from the size of the bottle down to the scale at which the energy input is dissipated by viscosity. This sets up the classical turbulent cascade where energy is input at large scales (the scale of the bottle) and dissipated at some small scale that adjusts to dissipate the energy.

This balance implies that the rate of dissipation per unit mass ϵ is equal to the rate of energy input per unit mass $\epsilon = U^3/L$ and the dimensions of $[\epsilon] = \mathrm{L}^2\mathrm{T}^{-3}$. This implies that motion within the bottle has large scales comparable with the scale

P.F. Linden (✉)
Department of Applied Mathematics and Theoretical Physics, Centre for Mathematical Sciences, University of Cambridge, Cambridge, UK
e-mail: P.F.Linden@damtp.cam.ac.uk

H.J.H. Clercx and G.J.F. Van Heijst (eds.), *Mixing and Dispersion in Flows Dominated by Rotation and Buoyancy*, CISM International Centre for Mechanical Sciences 580,
https://doi.org/10.1007/978-3-319-66887-1_2

of the bottle, and with velocity comparable with the boundary speed. This energy is dissipated by viscosity at small scales generated by turbulence that in turn generate large rates of strain.

A main idea put forward by Kolmogorov in 1941 is that the rate of dissipation is independent of viscosity (Kolmogorov 1941a, b, c): that the scales of the flow simply adjust so that the dissipation achieves the required value to balance the rate of energy input into a system. As illustrated by the bottle, a statistical steady state is reached in which the average speeds in the bottle equilibrate and the work applied by shaking the bottle is balanced by the dissipation. The more viscous the fluid in the bottle, the larger the scales become at which dissipation occurs.

This leads to the notion of the Kolmogorov length scale (or dissipation scale) l_η which must depend on ϵ and ν only. Then, on dimensional grounds since $[\epsilon] = \mathrm{L}^2\mathrm{T}^{-3}$ and $[\nu] = \mathrm{L}^2\mathrm{T}^{-1}$, we obtain $l_\eta = (\nu^3/\epsilon)^{1/4}$. By a similar argument we construct an equivalent velocity scale $u_\eta = (\nu\epsilon)^{1/4}$. Note that $Re_\eta = u_\eta l_\eta/\nu = 1$, indicating that viscous stresses provide dissipation at these velocity and length scales.

Suppose, the bottle contains water and is such that $L = 10\,\mathrm{cm}$ and $U = 10\,\mathrm{cms}^{-1}$. The Reynolds number of the large scale flow $Re \equiv UL/\nu \sim 10^4$, implying that viscous forces are small compared to the fluid inertia at these large scales. Then $\epsilon \sim 100\,\mathrm{cm}^2\mathrm{s}^{-3}$. Water has $\nu \approx 10^{-2}\,\mathrm{cm}^2\mathrm{s}^{-1}$ which implies that $u_\eta \sim 1\,\mathrm{cms}^{-1}$ $l_\eta \sim 10^{-2}$ cm (0.1 mm). So dissipation is taking place on very small scales, even in this relatively weakly forced system and $Re_\eta \equiv u_\eta l_\eta/\nu \sim 1$, implying viscous and buoyancy forces balance at these small scales.

Suppose now that the 'bottle' is stratified—in this case we imagine heating is applied to the top surface and cooling is applied to the bottom surface to maintain some mean (stable) gradient of density with cool water at the bottom and warm water at the top. Suppose that the rate at which heat is added at the top—the heat flux $\mathcal{H}$—is the same as that removed at the bottom so that the average temperature of the fluid within the bottle remains constant in time.

If the fluid is at rest the heat transport from the top to the bottom of the bottle is achieved by conduction with $\mathcal{H} = k\frac{\partial T}{\partial z}$, where k is the conductivity of water and $\frac{\partial T}{\partial z}$ is constant.

Now suppose the bottle is shaken as before. In general any motion will result in warm fluid being lowered and cool fluid being raised (since the warmest fluid was at the top and the coolest at the bottom when at rest). These motions require work to be done against the buoyancy forces, so some of the kinetic energy is now used to maintain the imposed heat flux, and presumably the viscous dissipation is reduced. How much of the input energy is used to work against the buoyancy forces is known as the *mixing efficiency*. Further, overall the vertical temperature gradient is reduced—as a result of mixing by the turbulence.

This thought experiment exemplifies the questions addressed in these lectures. What is the rate of mass and momentum transport in a stably stratified fluid subject to a given forcing? How does the change in potential energy that results from mixing actually occur? What parameters govern the dynamics? We begin by defining the governing equations and examine implications for stratified turbulence.

2 Governing Equations

2.1 Mass and Momentum Conservation

The Navier–Stokes equations for mass and momentum conservation are

$$\rho \frac{Du_i}{Dt} = \frac{\partial \tau_{ij}}{\partial x_j} - g\rho\delta_{i3} \,, \tag{1}$$

$$\boldsymbol{\nabla} \cdot \boldsymbol{u} = 0 \,, \tag{2}$$

$$\frac{D\rho}{Dt} = \kappa \nabla^2 \rho \,, \tag{3}$$

where κ is the molecular diffusivity of the scalar responsible for the density variations ρ. The stress tensor τ_{ij} is

$$\tau_{ij} \equiv -p\delta_{ij} + 2\nu S_{ij} \,, \tag{4}$$

where the rate of strain tensor is

$$S_{ij} \equiv \tfrac{1}{2}\left(\frac{\partial u_i}{\partial x_j} + \frac{\partial u_j}{\partial x_i}\right). \tag{5}$$

2.2 Boussinesq Approximation

In most geophysical and environmental flows density variations are small and we invoke the Boussinesq approximation. Write density $\rho(\mathbf{x}, t)$ as the sum of a constant density ρ_0 and a variable field $\rho^*(\mathbf{x}, t)$, such that

$$\rho(\mathbf{x}, t) = \rho_0 + \rho^*(\mathbf{x}, t) \,, \tag{6}$$

where, under the Boussinesq approximation, $\rho^*(\mathbf{x}, t) \ll \rho_0$. When the fluid is at rest in a gravitational field, lines of constant density are horizontal (normal to the gravity field). Then the density may be written as

$$\rho^*(\mathbf{x}, t) = \overline{\rho}(z) + \rho'(\mathbf{x}, t) \,, \tag{7}$$

where z is the vertical (antiparallel to gravity) coordinate, $\overline{\rho}$ is the background vertical density variation of the stationary fluid, and $\rho'(\mathbf{x}, t)$ is the density perturbation due to fluid motion.

The corresponding pressure field is

$$p(\mathbf{x}, t) = -g\rho_0 z + \overline{p}(z) + p'(\mathbf{x}, t) \,, \tag{8}$$

where the hydrostatic pressure field $\overline{p}(z)$ of the stationary fluid is given by

$$\frac{d\overline{p}}{dz} = -g\overline{\rho} \,. \tag{9}$$

In addition, the pressure consists of a linear variation $-g\rho_0 z$ associated with the hydrostatic component due to the (uniform) reference density ρ_0 and $p'(\mathbf{x}, t)$ is the pressure perturbation corresponding to the fluid motion. Division of Eq. (1) by the density and substitution of Eq. (6) gives

$$\frac{\partial \boldsymbol{u}}{\partial t} + \boldsymbol{u} \cdot \boldsymbol{\nabla} \boldsymbol{u} = -\frac{1}{\rho_0 + \overline{\rho} + \rho'} \boldsymbol{\nabla} p + \boldsymbol{g} + \nu \nabla^2 \boldsymbol{u} \,, \tag{10}$$

with gravity defined according to $\boldsymbol{g} = (0, 0, -g)$. Subtract the hydrostatic pressure field using Eqs. (8) and (9) and obtain

$$\frac{\partial \boldsymbol{u}}{\partial t} + \boldsymbol{u} \cdot \boldsymbol{\nabla} \boldsymbol{u} = -\frac{1}{\rho_0 + \overline{\rho} + \rho'} \boldsymbol{\nabla} p' + \boldsymbol{g} \frac{\rho'}{\rho_0 + \overline{\rho} + \rho'} + \nu \nabla^2 \boldsymbol{u} \,. \tag{11}$$

Define the buoyancy by

$$b \equiv -g \frac{\rho - \rho_0}{\rho_0} \,, \tag{12}$$

so that

$$b^* = B(z) + b' \,. \tag{13}$$

The *Boussinesq approximation* assumes that all density variations are small compared to ρ_0 so that $\overline{\rho} + \rho' \ll \rho_0$, but the limit $\boldsymbol{g} \frac{\rho'}{\rho_0} = b' \delta_{i3}$ is finite. Then the Boussinesq equations become

$$\frac{\partial \boldsymbol{u}}{\partial t} + \boldsymbol{u} \cdot \boldsymbol{\nabla} \boldsymbol{u} = -\frac{1}{\rho_0} \boldsymbol{\nabla} p' + b' \delta_{i3} + \nu \nabla^2 \boldsymbol{u} \,. \tag{14}$$

In this limit the buoyancy equation can be written as

$$\frac{Db'}{Dt} - wN^2 = \kappa \nabla^2 b' \,, \tag{15}$$

where the *buoyancy frequency* is

$$N \equiv \sqrt{-\frac{g}{\rho_0}\frac{\partial \overline{\rho}}{\partial z}} = \sqrt{\frac{\partial B}{\partial z}}\,, \tag{16}$$

with

$$B \equiv -\frac{g}{\rho_0}\overline{\rho}(z)\,. \tag{17}$$

2.3 Scaling

We now examine the relevant balance of terms in the governing equations by defining a horizontal length scale l_h, a vertical length scale l_v, with $\alpha = l_v/l_h$ and a horizontal velocity scale U. We scale horizontal velocity by U, vertical velocity by $UF_h^2/\alpha = UF_v^2\alpha$, b' by U^2/l_v, and p' by $\rho_0 U^2$, where the horizontal Froude number $F_h \equiv U/(Nl_h)$. The vertical Froude number $F_v \equiv U/(Nl_v)$. Then, for $i, j = 1, 2$

$$\frac{\partial u_i}{\partial t} + u_j\frac{\partial u_i}{\partial x_j} + \frac{F_h^2}{\alpha^2}u_3\frac{\partial u_i}{\partial x_3} = -\frac{\partial p}{\partial x_i} + \frac{1}{Re}\left(\frac{1}{\alpha^2}\frac{\partial^2 u_i}{\partial x_3^2} + \frac{\partial^2 u_i}{\partial x_j^2}\right), \tag{18}$$

and

$$F_h^2\left(\frac{\partial u_3}{\partial t} + u_j\frac{\partial u_3}{\partial x_j} + \frac{F_h^2}{\alpha^2}u_3\frac{\partial u_3}{\partial x_3}\right) = -\frac{\partial p}{\partial x_3} + b + \frac{F_h^2}{Re}\left(\frac{1}{\alpha^2}\frac{\partial^2 u_3}{\partial x_3^2} + \frac{\partial^2 u_3}{\partial x_j^2}\right), \tag{19}$$

$$\frac{\partial u_i}{\partial x_i} + \frac{F_h^2}{\alpha^2}\frac{\partial u_3}{\partial x_3} = 0\,, \tag{20}$$

$$\frac{\partial b}{\partial t} + u_j\frac{\partial b}{\partial x_j} + \frac{F_h^2}{\alpha^2}u_3\frac{\partial b}{\partial x_3} = u_3 + \frac{1}{ReSc}\left(\frac{1}{\alpha^2}\frac{\partial^2 b}{\partial x_3^2} + \frac{\partial^2 b}{\partial x_j^2}\right). \tag{21}$$

The other dimensionless parameters are the Reynolds number $Re \equiv Ul_h/\nu$—note this is based on the horizontal length scale l_h—and the Schmidt (Prandtl) number $Sc \equiv \nu/\kappa$.

The ratio of magnitude of the buoyancy force in the vertical momentum equation is

$$F_h^2/\alpha^2 = F_v^2 = \frac{U^2}{N^2 l_v^2} = Ri_O^{-1}\,,$$

where the overall Richardson number is defined as

$$Ri_O \equiv \frac{N^2 l_v}{U^2} \, .$$

In the case of strongly stratified flows $Re \gg 1$, $F_h \ll 1$, the equations reduce to (see Brethouwer et al. 2007)

$$\frac{\partial u_i}{\partial t} + u_j \frac{\partial u_i}{\partial x_j} + \frac{F_h^2}{\alpha^2} u_3 \frac{\partial u_i}{\partial x_3} = -\frac{\partial p}{\partial x_i} + \frac{1}{Re\alpha^2} \frac{\partial^2 u_i}{\partial x_3^2} \, , \; i = 1, 2 \, , \tag{22}$$

$$0 = -\frac{\partial p}{\partial x_3} + b \, , \tag{23}$$

$$\frac{\partial u_i}{\partial x_i} + \frac{F_h^2}{\alpha^2} \frac{\partial u_3}{\partial x_3} = 0 \, , \tag{24}$$

$$\frac{\partial b}{\partial t} + u_j \frac{\partial b}{\partial x_j} + \frac{F_h^2}{\alpha^2} u_3 \frac{\partial b}{\partial x_3} = u_3 + \frac{1}{ReSc\alpha^2} \frac{\partial^2 b}{\partial x_3^2} \, . \tag{25}$$

There is a natural length scale for a flow with characteristic speed U and stratification N—the overturning scale

$$l_{ot} = \frac{U}{N} \, . \tag{26}$$

In the case of large vertical scales $l_v \gg l_{ot}$, then $\alpha \gg F_h$ and, at high Re with $\alpha \gg 1/\sqrt{Re}$, the advective terms can be neglected and the continuity equation becomes $\frac{\partial u_i}{\partial x_i} = 0, i = 1, 2$. Thus the governing equation for the horizontal velocity is purely horizontal which implies the motion is similar to 2D turbulence with an inverse cascade of energy (Lilly 1983). This assumes that l_v is not a free parameter and is imposed such that $F_v \ll 1$.

Large buoyancy Reynolds number We define the *buoyancy Reynolds number* as $Re_B \equiv ReF_h^2$. When $Re_B \gg 1 \Rightarrow$ viscous and diffusive terms can be neglected compared to $O(F_h^2/\alpha^2 = F_v^2)$ terms (if $Sc \gtrsim 1$) and the above equations reduce to

$$\frac{\partial u_i}{\partial t} + u_j \frac{\partial u_i}{\partial x_j} + \frac{F_h^2}{\alpha^2} u_3 \frac{\partial u_i}{\partial x_3} = -\frac{\partial p}{\partial x_i} \, , \; i = 1, 2 \, , \tag{27}$$

$$0 = -\frac{\partial p}{\partial x_3} + b \, , \tag{28}$$

$$\frac{\partial u_i}{\partial x_i} + \frac{F_h^2}{\alpha^2} \frac{\partial u_3}{\partial x_3} = 0 \, , \tag{29}$$

$$\frac{\partial b}{\partial t} + u_j \frac{\partial b}{\partial x_j} + \frac{F_h^2}{\alpha^2} u_3 \frac{\partial b}{\partial x_3} = u_3 \, . \tag{30}$$

These equations are invariant under the transformation (constant γ)

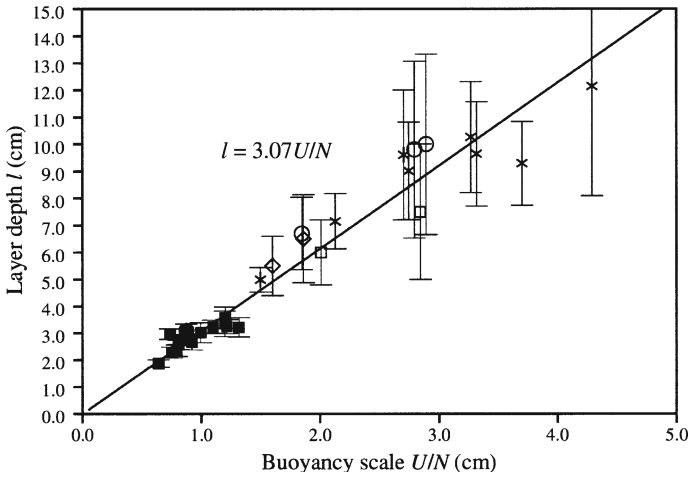

Fig. 1 Layer depths observed in a stably stratified fluid stirred by a rake of *vertical bars*. Courtesy of Holford and Linden (1999)

$$N = \frac{N^*}{\gamma}; \quad x_3 = x_3^* \gamma; \quad u_3 = u_3^* \gamma; \quad b = \frac{b^*}{\gamma}.$$

So by dimensional analysis these equations are self-similar with respect to $x_3 N/U$, see Billant and Chomaz (2001), suggesting that

$$l_v \sim \frac{U}{N} \quad \Rightarrow \alpha \sim F_h \quad F_v \sim 1\,, \tag{31}$$

as has been observed in Holford and Linden (1999) (see Fig. 1).

This also suggests a forward cascade of highly anisotropic 3D turbulence (Lindborg 2006) with $\epsilon \sim U^3/l_h$, in which case

$$Re = \frac{U^4}{\nu\epsilon}\,, \quad F_h = \frac{\epsilon}{NU^2}\,, \quad Re_B = \frac{\epsilon}{\nu N^2}\,. \tag{32}$$

Hence for viscous effects to be unimportant $Re^{-1/2} \ll F_h \ll 1$. Similarly, for diffusion to be unimportant $Re^{-1/2} Sc \ll F_h \ll 1$.

The *Ozmidov scale*, the smallest scale to be affected by buoyancy forces, is defined as $L_O \equiv \sqrt{\frac{\epsilon}{N^3}}$. Thus

$$\frac{l_h}{L_O} = F_h^{-3/2} \quad \text{and} \quad \frac{l_v}{L_O} = F_h^{-1/2}\,. \tag{33}$$

Since $F_h \ll 1$ (Lindborg 2006 suggests $F_h < 0.02$) this shows that the Ozmidov scale sets lower limits in the horizontal as well as the vertical on scales of stratified turbulence. Note further that

$$Re_B = \left(\frac{L_O}{l_\eta}\right)^{4/3}, \tag{34}$$

so the condition $Re_B \gg 1$ means there is a significant range of scales between the Ozmidov scale and the Kolmogorov scale.

Internal waves Consider the dimensional form of (18) in the limit $F_h \to 0$ and linearise (with $v = u_2 = 0$):

$$\frac{\partial u}{\partial t} = -\frac{\partial p}{\partial x}, \tag{35}$$

$$0 = -\frac{\partial p}{\partial z} + b, \tag{36}$$

$$\frac{\partial u}{\partial x} + \frac{\partial w}{\partial z} = 0, \tag{37}$$

$$\frac{\partial b}{\partial t} = wN^2, \tag{38}$$

and write $(u, w, p, b) \propto e^{i(kx+mz-\omega t)}$. Then the dispersion relation is

$$\omega^2 = \frac{k^2}{m^2}N^2, \tag{39}$$

which is the usual dispersion relation of long internal gravity waves when $k \ll m$. Thus these waves are *slow* $c = N/m$, and have large horizontal scales compared to vertical scales. Internal waves have $\omega \in [0, N]$. So even if $N \gg u/l_h$, ($F_h \ll 1$) there are slow internal waves with $\omega \sim u/l_h$ and corresponding vertical wavenumber $m \sim N/U$. This implies that internal waves can interact with horizontal advective motions, and may be responsible for organising the turbulence and promoting the formation of layers (Thorpe 2016). This is likely the reason why the vertical scale of the layers in the grid-stirred experiments of Holford and Linden (1999) (see Fig. 1) have a scale $\sim 3U/N$, which is the vertical half-wavelength of long internal waves travelling at the same speed as the grid.

3 Richardson Number

The stability of stratified shear flow is characterised by a measure of the stabilising effect of stratification and the destabilising effect of shear. There are several measures of this ratio, all called a Richardson number—which can also be considered as a ratio of the potential energy required to mix the fluid to that supplied by the velocity field. In terms of bulk properties, a flow with a velocity difference ΔU, and buoyancy difference ΔB, across a region of height H (Fig. 2), the *overall* (bulk) Richardson number is defined, in terms of the external parameters as

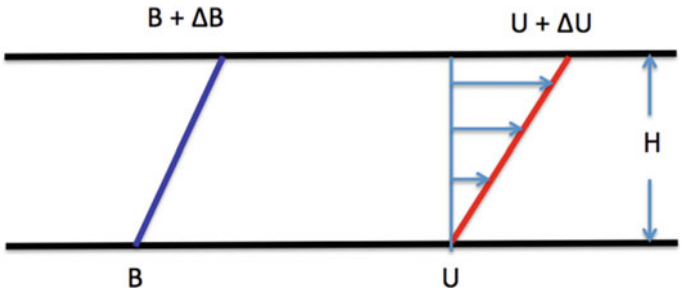

Fig. 2 A schematic of stratified shear flow showing mean constant gradients of buoyancy B and velocity U

$$Ri_O \equiv \frac{\Delta B H}{\Delta U^2} \,. \tag{40}$$

In many situations $Ri_O \gg 1$, suggesting that there is not sufficient energy to allow for turbulent mixing. For example, considering the ocean as a whole $\Delta U \sim 1$ ms^{-1}, $\Delta B \sim 0.25$ ms^{-2}, and $H \sim 4000$ m, implying $Ri_O \sim 10^3$. The way round this dilemma is to consider the *gradient* Richardson number, defined in terms of the local gradients of buoyancy and velocity

$$Ri_g \equiv \frac{N^2}{\left(\frac{\partial U}{\partial z}\right)^2} \,. \tag{41}$$

Since the velocity gradient is squared it is possible to choose any value of Ri_g (such as 0.2, say, consistent with the Miles-Howard stability criterion (Miles 1961; Howard 1961 stability criterion) *throughout the fluid* regardless of the value of Ri_O (Turner 1973).

4 Turbulent Kinetic Energy Equation

The turbulent kinetic energy (TKE) equation is formed by multiplying Eq. (1) by u_i to give

$$\tfrac{1}{2}\frac{\partial u_i u_i}{\partial t} + u_i u_j \frac{\partial u_i}{\partial x_j} = wb + u_i \frac{\partial \tau_{ij}}{\partial x_j} \,. \tag{42}$$

Define the kinetic energy per unit mass $E \equiv \frac{1}{2}u_i u_i$ and note that with $u_j \frac{\partial u_i^2}{\partial x_j} = 2u_i u_j \frac{\partial u_i}{\partial x_j}$, then

$$\frac{DE}{Dt} = wb + \frac{1}{\rho_0} u_j \frac{\partial p}{\partial x_j} + \tfrac{1}{2}\nu \left(\frac{\partial u_i}{\partial x_j} + \frac{\partial u_j}{\partial x_i} \right). \tag{43}$$

Some elementary algebra gives

$$u_i \frac{\partial \tau_{ij}}{\partial x_j} = \frac{\partial u_i \tau_{ij}}{\partial x_j} - \tau_{ij} \frac{\partial u_i}{\partial x_j} ,$$
$$= \frac{\partial u_i \tau_{ij}}{\partial x_j} - \tfrac{1}{2} \tau_{ij} \left(\frac{\partial u_i}{\partial x_j} + \frac{\partial u_j}{\partial x_i} \right) = \frac{\partial u_i \tau_{ij}}{\partial x_j} - \tau_{ij} S_{ij} .$$

Substitute for τ_{ij} gives

$$\frac{DE}{Dt} + \nabla \cdot \boldsymbol{T} = wb - 2\nu S_{ij} S_{ij} , \tag{44}$$

where

$$T_i = = \frac{1}{\rho_0} u_i p - 2\nu u_i S_{ij} . \tag{45}$$

Integrate Eq. (44) over a fixed control volume V, with surface ∂V, which gives:

$$\frac{\partial}{\partial t} \int_V E dV + \int_{\partial V} (u_j E + T_j) n_j dA = \int_V wb dV - 2\nu \int_V S_{ij} S_{ij} dV . \tag{46}$$

If V is such that $u_i = 0$ on the boundary, or the domain is periodic (the outward normals on the periodic faces cancel) then

$$\int_{\partial V} (u_j E + T_j) n_j dA = 0 ,$$

and the change in kinetic energy E is due to:

- the buoyancy flux $\int_V wb dV$, which may be positive or negative;
- viscous dissipation $\epsilon \equiv -2\nu \int_V S_{ij} S_{ij} dV$, which is negative definite.

At this point it is convenient to define the average $\langle \cdot \rangle$ as an average over space and/or time, or an ensemble over different realizations. Then any variable A can be written as a sum of the mean $\langle A \rangle$ and the variation a about the mean, such that

$$A = \langle A \rangle + a ,$$

where

$$\langle a \rangle = 0 .$$

Then the mean kinetic energy $\langle E \rangle \equiv \frac{1}{2} \langle \boldsymbol{U} \rangle \cdot \langle \boldsymbol{U} \rangle$ and the TKE $k \equiv \langle \frac{1}{2} \boldsymbol{u} \cdot \boldsymbol{u} \rangle$ satisfy

$$\frac{\overline{D}E}{\overline{D}t} + \nabla \cdot \langle \boldsymbol{T} \rangle = -P + WB - \overline{\epsilon} \,, \tag{47}$$

$$\frac{\overline{D}k}{\overline{D}t} + \nabla \cdot \boldsymbol{t} = P + \langle wb \rangle - \epsilon \,. \tag{48}$$

The production term P is given by

$$P = -\langle u_i u_j \rangle \frac{\partial \langle U_i \rangle}{\partial x_j} \,,$$

which represents the transfer of kinetic energy from the mean flow to the turbulence. The quantity $-\langle u_i u_j \rangle$ is known as the *Reynolds stress*.

In stratified flow there is also production/dissipation of TKE through the *buoyancy flux* $\mathcal{B} = -\langle wb \rangle$, and TKE is generated/lost when $\langle wb \rangle \neq 0$. TKE is generated when buoyant fluid ($b > 0$) is advected upwards ($w > 0$) and heavy fluid ($b < 0$) advected downwards ($w < 0$). In both cases the movement of the fluid lowers the centre of mass of the fluid and so releases potential energy and converts it to kinetic energy. TKE is lost when buoyant fluid ($b > 0$) is advected downwards ($w < 0$) and heavy fluid ($b < 0$) advected upwards ($w > 0$)—as in the shaking bottle. In both cases the movement of the fluid raises the centre of mass of the fluid and so converts kinetic energy to potential energy.

5 Stirring Versus Mixing

Since raising heavy fluid increases the potential energy, then if this fluid is then allowed to drop, the potential energy is lowered and the energy converted back into kinetic energy. Thus the *loss of kinetic energy is only irreversible* if the fluid that is raised is *mixed* with the surrounding fluid so that it cannot fall again. Mixing, like dissipation, is an irreversible molecular process that occurs on small scales and it depends on the diffusivity κ of the scalar field (temperature or concentration of a solute) that is responsible for the density variations in the fluid.

Take b times the buoyancy Eq. (3)

$$b\frac{Db}{Dt} = \kappa b \nabla^2 b, \tag{49}$$

and average to obtain

$$\frac{D\langle b^2 \rangle}{Dt} = 2\kappa \langle b \nabla^2 b \rangle = -2\kappa \langle |\nabla b|^2 \rangle \equiv -\chi \,, \tag{50}$$

Table 1 Schmidt numbers for heat in air and heat and salt in water

	Sc
Heat in air	0.7
Heat in water	7
Salt in water	700

where we have used $b\frac{\partial^2 b}{\partial x_i^2} = \frac{\partial}{\partial x_i}\left(b\frac{\partial b}{\partial x_i}\right) - \frac{\partial b}{\partial x_i}\frac{\partial b}{\partial x_i}$ and noted that the first term is always zero when averaged over a volume as either $b = 0$ or $\frac{\partial b}{\partial x_i} = 0$ on the boundary of the domain.

5.1 Batchelor Scale

By an argument similar to that for the Kolmogorov length scale irreversible mixing also occurs at small scales. In this case the Batchelor scale l_B (Batchelor 1958) is the size over which a scalar will diffuse during the time $\tau_\eta = l_\eta/u_\eta$ it takes for a turbulent eddy to dissipate. Thus

$$l_B = \sqrt{\kappa\tau_\eta} = \sqrt{\frac{\kappa l_\eta}{u_\eta}} = \left(\frac{\kappa^2\epsilon}{\nu}\right)^{1/4}.$$

The ratio of the Kolmogorov scale to the Batchelor scale is

$$\frac{l_\eta}{l_B} = \sqrt{\frac{\nu}{\kappa}} \equiv Sc^{1/2},$$

where Sc is the Schmidt/Prandtl number (Table 1 for typical values).

6 Stratified Bottle

We return to the stratified 'bottle'—with heating applied to the top surface and cooling applied to the bottom surface to maintain some mean gradient of density. We denote the strength of the stratification by the buoyancy frequency $N \equiv \sqrt{\frac{\partial B}{\partial z}}$. (In practice this would be achieved by say imposing a constant heat flux—a so-called Neumann conditions on the boundaries). Suppose in these circumstances it is possible to maintain a constant density (temperature) gradient. Then the buoyancy flux $\mathcal{B}$ would be given by

$$\mathcal{B} = -\langle wb \rangle = K_B N^2 \,, \tag{51}$$

which defines the 'eddy diffusivity' K_B of buoyancy. Further the TKE Eq. (48) becomes

$$0 = P - \mathcal{B} - \epsilon \,. \tag{52}$$

Thus the TKE produced by P either goes into maintaining this buoyancy flux $\mathcal{B} > 0$ or into dissipation.

7 Mixing Efficiency

An important question in stratified turbulence is the amount of energy that goes into *irreversibly* changing the density field. Equation (52) can be interpreted as a division of energy flow into work against buoyancy and dissipation by viscosity and we define the mixing efficiency $\mathcal{E}$

$$\mathcal{M} \equiv \frac{\mathcal{B}}{P} = \frac{\mathcal{B}}{\mathcal{B} + \epsilon} \,. \tag{53}$$

In Eq. (53) it is assumed that the buoyancy flux represents an irreversible conversion of kinetic energy to potential energy so that it can also be written as

$$\mathcal{M} \equiv \frac{\mathcal{B}}{P} = \frac{\chi}{\chi + \epsilon} \,. \tag{54}$$

In an unstratified flow $\mathcal{M} = 0$ and for weak stratification $\chi \ll \epsilon$, so that

$$\mathcal{M} \sim \frac{\chi}{\epsilon} \,.$$

Thus the mixing efficiency increases linearly with the imposed buoyancy flux for small fluxes. This behaviour is confirmed in recent DNS studies in stratified plane Couette flow up to $Ri = 0.2$, see Fig. 3.

A major question is: what happens to $\mathcal{M}$ as the imposed buoyancy flux increases? Does $\mathcal{M}$

- increase monotonically?
- reach an asymptotic value?
- reach a maximum and then decrease for further increases in the buoyancy flux?

Flux Richardson number We now consider a stability parameter in terms of vertical fluxes of buoyancy and momentum. The turbulent kinetic energy for a statistically steady flow can be written as relation (52)

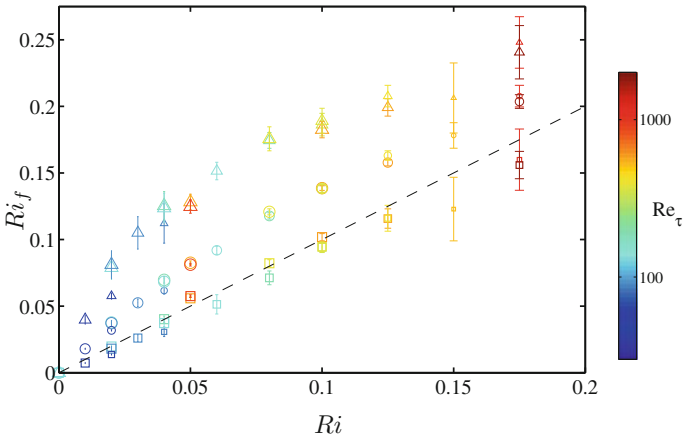

Fig. 3 Flux Richardson number as a function of the gradient Richardson number in a DNS calculation of stratified plane Couette flow. Courtesy of Deusebio et al. (2015)

$$0 = P - \mathcal{B} - \epsilon \, .$$

The *flux* Richardson number Ri_f is defined by

$$Ri_f \equiv \frac{\mathcal{B}}{P} \, , \tag{55}$$

and, since $\epsilon > 0$, $Ri_f < 1$. Assuming $\mathcal{B} = \chi$ so that it is associated with irreversible mixing

$$Ri_f = \mathcal{M} \, , \tag{56}$$

and the flux Richardson number is equivalent to the mixing efficiency.

The form of the 'flux' *versus* 'stability', defined in a somewhat imprecise sense, has been the subject of significant investigation. As indicated by definition (55) the flux is expected to increase with stability for weakly stratified flows, and it may be reasonable to expect the flux to decrease in very stable flows, because vertical motions are inhibited. This form is sketched in Fig. 4 and this form has been measured in experiments where a horizontal grid falls freely through a sharp density interface, see Linden (1980). However, this form of the curve is not universally agreed upon.

If the form of the curve does look like that shown in Fig. 4, then this implies, as first argued by Phillips (1972), that for weakly stratified flows—on the left of the maximum flux, the 'left flank'—perturbations in the density gradient will be reduced, while at high stabilities on the 'right flank' perturbations will be increased by the flux convergence leading to layered stratification. Consequently, there is continued interest in determining the form of the mixing efficiency curve (Fig. 5).

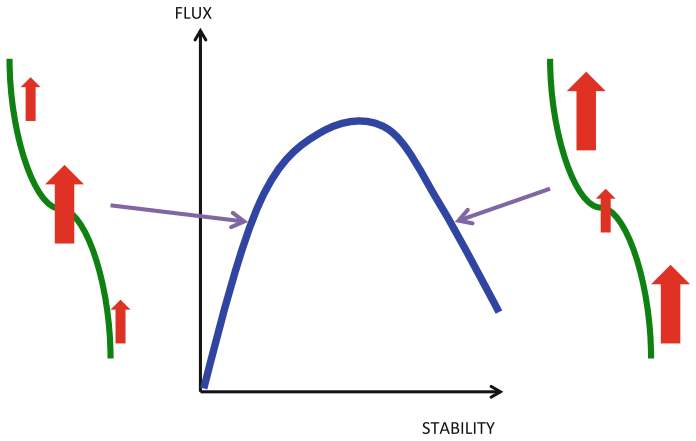

Fig. 4 Schematic of a general flux–stability *curve*. On the *left* 'flank', gradients weaken while on the *right* 'flank' gradients increase and layers form (Phillips (1972); Posmentier (1977))

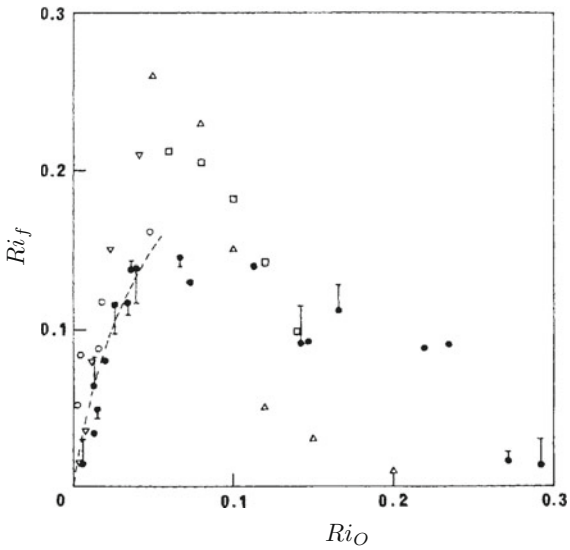

Fig. 5 Mixing efficiency—compilation of different experiments. Courtesy of Linden (1979)

8 Boundary Layer Similarity Theory

8.1 Unstratified Boundary Layer

Consider steady flow $\boldsymbol{U} = (U(z), 0, 0)$ producing a stress τ on a horizontal surface $z = 0$. The stress gives a velocity scale—the friction velocity

$$u_* \equiv \sqrt{\frac{\tau}{\rho}} \, .$$

Assuming the stress (and, therefore, u_*) is constant and that mean flow profile depends only on u_* and the distance z from the boundary, dimensional analysis implies

$$\frac{\mathrm{d}U}{\mathrm{d}z} = \frac{u_*}{kz} \, ,$$

where k (dimensionless and $\approx$0.4) is von Kármán's constant. Then

$$U(z) = \frac{u_*}{k} \ln(z/z_0). \tag{57}$$

—the 'law of the wall' or logarithmic boundary layer: z_0 is the roughness length.

Eddy viscosity The turbulent transfer of momentum can be characterised by an 'eddy viscosity' defined in terms of the stress and the mean velocity gradient

$$\tau \equiv \rho K_M \frac{\mathrm{d}U}{\mathrm{d}z} \, . \tag{58}$$

Then in the logarithmic boundary layer

$$K_M = k u_* z \, , \tag{59}$$

which increases linearly with distance from the boundary.

In the constant-stress layer $-\langle uw \rangle = {u_*}^2$ and the production term $\mathcal{P} = {u_*}^2 \frac{\mathrm{d}U}{\mathrm{d}z}$. Hence

$$\mathcal{P} = K_M \left(\frac{\mathrm{d}U}{\mathrm{d}z} \right)^2 \, . \tag{60}$$

8.2 Stratified Boundary Layer

Now suppose there is a stabilising buoyancy flux $\mathcal{B}$ imposed on the boundary $z = 0$. This provides another length scale, the *Monin-Obukhov* length L_{MO}

$$L_{MO} \equiv -\frac{{u_*}^3}{k\mathcal{B}} \, .$$

If the buoyancy flux is stabilising $\mathcal{B} < 0$ and $L_{MO} > 0$ is the length at which the flow feels the effects of the stratification. Dimensional analysis now gives

$$\frac{\mathrm{d}U}{\mathrm{d}z} = \frac{u_*}{kz}\phi_M\left(\frac{z}{L_{MO}}\right),$$

where ϕ_M is an unknown dimensionless function and

$$K_M = \frac{ku_*z}{\phi_M}\,. \tag{61}$$

Stratified boundary layer: weak stratification In the case of weak stratification $z/L_{MO} \ll 1$, then a Taylor series expansion gives $\phi_M \approx 1 + z/L_{MO}$ and

$$U(z) = \frac{u_*}{k}(\ln(z/z_0) + \alpha z/L_{MO})\,, \tag{62}$$

where $\alpha \approx 5$ is an empirical constant. Then

$$K_M \sim ku_*z(1 - \alpha z/L_{MO})\,, \tag{63}$$

so momentum diffusivity is reduced. In this case we can define an eddy diffusivity for buoyancy K_B, see Eq. (51), such that

$$\mathcal{B} \equiv -K_B N^2\,. \tag{64}$$

With Eqs. (60) and (64) the mixing efficiency is

$$\mathcal{M} = Ri_f = \frac{K_B}{K_M}\frac{N^2}{\left(\frac{\mathrm{d}U}{\mathrm{d}z}\right)^2} = \frac{K_B}{K_M}Ri_g\,. \tag{65}$$

Stratified boundary layer: moderate stratification We have defined Ri_g, Ri_f, K_M, K_B. In an analogous manner to ϕ_M we can define ϕ_B, and gradient Richardson number can be written as

$$Ri_g \equiv \frac{N^2}{\left(\frac{\partial U}{\partial z}\right)^2} = \frac{z}{L_{MO}}\frac{\phi_B}{\phi_M^2}\,. \tag{66}$$

Then Eq. (65) implies

$$Ri_f = \frac{K_M}{ku_*L_{MO}} = \frac{z}{L_{MO}}\frac{1}{\phi_M}\,. \tag{67}$$

Thus

$$\frac{z}{L_{MO}} = \phi_M Ri_f\,, \quad \text{and} \tag{68}$$

$$\phi_M = 1 + \alpha\phi_M Ri_f\,. \tag{69}$$

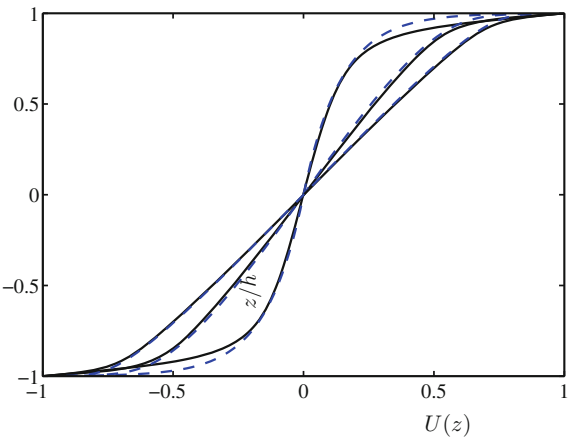

Fig. 6 Velocity profiles obtained from DNS computations (*solid curves*) and Monin-Obukhov theory (*dashed curves*) of stratified plane Couette flow for $(Re_O, Ri_O) = (2150, 0)$; (12650, 0.08); (35000, 0.125). Note the progression to a linear profile with increasing stability. Courtesy of Deusebio et al. (2015)

In turn, this implies

$$\phi_M = \frac{1}{1 - \alpha Ri_f} \,. \tag{70}$$

Hence $\phi_M \to \infty$, $K_M \to 0$ as $Ri_f \to 0.2$. This suggests that the limit on mixing efficiency may be significantly smaller than 1.

Recent direct numerical simulations (DNS) show close agreement with the forms predicted by Monin-Obukhov theory, see Fig. 6, in this stability range.

Stratified boundary layer: strong stratification In the case of strong stratification $z/L_{MO} \gg 1$, the distance z from the boundary is no longer relevant. The flow depends only on u_* and L_{MO}, so dimensionally

$$\frac{\partial U}{\partial z} = k_1 \frac{u_*}{L_{MO}} \,, \tag{71}$$

$$N^2 = k_2^2 \frac{{u_*}^2}{{L_{MO}}^2} \,. \tag{72}$$

Thus the profiles of velocity and density are linear with height and the gradient Richardson number Ri_g

$$Ri_g \equiv \frac{N^2}{\left(\frac{\partial U}{\partial z}\right)^2} = \frac{k_2^2}{k_1^2} = Ri_e \,, \tag{73}$$

where Ri_e is an '*equilibrium*' Richardson number (Turner 1973). Again this is consistent with recent DNS calculations (see Fig. 6).

Further

$$K_M = \frac{u_* L_{MO}}{k_1} \; ; \quad K_B = \frac{u_* L_{MO}}{k_2^2} \; ; \quad \frac{K_B}{K_M} = \frac{k_1}{k_2^2} \, , \tag{74}$$

so that the 'turbulent Prandtl number' is a constant (not necessarily equal to one).

Large bulk Richardson number Consider, as above, flow in a domain in which $Ri_O \equiv \frac{\Delta B H}{(\Delta U)^2} \gg 1$. Then there are three possibilities:

1. $Ri_O \ll Ri_e$: the shear is too large for very stable scaling to apply so return to z/L_{MO} scaling;
2. $Ri_O = Ri_e$: this case can match with linear gradients of density and velocity throughout the domain;
3. $Ri_O \gg Ri_e$: need non-uniform velocity and density gradients. Can match Ri_e throughout since

$$\left(\frac{\Delta U}{H}\right)^2 \ll \overline{\left(\frac{\partial U}{\partial z}\right)^2} \, ,$$

which implies layers with weak shears and small density gradients separated by interfaces with large shears and strong density gradients.

9 Layers and Interfaces

From Eq. (71) the vertical shear can be written as

$$\frac{\partial U}{\partial z} = \frac{u_*}{L_{MO}} = \frac{k_1 \mathcal{B}}{{u_*}^2} \propto \frac{\text{buoyancy flux}}{\text{momentum flux}} \, .$$

This implies that:

- interfaces: strong shear $\Rightarrow$ small momentum flux compared to buoyancy flux;
- layers: weak shear $\Rightarrow$ large momentum flux compared to buoyancy flux.

If the buoyancy flux is constant with depth, then there needs to be an alternative way of transferring momentum across the layers. This can be provided by internal waves—which transfer momentum but not buoyancy (unless they break).

9.1 Energetics

Following (Turner 1973) let $r = \frac{\text{interface thickness}}{\text{layer thickness}}$. If the layers have constant density and velocity and $Ri_g = Ri_e$ in the interfaces (see Eq. 73), then

$$r \equiv r_0 = \frac{Ri_e}{Ri_O} \,. \tag{75}$$

Consider changes in energy from linear gradients $u = \alpha z$, $\rho = \rho_0 - \beta z$ to a well-mixed layer of depth h bounded by sharp steps above and below. Then

$$\Delta KE = T = \frac{1}{24}\alpha^2 h^3 \,,$$
$$\Delta PE = V = -\frac{1}{12} g\beta h^3 \,,$$

with KE representing the kinetic energy and PE the potential energy. These balance when $Ri_O = g\beta/\alpha^2 = \frac{1}{2}$. If the interface has a finite thickness (with $r = r_0$ and $Ri_g = Ri_e$) then this requires

$$Ri_O = \tfrac{1}{2}(Ri_e + 1) \,. \tag{76}$$

For larger values of Ri_O there is not enough local kinetic energy to mix and some form of external energy supply is needed, which leads to the idea of 'external mixing processes' (Turner 1973).

The interfacial Reynolds number Re_i based on the velocity difference and interfacial length scale r is given by

$$Re_i = \frac{Ri_e}{3Ri_e + Ri_O} \frac{Uh}{\nu} \,. \tag{77}$$

For large $Ri_O \sim N^2 h/U^2 \gg Ri_e$ this gives

$$Re_i \sim \frac{U^3/h}{\nu N^2} \sim \frac{\epsilon}{\nu N^2} = Re_B \,, \tag{78}$$

which is the buoyancy Reynolds number. Thus the interfacial Reynolds number in this limit is equivalent to the buoyancy Reynolds number.

10 Stratified Mixing Box Experiment

An experiment that exemplifies external mixing is the stratified mixing box first studied by Turner (1968). The experiment consists of a two-layer fluid where one or both of the layers is stirred by an oscillating horizontal grid, see Fig. 7.

In this case fluid is entrained across the interface, reducing the density difference between the two layers with time, and raising the centre of mass of the system. The rate of entrainment is characterised by an entrainment velocity u_e, which is the velocity the interface would move if only one of the layers was stirred. As shown in

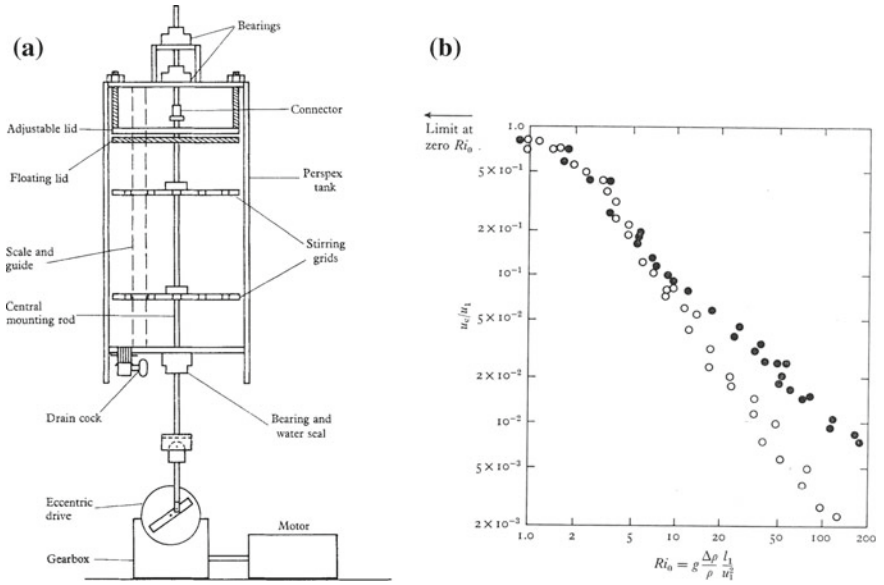

Fig. 7 **a** A sketch of the stratified mixing box showing the case when both layers are stirred. **b** The entrainment rate as a function of the interfacial Richardson number. $\circ - Pr = 700, \bullet - Pr = 7$. Courtesy of Turner (1968)

Fig. 7 the entrainment rate is a function of the stability of the interface, here described in terms of an interfacial Richardson number

$$Ri_i = \frac{g\Delta\rho l}{\rho_0 u^2} ,$$

where $\Delta\rho$ is the density jump across the interface and u and l are the turbulent velocity and integral length scale, respectively, *at the interface*.

We can calculate the mixing efficiency by noting that the rate of increase in PE = $\frac{1}{2}bu_eH^2$ and the rate of supply of KE = $\frac{1}{2}u^3H$. Then the ratio is the flux Richardson number

$$Ri_f = \frac{u_e}{u}\frac{bH}{u^2} \propto \frac{u_e}{u}Ri_i . \tag{79}$$

Given that $u_e/u \propto Ri_i^{-n}$, see Fig. 7,

$$Ri_f \propto Ri_i^{1-n} . \tag{80}$$

Thus for $n < 1$, R_f increases with Ri_i and interfaces decay, while for $n > 1$, R_f decreases with Ri_i and interfaces sharpen. This behaviour can been seen in Fig. 8 where the interface remains sharp at $Ri_i = 9.4$, but is smeared out at $Ri_i = 3.4$. Note

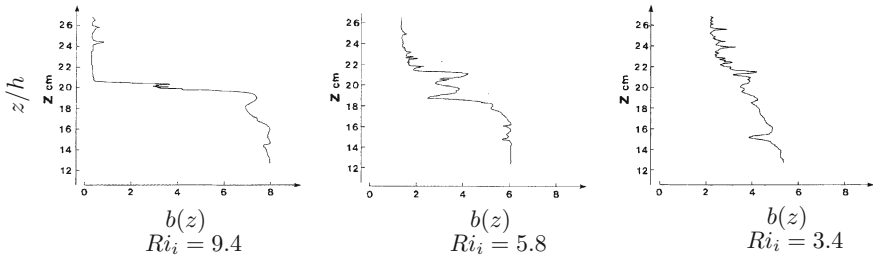

Fig. 8 Density profiles for salt experiments in the stratified mixing box at different interfacial Richardson numbers. Courtesy of Linden (1979)

that $n > 1$ at $Ri_i = 9.4$, but $n < 1$ at $Ri_i = 3.4$ (Fig. 7), consistent with the expected behaviour. It is also worth noting that Turner's experiments show that entrainment is different for fluid stratified with salt ($Pr = 700$) compared to that stratified with heat ($Pr = 7$). Recent work on mixing in a stratified shear flow shows a similar dependence.

11 Mixing Efficiency from Available Potential Energy

In some circumstances it is possible to calculate the mixing efficiency $\mathcal{M}$ from changes in available potential energy (PE_a). In situations where a complete mixing event life-cycle occurs this is probably the most unambiguous way of calculating $\mathcal{M}$. We will discuss two cases: flows driven by Rayleigh-Taylor instability and gravity currents generated by lock exchange.

11.1 Tall Rayleigh-Taylor Instability

Rayleigh-Taylor instability (RTI) occurs when dense fluid is placed over less dense fluid under gravity. It drives mixing as the heavy fluid falls and the light fluid rises and it takes a particularly simple form in a tall tube. As can be seen in Fig. 9, the mixing front grows parabolically in time and the final state is one in which the fluid is essentially mixed throughout the tube.

In this case it is possible to calculate the maximum mixing efficiency when all the fluid is mixed, and in the final state all the fluid in the tube is at the mean density of the initial fluid.

The initial potential energy PE_i is

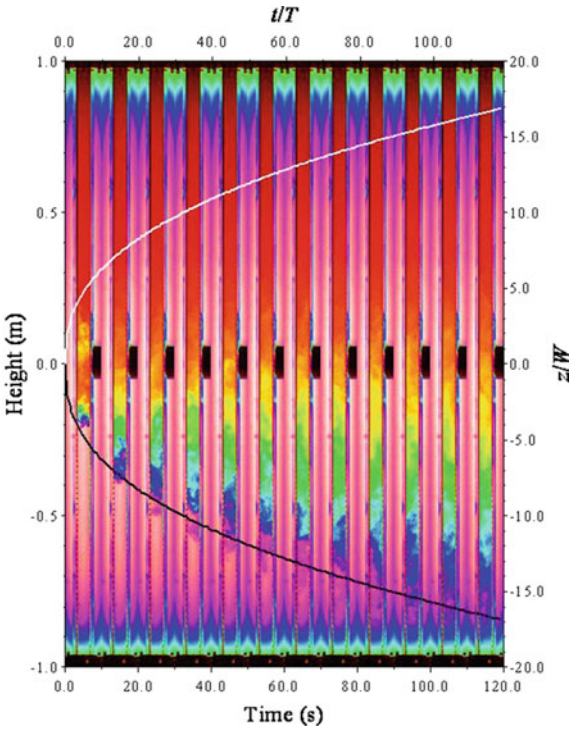

Fig. 9 Mixing observed in a tall tube due to RTI. Courtesy of Lawrie and Dalziel (2011)

$$PE_i = g\int_{-H}^{0} \rho_L z dz + g\int_{0}^{H} \rho_U z dz = \tfrac{1}{2} g H^2 (\rho_U - \rho_L)\,, \tag{81}$$

and the background potential energy PE_b, when the fluid is arranged to be adiabatically stable is

$$PE_b = g\int_{-H}^{0} \rho_U z dz + g\int_{0}^{H} \rho_L z dz = -\tfrac{1}{2} g H^2 (\rho_U - \rho_L)\,. \tag{82}$$

Consequently, the available potential energy $PE_a = PE_b - PE_i$ is

$$PE_a = g H^2 (\rho_U - \rho_L)\,. \tag{83}$$

If the final state is perfectly mixed with density $\rho = \frac{1}{2}(\rho_L + \rho_U)$ then the final PE_f is

$$PE_f = \tfrac{1}{2} g \int_{-H}^{H} (\rho_L + \rho_U) z dz = 0\,. \tag{84}$$

So the amount of PE_a converted into mixing is $PE_c \equiv PE_i - PE_f = \frac{1}{2}gH^2(\rho_U - \rho_L)$, and the mixing efficiency

$$\mathcal{M} \equiv \frac{PE_c}{PE_a} = \tfrac{1}{2}\,. \tag{85}$$

The time-dependent approach to the ultimate state is shown in Fig. 10.

11.2 Mixing Efficiency in Lock Exchange Gravity Currents

This section describes work recently published in Hughes and Linden (2016) and the reader is referred to the original paper for more details about the experiments etc. To calculate the mixing efficiency first calculate the initial potential energy. The initial density distribution is

$$\rho = \begin{cases} \rho_L,\ 0 \le x < L - L_{\rm lock},\ 0 \le z \le H_{\rm L}\,, \\ \rho_H,\ L - L_{\rm lock} < x \le L,\ 0 \le z \le H_{\rm H}\,. \end{cases} \tag{86}$$

Hence the initial potential energy PE_i is

$$PE_i = g\int_0^L \int_0^{H_i} \rho(x,z) z\,dx\,dz = \tfrac{1}{2}gL\left[\rho_{\rm L}(1-\gamma)H_{\rm L}^2 + \rho_{\rm H}\gamma H_{\rm H}^2\right], \tag{87}$$

where $\gamma \equiv L_{\rm lock}/L$ ($\approx$0.5 in this case) and H_i is the initial depth, $H_{\rm L}$ or $H_{\rm H}$, from Eq. (86). Now consider the final state after the gravity current and all subsequent motion in the channel has ceased. Conservation of volume implies initial and final free surface heights are related by $H = (1-\gamma)H_{\rm L} + \gamma H_{\rm H}$ (Fig. 11).

If there is no mixing and $\rho_{\rm L} < \rho_{\rm R}$, the final stratification is

$$\rho = \begin{cases} \rho_{\rm H},\ 0 \le x \le L,\ 0 \le z \le H_{\rm H}\gamma\,, \\ \rho_{\rm L},\ 0 \le x \le L,\ H_{\rm H}\gamma < z \le H\,. \end{cases} \tag{88}$$

The final potential energy PE_{nm} in this no-mixing case is

$$PE_{nm} = \tfrac{1}{2}gH^2L\rho_{\rm L} + \tfrac{1}{2}g{H_{\rm H}}^2L(\rho_{\rm H} - \rho_{\rm L})\gamma^2\,. \tag{89}$$

Thus the *maximum* potential energy that can be released in this flow, the available potential energy $PE_a = PE_i - PE_{nm}$, is

$$\begin{aligned} PE_a = {} & \tfrac{1}{2}gL(1-\gamma)\left[\rho_{\rm L}(H_{\rm L}^2 - H^2) + (\rho_{\rm L} - \rho_{\rm H})\gamma^2{H_{\rm H}}^2\right] \\ & + \tfrac{1}{2}gL\gamma\left[\rho_{\rm H}({H_{\rm H}}^2 - H^2) + (\rho_{\rm H} - \rho_{\rm L})(H^2 - \gamma^2{H_{\rm H}}^2)\right], \end{aligned} \tag{90}$$

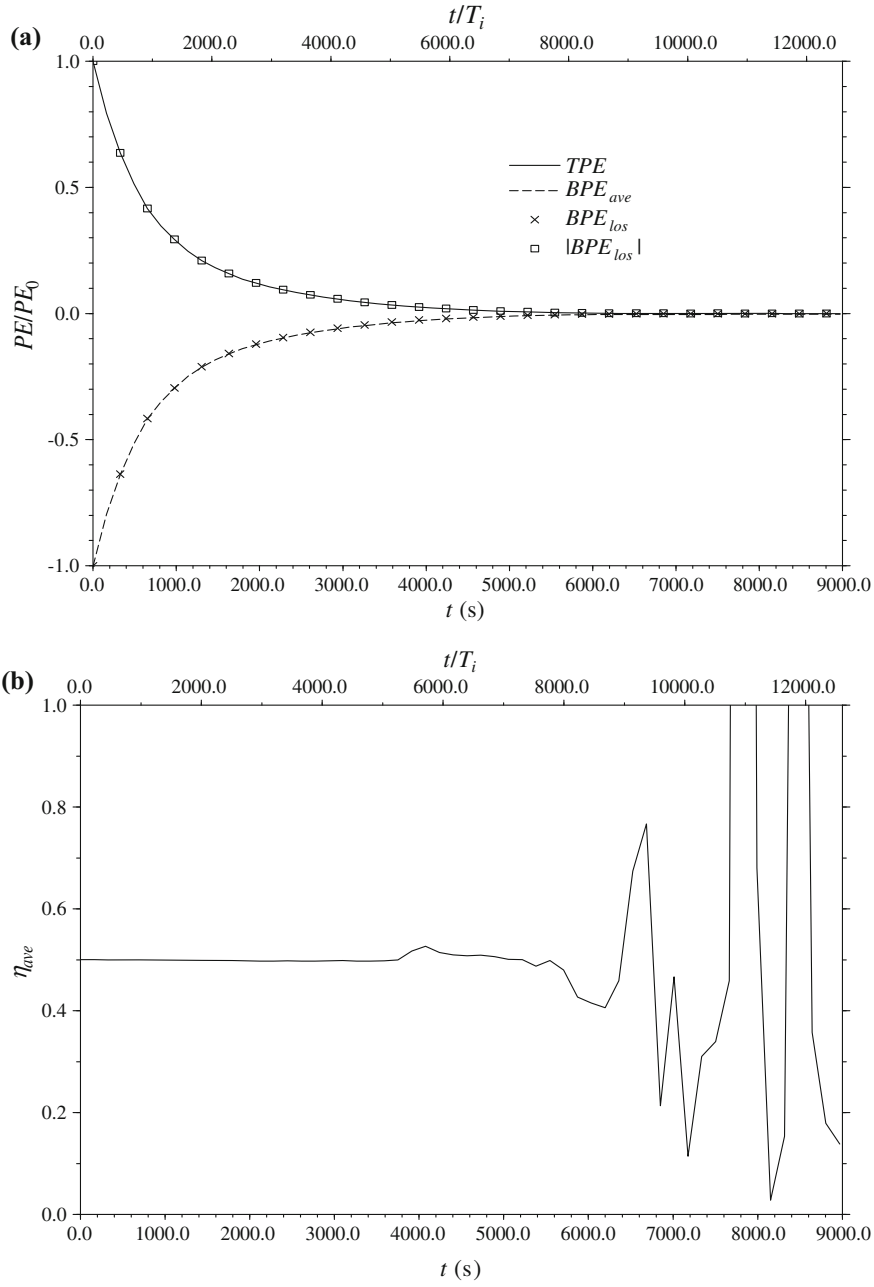

Fig. 10 Measurements of mixing efficiency in time-dependent RTI in a tall tube. Courtesy of Dalziel et al. (2008)

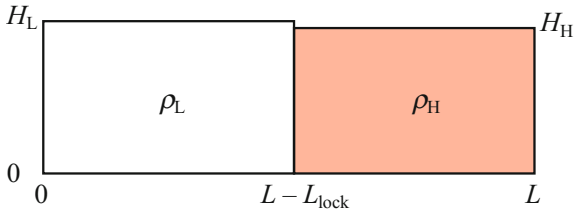

Fig. 11 Schematic of the lock release experiment. Salty water of density ρ_H fills a lock of length L_{lock}, and fresher water of density ρ_L fills the remainder of the channel. The depth $H_L > H_H$ and is set so that the pressures on the two sides of the lock gate are the same at mid-depth of the channel

where the first and third terms on the right are associated with changes in free-surface height, and the second and fourth terms are associated with changes in density between the initial and 'non-mixed' states.

For a general final stratification with potential energy PE_f the mixing efficiency $\mathcal{M}$ is defined as

$$\mathcal{M} \equiv \frac{PE_f - PE_{nm}}{PE_a}\,, \tag{91}$$

and can be calculated from the final density field in the channel after all motion has ceased. Note that if the mixing is complete so that the final density $\rho_f = \rho_L(1-\gamma)H_L/H + \rho_H\gamma H_H/H$ is uniform throughout the channel, the final potential energy approaches PE_i given by Eq. (87) and the mixing efficiency $\mathcal{M} \to 1$ in the limit where the initial differential of free surface height across the barrier vanishes, i.e. $H = H_L = H_H$.

An image of a gravity current is shown in Fig. 12. This current has $Re = 72,000$ and $Re_B = 21,000$, and exhibits large scale billow structures on the interface between the current and the counter-flowing current above. These structures are common to all the currents, although the intensity of the turbulence along the interface was noticeably reduced at lower Reynolds numbers.

Figure 13 shows the final density profiles after all motion in the channel has ceased. The profiles are approximately self-similar when normalized by the initial density difference, with a final interfacial region that is symmetrical about mid-depth (defined as $z' = 0$) and significant mixing evident in the region $-0.2 \lesssim z'/H \lesssim 0.2$.

Fig. 12 Visualization of a gravity current. The current is dyed with food colouring and viewed against a translucent lined sheet. Courtesy of Hughes and Linden (2016)

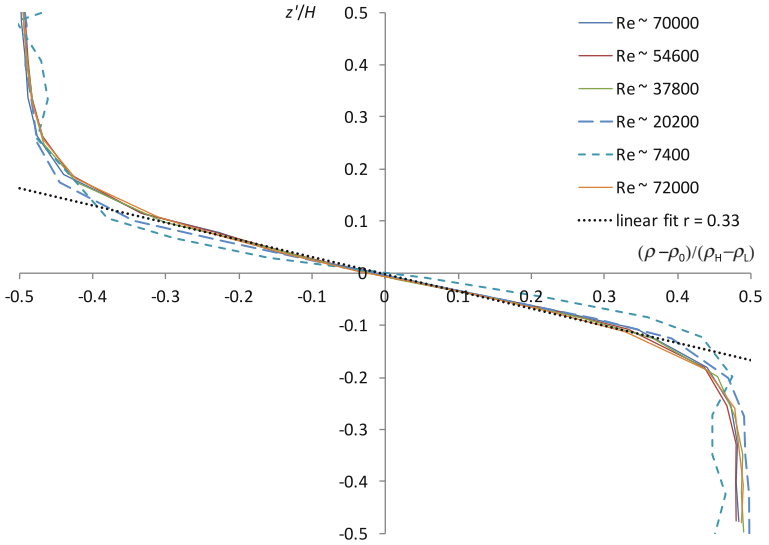

Fig. 13 Final density profiles for the experiments in Table 2 normalized by the initial density difference. The profiles were measured by withdrawing samples at different depths and the profiles are drawn with linear segments between the data points. Also shown is the assumed linear variation of density corresponding to an interfacial region of dimensionless thickness $r = 0.33$ (see Eq. 95). Courtesy of Hughes and Linden (2016)

Table 2 Values of the dimensionless density difference $(\rho_H - \rho_L)/\rho_0$, the overall Richardson number $Ri_O = (g(\rho_H - \rho_L)H/4\rho_0 U_M^2)$, where U_M is the gravity current propagation measured along the bottom, see Hughes and Linden (2016), the dimensionless mass anomaly α transported from one layer into the other by mixing (see Eq. 92), the Reynolds number $Re = (U_M H/2\nu)$ and the buoyancy Reynolds number $Re_B = (C\rho_0 U_M^3 \delta/g(\rho_H - \rho_L)\nu(H/2))$ (where this expression uses an estimate of N^2 based on the interface thickness δ and $C = 0.04$ is the constant in the assumed scaling for dissipation $\epsilon = CU_M^3/(H/2)$). The reference density ρ_0 is taken to be the average of ρ_L and ρ_H, and the uncertainties in Ri_O is based on the finite time taken to withdraw the barrier at the start of the experiment. For further details see Hughes and Linden (2016)

Exp	$(\rho_H - \rho_L)/\rho_0$	Ri_O	α	Re	Re_B
1	0.171	1.28 ± 0.11	0.102 ± 0.005	70, 000	760
2	0.086	1.10 ± 0.07	0.106 ± 0.006	54, 600	680
3	0.043	1.17 ± 0.05	0.109 ± 0.007	37, 800	440
4	0.012	1.20 ± 0.02	0.099 ± 0.007	20, 200	230
5	0.002	1.35 ± 0.02	0.097 ± 0.006	7, 400	70
6	0.172	1.22 ± 0.11	0.106 ± 0.006	72, 000	840

A weak departure from this self-similar form is suggested at the two lowest Reynolds numbers by a larger density gradient at the centre of the interface. The proportions of the less dense and more dense initial fluid volume that are mixed by the current into the other volume,

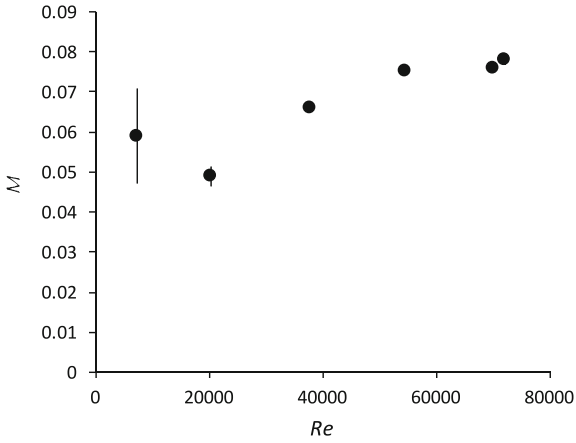

Fig. 14 Mixing efficiency results plotted as a function of the Reynolds number Re. Error bars are calculated for each experiment and are determined mainly by the relative accuracy with which the changes in free surface height $H_{\mathrm{L}} - H$ and $H_{\mathrm{H}} - H$ in (90) can be measured. The error bars exceed the symbol size only for the lowest two Re experiments. Courtesy of Hughes and Linden (2016)

$$\alpha_L = \frac{\int_0^{\gamma H_H} (\rho_H - \rho) L dz}{(1-\gamma) H_L L (\rho_H - \rho_L)} \quad \text{and} \quad \alpha_H = \frac{\int_{\gamma H_H}^{H} (\rho - \rho_L) L dz}{\gamma H_H L (\rho_H - \rho_L)}, \tag{92}$$

respectively, are found to be almost identical, with $\alpha_L \approx \alpha_H \equiv \alpha \approx 0.1$.

The mixing efficiency determined from the initial and final density fields is shown in Fig. 14. The values range from 0.05 to 0.08, and suggest a slight increase with Re to an asymptote at high Re. Unfortunately, we were unable to reach higher Re values with our laboratory facilities and so the asymptotic value cannot be confirmed. However, we have reason to believe this is the high Re limit, as we discuss below.

Lock-exchange gravity current model We now develop a model of a lock-exchange gravity current that accounts for dissipation and stratified mixing. First, we define general conventions applicable to both (idealized) non-dissipative and dissipative currents, and then proceed to use these to characterize the properties and energy budget of the dissipative lock exchange flow.

We assign (see Fig. 11) the reservoir of relatively light (heavy) fluid of density ρ_{L} (ρ_{H}) to be initially to the left (right) of the lock. Consider the (coupled) evolution of a column of fluid from each reservoir of height H and width ΔL, such that its volume (per unit spanwise width) is $\Delta Q = H \Delta L$. We denote the volume exchanged (i.e. that carried in each layer) in a time Δt as the exchange volume flux $\dot{Q} = \Delta Q / \Delta t$.

In the idealized limit of inviscid flow (a situation denoted by the subscript i), conservation of energy can be used to predict the flow speed U_i, which is assumed uniform in each layer. Symmetry of the flow about the lock position implies that each layer in the exchange has depth $H/2$, and $\dot{Q}_i = \frac{1}{2} U_i H$.

Following (Yih 1947, 1965) we equate the rate of release of potential energy $\dot{E}$ (which corresponds physically to a raising (lowering) of the height of the centre of mass of the dense (light) fluid by $H/4$) with the rate at which kinetic energy is generated in the flow, i.e.

$$\dot{E} = \frac{1}{4} g \rho_{\mathrm{H}} H \dot{Q}_i - \frac{1}{4} g \rho_{\mathrm{L}} H \dot{Q}_i = 2 \dot{Q}_i \tfrac{1}{2} \rho_0 U_i^2 \,. \tag{93}$$

This recovers the usual result (e.g. Benjamin 1968 and Simpson 1997) for the speed of an inviscid lock-exchange gravity current,

$$U_i = \tfrac{1}{2} \sqrt{g' H} \,, \tag{94}$$

where $g' = g(\rho_H - \rho_L)/\rho_0$ is the reduced gravity.

The idealized two-layer inviscid lock-exchange flow (which requires a step-change in the density and velocity profiles) is unstable to shear at the interface. We assume that instability arises in the vicinity of each gravity current head, and then develops and saturates at some distance behind the head. Thus in a lock-exchange flow with dissipation, we expect instability and turbulent mixing at a given location to be associated with the passage of the gravity current. We also assume that turbulence with sufficient intensity to support mixing is suppressed once the instability has run its course and left behind a stabilized interfacial structure in the wake of the current, consistent with our qualitative observations, previous studies (Thorpe 1973) and the subsequent predictions of this model.

For simplicity we adopt mean velocity and density profiles in the wake of the current that (have evolved via instability from idealized step profiles to) vary linearly with height through the stabilized interfacial region (of thickness δ) in order to match the freestream flow velocities and densities in the layers above and below (Fig. 15). We define the dimensionless thickness r of the stabilized interface in a dissipative current to be

$$r \equiv \frac{\delta}{H} \,. \tag{95}$$

Volume and mass transport In the dissipative lock-exchange flow we assume that each layer will evolve to consist of a region of depth $\frac{1}{2} H(1-r)$ of unmixed reservoir fluid moving at the freestream speed U, with reduced flow in the interfacial layer sandwiched between, see Fig. 15. Thus the exchange volume transport in the flow with dissipation, $\dot{Q}_d = \Delta Q_d / \Delta t \; (< \dot{Q}_i)$, is

$$\dot{Q}_d = \tfrac{1}{2} HU(1-r) + \int_0^{\delta/2} \frac{2Uz'}{\delta} dz' = \frac{1}{2}(1 - \frac{r}{2}) HU \,. \tag{96}$$

The volume transport in the upper layer can be related to the supply of unmixed fluid originating from the reservoirs by decomposing $\dot{Q}_d$ into the sum of three components (Fig. 15):

(i) an unmodified component from the left reservoir

$$\dot{Q}_{\mathrm{L}}^u = \tfrac{1}{2} HU(1-r) \,, \tag{97}$$

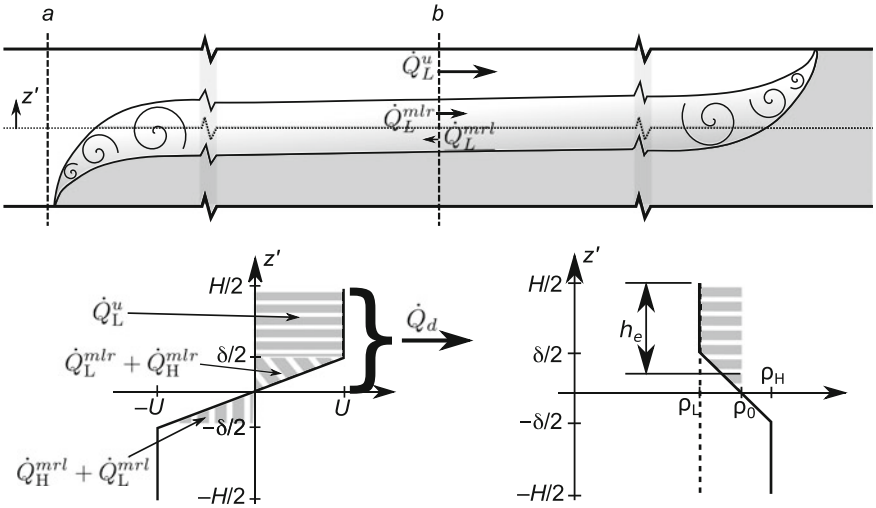

Fig. 15 Schematic diagram of the flow model. The *upper panel* indicates the overall flow structure and the *lower left* and *right panels* show the assumed (piecewise linear) velocity and density profiles, respectively. The *upper panel* indicates development of shear instability in the vicinity of each gravity current head, with intense turbulent eddies depicted by the swirls. Far enough behind each head, the interface between the counterflowing currents has stabilized. The *darkest grey* shading denotes fluid of density $\rho_{\rm H}$, with fluid of intermediate density indicated by lighter shading in the interfacial region between the two currents. Courtesy of Hughes and Linden (2016)

(ii) a component $\dot{Q}_{\rm L}^{mlr}$ from the left reservoir that is mixed as it flows to the right (in the same direction as $\dot{Q}_{\rm L}^{u}$)

$$\dot{Q}_{\rm L}^{mlr} = \int_0^{\delta/2} \frac{2Uz'}{\delta} c_{\rho_{\rm L}}(z')dz' = \frac{5}{24} rHU \ , \tag{98}$$

where $c_{\rho_L}(z') = \frac{1}{2}(1 + 2z'/\delta)$ is the volume fraction of the $\rho_{\rm L}$ source component in a water parcel at height z', and
(iii) a component $\dot{Q}_{\rm H}^{mlr}$ from the right reservoir that is mixed and joins the upper layer flowing from left to right

$$\dot{Q}_{\rm H}^{mlr} = \int_0^{\delta/2} \frac{2Uz'}{\delta} \left(1 - c_{\rho_{\rm L}}(z')\right) dz = \frac{1}{24} rHU \ . \tag{99}$$

The volume transport in the lower layer can be decomposed similarly into an unmodified component $\dot{Q}_{\rm H}^{u}$ from the right reservoir, a component $\dot{Q}_{\rm H}^{mrl}$ from the right reservoir that is mixed as it flows to the left and a component $\dot{Q}_{\rm L}^{mrl}$ from the left reservoir that is mixed and joins the lower layer flowing from right to left. Defining volume transport from left to right as positive and invoking symmetry in the problem, we can write

$$\dot{Q}_d = \dot{Q}^u_{\rm L} + \dot{Q}^{mlr}_{\rm L} + \dot{Q}^{mlr}_{\rm H} = |\dot{Q}^u_{\rm H}| + |\dot{Q}^{mrl}_{\rm H}| + |\dot{Q}^{mrl}_{\rm L}| \,, \tag{100}$$

and

$$\dot{Q}^u_{\rm L} = -\dot{Q}^u_{\rm H}, \quad \dot{Q}^{mlr}_{\rm L} = -\dot{Q}^{mrl}_{\rm H} \quad \dot{Q}^{mlr}_{\rm H} = -\dot{Q}^{mrl}_{\rm L} \,. \tag{101}$$

Equations (100) and (101) can be used to account for the volume transport of unmixed fluid that originates from one of the reservoirs, e.g.

$$\dot{Q}_d = \dot{Q}^u_{\rm L} + \dot{Q}^{mlr}_{\rm L} + |\dot{Q}^{mrl}_{\rm L}| \tag{102}$$

for the left reservoir. Furthermore, it follows from Eqs. (97)–(99) and (101) that the *net* left to right transport of fluid that originated from the left reservoir is

$$\dot{Q}^u_{\rm L} + \dot{Q}^{mlr}_{\rm L} + \dot{Q}^{mrl}_{\rm L} = \frac{1}{2}\left(1 - \frac{2r}{3}\right) HU \,. \tag{103}$$

We define the effective current depth h_e as the depth of unmixed fluid from the appropriate reservoir that would accommodate the buoyancy anomaly present in a layer of the assumed dissipative flow. Taking a layer to be either $-H/2 \le z' < 0$ or $0 < z' \le H/2$ and the buoyancy anomaly with respect to the midpoint density ρ_0, we find $h_e = (1 - r/2)H/2$ (see bottom right panel of Fig. 15). We proceed by assuming that the freestream speed U in each layer will be U_i on the physical basis that dissipation of energy along streamlines outside the interfacial layer will be relatively small.

Mixing and recirculation of fluid in the current head leads to a measured front speed U_M that is somewhat less than U_i, thus we now differentiate between a prediction for the front speed U_e and the freestream speed U. We predict U_e by equating $U_e h_e$ with Eq. (103) and setting $U = U_i$. In physical terms, we expect the net rate of horizontal transport of fluid that has originated from each reservoir to give the volume transport involved in extending each current (of effective depth h_e) in the dissipative exchange flow, i.e. to the right in the upper layer and to left in the lower layer. Hence

$$\frac{U_e}{U_i} = \frac{1 - \frac{2}{3}r}{1 - \frac{1}{2}r} \,. \tag{104}$$

To enable comparison with the experimental measurements, we can predict the overall Richardson number Ri^p_O for the current by using U_e in place of the measured front speed U_M in the expression for Ri_O, thus

$$Ri^p_O = \frac{g'H}{4U_e^2} = \frac{U_i^2}{U_e^2} = \frac{(1 - \frac{1}{2}r)^2}{(1 - \frac{2}{3}r)^2} \,, \tag{105}$$

upon substituting Eqs. (94) and (104). (Note that the assumption that the front and freestream speeds are the same and given by Eq. (94), as for an idealized inviscid

gravity current, (i.e. $U_e = U = U_i$) corresponds to $Ri_O^p = 1$). The measurements are consistent with a constant value for $Ri_O = 1.18$ (± 0.08). Thus, equating the measured Ri_O with Eq. (105) is consistent with $r = 0.38$ (± 0.1); however, a more accurate determination (estimated to within ± 0.02) is given below.

In our physical model, mixed fluid is created by the passage of each current at the rate $\dot{Q}_m = \dot{Q}_{\mathrm{L}}^{mlr} + \dot{Q}_{\mathrm{H}}^{mlr} (= \dot{Q}_{\mathrm{L}}^{mlr} + |\dot{Q}_{\mathrm{L}}^{mrl}|)$, which is the sum of the second and third terms on the right hand side of Eqs. (100) and (102). Upon substituting expressions (98) and (99) for $\dot{Q}_{\mathrm{L}}^{mlr}$ and $\dot{Q}_{\mathrm{H}}^{mlr}$, we find that the proportion of the exchange transport involved in mixing is

$$\frac{\dot{Q}_m}{\dot{Q}_d} = \frac{rHU_i/4}{(1-r/2)HU_i/2} = \frac{r}{2-r} \,. \tag{106}$$

Our model assumes that mixing will occur at a constant rate until each current first reaches the end of the channel (and is zero thereafter). Hence we expect $\dot{Q}_m/\dot{Q}_d$ to be equal to $\alpha_L + \alpha_H \approx 2\alpha$, which is calculated from Eq. (92) and is based on quantities that are measured accurately in experiments. As α is found to take a value close to 0.1, equating the result (106) to 2α yields $r = 0.33$ (± 0.02), a value that is consistent with the final density gradient through the centre of the interfacial region in the self-similar profiles—see Fig. 13.

It is worth remarking that the assumed piecewise linear density profile (lower right panel of Fig. 15) is fully consistent with the value of $r = 0.33$ above. This may be surprising given $r = 0.33$ seems to neglect curvature in the density profile and underestimate the volume of unmixed fluid that is passed to the other layer (as suggested by comparing the areas enclosed between either the measured or piecewise linear profile and the horizontal axis in Fig. 13). Indeed, evaluating expression (92) with the assumed piecewise linear density profile suggests coefficients $\alpha_L^* \approx \alpha_H^* \approx r/4 < \alpha$ for $\gamma = 1/2$ (i.e. for a lock at the channel midpoint)), where the asterix is used to denote the calculation with the assumed (rather than the measured) profile and Eq. (106) has been equated with 2α. However, we note that determination of r needs to take account of the *rates* of volume transport and creation of mixed fluid. The amount of mixing in the final density profiles is then associated with the exchange volume flux in the currents, which, because of dissipation, is somewhat less than the maximum possible volume flux for an idealized inviscid flow (i.e. $\dot{Q}_d < \dot{Q}_i$). In contrast, the calculation of α_L^* and α_H^* corresponds physically to the proportion of each reservoir volume that has been swapped to obtain the final state and, assuming the exchange flow is steady, would be equal to $\dot{Q}_m/\dot{Q}_i$. Upon comparison with Eq. (106), we reason that α_L^* and α_H^* (and α^*) will be a factor $\dot{Q}_d/\dot{Q}_i = (1 - r/2)$ smaller than α_L and α_H (and α), respectively. For $r = 0.33$, we therefore expect $\alpha_L^* \approx \alpha_H^* \approx \alpha^* = 0.83\alpha \approx 0.083$, or approximately $r/4$.

Energy budget for mixing We now consider the energetic consequences of the interfacial mixing, assuming that shear instability and turbulent mixing occur in the vicinity of each gravity current head. The drag associated with the turbulence causes the exchange transport $\dot{Q}_d$ to be less than $\dot{Q}_i$ and, for the same reasons

discussed above, we must analyze the energy budget by comparing the dissipative lock-exchange flow with an idealized non-dissipative counterpart that has the same exchange transport $\dot{Q}_d$. Viewed in this way, dissipation acts to "choke" the rate of release of potential energy $\dot{E}$ driving the flow,

$$\dot{E} = \frac{1}{4}\rho_0 g' H \dot{Q}_d \,, \tag{107}$$

which is obtained in a similar manner to Eq. (93) ($\dot{Q}_i$ being replaced by $\dot{Q}_d$). We can calculate the rate of mixing that would be associated with the linear variation of density through the interfacial layer, i.e. $\rho(z) = \rho_0 - (\rho_H - \rho_L)z'/\delta$. The density profile if no mixing occurred would be a step from ρ_L to ρ_R at $z' = 0$, thus the rate of change of potential energy owing to mixing at an interface lengthening at a rate $2U_e$ is

$$\begin{aligned}\dot{E}_p &= 2U_e \int_{-\delta/2}^{\delta/2} \rho_0 \frac{g'}{2}\left(\mathrm{sgn}(z') - \frac{2z'}{\delta}\right) z' dz' \\ &= \frac{1}{6}\frac{(1-\frac{2}{3}r)}{(1-\frac{1}{2}r)^2}\rho_0 g' H \dot{Q}_d \left(\frac{\delta}{H}\right)^2 \,,\end{aligned} \tag{108}$$

where Eqs. (96) and (104) have been used.

The energy budget can be used to characterize the mixing in terms of a mixing efficiency, and the proportion of total energy released and used for mixing is predicted to be

$$\mathcal{M} = \frac{\dot{E}_p}{\dot{E}} = \frac{2r^2}{3}\frac{(1-\frac{2}{3}r)}{(1-\frac{1}{2}r)^2} \,, \tag{109}$$

which is dependent only upon the parameter r characterizing the self-similar behaviour. The mixing efficiency $\mathcal{M}$ predicted for $r = 0.33$ is 0.081, which corresponds well with the measured asymptotic value, see Fig. 14.

These conceptually simple experiments yield a range of insights into mixing caused by a gravity current. The qualitative observations and measurements are consistent with development of stratified shear instability associated with the passage of the gravity current head. The ensuing turbulence and mixing redistributes momentum and density in the vertical until the interface above or below the current is stabilized. At sufficiently high Reynolds number (of $O(30,000)$ based on the current depth), we find that the resulting density profile becomes self-similar; the thickness of the stabilized interface normalized by the total flow depth r is close to a third. Interestingly, the interfacial signatures resulting from fully-developed Kelvin-Helmholtz instability and mixing are essentially identical (Thorpe 1973).

Simple arguments suggest that the dimensionless interface thickness is a direct indication of the gradient Richardson number that evolves across the interface between the two currents (i.e. $r = Ri_g \equiv g'\delta/4U^2$, from Eq. (95) and with U_e in Eq. (105) replaced by $U = U_i$). Thus $r \approx 0.33$ is consistent with establishment of an interfacial

region that is stable to shear instability ($Ri_g \sim 0.3$). This dimensionless thickness is further consistent with current speed $U_e \approx 0.92U_i$ (see Eq. (104)), and thus a Froude number $Fr = U_e/(g'H)^{1/2} \approx 0.46$ as found in full-depth lock exchange experiments at high Re (Keulegan 1958; Shin et al. 2004).

We find that up to about 0.08 of the energy supplied to the flow is consumed by irreversible mixing. At first glance, this value represents a mixing efficiency that is small compared to values of 0.15–0.2 that are thought to characterize the mixing owing to shear instability. However, it is important to recognise that these efficiencies measure physically different quantities. In this study we include in the energy budget the amount required to sustain the mean flow (i.e. the gravity currents), whereas a variety of measures are instead based on the proportion of energy supplied to turbulence that is consumed by mixing. Furthermore, these measures may rely on some form of averaging (e.g. in a volume, temporal or ensemble sense) or may be applicable at a specific position in the flow. Given that the turbulence in a lock-exchange gravity current is neither homogeneous nor statistically steady, we have chosen to characterize the flow by a bulk mixing efficiency measure that is unambiguous. The results highlight the importance of this consideration in a situation where the mean flow is integral to the location and characteristics of the turbulent mixing.

We have further shown here that the mixing associated with a gravity current only attains a self-similar asymptotic state at Reynolds numbers in excess of about 50,000—well above the range typically considered in previous studies. The results suggest that the stratified turbulence is characterized by buoyancy Reynolds numbers Re_B approaching 700 in this state. If the Ozmidov and Kolmogorov scales,

$$L_o = \left(\frac{\epsilon}{N^3}\right)^{1/2} \quad \text{and} \quad L_k = \left(\frac{\nu^3}{\epsilon}\right)^{1/4}, \tag{110}$$

respectively, characterize the turbulence spectrum in the lock-exchange gravity current, then the range of scales is given by

$$\frac{L_o}{L_k} = \left(\frac{\epsilon}{\nu N^2}\right)^{3/4} = {Re_B}^{3/4}. \tag{111}$$

Hence, these experiments span the range $20 \lesssim L_o/L_k \lesssim 150$, and suggest that asymptotic mixing behaviour owing to shear instability could require a separation of scales $L_o/L_k \gtrsim 130$.

12 Concluding Remarks

These notes are a summary of my lectures on some basic considerations on turbulence and mixing in stratified fluids. This is a subject of strong current interest and the ideas expressed in these notes will undoubtedly be challenged and refined or discarded as our understanding of this fascinating subject continues to develop. What

is clear is that at this time current computational capabilities allow *for the first time* direct numerical simulations at scales relevant to laboratory experiments, along with diagnostics that provide complementary information about the three-dimensional velocity and density fields from these experiments that allow direct comparison with the DNS. Further, and perhaps even more important, is the recognition that both experiments and computations need to be at sufficiently large buoyancy Reynolds numbers for the results to be representative of field scale processes. Both of these considerations make for an exciting new era in the study of stratified turbulence, and I hope these notes provide some inspiration for the reader to explore the field further.

Acknowledgements I would like to thank the organisers of this summer school for inviting me to give the lectures on which these notes are based. I would also like to acknowledge the many discussions I have had on this subject with many colleagues especially Colm Caulfield, Stuart Dalziel, Graham Hughes, Jamie Partridge, and John Taylor. This work is supported by the UK EPSRC, through the Programme Grant EP/K034529/1 and by the Royal Society.

References

G.K. Batchelor, Small-scale variation of convected quantities like temperature in turbulent fluid. Part 1. general discussion and the case of small conductivity. J. Fluid Mech. **5**(1), 113–133 (1958)

T.B. Benjamin, Gravity currents and related phenomena. J. Fluid Mech. **31**(2), 209–248 (1968)

P. Billant, J.-M. Chomaz, Self-similarity of strongly stratified inviscid flows. Phys. Fluids **13**, 1645–1651 (2001)

G. Brethouwer, P. Billant, E. Lindborg, J.-M. Chomaz, Scaling analysis and simulation of strongly stratified turbulent flow. J. Fluid Mech. **585**, 343–368 (2007)

S.B. Dalziel, M.D. Patterson, C.P. Caulfield, I.A. Coomaraswamy, Mixing efficiency in high-aspect-ratio Rayleigh-Taylor experiments. Phys. Fluids **20**, 065106 (2008)

E. Deusebio, C.P. Caulfield, J.R. Taylor, The intermittency boundary in stratified plane Couette flow. J. Fluid Mech. **781**, 298–329 (2015)

J.M. Holford, P.F. Linden, Turbulent mixing in a stratified fluid. Dyn. Atmos. Oceans **30**(2–4), 173–198 (1999)

L.N. Howard, Note on a paper of John W. Miles. J. Fluid Mech. **10**(4), 509–512 (1961)

G.O. Hughes, P.F. Linden, Mixing in run-down gravity currents. J. Fluid Mech. **809**, 691–704 (2016)

G.H. Keulegan, The motion of saline fronts in still water. National Bureau of Standards Report, 5831, 1958

A.N. Kolmogorov, The local structure of turbulence in incompressible viscous fluid for very large Reynolds numbers. Comptes Rendus de l'Académie des sciences de l'URSS **30**, 299–303 (1941a)

A.N. Kolmogorov, On the degeneration of isotropic turbulence in an incompressible viscous liquid. Comptes Rendus de l'Académie des sciences de l'URSS **31**, 319–323 (1941b)

A.N. Kolmogorov, Dissipation of energy in locally isotropic turbulence. Comptes Rendus de l'Académie des sciences de l'URSS **32**, 19–21 (1941c)

A.G.W. Lawrie, S.B. Dalziel, Turbulent diffusion in tall tubes. I. models for Rayleigh-Taylor instability. Phys. Fluids **23**, 085109 (2011)

D.K. Lilly, Stratified turbulence and the mesoscale variability of the atmosphere. J. Atmos. Sci. **40**, 749–761 (1983)

E. Lindborg, The energy cascade in a strongly stratified fluid. J. Fluid Mech. **550**, 207–242 (2006)

P.F. Linden, Mixing in stratified fluids. Geophys. Astrophys. Fluid Dyn. **13**, 3–23 (1979)

P.F. Linden, Mixing across a density interface produced by grid turbulence. J. Fluid Mech. **100**, 691–703 (1980)

J.W. Miles, On the stability of heterogeneous shear flows. J. Fluid Mech. **10**(4), 496–508 (1961)
O.M. Phillips, Turbulence in a strongly stratified fluid—is it unstable? Deep Sea Res. **19**, 79–81 (1972)
E.S. Posmentier, The generation of salinity finestructure by vertical diffusion. J. Phys. Oceanogr. **7**, 298–300 (1977)
J.O. Shin, S.B. Dalziel, P.F. Linden, Gravity currents produced by lock exchange. J. Fluid Mech. **521**, 1–34 (2004)
J.E. Simpson, *Gravity Currents in the Environment and the Laboratory* (Cambridge University Press, 1997)
S.A. Thorpe, Experiments on instability and turbulence in a stratified shear flow. J. Fluid Mech. **61**(4), 731–751 (1973)
S.A. Thorpe, Layers and internal waves in uniformly stratified fluids stirred by vertical grids. J. Fluid Mech. **793**, 380–413 (2016)
J.S. Turner, The influence of molecular diffusivity on turbulent entrainment across a density interface. J. Fluid Mech. **33**(4), 639–656 (1968)
J.S. Turner, *Buoyancy Effects in Fluids* (Cambridge University Press, 1973)
C.S. Yih, A study of the characteristics of gravity waves at a liquid interface. MSc thesis, State University of Iowa, 1947
C.S. Yih, *Dynamics of Nonhomogeneous Fluids* (Macmillan, 1965)

Mixing in Stratified Lakes and Reservoirs

Damien Bouffard and Alfred Wüest

Abstract Aquatic physics in inland water is a crucial subject for studying aquatic ecosystems. Transport and mixing are of tremendous importance for the pace at which chemical and biological processes develop. Recent observations allow to distinguish mixing and transport processes in stratified lakes and reservoirs. The surface and bottom boundary layer are turbulent while the lake interior remains comparatively quiescent.

1 Introduction

Lakes and reservoirs receive thermal energy mainly through the lake surface. The net heat flux H is the sum of all heat flux contributions, including the shortwave absorption (positive), the longwave absorption (positive), the longwave emission (negative), the heat flux by evaporation and condensation, the heat convection (free and forced), and the heat flux caused by throughflow. The latter three components can have either sign. If H is negative, the water body loses heat (typically in autumn and winter in the Northern hemisphere) and if positive, thermal energy is stored in the water body (typically spring and summer). Most of the heat is stored in the very top layers and some of it is slowly transported into deeper parts by vertical turbulence. In lakes, reservoirs, and estuaries this vertical transport is slow, whereas in rivers the heat is quickly homogenized. In lakes, a change in the heat balance may have most effects on surface water temperatures and less effects on the much larger deep-water volume.

D. Bouffard (✉) · A. Wüest
Swiss Federal Institute of Aquatic Science and Technology,
EAWAG, Kastanienbaum, Switzerland
e-mail: Damien.bouffard@eawag.ch

A. Wüest
Physics of Aquatic Systems Laboratory, Ecole Polytechnique
Federale de Lausanne, EPFL, Lausanne, Switzerland
e-mail: alfred.wueest@eawag.ch

H.J.H. Clercx and G.J.F. Van Heijst (eds.), *Mixing and Dispersion in Flows Dominated by Rotation and Buoyancy*, CISM International Centre for Mechanical Sciences 580,
https://doi.org/10.1007/978-3-319-66887-1_3

The density ρ of natural waters depends on temperature and pressure as well as on dissolved and suspended constituents (relevant are salts, gases, and particles) in the water. Under natural conditions, the water column is always stratified to some extent, mostly by temperature gradients, often by salinity gradients (especially in oceans and deep lakes) and almost always by both (oceans). In the following, we only consider the temperature dependences.

Accumulation of thermal energy in the near-surface layers leads to a thermal stratification separating a warm upper layer from a colder lower layer with a thermal barrier called thermocline. The location of the thermocline varies over the season, depending on the competition between heat and momentum (wind) forcing. Stratification has many ecological consequences. During the stratified period, the thermocline prevents vertical fluxes, isolating the hypolimnion from gas exchanges with the atmosphere. Without an influx of oxygen, the hypolimnion can become depleted of oxygen during the summer stratified period due to oxygen use by bacterial decomposition of organic matter mostly in the sediment.

The annual cycle of lake water temperatures in temperate lakes is typically as follows. In spring, an overturn, a complete vertical mixing, of the lake water body happens. Another overturn happens in autumn, when the surface waters have been cooled so that they are heavier than the deep waters. Overturns and deep mixing events are important to the vertical exchange and renewal of deep waters, for instance for deep oxygen enrichment. In summer most of the lakes in the temperate climatic zone are stratified. The warm surface layer extending down to 5–20 m is called the epilimnion. Below is the thermocline (also called metalimnion), where the water temperature decreases rapidly over a few meters. Below is a colder layer called the hypolimnion. Besides the seasonal temperature and stratification variation, diurnal thermal variations are also present in lakes and reservoirs. This happens especially during calm cloudless summer days and nights. The solar radiation heats up the surface waters increasing day-time stratification with some extra layers in the epilimnion. Nocturnal cooling of air leads to strong sensible heat loss from the lake surface, which is also emitting heat by long-wave radiation. The cooled waters sink down and cause vertical mixing and this leads to the well mixedness of the epilimnion.

2 Surface and Bottom Boundary Layers in Lakes

2.1 The Role of Boundary Layers in Natural Waters

In stratified waters (ocean, lakes, reservoirs, wetlands) the boundary layers are the most dynamic zones. In the surface boundary layer (SBL) light and nutrients enable photosynthesis by phytoplankton, which provides the basis of the food web for zooplankton and fish. Also physical, biological, geochemical, and photochemical processes undergo the strongest dynamics here owing to exchange with the adjacent atmosphere, light intensity and heat fluxes. Hence, for understanding the ecologically

most relevant phenomena, the atmosphere-water relationship is crucial. Depending on the properties of the atmosphere (wind, temperature, humidity, etc.) and the water surface (waves, surfactants, etc.) the air-water interface creates a bottleneck for the exchange of the physical quantities such as heat and matter (gases, vapour, aerosols; in both directions) or momentum and mechanical energy (from air to water). These exchanges of physical and chemical properties are driven by wind and heat flux induced turbulence on both sides of the interface, see the schematics in Figs. 1 and 2.

Also the bottom boundary layer (BBL) is an active zone, as there the currents approach zero and therefore shear zones develop with much higher level of turbulence than in the interior of the stratified water body, see Fig. 1. The BBL is also important for the exchange of oxidants and reduced substance with the sediment and the resuspension and net sedimentation of particulate substances. Especially important are fluxes of oxygen for the decomposition of organic matter in the sediment.

First we discuss the SBL, which is more complex due to the free surface (velocity not zero at the surface) and the presence and breaking of waves and the subsequent entrainment of air into the water.

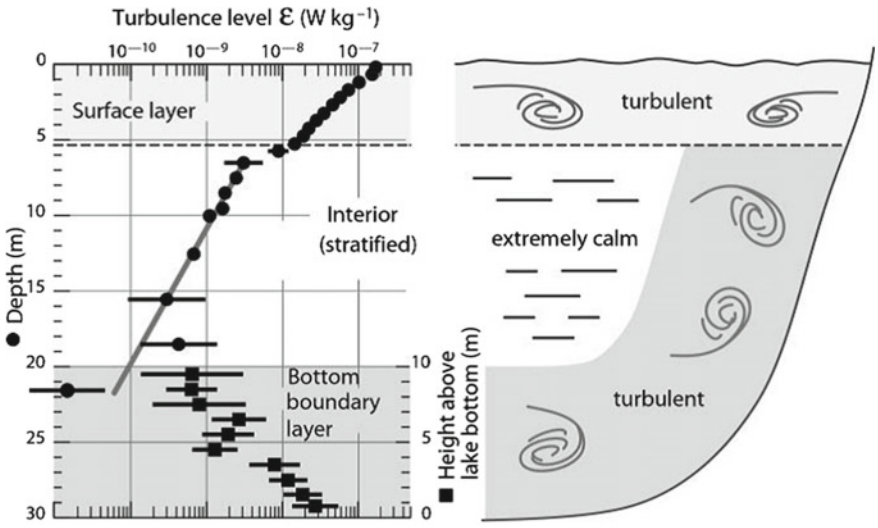

Fig. 1 Level of turbulence in a medium-sized lake, expressed by dissipation ε of turbulent kinetic energy, as a function of depth (*circles*) and as a function of height above the *bottom* (*squares*). The plot motivates characterizing the three distinctly different water bodies separately: the energetic SBL, the slightly less turbulent bottom boundary layer, and the strongly stratified and almost laminar interior. Courtesy of Wüest and Lorke (2003)

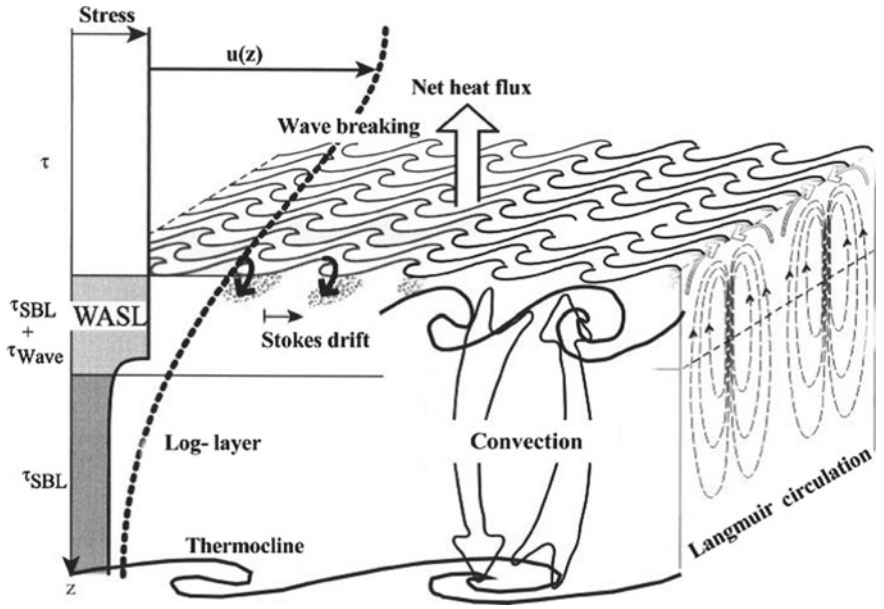

Fig. 2 Schematic overview of the surface boundary processes, the shear stress, and the associated vertical structure of the SBL. Stokes drift = net horizontal flow due to the effect of the inhomogeneous orbiting of wave-induced currents. Convection = vertical up/down plumes due to surface cooling. Log-layer = turbulent BL, where logarithmic $u(z)$ profiles applies. Langmuir circulation = second-order flow cells perpendicular to the driving wind. Courtesy of Wüest and Lorke (2003)

2.2 The Turbulent Kinetic Energy Balance

We derive the equation for the turbulent kinetic energy (TKE) from the simplified Navier Stokes equation,

$$\frac{\partial U_i}{\partial t} + U_j \frac{\partial U_i}{\partial x_j} = -\delta_{i3} g - \frac{1}{\rho} \frac{\partial p}{\partial x_i} + \nu \frac{\partial^2 U_i}{\partial x_j^2}$$

$$(I) + (II) = (III) + (IV) + (V)$$

(I = acceleration of velocity i; II = advection; III = gravity (3^{rd} (z) component only); IV = pressure force and V = friction by viscosity). Here, and later on, the Einstein summation convention is adopted which means that a repeated index (for example, $U_i U_i$) is summed over all the directions of the coordinate system. Thereafter, we apply the Reynolds decomposition: $\mathbf{U} = \mathbf{u} + \mathbf{u}'$, take the inner product of the equation with the velocity $\mathbf{U} = (U_1, U_2, U_3)$ and apply the averaging rules. The resulting balance for the velocity fluctuations squared, $\mathbf{u}' \cdot \mathbf{u}' = u_i'^2$, correspond to twice the balance of the kinetic energy of the turbulent fluctuations (TKE). Under homogeneous condition

(no fluxes of TKE in space) the following four terms show up in the balance

$$\frac{1}{2}\frac{\partial\overline{(u_i')^2}}{\partial t} = -\overline{u_i'u_j'}\frac{\partial u_i}{\partial x_j} - \overline{\rho' u_3'}\frac{g}{\rho} - \nu\overline{\left(\frac{\partial u_i'}{\partial x_j} + \frac{\partial u_j'}{\partial x_i}\right)\frac{\partial u_i'}{\partial x_j}}$$

$$(I) = (II) + (III) + (IV) .$$

The interpretation of the four terms is as follows:

- (I) = rate of change of the TKE;
- (II) = rate of production (source) of TKE, $J_R = -\overline{u_i'u_j'}\frac{\partial u_i}{\partial x_j}$;
- (III) = turbulent buoyancy flux, $J_B = \frac{g}{\rho}\overline{\rho' u_3'}$;
- (IV) = turbulent kinetic energy dissipation, ε, which is always a sink of energy due to viscosity.

Under steady, homogeneous conditions and horizontal flow, the TKE reads

$$J_R = -\overline{u'w'}\frac{\partial u}{\partial z} = J_B + \varepsilon .$$

This is the most simple situation of a TKE balance. On the left, J_R, is the production term of TKE. As shown above, its source is the Reynolds stress acting on the background shear. The production J_R is equal to the so-called buoyancy flux J_B (change of potential energy in the flow field) plus dissipation ε of TKE. In the following this TKE balance equation will be applied to the surface and to the bottom boundary layer.

Using the eddy diffusivity formulation, the density flux can be rewritten as

$$\overline{\rho'w'} = -K_\rho\frac{\partial\rho}{\partial z} ,$$

with K_ρ the diapycnal diffusivity. Introducing the definition for the stability $N^2 = -(g/\rho)\frac{\partial\rho}{\partial z}$ (also known as the Brunt-Väisälä frequency), shows the relation between the change (here increase) of the potential energy J_B and the diffusivity and stability

$$J_B = \frac{g}{\rho}\overline{\rho'w'} = -K_\rho\frac{g}{\rho}\frac{\partial\rho}{\partial z} = K_\rho N^2 .$$

If the relationship between ε and J_B is known or given, e.g., $\gamma_{mix} = J_B/\varepsilon$ with γ_{mix} the mixing efficiency, the diapycnal diffusivity can be calculated from

$$K_\rho = \frac{J_B}{N^2} = \frac{\gamma_{mix}\,\varepsilon}{N^2} .$$

Therefore, measurements of ε and N^2 can yield important information about the diapycnal diffusivity. The mixing efficiency γ_{mix} is generally not constant ($\gamma_{mix} \approx$

$0.05 - 0.2$) and not a well-known function (Ivey and Imberger (1991); Ivey et al. (2008); Bouffard and Boegman (2013)).

Stratification suppresses turbulence in the vertical direction. At very small scales (<0.1 m), stratification plays a subordinate role, and viscosity (ν) and dissipation (ε) are the relevant physical quantities. Larger eddies, however, feel the stratification (N^2) and influence turbulence and the form of the spectra. For a given density stratification N^2, a vertical eddy of size L can therefore develop, if the TKE is sufficient to feed the required power to the eddy, i.e., if $L^2 N^3 < \varepsilon$. The maximum eddy size, called the Ozmidov length scale L_o, is therefore $L_o = \sqrt{\varepsilon / N^3}$. Length scales larger than L_o are influenced by stratification and turbulence at these length scales is not isotropic. The range $L \approx [L_o - 10 L_o]$ is called the buoyancy range. It is located in the spectra between the internal wave range at larger scales and the inertial and dissipation range at smaller scales.

2.3 *Vertical Structure of Wind-Induced Surface Boundary Layers*

The most crucial parameter governing the wind-driven regime is the surface shear stress τ, the force per unit area, acting on the water surface as a result of the wind. The source of this stress can be interpreted as the downward eddy-transport of horizontal momentum, $\tau = \rho_{air} \overline{U' W'}$, from the atmosphere. The concept of constant stress calls for the same Reynolds momentum flux right at the surface, $\tau = \rho \overline{u' w'}$, in the underlying water, where U, W (u, w) are the horizontal and vertical velocities of air (water), ρ_{air} (ρ) is air (water) density, and (prime) denotes fluctuations. The constant stress assumption holds for quite some height in the atmosphere and over some extent (several meters) into the SBL.

The conservation of momentum right at the interface implies that τ is equal on both sides of the interface. Owing to the presence of waves, the momentum flux into the SBL, τ_{sbl} is smaller than the applied stress τ from the air, see Fig. 2. Part of τ is consumed by the acceleration and maintenance of waves (so-called wave stress τ_{wave}), whereas the remaining momentum flux τ_{sbl} is forcing the SBL water underneath the waves. The conservation of momentum at the interface implies that the two momentum fluxes on the water-side add to the total wind stress, $\tau = \tau_{sbl} + \tau_{wave}$. This formulation indicates that waves act as a second pathway for the momentum transfer to the water. As a consequence, the wind stress, which is usually parameterized by $\tau = \rho_{air} C_{10} U_{10}^2$, using the wind drag coefficient C_{10}, depends not only on the wind speed U_{10} (measured at standard 10-meter height above the surface, but also on the presence and state of the surface waves. In fact, the wave field is crucial for the amount of momentum transferred into the water and for its vertical distribution within the SBL.

The Law-of-the-Wall A wind speed U_{10} creates a stress τ (constant stress layer), given by the Reynolds stress. Based on similarity scaling, the vertical gradient of

the horizontal velocity depends on the stress and the distance h (here h is the height above the ground or water surface; positive upward) to the surface as follows:

$$\frac{\partial U}{\partial h} = \frac{\sqrt{\tau/\rho_{air}}}{k\,h} .$$

An alternative explanation is provided by the Prandtl assumption. This equation is known as the Law-of-the-Wall and $k = 0.41$ is the von Kármán constant (experimental value). Integration leads to the well-known logarithmic wind profile

$$U(z) = U_0 + \frac{w_*}{k} \ln(\frac{h}{h_0}) .$$

For the wind-induced stress in the SBL, the above arguments can be repeated (with z now the depth, positive downward)

$$\frac{\partial u}{\partial z} = -\frac{\sqrt{\tau_{sbl}/\rho}}{k\,z} ,$$

$$u(z) = U_0 - \frac{u_*}{k} \ln(\frac{z}{z_0}) ,$$

where z_0 is the water-side roughness and u_* is the friction velocity in the SBL of the water. The rate of production of TKE, J_R, is given by the vertical divergence of the energy flux. Within the boundary layer, where the stress is constant ($\frac{\partial \tau_{sbl}}{\partial z} = 0$), this results in

$$J_R = -\overline{u'w'}\frac{\partial u}{\partial z} = -\frac{\tau_{sbl}}{\rho}\frac{\partial u}{\partial z} .$$

After inserting the definition of u_*, the production of TKE in the logarithmic boundary layer is given by

$$J_R = u_*^2 \frac{\sqrt{\tau_{sbl}/\rho}}{k\,z} = \frac{u_*^3}{kz} .$$

According to Ficks second law, the rate of change of TKE is given by the vertical divergence of the energy flux (J_R, source term), minus dissipation (ε, sink term), minus buoyancy flux (J_B, sink term). For isotropic and steady-state turbulence, the production J_R of TKE must be in equilibrium with the dissipation ε and the buoyancy flux J_B, i.e. $J_R = \varepsilon + J_B$. If the boundary layer is not density-stratified (i.e. the boundary layer is homogeneous and therefore $J_B = K_z N^2 = 0$), the following equation results for the energy dissipation ε:

$$\varepsilon = J_R = \frac{u_*^3}{k\,z} .$$

If the wave-induced stress, τ_{wave}, is small, then $\tau \approx \tau_{sbl}$ and the dissipation can be expressed in terms of the wind forcing: $\tau_{sbl} = \rho u_*^2 = \rho_{air} C_{10} U_{10}^2$, with U_{10} the wind speed measured at 10 m above the water surface,

$$\varepsilon = \left(\frac{\rho_{air}\ C_{10}}{\rho}\right)^{3/2} \frac{U_{10}^3}{kz} .$$

The level of wind-induced turbulence as a function of depth z can be estimated based only on the wind speed U_{10}. The most detailed turbulence measurements in the ocean, performed with the dissipation method, are consistent with $\varepsilon \propto U_{10}^3$ and follow the empirical relation

$$\varepsilon \simeq 1.8 \left(\frac{\rho_{air}\ C_{10}}{\rho}\right)^{3/2} \frac{U_{10}^3}{kz} .$$

The factor 1.8 includes much uncertainty, as C_{10} is not well defined. Despite this uncertainty, the level of turbulent dissipation in a wind-induced surface boundary layer is therefore quite well defined.

Viscous boundary layer Due to wave breaking, the very top layer as well as the very last millimeters of the transition from water-to-air is not well defined. One can think of a well-defined boundary layer with molecular/laminar interfaces interrupted regularly by breaking waves, where the contact between water and air is torn in pieces and bubbles enhance the contact surface between air and water by orders of magnitudes. During those short moments, the contact between water and air is much intensified. After a few seconds the boundary layer is again established and the contact between water and air is back to normal (weak, molecular bottleneck). The thickness δ_ν, where the turbulent eddy viscosity K_{turb} falls below the kinematic viscosity ν, defines the viscous boundary layer (VBL). Within this sublayer, the viscous forces dominate the resistance to momentum transfer. Subsequently in the viscous sublayer the greatest changes in velocity occur and the horizontal flow becomes laminar. The shear stress τ is still equal to the (constant) stress above, but the momentum flux becomes now only a function of the (molecular) viscosity. Therefore, with $\tau_{sbl} = \rho\nu \frac{\partial u}{\partial z}$ we obtain

$$\frac{\partial u}{\partial z} = \frac{u_*^2}{\nu} ,$$

and the shear gradient depends only on the (friction) velocity and the viscosity. The distance from the bottom—where the flow is laminar—is given by $\delta_\nu \approx 10\nu/u_*$. The same arguments apply for the air-side and one can define a VBL on the atmospheric side.

Diffusive boundary layer and gas exchange velocity Following the same argumentation as above for the specific case of the turbulent eddy viscosity K_{turb}, the turbulent diffusivity is decreasing as the air-water interface is approached and at some small distance from the interface the turbulent diffusivity would fall below the

molecular diffusivity D_c. As diffusivity can never drop below the molecular diffusivity, we define the layer of only molecular flux through the interface (Ficks first law)

$$J_C \;=\; -D_C \frac{\partial C}{\partial z} \;\approx\; \frac{D_C}{\delta_{dbl}} \Delta C \;=\; V_{tot}\ \Delta C\ ,$$

as the diffusive boundary layer (DBL) with thickness δ_{dbl}. The DBL thickness is slightly solute-specific because δ_{dbl} depends on D_c which is substance (C) and temperature dependent. The gas exchange is often characterized by the piston velocity $V_{tot} = D_c/\delta_{dbl}$, which in the literature is called gas exchange velocity or mass transfer velocity/coefficient. As indicated by the previous equation, $V_{tot} = D_c/\delta_{dbl}$ includes two influences: (i) the molecular properties of the substance C and (ii) the effect of the wind forcing expressed by δ_{dbl}. Therefore, V_{tot} depends on the substance, the temperature and the wind.

Wave dependency of wind-induced stress The total surface stress is usually parameterized by the drag coefficient C_{10}, which quantifies the total vertical momentum flux τ well above the wave-affected boundary (at standard 10 m height). The experimental data show a large scatter, but nevertheless, there is a relatively clear conceptual picture. The drag coefficient depends to large extent only on wind speed and the wave development state.

From these two factors, we consider first the situation of developed waves at different wind speeds. There are basically two ranges to be considered: wind larger than 5 ms^{-1} and wind below 5 ms^{-1}. For strong winds (>5 ms^{-1}) the surface roughness is determined by the height of the gravity waves, and subsequently, friction is dominated by those waves. The wind speed depends on the measurement height z as

$$U(z) \approx w_* \left(k^{-1} \ln \left(\frac{gz}{w_*^2} \right) + K \right)$$

for different wind velocities ($k = 0.41$ is the Von Kármán constant). The denominator w_*^2/g is the so-called waveheight scale, which represents a measure of the roughness of the surface waves. The constant K is relatively universal and has been determined to be $K \approx 11.3$. Introducing this function of $U(z)$ into the definition of C_{10} allows determining C_{10} by

$$C_{10} \approx \left(k^{-1} \ln \left(\frac{10g}{C_{10} U_{10}^2} \right) + K \right)^{-2} .$$

This equation is an implicit relation in C_{10}, converging quickly after about four iterations. The typical values of C_{10}, see Fig. 3, range from 0.0011 (at $U_{10} = 5\,\mathrm{ms}^{-1}$) to 0.0021 (at $U_{10} = 25\,ms^{-1}$).

For weak winds (<5 ms^{-1}) the influence of gravity waves on surface stress eases, and surface tension or small-scale capillary waves, generating virtual roughness, become increasingly important. At low wind, one could expect the smooth law

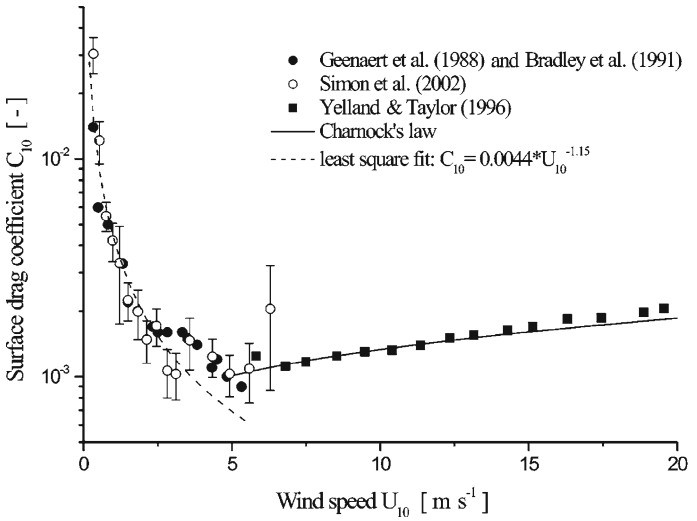

Fig. 3 Wind-drag coefficients C10 for developed waves as a function of wind speed U10 at standard (10 m) height above water. Courtesy of Wüest and Lorke (2003)

$U(z) = w_*(k^{-1}\ln(w_* z \nu_{air}^{-1}) + 5.7)$ to apply (where ν_{air} is the kinematic viscosity of air). Indeed, for wind velocities of 3 to 5 ms^{-1}, see Fig. 3, experimental evidence confirms the smooth-law value for $C_{10} \sim 0.001$. However, at even lower wind ($<3\,ms^{-1}$), the experimental values of C_{10} consistently increase much faster (Fig. 3) with decreasing wind compared to the smooth-law prediction. According to the data shown in Fig. 3, the empirical parameterization $C_{10} \approx 0.0044 U_{10}^{-1.15(\pm 0.09)}$ (with U_{10} in ms^{-1}) for wind speeds less than $3\,ms^{-1}$ can be used. Astonishingly enough, such weak winds have drag coefficients larger than those for $25\,ms^{-1}$ winds. In lakes, the light-wind C_{10} value is of great relevance because most inland waters (especially small-to-medium-sized lakes) are exposed for most of the time to light winds only.

The above C_{10} approximations represent lower bounds because they are based on developed wave fields. For young, accelerating, and breaking waves, the friction, and thereby also C_{10}, will be larger than in Fig. 3.

Langmuir circulation In addition to wind-induced small-scale turbulence, an organized vertical motion of the scale of the epilimnion depth also evolves under the action of surface wind-stress. The hydrodynamics of these vortices, termed Langmuir cells, is not simple. We refer to Leibovich (1983) for an overview of the relevant theories and more detailed description.

When the wind speed exceeds a certain threshold speed of $\sim 3\ ms^{-1}$, within a few minutes, streaks, aligned approximately parallel to the wind direction and composed of floating objects such as bubbles and leaves can develop on the lake surface. As Langmuir (1938) showed, these streaks result from the convergence of two counter-rotating vortices at the top of the epilimnion with axes nearly parallel to the wind. Hence, surface water is transported downward at the streaks and upwelling

occurs in between. This circulation pattern establishes itself independently of surface heating or cooling. A destabilizing surface heat flux may lower the threshold for the onset of these convective rolls.

The form of the rolls is asymmetric, but the lateral width (approximately half of the streak spacing L; see Fig. 2) and the vertical penetration depth of the rolls are observed to be approximately equal. Generally, the spacing L of the streaks increases with wind speed U_{10} and can be approximated according to Leibovich (1983) by: $L \sim (2 - 5\mathrm{s}) \times U_{10}$.

However, the vertical scale of the circulation is limited by the base of the mixed layer, where strong density gradients suppress vertical motion. Thus, the above equation can only hold as long as $L/2$ is smaller than the epilimnion depth. Hence, the wind threshold and the epilimnion depth put lower and upper limits on the size of the Langmuir vortices. In fact, the size of the cells in lakes is mostly on the order of 10 m.

Downwelling at the convergence streaks can attain maximum vertical velocities of ~1% of the wind speed. The structure of the rolls is asymmetrical, with downwelling currents being of higher velocity than the upwelling currents. In general, downwelling velocities increase with wind speed and are comparable to the wind-induced surface drift. The downwelling velocities suggest that Langmuir circulation may cause epilimnion mixing. While observations led Langmuir (1938) to believe that the vortices are responsible for the formation and maintenance of the mixed layer, at present it is not certain whether Langmuir circulation is responsible for a significant part of the stirring. Nevertheless, Langmuir cells are important for the ecology of surface waters, since the environment to which an algal cell is exposed—especially light intensity—depend critically on whether or not it is undergoing vertical transport by such vortices.

2.4 Vertical Structure of the Bottom Boundary Layer

The bottom boundary layer (BBL) follows the same concept as the SBL with more simple boundary conditions. The transition from the background flow, far away from the sediment, to the flow at the sediment/water interface is less complex than in the SBL because of the absence of waves, the lower variability of the forcing, and the rigid boundary (zero velocity). The temporal structure of the BBL is also steadier than the SBL, owing to the different nature of the forcing. Whereas the SBL is exposed to fluctuating wind stress, the BBL is defined by friction, which damps unsteady currents and removes fluctuations. Nevertheless, there are many similarities between the BBL and SBL. The BBL of lakes is usually actively turbulent, with the exceptions of small and wind-protected lakes, where strong stratification can reach all the way to the sediment.

The BBL can be split up into three different layers, see Fig. 5: the logarithmic layer, where the flow is turbulent and the Law-of-the-Wall is mostly applicable, the

viscous boundary layer (VBL), where the flow becomes laminar due to viscosity, and the diffusive boundary layer (DBL), where fluxes are limited by molecular diffusion.

The bottom stress τ_{bbl}—here assumed again to be constant through the BBL—defines the friction velocity $u_* = \sqrt{\tau_{bbl}/\rho}$, the characteristic velocity scale within the BBL (imagine as the velocity of the turbulent eddies in the BBL). In the turbulent logarithmic layer, the TKE balance is given by production = dissipation (assuming negligible BBL stratification, $N^2 = 0$); i.e.,

$$J_R = -\overline{u'w'}\frac{\partial u}{\partial z} = \frac{\tau_{bbl}}{\rho}\frac{\partial u}{\partial z} = \varepsilon \, .$$

We assume again (as in the SBL), that the eddy viscosity satisfies Prandtl's mixing length hypothesis where the eddy sizes and diffusivity increase with distance h to the wall. This leads also here to the Law-of-the-Wall with $\frac{\partial u}{\partial z} = u_*/kh$ and $\varepsilon = u_*^3/kh$. Current measurements in lakes indeed match these relations with stunning agreement. In the example presented in Fig. 5, 8.5 min averages of the currents follow the logarithmic profile over several meters within the BBL.

In the BBL the energy dissipation (kinetic energy loss) is due to bottom friction. The dissipation—in steady state—is equal to the total energy flux into the BBL. The dissipation within the layer from the sediment to 1 m above the sediment is given by

$$P_{diss,1m} = \tau_{bbl}U_{1m} = \rho C_{1m}U_{1m}^3 = \frac{\rho}{C_{1m}^{1/2}}u_*^3 \, .$$

In weakly forced water bodies the low turbulence level may not be able to keep the BBL well mixed. The continuous release of dissolved solids from the sediment (by mineralization and other sediment processes) can stabilize the BBL ($N^2 > 0$) and suppress mixing. In this case, the Osborn model for the eddy viscosity can be used, $K_\nu = \gamma_{mix}\varepsilon N^{-2}$ which is a function of the distance from the sediment. In contrast to the well-mixed case, K_ν is increasing toward the sediment until the distance $h \approx \sqrt{\gamma_{mix}}u/(kN)$ is reached. Below this critical height, the diffusivity is decreasing again according to Law-of-the-Wall and even faster close to the sediment.

The diffusivity K_ν is the sum of the molecular diffusivity and turbulent eddy diffusivity, K_{turb}. Compiling the many parameterizations for K_{turb} reveals that it decreases steeply as h^3 to h^4 when approaching the sediment. Subsequently, there are two heights where K_{turb} becomes smaller than the molecular viscosity and the molecular diffusivity, see Fig. 4, respectively. The height δ_ν, where K_{turb} falls below the kinematic viscosity, defines the top of the viscous boundary layer (VBL). Within this sublayer, the viscous forces dominate the resistance to momentum transfer. Subsequently in the viscous sublayer the greatest changes in velocity occur and the horizontal flow becomes laminar. The boundary-layer thickness δ_{bbl} is still equal to the constant value above, but the momentum flux is only a function of the (molecular) viscosity. Therefore,

$$\frac{\partial u}{\partial z} = \frac{\tau_{bbl}}{\rho\nu} = \frac{u_*^2}{\nu}$$

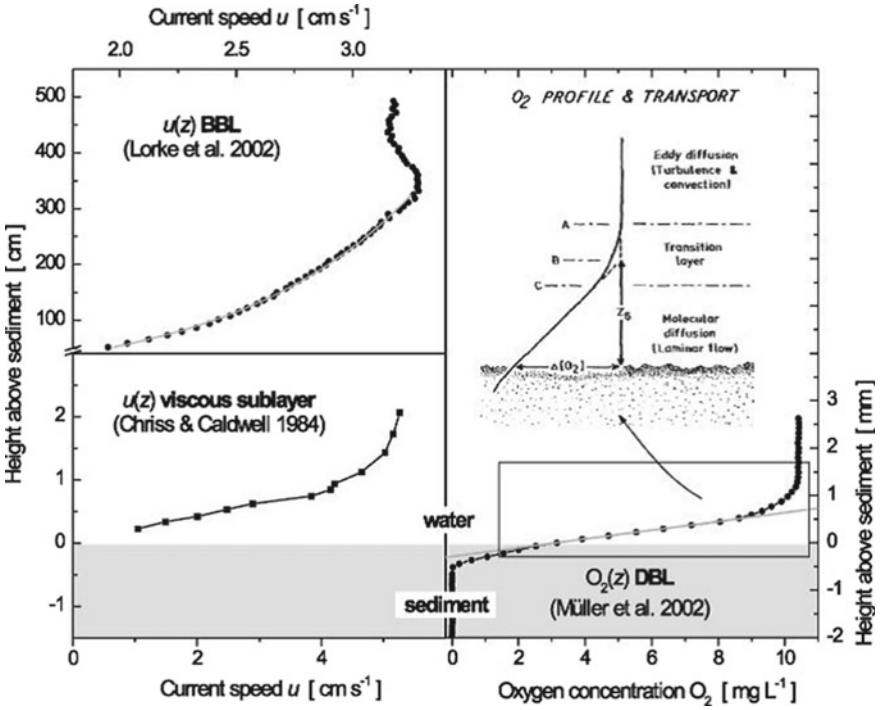

Fig. 4 Measured seiching currents (*upper left*), showing a perfect BBL logarithmic layer in a lake, from Lorke et al. (2002), and deep ocean currents (*lower left*), exemplifying the linear profile in the viscous sublayer, from Caldwell and Chriss (1979). The oxygen profile is on a sub-mm scale and shows the 0.7 mm thick diffusive boundary layer in a lake, from Mueller et al. (2012) *lower right*). The schematic, adapted from Jorgensen and Des Marais (1990), defines the outer limit (*A*), the true (*C*), and the effective (*B*) diffusive boundary layer (typically 1 mm thick; *upper right*). The transition layer (broken line) is also perfectly identifiable in the oxygen micro-gradient (*lower right*). Courtesy of Wüest and Lorke (2003)

and the gradient depends only on the friction velocity and the viscosity. The distance from the bottom—where the flow becomes laminar—is given by $\delta_\nu \approx 10\nu/u_*$, typically millimeters to centimeters, see Fig. 4. Within the viscous sublayer, turbulent eddies are virtually absent. The Reynolds number $Re = u\delta_\nu/\nu$ is only of order 100 or smaller and therefore indicates no turbulence. The flow in the viscous sublayer is practically laminar. In the viscous boundary layer, turbulent kinetic energy dissipation is at its maximum, even though the flow is laminar. The TKE balance, leads to

$$\varepsilon_\nu = \frac{\tau_{bbl}}{\rho}\frac{\partial u}{\partial z} = \frac{u_*^4}{\nu}\,.$$

The dissipation in the VBL increases with the power 4 with the friction velocity—as to be confirmed easily by dimensional analysis. Hence the total dissipation in the viscous sublayer is given by

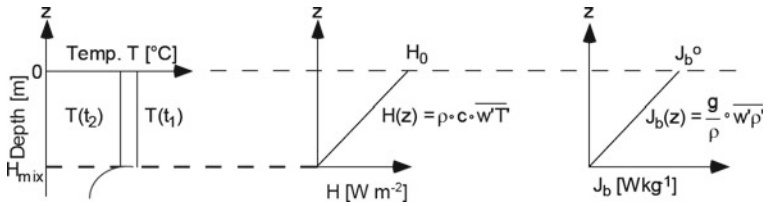

Fig. 5 Schematics of the heat flux (*middle*) and the buoyancy flux (*right*) as an effect of homogeneous cooling of a mixed SBL (*left*)

$$P^{\nu}_{diss} = \rho\varepsilon_{\nu}\delta_{\nu} = \frac{\rho}{\nu}u_*^4\delta_{\nu} \approx 10\rho u_*^3 \,.$$

Comparing the total VBL dissipation with the total BBL dissipation, provides a ratio of $P^{\nu}_{diss}/P_{diss} = 10C_{1m}^{0.5} \approx 0.4$. Thus, about 40% of the total energy entering the BBL is dissipated within the VBL (laminar), the remainder being dissipated within the logarithmic layer (turbulent). The practical implication is, that about 40% of the energy dissipation in the BBL is laminar (causing no mixing), whereas about 60% is turbulent (causing mixing).

Analogously, $K_{turb} \sim D_c$ defines the top of the diffusive boundary layer (DBL) (Fig. 4), which extends, according to the z-dependence of K_{turb} to $\delta_D \approx \delta_{\nu}(D_C/\nu)^a$ (a is between 1/4 and 1/3). Since molecular diffusivity is about three orders of magnitude lower than viscosity, the thickness δ_D is about 10 times smaller than δ_{ν}. Within the DBL, transport by eddies becomes insignificant compared to molecular diffusion.

The diffusive bottom boundary layer As evidenced from the first Fick law, $D_C\partial C/\partial z \approx (D_C/\delta_{dbl})\Delta C$, the key parameter for the sediment/water flux of a solute C is the gradient within the DBL. Those gradients depend on the thickness δ_{dbl} and the rate of consumption (or production) of solute C in the sediment, the latter affecting the concentration driving force ΔC across the interface. The DBL thickness is solute-specific because δ_{dbl} depends on D_C (varying by a factor of ~2 among the different solutes) and is slightly temperature-dependent, as ν and D_C are both functions of temperature.

The DBL thickness is not well defined for several reasons. Most obviously the top end of the DBL (in fact also the top of the VBL) is not sharp, because the turbulence cut-off at the Kolmogorov scale $\eta = (\nu^3/\varepsilon)^{1/4}$ is a gradual roll-off following the turbulence spectrum ~ (eddy size)$^{-b}$ with $b = 3 - 4$. Therefore, a transition zone exists between the pure molecular and fully turbulent zones above, where K_{turb} and D_C are approximately equal. To remove this ambiguity, the effective DBL is defined by extrapolating the linear concentration gradient right above the sediment to the bulk water concentration, see Fig. 4. This theoretical DBL thickness provides a practical procedure to calculate the true flux through the interface based on ΔC, the concentration difference between the sediment surface and the bulk water above.

The relevance of the deep currents for the sediment/water transfer of solutes becomes more obvious by expressing the molecular flux by the mass transfer coefficient (D_C/δ_{dbl}). Because the mass transfer coefficient is $\frac{D_C}{\delta_{dbl}} = \nu/\delta_\nu \sim u_*$, the interfacial flux becomes proportional to the flow acting on the BBL. As a practical consequence, wind-exposed aquatic systems will show higher rates of degradation and turnover of organic matter than weakly forced ones. As a global consequence, old lacustrine sediments contain more organic carbon and nutrients than relic marine sediments. Besides the molecular DBL fluxes, there are additional pathways between the sediment and water. In Lake Erie, for instance, zebra mussels have created densely populated reefs (with several thousand mussels per m^2), which have been identified for their enormous venting capacity. As another example, in shallow waters, heating of the sediments by short-wave radiation causes buoyant porewater to convect through the interface. Such nonlocal processes are often more effective than molecular diffusion. In eutrophic waters, advective transport through the sediment-water interface occurs mainly by methane and carbon dioxide bubbles formed in the anoxic sediment. Whereas in oligotrophic lakes, where the sediment surfaces remain oxic, worms or other macrofauna (such as insect larva) act as conveyor belts through the interface and produce ventilation dips and mounds. The biotic invasion has a positive feedback effect: Enhanced activities of macro- and meiofauna, which move sediment around and pump oxygen-rich water into their burrows, improve the oxic conditions in the sediment and thereby improve the living conditions for more bottom biota. Bioturbation by benthic organisms, therefore, is of general importance for the distribution and flux of soluble and colloidal material in lacustrine sediments. Besides the direct effect on the flux of matter between sediments and water, biota has an indirect effect on the ex-change by influencing the BBL roughness. Faecal pellets, tracks, trails, tubes, pits, and mounds enhance the structuring and spatial heterogeneity and increase the bottom roughness, leading to an increase in the mass and momentum transfer.

2.5 Convectively-Induced Turbulence and Mixing in the Boundary Layers

Convectively-driven turbulence occurs in natural waters under several circumstances:

1. Cooling-induced turbulence in the surface boundary layer (SBL)
2. Warming-induced turbulence in the bottom boundary layer (BBL)
3. Convective turbulence caused by thermobaric-instabilities
4. Local instabilities caused by double diffusion
5. Shear-induced convective instabilities in the bottom boundary layer (BBL).

These occasions are the classical examples, however, there are more possibilities. In general, convective turbulence occurs when some density-modifying processes manoeuvre or produce heavier water on top of lighter water. Further examples are: (i) evaporation in salty waters causing higher salinity/higher density at the very top

of the water body; (ii) the release of bubbles at the sediment—reducing density at the bottom of the water column.

Surface boundary layer convective turbulence In the boundary layer near the surface (SBL) convection occurs, when higher density is produced at the very top (right at the surface) of the water column. Higher density is produced by cooling when $T > T_{MD}$ (temperature for maximum density) or by salinity-production via evaporation. As a result, the surface water column becomes unstable and convective turbulence sets in (Rayleigh instability). The net density (mass) flux $\overline{w'\rho'} = F_\rho$ is directed downwards (heavier parcels moving down and lighter ones moving up, see Fig. 6) and causes a contribution in the buoyancy flux term. In the TKE budget, the term $J_B = (g/\rho)\overline{w'\rho'}$ makes a positive contribution (= production of turbulence; here J_b is a source of turbulence).

The most common way to generate heavier water parcels at the top is by cooling the SBL (loss of heat to the atmosphere). The effect of cooling is the formation of small parcels right at the top of the surface which are slightly cooler than the parcel below. If $T > T_{MD}$ then the slightly cooler parcels are also slightly heavier by $\Delta\rho$ and subsequently sink. Relative to the base of a mixed layer (of thickness h_{mix}), these

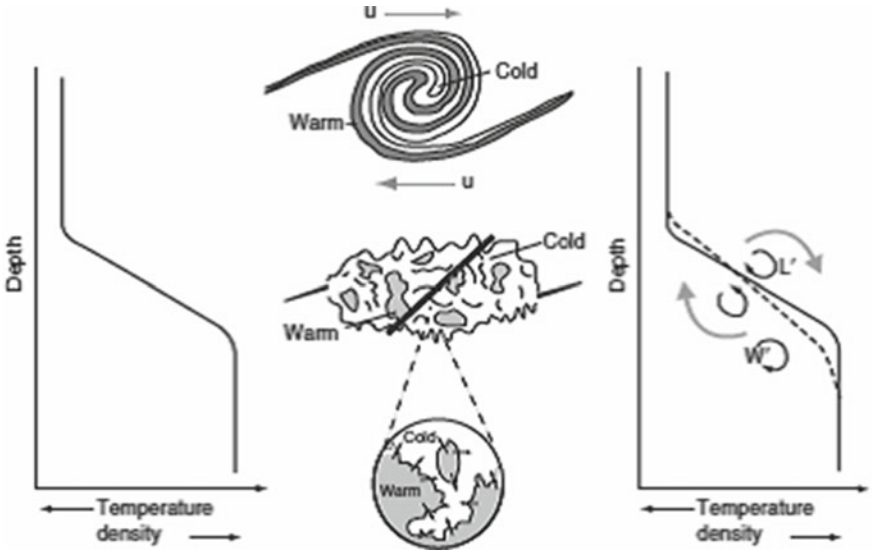

Fig. 6 The effect of turbulent mixing in a stable stratification: if the vertical gradient of horizontal currents (current shear) is stronger than the stability of the water column, Kelvin-Helmholtz instabilities can develop (*top* of *middle* panel) bringing warmer (lighter) and cooler (heavier) water in close proximity (*bottom* of *middle* panel). Finally, heat (or any other water constituent) is mixed by molecular diffusion across the manifold small-scale interfaces, which are generated by turbulence (see inset). The turbulent exchange of small water parcels leads to a fluctuating vertical heat flux which averages to a net downward heat flux. As a result, the original temperature profile (*left*) is modified (*right*): the vertical gradient is weakened and expanded vertically with heat transported from *top* to *bottom* across the interface. Courtesy of Wüest and Lorke (2009)

parcels have a potential energy (per kg of parcel mass) given by $(gh_{mix}/\rho)\Delta\rho$, where $\Delta\rho$ is the density difference of the water parcel relative to the background density. We assume that the "density producing process" lasts for some time. Then we can express the potential energy production per time interval Δt (rate of potential energy production) as $(gh_{mix}/\rho)\frac{\Delta\rho}{\Delta t}$. Because the density and potential energy production occurs right at the very top, we call this production term in the following as (index o for surface and b for buoyancy), the surface buoyancy flux,

$$J_B^o = \frac{gh_{mix}}{\rho}\frac{d\rho}{dt} .$$

This equation can intuitively be interpreted. Assume that the sinking parcels have a higher density by $\Delta\rho$. They replace lighter water parcels below (ρ) until the entire mixed layer has a density of $\rho + \Delta\rho$. We assume that the time interval Δ_t is needed to replace all the parcels of the mixed-layer with water of density $\rho + \Delta\rho$. One can think of a front of higher density water moving downwards with a velocity of $w = -h_{mix}/\Delta t$ with an associated density flux $F_\rho = w\Delta\rho$. For a mixed layer of thickness h_{mix} and a rate of density increase of $d\rho/dt$, the change of potential energy per area of the entire mixed layer is given by

$$F_{pot} = \frac{gh_{mix}^2}{2}\frac{d\rho}{dt} ,$$

where the factor 1/2 is due to the vertical integration of hdh over the entire mixed layer h_{mix}. Using the definition of J_B^o (above) leads to the following relation between F_{pot} and J_b^o:

$$F_{pot} = \frac{h_{mix}\rho}{2}J_b^o .$$

Cooling-induced convective turbulence The TKE balance in the non-stratified and non-sheared SBL (i.e. no other turbulence sources than convection; no large-scale shear) has a simple form, $\varepsilon = J_B = (g/\rho)\overline{w'\rho'}$.

In Fig. 5, the buoyancy flux is schematically shown for a mixed layer loosing heat while cooling from temperature $T(t_1)$ to $T(t_2)$. For a homogeneous rate of cooling $\frac{\partial T}{\partial t} = \frac{T(t_2)-T(t_1)}{\Delta t}$ within the mixed-layer of thickness h_{mix} the vertical heat flux as a function of depth is given by

$$H(z) = c_p\rho\overline{w'T'}(z) = c_p\rho\frac{\partial T}{\partial t}(-h_{mix} - z) .$$

Temperature T and density ρ are connected via the expansion coefficient α via $\frac{\partial\rho}{\partial T} = -\rho\alpha$. The same holds for the fluctuations, $\rho' = -\rho\alpha T'$. Therefore, the heat flux $H(z)$ and the buoyancy flux $J_B(z)$ are directly related by

$$J_B = \frac{g}{\rho}\overline{w'\rho'} = -\frac{g}{\rho}\alpha\rho\overline{w'T'} = -\frac{\alpha g}{c_p\rho}H(z) .$$

The heat flux $H(z)$ is positive upwards and ρc_p is the heat capacity. For the example in Fig. 6, where $H(z)$ is linear in z and also $J_b(z)$ is therefore a linear function with depth,

$$J_B(z) = \alpha g \frac{\partial T}{\partial t}(-h_{mix} - z) \; .$$

The average dissipation ε within the mixed layer h_{mix} is therefore $0.5 J_B^o$, as follows directly from inserting the above relations into the definition of the average,

$$\overline{\varepsilon} = \frac{1}{h_{mix}} \int_{h_{mix}}^{\varepsilon} (z) dz = \frac{1}{h_{mix}} \int_{h_{mix}}^{J_b} (z) dz = \frac{1}{h_{mix}} \frac{g\, h_{mix}^2}{2\rho} \frac{d\rho}{dt} = \frac{1}{2} J_B^0 \; .$$

It implies that the average dissipation is a function of the surface buoyancy flux alone. As a consequence, there are only two relevant physical parameters defining the similarity scaling for convective turbulence: thickness h_{mix} and surface buoyancy flux J_B^o.

Sources of buoyancy flux The buoyancy flux is a source or sink term in the turbulent kinetic energy (TKE) balance. The sign of the buoyancy flux has the following meaning for the TKE balance:

- $J_B^o > 0$: Production of TKE (i.e., sinking heavier water parcels or rising lighter water parcels), $J_B(z) > 0$ in the entire SBL.
- $J_B^o < 0$: Strengthening of stratification; no turbulence is produced, therefore $J_B(z) = 0$ in the interior.

The following processes can lead to a positive buoyancy flux and therefore to convective mixing, both at the water surface or within the water column:

1. Heat flux at the water surface (H_{net} = heat flux from the water surface to the atmosphere):

$$J_B^o = \frac{g h_{mix}}{\rho} \frac{d\rho_o}{dt} = -g h_{mix} \alpha \frac{dT_o}{dt} = \frac{\alpha g}{\rho c_p} H_{net,o} \; .$$

2. Change in salinity:

$$J_B^o = g h_{mix} \beta \frac{dS}{dt} = \frac{g\beta s}{\rho} m_E = g\beta S E = \frac{g\beta s}{\rho \lambda e} H_E \; .$$

Here, $\beta \sim 0.8 \times 10^{-3} ‰^{-1}$: coefficient of haline contraction, S = salinity, λ_e = specific latent heat; H_E = latent heat flux, m_E = evaporation rate, E = evaporation. Increasing salinity at the surface increases density and generates turbulence ($J_b^o > 0$). Decreasing surface salinity leads to a negative buoyancy flux. E must then be replaced by precipitation, ice melting, or freshwater addition (inflow).

3. Heat fluxes through the water-sediment boundary ($H_{net,B} > 0$ means heat flux into the water, index b for bottom):

$$J_B^b = -\frac{gh_{mix}}{\rho}\frac{d\rho_b}{dt} = gh_{mix}\alpha\frac{dT_b}{dt} = -\frac{\alpha g}{\rho c_p}H_{net,b} \ .$$

4. Remineralisation of salts: negative buoyancy flux, leads to stabilization.
5. Double diffusion: production of TKE by sinking salt fingers (finger regime) or rising thermals (diffusive regime).
6. Particles settling from density currents.

3 Stratified Turbulence in Lakes Interior

Below the surface boundary layer (SBL), almost all natural waters (lakes, reservoirs, estuaries, oceans) are density-stratified to some extent. The turbulence in this stratified part of the water body (stratified deep ocean; stratified hypolimnia of lakes, etc.) is strongly reduced and vertical exchange occurs over relatively short vertical scales. Large vertical eddies have not enough energy to be maintained and do not exist. Due to these short exchange lengths the vertical fluxes are more of "diffusion-type" and therefore it is adequate to quantify the fluxes by turbulent diffusivities. However, the prominent feature of the thermocline is not turbulence but the persistent existence of internal waves (which may cause turbulence, if intense enough).

Kelvin-Helmholtz instability and Richardson number The shear flow in a stratified fluid is characterized by two relevant physical quantities, shear and stability. Similar to the Reynolds number and the Rayleigh number, here again a dimensionless number is formed to characterize the phenomenon. The Richardson number is defined as the ratio of the stabilizing to the destabilizing force

$$\frac{\text{buoyancy}}{\text{inertia}} = \frac{N^2}{\Delta u^2/L^2} = Ri \ ,$$

or

$$Ri = \frac{N^2}{(\partial u/\partial z)^2} \ .$$

Two cases can be distinguished separated by the critical Richardson number $Ri_c \sim 0.25$. This critical value can be determined experimentally, as indicating the transition from stable (laminar) to turbulent flow. In the case that $Ri < Ri_c$: Kelvin-Helmholtz instability, the flow field is dominated by overturns, and the fluid flow is turbulent with enhanced vertical transport, see Fig. 6. For $Ri \gg Ri_c$: the density stratification is dominant, stability is stronger than shear, i.e., small perturbations are damped by stability and do not grow to turbulence. The energy contained in the perturbations is radiated (distributed) by internal waves.

Turbulence measurements in natural waters In the following sections, some techniques that are used to determine energy dissipation rates in natural stratified waters are briefly described. They all have in common that they rely on instruments that allow measuring either velocity fluctuations or temperature fluctuations (salinity fluctuations: today technically not yet possible) with a very high spatial and temporal resolution. The need to resolve the smallest scales that still contribute significantly to the total variance of velocity or temperature (or salt) is the major challenge. The drop-off of the spectra at high wave numbers is determined by the level of energy dissipation ε, since both the Kolmogorov k_K and the Batchelor k_B wave numbers depend on ε:

$$k_K = \left(\frac{\varepsilon}{\nu^3}\right)^{1/4},$$

$$k_B = \left(\frac{\varepsilon}{\nu D^2}\right)^{1/4}.$$

Therefore, ε determines the required spatial resolution of the measurements, see also Fig. 7. Since the maxima of the spectra are in the range of millimeters or centimeters, measurements need to be performed with such a high resolution. Consequently, the experiments are laborious and include the processing of large amounts of data. Fluctuations of temperature and velocity are sampled as time series. The wave number k is calculated from the frequency f and the sinking velocity W of the sensor (typically 0.1–1 ms^{-1}) by $k = f/W$.

Turbulence techniques—inertial dissipation method According to the discussion above, the equilibrium range consists of the inertial subrange (*left* side of the spectrum; larger scales) and the dissipation subrange (*right* side of the spectrum; smaller scales and viscous cut-off). In the inertial subrange the energy spectrum follows $\Phi(k) = a\varepsilon^{2/3}k^{-5/3}$.

The dissipation level can be determined, if the energy of the power spectrum $\Phi(k)$ can be measured in the inertial subrange. Ideally, the instrument is able to resolve the turbulence *down* to the Kolmogorov length scale. An example of a measured energy spectrum in the ocean is given in Fig. 8.

Turbulence techniques—dissipation method and shear probes Vertical profiles of horizontal velocity fluctuations u are measured using a microstructure shear probe, which can sample vertical gradients of horizontal velocity $\partial u'/\partial z$ with an accuracy of about 10^{-4} s^{-1} and a resolution on the millimeter scale. The probe is mounted at the front of a free-falling device which descends at a speed of typically 0.5–1 ms^{-1}. The dissipation rate is then directly calculated from the spectrum of the shear

$$\varepsilon = 7.5\nu\overline{\left(\frac{\partial u'}{\partial z}\right)^2} = 15\nu\int_0^\infty \Phi_S dk\ .$$

The factor 7.5 is due to the fact that only one component of the shear is actually measured.

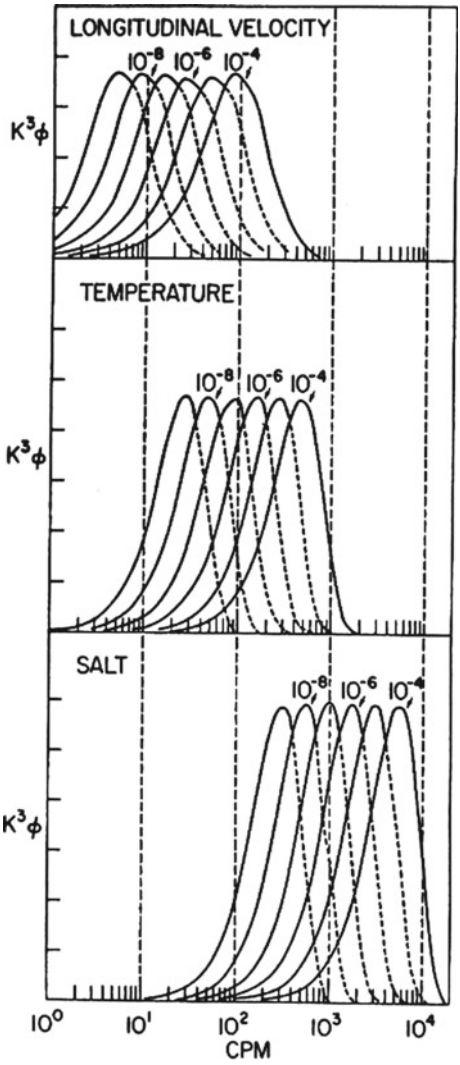

Fig. 7 Energy-preserving plot of the spectra of shear (*upper* panel) temperature gradients (*middle* panel) and salt gradients (*lower* panel). The area beneath the curves is equal to ε (shear) and χ_T (temperature) and χ_S (salt), respectively. To get accurate results, measurements need to resolve the fluctuations at least down to the scales where the maxima of the curves are located. This is in the cm or mm range for most practical applications. A device that is able to sufficiently resolve the salt gradients still needs to be developed. (CPM = cycles per meter)

Turbulence techniques—Batchelor method The Batchelor method for measuring turbulence is based on the scalar spectrum for temperature between the Kolmogorov (η) and the Batchelor (η_B) length scales. In lakes or oceans, vertical temperatures are profiled with a sufficiently high resolution to measure the smallest vertical scales of turbulence. This is performed using a free-falling microstructure probe which samples temperature at a fast rate and with a high resolution. For example, the spectrum shown in Fig. 9 was derived from data measured with a probe moving at a speed of about 0.1 ms^{-1} and sampling temperature with a frequency of 96 Hz and a resolution of 5×10^{-4} C (0.5 mK). Sections of the temperature profile are

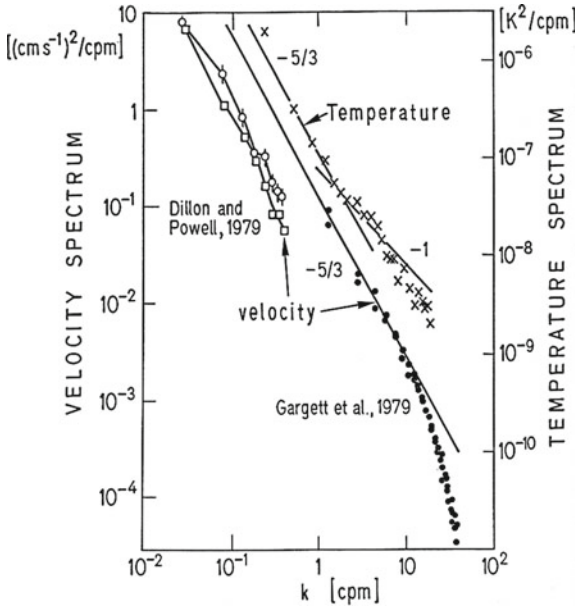

Fig. 8 Two curves on the *left* refer to energy spectra (scale on the *left* axis). Dillon and Powell (1979) refers to lake surface waters. Gargett et al. (1979) represents data from the ocean interior. In both cases, the $-5/3$ slope indicates the inertial subrange. The temperature spectrum shows the $-5/3$ and the -1 (Batchelor spectrum). Courtesy of Imboden and Wüest (1995)

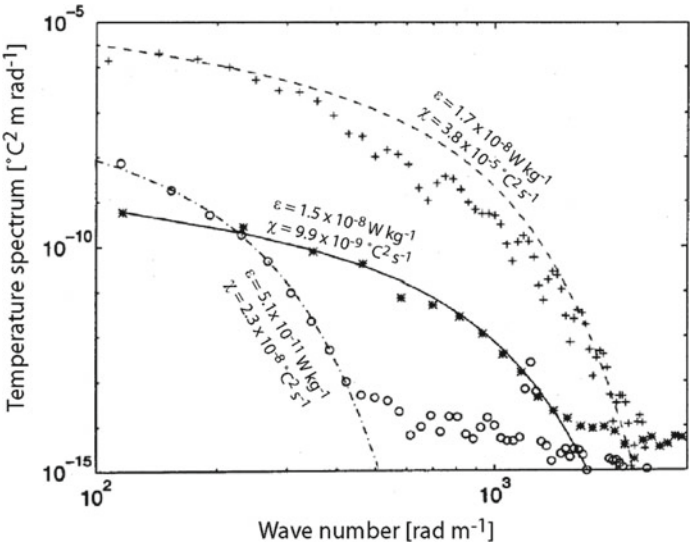

Fig. 9 Temperature spectra calculated from three different sections of a microstructure profile measured in Lake Baikal, and theoretical functions fitted to the spectra. The function has two fit parameters: the dissipation rate ε, which determines the form of the curve, and the rate of diffusive smoothing of temperature, χ, which determines the absolute level of the curve

then converted to spectra by Fourier transformation. The theoretical one-dimensional spectrum

$$\Phi_T = \frac{\chi_T}{2}\sqrt{\frac{D_T}{\gamma^3}}\left[\frac{1}{x}e^{-x^2} - \sqrt{\pi}\,(1 - \mathrm{erf}(x))\right]$$

where $x = k\sqrt{DT/\gamma}$, is finally fitted to the observed spectrum using the two fit parameters χ_T and γ.

4 Wind Set-up, Internal Standing Waves and Modes

Wind set-up Wind blowing in a constant direction over a water body exerts a surface stress $\tau = \rho_{air}\, C_{10}\, U_{10}^2$, which moves the water of the surface layer towards the downwind end. As indicated in Fig. 10 it has two effects on the water body:

- the water level becomes tilted, piling up water on the downwind end and lower the water level on the upwind end, see Fig. 10; and
- the lighter surface layer (epilimnion) becomes deeper on the downwind end, where more surface water is moved to and it becomes thinner on the up-wind end where deep-water is upwelling and replacing surface water, see Fig. 10.

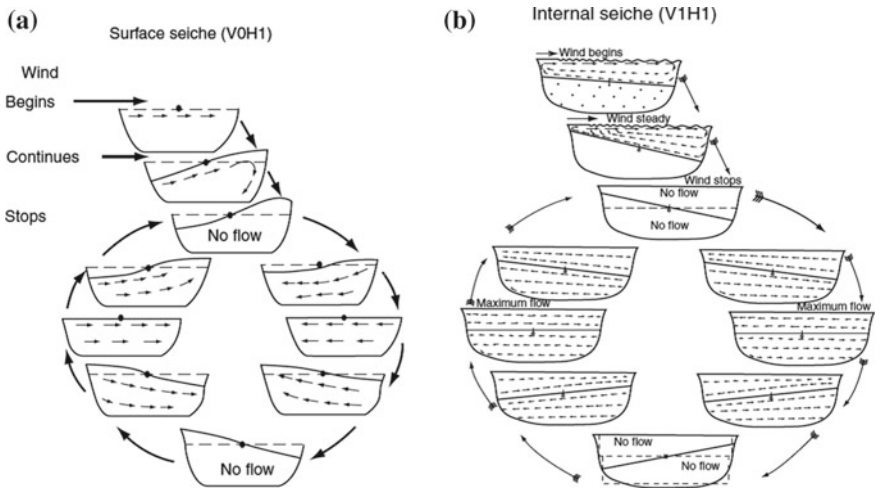

Fig. 10 Movement caused by steady moderate wind stress on a hypothetical layered lake and subsequent internal seiche motion. (*Left*) Horizontal mode-one surface seiche in a homogeneous one-layered system. (*Right*) horizontal-mode one vertical-mode one internal seiche in a two-layered system. The *top* two schemes show the set-up for both modes. The circle below is a schematic of the temporal development of the surface level (*left*) and the pycnocline (*right*) in steps of 1/4 of the seiching period. At 0 and 1/2 period, the energy is purely potential and there is no flow. At 1/4 and 3/4 period, the dislocation is zero and all energy is in kinetic form. Courtesy of Mortimer (1952)

This forcing on stratified lakes leads to internal waves of various temporal and spatial scales. Roughly 20% of the wind energy entering the lake is transferred to large-scale wave motions, called basin-scale internal waves (hereafter BSIW); the remainder being dissipated in the surface layer. These waves temporarily store the wind energy until it is dissipated, mainly by friction along the lake bed. They play a crucial role in the transport of mass and momentum in the lake, driving horizontal dispersion and vertical mixing with great implications for biogeochemical processes and contaminant transport.

Generation of basin scale internal waves To describe the generation of these waves, we start with a simple rectangular lake of length L, width B, and depth H, with a sharp thin thermocline separating a homogenous warm epilimnion of thickness h_1 and density ρ_1 and from a homogeneous cold hypolimnion of thickness h_2 and density ρ_2. A steady wind applied to the lake surface, see Fig. 10, causes an upwelling (setup) of the free-surface and a lowering of the thermocline at the downwind shore. If the wind forcing lasts for more than a quarter of the fundamental mode-one BSIW period (defined below), the thermocline tilt will span the entire basin with a maximum amplitude $\eta_o = Lu_*^2/g'h_1$, where $g' = g(\rho_2 - \rho_1)/\rho_2$ is the reduced gravity as a result of the density difference across the thermocline. The gravitational force acting on the tilted interfacial free-surface and thermocline generates both surface (barotropic) and internal (baroclinic) pressure gradients, which balance the applied wind force. When the wind stops, the gravitational force is unbalanced and the interfaces relax, generating freely propagating basin-scale internal and surface waves, from both upwind and downwind ends of the lake. The upwind and downwind components combine to form basin-scale standing waves on both interfaces, referred to as surface and internal seiches.

A single wind burst or aperiodic wind events lead to free modes with natural periods that depend on the basin shape, the stratification and the Earth's rotation. Conversely, periodic wind forcing (e.g. sea breeze) systematically resets the phase of the wave, leading to forced BSIWs with periods that match those of the wind forcing.

Horizontal pattern of basin scale internal waves A two-layer system is a good approximation for most lakes at mid-latitude during the late summer, see Fig. 11. When the wind relaxes, the oscillation takes the form of a sinusoidal standing wave with antinodes at either end of the basin. The motion is described by the linear shallow water equation, the wave speed $C = \sqrt{g'H_e}$, where $H_e = h_1h_2/(h_1 + h_2)$ the equivalent depth. C depends on the stratification and will change during the season as the thermocline deepens. Different horizontal wave modes can be exited as long as they match the antinodal boundary condition, and the different periods associated with the horizontal modes are $T_n = 2L/nC$, where n is the number of nodes in the horizontal (i.e. the horizontal mode). The first horizontal mode can contain up to 98% of the energy embodied in the initial wind induced thermocline tilt, but basin shape and/or wind forcing can enhance the importance of secondary modes in some cases, see Boegman et al. (2005b).

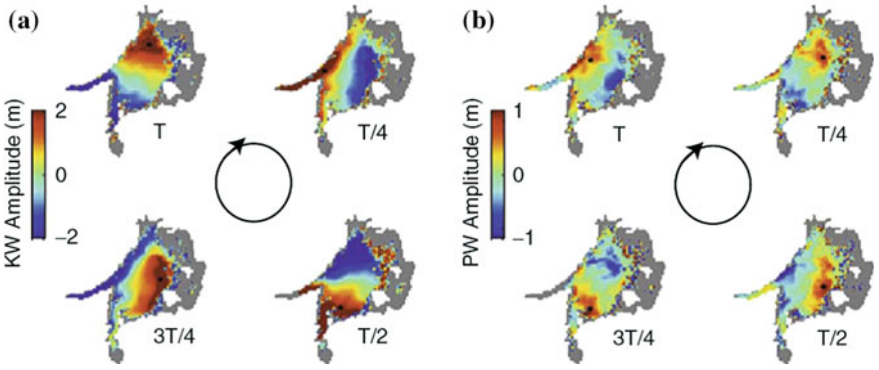

Fig. 11 Example of a Kelvin wave in Lake Simcoe shown as temporal evolution in 1/4 of a period. Evolution of the 15 °C isotherm, representing the thermocline displacement from a three-dimensional hydrodynamic simulation. *Left* Data have been band-pass filtered around the 95-h Kelvin wave period. Each image is offset by a 1/4 of Kelvin wave period (24 h) and shows the counter-clockwise evolution of the wave. *Right* Data have been band-pass filtered around the 14-h Poincaré wave period. Each image is offset by a 1/4 of Poincaré wave period (3.5 h) and shows the clockwise evolution of the wave. The *black dot* in each panel highlights the rotation of the wave crest, and the black *circle* represents the time evolution

Effects of Earth's rotation In large lakes, the Coriolis force, resulting from the Earth's rotation, becomes significant and can modify the wave pattern. The relative importance of the Coriolis force is quantified with the Rossby radius, $R_o = C/f$, and the Burger number, $S = R_o/f$, where $f = \frac{4\pi}{T} \sin\theta$ is the Coriolis parameter, $T = 1$ day, is the period of rotation of the Earth, θ is the latitude and R is a typical length scale characterizing the basin length or width (usually $L/2$). For lakes with $R > R_o$, and $S < 1$ rotational effects are expected. Conversely, in the case $S > 1$, rotational effects can be neglected.

We illustrate the effects of rotation on BSIWs by considering its influence on a longitudinal internal seiche in a large northern hemisphere lake. As the wind-displaced thermocline relaxes, and the seiche begins to propagate across the basin, the Coriolis force pushes the wave toward the right, where it is bounded by the shoreline, causing it to propagate cyclonically (counter-clockwise in the northern hemisphere) along the shore with the wave amplitude decaying exponentially in the offshore direction, see Fig. 11. This wave is called a Kelvin wave, and its period must be greater than the local inertial period, $T_i = 2\pi/f$. The phase velocity and corresponding wave period, T_1, remain the same, for the Kelvin wave, as in the non-rotational case. At a distance of $2R_o$ offshore, the wave is only 10% of its maximum amplitude, so in very large lakes, such as the Laurentian Great Lakes, where $R \gg R_o$, the Kelvin wave is a nearshore phenomenon that takes the form of a coastal jet. In smaller lakes, where $R \sim R_o$, the Kelvin wave signature can be found throughout the basin (e.g. Lake Simcoe, Canada, Fig. 11). We now consider the effect of rotation on the transverse basin-scale internal seiche. Because $L > B$, contrary to the longitudinal seiche, the transverse seiche is not constrained by the boundaries at the longitudinal ends of

the lake. When deflected to the right, by the Coriolis force, the seiche is, therefore, modified into a progressive anticyclonic (clockwise in the northern hemisphere) wave form. Fluid particles displaced by the wave follow anticyclonic circular or elliptical trajectories, known as inertial circles, with radius $r = u/f$, where u is the wave induced current speed. These transverse waves are called inertia-gravity waves or Poincaré waves and the dispersion relation for a rectangular basin, in terms of the wave period, is given by: $1/T_{PW}^2 = 1/T_i^2 + (1 + r^2)/T_1^2$, where $r = B/L$, is the basin aspect ratio at the thermocline depth. The dual character of this wave can be seen in the dispersion relation, where the first term on the right hand side describes the inertial behavior of the inertial circles and the second term has gravitational wave behavior with rectilinear motion. This explains the elliptical pattern of the Poincaré wave with the eccentricity depending on the relative intensity of these two terms. The dispersion relation (above) shows that the Poincaré wave period is typically close but always lower than the inertial period, the shift being a function of the basin shape (through r) and the stratification (through T_1) and can therefore be expressed as a function of S (Antenucci and Imberger (2001)) with the same trend of T_{PW} approaching Ti (inertial wave behavior) as S decreases (i.e., large lake).

Basin scale internal wave damping processes BSIW energy is ultimately damped by dissipation (friction) and the work required by diapycnal mixing. The processes responsible for dissipation and mixing can be linked to external driving factors, such as wind, stratification and basin shape, which energize the waves, using the dimensionless Wedderburn number, W. The magnitude of the wind induced thermocline setup can be quantified according to $W = h_1/\eta_o$, which is the ratio of the restoring baroclinic pressure force (i.e. gravitational force acting on the tilted thermocline) to the applied wind force. In the case of linear BSIWs, $W^{-1} < 0.3$, 90% of the wave energy is dissipated by friction as the seiche induced currents oscillate along the bottom boundary (Imberger (1998); Wüest et al. (2000); Bouffard et al. (2012)). These currents generate a turbulent bottom boundary layer and shear instabilities form where the thermocline oscillates in a swash zone along the lake bed. For $0.3 < W^{-1} < 1.0$, the BSIWs begin to lose energy to smaller-scale nonlinear internal waves, e.g. solitary waves, see Boegman et al. (2005a), which propagate with little energy loss until they shoal and break on sloping topography at the depth of the thermocline; leading to localized dissipation, mixing and sediment resuspension. Under conditions of strong forcing and weak stratification, $W^{-1} > 1.0$, BSIWs will degenerate through the formation of internal hydraulic jumps and/or shear instability in metalimnion of the basin interior. Detailed quantifications of the energy flux paths in lakes can be found in Wüest et al. (2000), Boegman et al. (2005b), Bouffard et al. (2012).

5 Concluding Remarks

Lake and reservoir ecosystems are strongly affected by anthropogenic pressure. A first example is the lake eutrophication and related harmful algae bloom development. A second example is the impact of climate change and related increased stratification strength and duration. Both require good managing strategies to preserve or restore the ecosystem integrity. Efficient guidance for lake and reservoir managers comes with capabilities to evaluate mixing and transport in stratified flows. In the past, many studies have focused on the connection between small-scale turbulence and the large-scale basin-scale internal waves transport. While still an active research field, recent developments of measurement techniques such as satellite observation, autonomous underwater vehicles, automatized profilers have open new horizons and, today, allow to investigate at high frequency the lateral variability in lakes. Yet, the role of mesoscale rotating eddies in the large to small-scale energy transfer remains largely unexplored in lakes and is a promising research topic.

References

J.P. Antenucci, J. Imberger, Energetics of long internal gravity waves in large lakes. Limnol. Oceanogr. **46**(7), 1760–1773 (2001)

L. Boegman, G.N. Ivey, J. Imberger, The degeneration of internal waves in lakes with sloping topography. Limnol. Oceanogr. **50**(5), 1620–1637 (2005a)

L. Boegman, G.N. Ivey, J. Imberger, The energetics of large-scale internal wave degeneration in lakes. J. Fluid Mech. **531**, 159–180 (2005b)

D. Bouffard, L. Boegman, Y.R. Rao, Poincaré wave-induced mixing in a large lake. Limnol. Oceanogr. **57**(4), 1201–1216 (2012)

D. Bouffard, L. Boegman, A diapycnal diffusivity model for stratified environmental flows. Dyn. Atmos. Oceans **61**, 14–34 (2013)

D.R. Caldwell, T.M. Chriss, The viscous sublayer at the sea floor. Science **205**(4411), 1131–1132 (1979)

T.M. Dillon, T.M. Powell, Observations of a surface mixed layer. Deep-Sea Res. Part A Oceanographic Res. Papers, **26**(8), 915–932 (1979)

A.E. Gargett, T.B. Sanford, T.R. Osborn, Surface mixing layers in the Sargasso Sea. J. Phys. Oceanogr. **9**(6), 1090–1111 (1979)

J. Imberger, Flux paths in a stratified lake. Phys. Processes Lakes Oceans **54**, 1–17 (1998)

D.M. Imboden, A. Wüest, Mixing mechanisms in lakes. in *Physics and Chemistry of Lakes*, (Springer, New York , 1995), pp. 83–138

G.N. Ivey, J. Imberger, On the nature of turbulence in a stratified fluid. Part I: The energetics of mixing. J. Phys. Oceanogr. **21**(5), 650–658 (1991)

G.N. Ivey, K.B. Winters, J.R. Koseff, Density stratification, turbulence, but how much mixing? Annu. Rev. Fluid Mech. **40**, 169–184 (2008)

B.B. Jorgensen, D.J. Des Marais, The diffusive boundary layer of sediments: Oxygen microgradients over a microbial mat. Limnol. Oceanogr. **35**(6), 1343–1355 (1990)

I. Langmuir, Surface motion of water induced by wind. Science **87**(2250), 119–123 (1938)

S. Leibovich, The form and dynamics of Langmuir circulation. Annu. Rev. Fluid Mech. **15**, 391–427 (1983)

A. Lorke, L. Umlauf, T. Jonas, A. Wüest, Dynamics of turbulence in low-speed oscillating bottom-boundary layers of stratified basins. Environ. Fluid Mech. **2**(4), 291–313 (2002)
C.H. Mortimer, Water movements in lakes during summer stratification–Evidence from the distribution of temperature in Windermere. Philosophical Trans. R. Soc. London B Biological Sci. **236**(635), 355–398 (1952)
B. Mueller, L.D. Bryant, A. Matzinger, A. Wüest, Hypolimnetic oxygen depletion in eutrophic lakes. Environ. Sci. Technol. **46**(18), 9964–9971 (2012)
A. Wüest, G. Piepke, D.C. van Senden, Turbulent kinetic energy balance as a tool for estimating vertical diffusivity in wind-forced stratified waters. Limnol. Oceanogr. **45**(6), 1388–1400 (2000)
A. Wüest, A. Lorke, Small-scale hydrodynamics in lakes. Annu. Rev. Fluid Mech. **35**, 373–412 (2003)
A. Wüest, A. Lorke, Small-scale turbulence and mixing: Energy fluxes in stratified lakes. Encyclopedia Inland Waters **1**, 628–635 (2009)

Energy Balance in Stably-Stratified, Wall-Bounded Turbulence

Oscar Flores and James J. Riley

Abstract We present DNS of stably-stratified, open-channel flows and capped Ekman layers, where the stable stratification is imposed by ground cooling. These flows have very different outer regions, yet the development of the stratification and the flow fields in their buffer regions is very similar. In particular, in both cases turbulence collapse occurs when $Lu_\tau/\nu \lesssim 100$, suggesting that this is a local process, independent of the details of the outer flow. Analysis of the spectra and energy budgets shows that stable stratification leads to an increase in normalized production, dissipation and pressure strain-rate (inter-component energy transfer). These changes are associated with the increase in the mean shear, which in turn increases the energy at the small scales. On the other hand, the large scales are damped by the direct effect of the stable stratification.

1 Introduction

The physics of stably-stratified, wall-bounded turbulence are of great importance for geophysical flows like the atmospheric boundary layer (ABL) or oceanic flows. The latter are almost always stably stratified, both by temperature and salinity, and boundary effects are important near the free surface and at the bottom benthic layer. The ABL is stably stratified on clear nights, during which the radiative heat loss of the ground cools the overlying air. The resulting stably-stratified ABL is usually categorized as either weakly-stable or very-stable (Mahrt et al. 1998). The Monin-Obukhov similarity theory describes well the former, but fails in the latter, in which turbulence typically exhibits periods of weak or unmeasurable fluctuations. Indeed,

O. Flores (✉)
Departamento de Bioingeniería e Ingeniería Aeroespacial,
Universidad Carlos III de Madrid, 28911 Madrid, Spain
e-mail: oflores@ing.uc3m.es

J.J. Riley
Department of Mechanical Engineering, University of Washington, Seattle, WA 98195, USA
e-mail: rileyj@u.washington.edu

H.J.H. Clercx and G.J.F. van Heijst (eds.), *Mixing and Dispersion in Flows Dominated by Rotation and Buoyancy*, CISM International Centre for Mechanical Sciences 580,
https://doi.org/10.1007/978-3-319-66887-1_4

several Large Eddy Simulation (LES) of the stable ABL have been published since the work of Mason and Derbyshire (1990), all of them in the weakly-stable regime, where turbulence is more or less continuous and the LES subgrid models behave nicely.

In order to study the very stable cases, Nieuwstadt (2005) first and Flores and Riley (2011) later performed Direct Numerical Simulations (DNS) of open-channel flows with cooling in the bottom wall/ground, which provide a very rough model for the stable ABL. Their results show that, for sufficiently strong cooling, turbulence collapses and the flow relaminarizes. Nieuwstadt (2005) found this behavior when $h/L < 0.51$, where h is the channel height and L is the Obukhov lengthscale. However, Flores and Riley (2011) found it to be $h/L < 0.82$ at a higher Reynolds number, and suggested $L^+ = Lu_\tau/\nu < 100$ as the critical condition for turbulence collapse independent of the Reynolds number (the $^+$ superindex indicates wall units, variables normalized using the friction velocity u_τ and the viscosity ν). This criterion was interpreted as the value of the ground cooling at which the height of the surface layer ($\sim L$) has dropped into the buffer region ($z^+ < 100$), so that stable stratification directly affects this region, the most active region of non-stratified wall-bounded turbulent flows.

Open-channel flows provide a very rough approximation to the ABL, which raises the question as to what extent the results obtained by Nieuwstadt (2005) and Flores and Riley (2011) are applicable to the ABL. Other than the difference in the Reynolds number, the most important additional issues are rotation (Coriolis) and the presence of an overlying inversion, which completely change the structure of the outer region of the boundary layer. These two effects have been addressed independently in the literature. Coleman et al. (1992) and Shingai and Kawamura (2002) presented DNS of turbulent Ekman layers (rotation) with stable stratification imposed by ground cooling. Taylor and Sarkar (2008) analyzed the effect of imposing an overlying inversion on a turbulent Ekman layer, keeping an adiabatic bottom wall. Here we will present a new set of stably-stratified Ekman layers with an overlying inversion, in order to explore the generality of the results obtained by Flores and Riley (2011) in open-channel flows.

2 Description of the DNS Database

We present here results from Direct Numerical Simulations (DNS) of two stable-stratified, wall-bounded flows, an open-channel flow (case C) and a turbulent Ekman layer with a capping inversion (case E). Both DNS databases are briefly described here, and a more complete description of the algorithm can be found in Flores and Riley (2011).

For both configurations, the Navier-Stokes equations are solved in terms of two evolution equations, as in Kim et al. (1987). Stratification is introduced using the Boussinesq approximation, and the corresponding heat equation is written in terms of the density fluctuations. Time integration is performed with a 3-step Runge-Kutta

method, with implicit treatment of the viscous terms. The spatial discretization is Fourier in the wall-parallel directions (x and y), and 4th order compact finite differences on an stretched mesh in the vertical direction (z). The spatial resolution is approximately $\Delta_x^+ \approx 10$, $\Delta_y^+ \lesssim 10$, $\Delta_z^+ \lesssim 0.1$ at the ground and $\Delta_z^+ \lesssim 10$ in the central part of the domain.

2.1 Case C: Open-Channel Flow

The flow is driven by a constant pressure gradient in the streamwise direction (x), without rotation. The height of the channel is h, and the horizontal periodicities are $L_x \times L_y = 8\pi h \times 4\pi h$, sufficiently large to capture the large scales in the neutral case (Hoyas and Jimenez 2006). The boundary conditions at the ground ($z = 0$) are no-slip for the velocity and constant density gradient (i.e., constant heat flux). The boundary conditions at the top are free-slip for the velocity and $\rho = 0$, the latter condition which corresponds to a constant temperature. The non-dimensional numbers that describe the flow are

$$Re_\tau = \frac{u_\tau h}{\nu}, \qquad Pr = \frac{k}{\nu} \quad \text{and} \quad h/L = \frac{u_\tau^3/\kappa}{g/\rho_r (\rho w)_w}, \tag{1}$$

where k is the thermal diffusivity, L is the Obukhov length, $\kappa \approx 0.41$ is the Von Kármán constant and $(\rho w)_w = k\partial_z \rho|_w = u_\tau \rho_\tau$ is the (cooling) heat flux at the ground, and ρ_r is the reference density in the Boussinesq approximation.

2.2 Case E: Capped Ekman Layer

This case introduces the two outer-region effects discussed in the introduction: rotation and a capping inversion. The rotation around the vertical axis is modeled with a Coriolis term in the momentum equations, so that the flow is driven by constant pressure gradient in the spanwise (y) direction, yielding a geostrophic velocity G in the streamwise (x) direction. The capping inversion limits the height of the Ekman layer h, defined here as the height at which the mean horizontal velocity peaks. For the cases presented here, $h = 0.067 u_\tau / f$, where f is the Coriolis parameter. The non-dimensional parameters that characterize the capped Ekman layers are

$$Ro = \frac{G}{fh}, \quad \text{and} \quad Fr_I = \frac{G}{Nh}, \tag{2}$$

together with Re, h/L, and Pr. N is the Brunt-Väissälä frequency of the inversion ($N^2 = -g/\rho_r \partial_z \rho|_I$). All the capped Ekman layers discussed here have $Ro = 137$,

Table 1 Intensities of the ground cooling and length of the time histories of the present data. The subindex $_0$ means variables evaluated at $t = 0$.

Cases:	C0	C1	C2	C3	E0	E1	E2	E3
h/L_0	0.0	0.41	0.82	1.02	0	0.5	1.2	2.4
$\partial_z \rho_w / \partial_z \rho_I$	–	–	–	–	0	10	25	50
$Tu_{\tau,0}/h$	22	26	63	16	1.1	4	4	11

$Pr = 0.7$ and $Fr_I = 1.65$. Also $Re = Gh/\nu = 7 \times 10^4$, resulting in $Re_\tau \approx 2800$ for the neutral case.

It should be noted that the results of the horizontal periodicities of the capped Ekman layers presented here ($L_x \times L_y \approx 4.3h \times 4.3h$) are somewhat marginal to capture the largest scales of the flow, and the length of the time series (see Table 1 below) is too short to provide accurate statistics for the outer region. However, due to the high values of Re_τ, this database is sufficient to analyze the development of the stable stratification in the buffer region ($z^+ \lesssim 100$), where the characteristic length- and time-scales are considerably shorter.

2.3 *Flow Initialization*

All cases are initialized as follows. First, a neutral case with no ground cooling is run until it reaches a statistically steady state (cases C0 and E0). Then, the cases with ground cooling are initialized using a snapshot of the corresponding neutral case. The intensities of the ground cooling are given in Table 1.

Note that case C0 is an intrinsically steady-state flow, in which the streamwise pressure gradient and ground friction are in equilibrium. But the same is not true for case E0, where the thickness of the turbulent Ekman layer continues to grow slowly with time. This case is obtained in the same fashion as in Taylor and Sarkar (2008): an initial density profile is imposed on a turbulent Ekman layer, and the resulting flow is allowed to reach a slowly varying state.

Figure 1 shows the profiles of mean velocities (U, V) and velocity fluctuation intensities for the neutral cases. For E0, the angle that the shear stress at the wall makes with the x-direction is 18.12^o. The mean velocities show the expected logarithmic behavior, and the kinetic energy in the horizontal and vertical velocity fluctuations in the buffer and logarithmic regions agree well with those obtained in non-stratified channel flows at comparable Re_τ (Hoyas and Jimenez 2006).

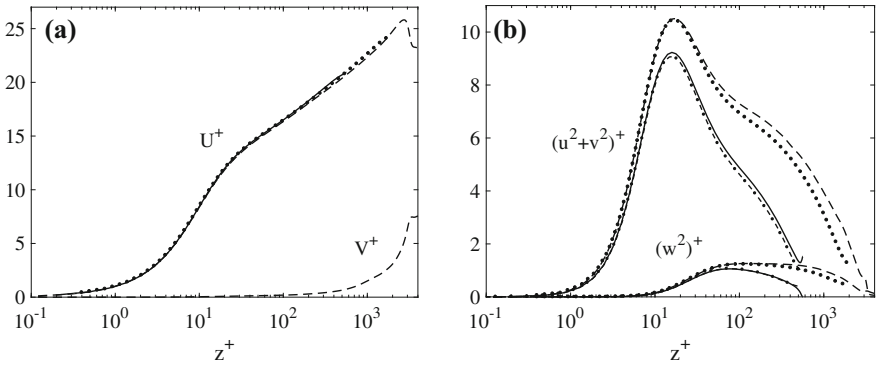

Fig. 1 **a** Mean velocities profiles. For case C0, U is the streamwise component and V is the spanwise component. For cases E0, U is the along-shear component and V is the cross-shear component. **b** Turbulent velocity fluctuations in the *horizontal* and *vertical* directions. In both panels: *solid line*, C0; *dashed line*, E0. For reference, the non-stratified channel flows of Hoyas and Jimenez (2006) are also included: *dash-dotted line* represents $Re_\tau = 547$ and the *dotted line* represents the case $Re_\tau = 2003$

3 Results

3.1 Time Evolution and Turbulence Collapse

As the cooling heat flux is applied at the lower boundary, a stable stratification develops in the flow. The main effect of that stable stratification is to damp the vertical motions, therefore weakening the Reynolds stresses and limiting the vertical transport of momentum and energy. In the open-channel flows this results in a larger mass flux through the channel, but in the Ekman layers it results in an increase of the veering angle of the Ekman spiral at the wall (Coleman et al. 1992; Shingai and Kawamura 2002), which can be observed in the hodographs plotted in Fig. 2b.

The evolution of the mean density at the ground is plotted in Fig. 2a. Initially, it grows as $t^{1/2}$, since the density fluctuations are initially zero everywhere and all the heat flux is due to molecular diffusion. For cases C1 and E1, that behavior rapidly transitions into a linear growth, which is indicative of a turbulent flow, and is confirmed by the well-mixed region exhibited by E1 at $tu_{\tau,0}/h = 3$ in Fig. 2c below $z/h \sim 0.5$ (a similar plot is obtained for C1). As the cooling flux increases so does the density gradient above the ground, and eventually the $t^{1/2}$ behavior does not transition into a linear growth (cases C3 and E3). Although difficult to see in Fig. 2c, the mean density at $z \sim 0.5h$ for case E3 is lower than for cases E2 and E1, indicating a diffusive/laminar heat transport in E3, as opposed to the advective/turbulent heat transport in E1 and E2.

The laminar/turbulent character of the buffer region in these flows is illustrated in Fig. 3a, which shows the time history of the energy in the vertical velocity component at the upper limit of the buffer region, $z^+ = 50$. Following Flores and Riley (2011),

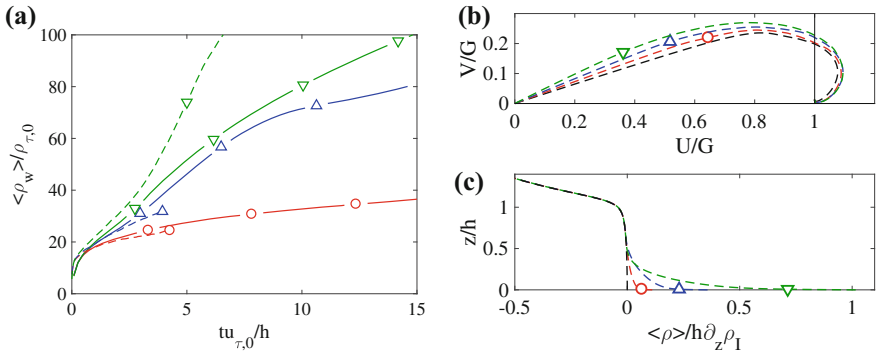

Fig. 2 **a** Time evolution of the density at the wall. **b** Hodograph and **c** *vertical* profiles of mean density at $tu_{\tau,0}/h = 3$ for the capped Ekman layers. *Solid*, C0; *solid circle*, C1; *solid triangle up*, C2; *solid triangle down*, C3; *dashed*, E0; *dashed circle*, E1; *dashed triangle up*, E2; *dashed triangle down*, E3

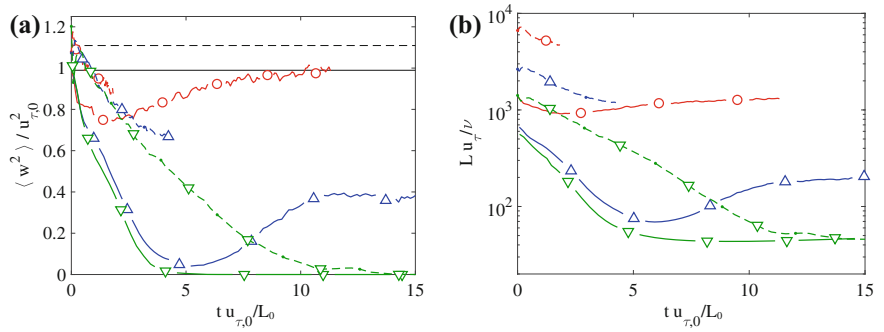

Fig. 3 **a** Time evolution of $\langle w^2 \rangle$ at $z^+ = 50$. **b** Time evolution of the Obukhov lengthscale. Lines as in Fig. 2

time is normalized using $L_0/u_{\tau,0}$, which provides the time scale at which the effect of stratification is felt in the buffer region. Such normalization collapses the evolution of the energy for cases C1-C3 and E1-E3. Note that, since w^2 is slightly larger in E0 than in C0 (see w^2 in Fig. 1b), cases C1-C3 and E1-E3 collapse in two different lines.

Figure 3b shows that the collapse (relaminarization) of the turbulent motions occurs when $L^+ \lesssim 100$, both for open-channel and capped Ekman layer flows. Since these flows have completely different structures in the logarithmic and outer region, this suggests that turbulence collapse is a local process, that depends little on the conditions far from the buffer region. Similar decays are also observed for the other components of the velocity, Reynolds stresses, triple moments, and related quantities.

The decrease of the velocity fluctuations in the buffer region has two distinct components. First, the change in the Reynolds stresses result in a decrease of the friction velocity at the wall, related to the changes in the hodograph of Fig. 2b for

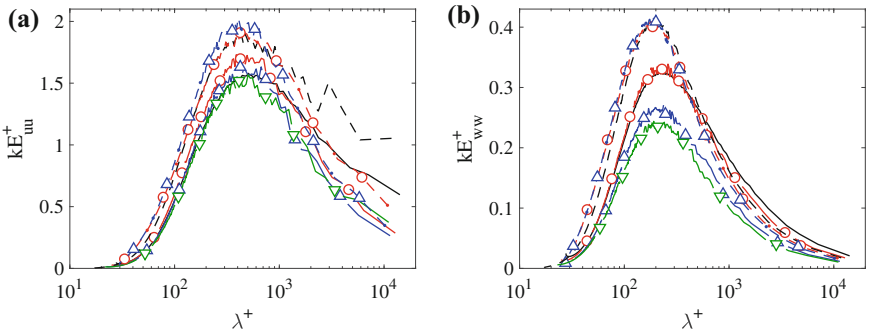

Fig. 4 Premultiplied energy spectrum of the (**a**) *horizontal* and (**b**) *vertical* velocities at time $tu_{\tau,0}/L_0 = 3$ and $z^+ = 50$. For the open channel cases, λ is the streamwise wavelength. For the capped Ekman layers, λ is the along-shear wavelength. Lines as in Fig. 2

cases E, or the increase of the mass flux in cases C reported in Flores and Riley (2011). Indeed, when the velocity fluctuations of cases C1 and E1 are normalized with the instantaneous friction velocity, they essentially remain equal to the neutral case values (instantaneous equilibrium). This behavior can be observed in Fig. 4, which shows the premultiplied energy spectrum in the buffer region at a given time, normalized with the instantaneous wall units. It can be observed, see Fig. 4b, that the vertical velocity spectrum of cases C0 and C1 (and E0 and E1) fall on top of each other, suggesting that instantaneous equilibrium is reasonably satisfied in the buffer region of those cases. As L^+ decreases (cases C2, C3, E2 and E3), the changes in the density gradient occur faster, and the instantaneous equilibrium is not maintained.

The second effect is the damping of the large-scale motions, in agreement with classical overturning arguments. This effect can better appreciated in the spectrum of the horizontal energy, see Fig. 4a, where E0 and C0 have more energy on scales $\lambda^+ \gtrsim 2000$ than the corresponding stratified cases. Figure 5 shows instantaneous visualizations of the capped Ekman layers, where the damping of the largest scales in the flow is clearly observed.

3.2 Energy Budgets

Apart from the damping of the large scales, Fig. 4 also shows that stratification seems to increase the energy in the small scales, $\lambda^+ \sim 100$, especially for the horizontal velocity components, see Fig. 4a. This effect is clearer in the final steady states, or further away from the wall (not shown here). In order to get a better understanding of this effect, we analyze the different terms in the evolution equations for the horizontal and vertical kinetic energies, $q_u = (u^2 + v^2)/2$ and $q_w = w^2/2$, respectively. These balances can be written as

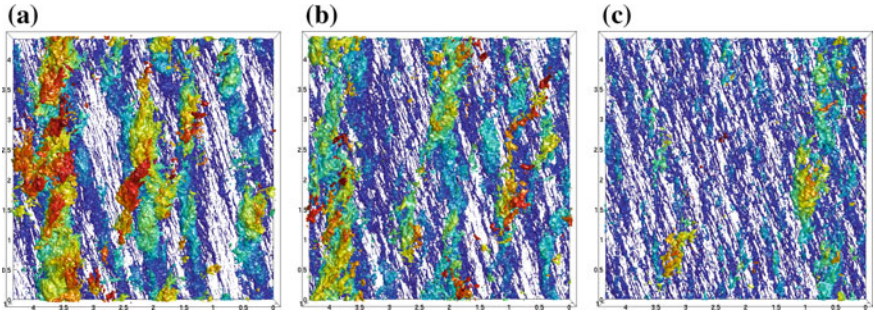

Fig. 5 Instantaneous visualizations of positive u fluctuations ($u' = 2u_\tau$) in the capped Ekman layers at time $tu_{\tau,0}/L_0 \approx 3$. **a** E0, **b** E1, and **c** E2. The isosurfaces are colored with z: *blue* is $z = 0$ (ground), and *red* is $z = h$ (inversion)

$$\partial_t \langle q_u \rangle = -\partial_z \langle q_u w - \nu \partial_z q_u \rangle + \langle p \partial_z w \rangle - \nu \langle (\partial_k u_i)^2 \rangle - \langle u_i w \rangle \partial_z U_i \ , \tag{3}$$

$$\partial_t \langle q_w \rangle = -\partial_z \langle q_w w - \nu \partial_z q_w + wp \rangle - \langle p \partial_z w \rangle - \nu \langle (\partial_k w)^2 \rangle - g/\rho_0 \langle w\rho \rangle \ , \tag{4}$$

where summation is implied for repeated indices $i = 1, 2$ and $k = 1, 2, 3$. The first term on the right-hand side of both Eqs. (3) and (4) is the vertical flux (turbulent transport + viscous diffusion + pressure velocity correlation), the second is the inter-component transport (pressure strain-rate, or return to isotropy), and the third is the dissipation. In Eq. (3), the fourth term is the turbulent kinetic energy production, and in Eq. (4) it is the buoyancy flux, which represents the energy transfer from kinetic to potential energy. Figures 6 and 7 show these terms for cases C and E, respectively, at time $tu_{\tau,0}/L_0 = 3$. As in Fig. 4, the energy balance terms are normalized in instantaneous wall units to check for instantaneous equilibrium. Note also that since the kinetic energy is changing, the terms do not need to be in balance.

First, it is worth noting that the terms in Eq. (3) are one order of magnitude larger than the terms in Eq. (4), for both cases C and E. Even for the cases with strongest cooling (cases C3 and E3), the ratio between buoyancy flux and turbulent kinetic energy production in the buffer region is smaller than 0.2. Horizontal motions are more intense than vertical motions, as expected in boundary layers.

Nieuwstadt (2005) argued that stable stratification increases the production of turbulent kinetic energy far from the ground. Indeed, it is possible to show that for an open channel in steady state, the damping of the Reynolds stresses due to stable stratification yields an increase in mean shear that results in an increase of production of turbulent kinetic energy. Figures 6a and 7a show an increase in normalized production for $z^+ > 100$ in the cases that stay close to equilibrium, C1 and E1. On the other hand, strongly damped cases (C2 and C3) show a decrease in production, consistent with the strong decrease of w^2 shown in Fig. 3. A plausible interpretation is that for those cases, the development of the stable stratification on the flow is too fast for the mean velocity to adapt to it, and production of turbulent kinetic energy cannot be maintained. Finally, in the lower part of the buffer region ($z^+ < 10$) the behavior of

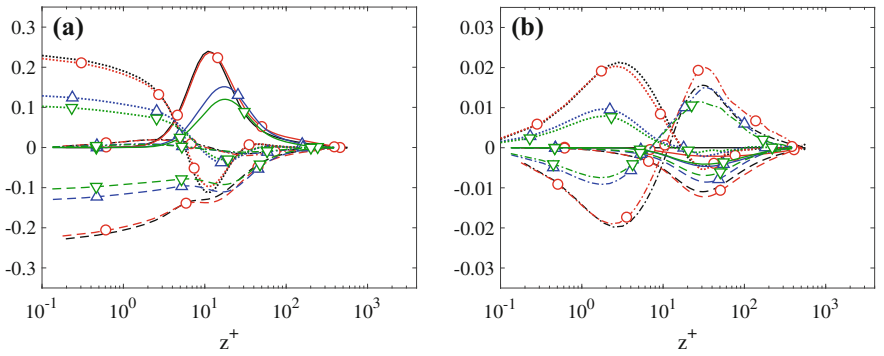

Fig. 6 Energy balance terms at time $tu_{\tau,0}/L_0 = 3$ for the open channel flows, normalized with the instantaneous u_τ and h. **a**, q_u balance, see Eq. (3). **b**, q_w balance, see Eq. (4). Line types correspond to different terms in the equations: *solid*, production in (**a**) and buoyancy flux in (**b**); *dashed*, dissipation; *dash-dotted*, pressure strain-rate; *dotted*, *vertical* fluxes. Symbols in line types correspond to the different cases: *no symbol*, C0; *circle*, C1; *triangle up*, C2; *triangle down*, C3

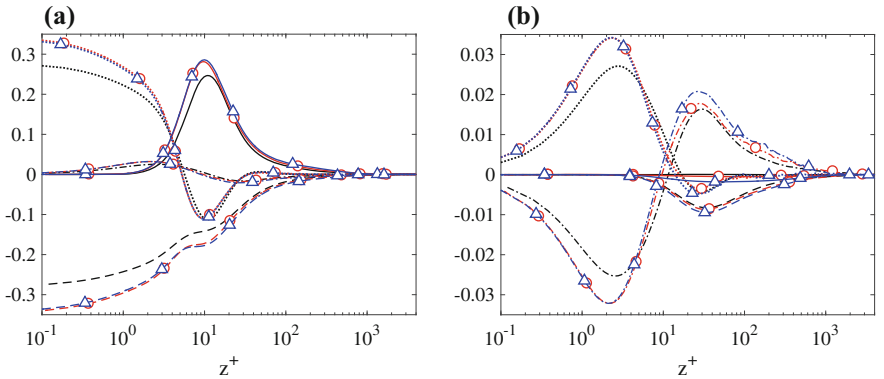

Fig. 7 Energy balance terms at time $tu_{\tau,0}/L_0 = 3$ for the capped Ekman layers, normalized with the instantaneous u_τ and h. **a**, q_u balance, see Eq. (3). **b**, q_w balance, see Eq. (4). Line types correspond to different terms in the equations: *solid*, production in (**a**) and buoyancy flux in (**b**); *dashed*, dissipation; *dash-dotted*, pressure strain-rate; *dotted*, *vertical* fluxes. Symbols in line types correspond to the different cases: *no symbol*, E0; *circle*, E1; *triangle up*, E2

open channels and capped Ekman layers is somewhat different. The latter show an increase on the intensity of all the terms in the balance, whose origin is uncertain. A possible explanation is a time lag between mean velocities and Reynolds stresses due to the veering of the shear stresses at the wall (see Fig. 2b), but other explanations are possible (e.g. insufficient resolution).

Interestingly, in both open channels and capped Ekman layers the changes in production are essentially balanced by changes in dissipation. The buoyancy flux is small compared to production, and only on the strongly stratified cases C2 and C3 it becomes comparable to the pressure strain. The vertical fluxes of q_w and q_u are

also weakened by the stable stratification, so that at any given height, production and dissipation are better balanced than in the corresponding neutral case. An interesting consequence of the enhancement of the normalized production and dissipation is that the pressure strain-rate term, than accounts for the energy transferred between q_u and q_w, also increases. Although not shown, these changes take place in the small scales, analogous to those observed in the spectra shown in Fig. 4.

4 Conclusions

We have performed DNS of open-channel flows and capped Ekman layers with stable stratification imposed from the ground. The results show that the effect of ground cooling is to damp the vertical motions of the large scales, in agreement with the classical overturning arguments. When the Obukhov lengthscale L becomes comparable to the scales of the buffer region ($L \sim 100\nu/u_\tau$), all turbulent production at the ground shuts down and the flow relaminarizes locally (Flores and Riley 2011). This behavior is observed both flow configurations suggesting that, contrary to previous speculation, the flow in the buffer layer is not strongly affected by the conditions of the flow in the outer region.

We have also analyzed the different terms of the energy equation for each velocity component for cases C and E. Although the behavior of these cases is different in the outer region, it is similar closer to the ground. For weak stratification, the flow in the buffer region scales with the instantaneous friction velocity u_τ, and it remains close to equilibrium. The energy loss caused by the buoyancy flux term is balanced by an increase in the pressure strain-rate term that transfers more energy from the horizontal components into vertical motions.

Acknowledgements This work has been supported by ARO Grant No. W911NF-08-1-0155. The numerical resources provided by the DoD HPCMP are gratefully acknowledged.

References

G.N. Coleman, J. Ferziger, P.R. Spalart, Direct simulation of the stably stratified turbulent Ekman layer. J. Fluid Mech. **244**, 677–712 (1992)

O. Flores, J.J. Riley, Analysis of turbulence collapse in the stably stratified surface layer using direct numerical simulation. Bound. Layer Meteorol. **139**(2), 241–259 (2011)

S. Hoyas, J. Jimenez, Scaling of the velocity fluctuations in turbulent channels up to Re_τ=2003. Phys. Fluids **18**(1), 011702 (2006)

J. Kim, P. Moin, R.D. Moser, Turbulence statistics in fully developed channel flow at low Reynolds number. J. Fluid Mech. **177**, 133–166 (1987)

L. Mahrt, J. Sun, W. Blumen, T. Delany, S. Oncley, Nocturnal boundary-layer regimes. Bound. Layer Meteorol. **88**(2), 255–278 (1998)

P.J. Mason, S. Derbyshire, Large-eddy simulation of the stably-stratified atmospheric boundary layer. Bound. Layer Meteorol. **53**(1–2), 117–162 (1990)

F. Nieuwstadt, Direct numerical simulation of stable channel flow at large stability. Bound. Layer Meteorol. **116**(2), 277–299 (2005)
K. Shingai, H. Kawamura, Direct numerical simulation of turbulent heat transfer in the stably stratified Ekman layer. Thermal Sci. Eng. **10**(1), 25–33 (2002)
J.R. Taylor, S. Sarkar, Stratification effects in a bottom Ekman layer. J. Phys. Oceanogr. **38**(11), 2535–2555 (2008)

Some Aspects of Lagrangian Dynamics of Turbulence

Mickaël Bourgoin

Abstract This chapter is dedicated to fundamental properties of Lagrangian transport in turbulence, emphasizing the role of anisotropy and 2D turbulence which are relevant for geophysical considerations. The focus is on three main aspects of Lagrangian turbulence: (i) the role of small-scale anisotropy on the Lagrangian energy spectrum, (ii) the role of Lagrangian intermittency and (iii) the relative dispersion of tracer particles.

1 Introduction

Turbulence governs the vast majority of fluid flows in nature and industrial applications from atmospheric dynamics to mixing and combustion. Despite its ubiquitousness, turbulence remains one of the deepest unsolved mysteries of classical physics. Even if the equations of motion of turbulent flows are perfectly known since Navier and Stokes, almost two centuries ago, its complexity (primarily driven by its nonlinearity) annihilates any hope of finding analytical solutions. We are then committed to turn to phenomenological modeling to gain insight into the behaviour of turbulent flows. In 1922 L. F. Richardson introduced the first description of turbulence as a multiple-scale phenomenon (Richardson cascade) where mechanical energy is injected at large eddies (with typical scale L, referred to as the *injection or integral scale*), and as they become unstable, they split into smaller eddies to which energy is transferred, and so on until eventually viscous dissipation stops the cascade at some small scale (η, referred to as the *dissipative scale*) where viscosity becomes dominant. This range of scales defines the *inertial range of turbulence*. In turbulent flows, the range of inertial range between the energy injection scale L and the dissipative scale η is directly related to the Reynolds number Re of the flow: $L/\eta \propto Re^{3/4}$ (see for

M. Bourgoin (✉)
Université de Lyon, ENS Lyon, Université Claude Bernard – Lyon 1, CNRS, Laboratoire de Physique, 69342 Lyon, France
e-mail: mickael.bourgoin@ens-lyon.fr

H.J.H. Clercx and G.J.F. Van Heijst (eds.), *Mixing and Dispersion in Flows Dominated by Rotation and Buoyancy*, CISM International Centre for Mechanical Sciences 580,
https://doi.org/10.1007/978-3-319-66887-1_5

instance Tennekes 1975). Reynolds numbers of the order 10^6 are usual in geophysical flows, implying that at least 4 decades of spatial dynamics are typically involved. Similarly in the time domain, the ratio between the eddy turnover time T of eddies at the injection scale and the eddy turnover time τ_η of eddies at the dissipation scale goes as $T/\tau_\eta \propto Re^{1/2}$, covering typically three decades of temporal dynamics. These dynamical ranges can be even further extended towards the largest scales due to inverse cascade mechanisms, which may become important in the atmosphere or the ocean, at scales where dynamics exhibits 2D-properties, where flow structures can extend over hundreds of kilometers. The notion of the energy cascade is therefore at the core of the physics of turbulence and its multi-scale nature. We know today that this cascade results from the non-linear interaction of Fourier modes of the velocity field, although we are still unable to analytically model and predict most of the turbulence statistics over the entire range of inertial scales. In 1941 Kolmogorov proposed a quantitative statistical description of turbulence (Kolmogorov 1941; Frisch 1995) as a self-similar cascade with universal properties. Originally this universality was stated by two self-similar hypotheses which form the foundation of Kolmogorov's phenomenology. Quoting Hinze's formulation (Hinze 1959), these hypotheses state that:

H1. At sufficiently high Reynolds number there is a range of small scales for which turbulence is statistically in equilibrium and uniquely determined by the viscosity ν and the mean energy dissipation rate $\langle\epsilon\rangle$; this equilibrium state is universal.

H2. In the limit of infinite Reynolds number, turbulence becomes independent of viscosity ν and is solely determined by $\langle\epsilon\rangle$.

Taken together, Kolmogorov's hypotheses state that in intense turbulence and well away from any boundaries or singularities the statistics of turbulent flow should be universal at lengthscales and timescales that are small compared to those of the injection of energy into the flow. This implies in particular that at sufficiently small scales, turbulence becomes homogeneous and isotropic, a hypothesis known as *local isotropy*. In Kolmogorov's approach the mean energy dissipation rate $\langle\epsilon\rangle$ then becomes the only relevant parameter governing the dynamics of structures in the inertial range (for clarity, in the sequel we shall refer to $\langle\epsilon\rangle$ simply as ϵ). Since then, statistical turbulence modeling has been dominated by Kolmogorov's ideas, whose 1941 hypotheses have so influenced the field that they are simply known as the K41 phenomenology. The great utility of the K41 model lies in its prediction of universal scaling laws for velocity increments statistics. However, K41 is known to fail describing important features of real turbulent flows, as for instance the *intermittency* phenomenon. This has stimulated many theoretical studies trying to refine K41 phenomenology, including Kolmogorov's refined hypotheses of self-similarity in 1962 (known as K62) and more recently multifractal models (Parisi and Frisch 1985).

In the same spirit of finding alternative, or at least complementary, descriptions of turbulence, new modeling paths have emerged, among which the Lagrangian

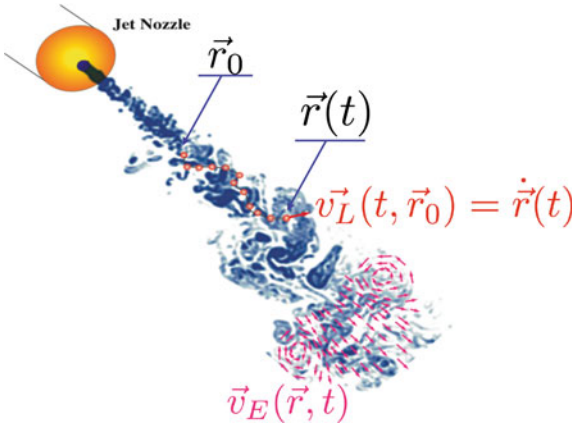

Fig. 1 Eulerian versus Lagrangian description of a flow. In the Eulerian framework the flow is described in terms of the velocity field, while in the Lagrangian framework it is characterized by the trajectories of fluid tracers

approach offers promising opportunities. Fluid dynamics in general, and turbulence in particular, is usually described in a Eulerian approach: the fluid velocity (or any other physical quantity as pressure, fluid acceleration, etc.) is studied as a spatial field $\vec{v}_E(\vec{r})$, function of the spatial coordinate $\vec{r}$. Although this field also experiences instantaneous temporal fluctuations (and should be written $\vec{v}_E(\vec{r}, t)$), in statistically stationary conditions, time t is generally considered as a statistical parameter which simply helps building ensemble averages by repeating the measurement at different instants (if the system is not statistically stationary, then time t becomes an actual variable of the problem, which accounts for non-stationary effects). Eulerian statistics are typically acquired by measuring the velocity (or any other quantity) at fixed points where different fluid particles are being probed at every instant. In the Lagrangian approach, instead of probing the flow at given fixed points $\vec{r}$ (where fluid particles do stream continuously), the velocity is measured along the path of given fluid elements which are tagged and tracked individually (see Fig. 1). Whereas most of our knowledge of turbulence (including Kolmogorov's ideas) comes from the Eulerian approach, the Lagrangian approach offers complementary observations. Moreover, in several cases the Lagrangian point of view offers a more natural framework (Yeung 2002). This is the case, for instance, for dispersion issues (and related mixing problems), for which a particulate description (rather than a field approach) is often more relevant. As a matter of fact, in the course of its long history, the study of turbulent flows always benefited from comings and goings between a field view and a particle view, that is between an Eulerian description and a Lagrangian approach. The relevance of the Lagrangian approach to address transport properties of turbulence was already pointed out in the 1920s in pioneering articles by Taylor (1922) and Richardson (1926). However, the Lagrangian statistical formalism suffered from a lack of reliable and precise experimental measurements. It is only during the last decades that, stimulated by important theoretical breakthroughs (for instance in the context of stochastic Lagrangian models of turbulence by, for example, Sawford 1991), new highly sophisticated laboratory experiments (Bourgoin et al. 2014a) and

high-resolution direct numerical simulations have attacked seriously the problem of Lagrangian turbulence, and more widely, the problem of the transport of impurities (not restricted to infinitesimal material fluid elements) by a turbulent flow (Bourgoin and Xu 2014b).

In this context, this chapter briefly recalls some of the main properties of Lagrangian turbulence in homogeneous isotropic turbulence, before addressing two important aspects, possibly relevant for atmospheric and oceanographic flows, which can be impacted by additional complexities such as stratification, background rotation and aspect ratio, related to anisotropy and bi-dimensionalization of turbulence. The role of these additional complexities will be presented from simplified experiments or models.

With this respect, this chapter focuses on two important questions of Lagrangian turbulence:

- The validity of Kolmogorov's local isotropy hypothesis;
- The relative dispersion of pairs.

2 Basic Multi-scale Properties of Lagrangian Turbulence

2.1 A Brief Recall of K41 Ideas in the Eulerian Framework

Since Kolmogorov's developments in 1941, the multi-scale nature of turbulence is described by means of statistics of velocity increments. In classical Eulerian approaches, spatial velocity differences are generally considered $\delta_E \boldsymbol{u}(r) = \boldsymbol{u}(\boldsymbol{r} + \boldsymbol{x}) - \boldsymbol{u}(\boldsymbol{x})$ and statistics are investigated in terms of their moments $S^E_{i,p}(\mathbf{r}) = \langle \delta_E u_i(\mathbf{r})^p \rangle$ (written here for the ith component of the velocity), also called structure functions. Note that in homogeneous isotropic turbulence, $S^E_{i,p}(\mathbf{r})$ is independent of i (for clarity, we shall omit the subscript i when dealing with the homogeneous isotropic case) and only depends on the norm $r = |\mathbf{r}|$ of the separation vector. Such incremental quantities are important for several reasons. Firstly, because the classical inertial range similarity hypothesis since K41 is best suited to increments rather than to the raw velocity field. With this respect we can quote Batchelor (1950) who wrote about the importance of velocity differences in this context, that "*it seems reasonable to suppose that when r is small enough the larger eddies make very little contribution to the velocity difference, so that this mean value is determined almost wholly by eddies whose diameters are of the same or smaller order than r, and we led to apply similarity hypotheses*". Increments are also important because they are directly related to common major statistical quantities, particularly in the case of second order structure function $S^E_2(r) = \langle \delta_E u(r)^2 \rangle$ which, for homogeneous turbulence, is directly related to the velocity Eulerian correlation function $R^E_{uu}(r) = \sigma_u^2(1 - S^E_2(r)/2\sigma_u^2)$ (with σ_u^2 the velocity variance), which is itself related to the velocity spectrum by simple Fourier transform. A last important aspect of

increments comes from the third order Eulerian structure function for which one of the only known exact analytical results (the celebrated Kolmogorov 4/5th law) is directly derivable from Navier–Stokes equations, stating that $S_3^{\parallel}(r) = -\frac{4}{5}\epsilon r$ (where $S_3^{\parallel}(r)$ is the longitudinal third order structure function). In K41 phenomenology, the self-similarity hypothesis implies that the dynamics of turbulence in the inertial range of scales (far from injection scale and far from dissipation), the only physical relevant parameter is the energy dissipation rate ϵ. This has an important implication regarding the scaling of spatial velocity increments, as simple dimensional analysis therefore imply that $\langle \delta_E u(r)^p \rangle \propto (\epsilon r)^{p/3}$. Important results of K41 phenomenology concern the consistency with the aforementioned 4/5th law (for $p = 3$) and the prediction of the celebrated $\epsilon^{2/3} k^{-5/3}$ energy spectrum (with k the spatial wave number) is the Fourier space equivalent of the scaling for $S_2(r) \propto (\epsilon r)^{2/3}$.

Closer studies, however, have shown that the K41 scaling predictions are not obeyed, especially for high-order moments. Instead, the exponents ζ_p^E increase non-linearly and slower than $p/3$ (Anselmet et al. 1984; Arneodo et al. 1996; Frisch 1995; Chen et al. 2005). This anomalous scaling is usually attributed to the phenomenon of intermittency that destroys the perfect self-similarity underlying the K41 phenomenology, and reflects the fact that energy dissipation ϵ is highly unevenly distributed. As an attempt of definition of intermittency (a consensual definition has not emerged yet in the turbulence community) we may see it as the fact that statistical quantities of a turbulent field dependent on the scale at which they are explored. As a consequence, if we consider increments at a given scale r of a given velocity field, intermittency causes their probability density function (PDF) to change depending on the observation scale r. Such a deformation of the increments PDF is now well-established and well characterized for Eulerian fields (though its physical origin remains mysterious): increments PDF are gaussian at large scale; they develop approximately exponential tails for separations in the inertial range; tails become stretched exponentially at even smaller scales. This evolution of the statistics across the scales reveals the non-self-similar nature of turbulence, in contradiction with original Kolmogorov's hypotheses, which is responsible for the departure from K41 predictions for structure-function scalings. To account for these anomalous exponents, Kolmogorov's original self-similar hypotheses had to be refined. Kolmogorov (1962) himself proposed such a refinement incorporating Obukhov's suggestion of strongly non-Gaussian fluctuations of the energy dissipation rate (Obukhov 1962) after Landau objected the averaged energy dissipation might not be a sufficient parameter to describe turbulent fields as assumed in the original K41 hypothesis. Since then, several other descriptions of intermittency have emerged, among which the most popular has become the multi-fractal description introduced by Parisi and Frisch (1985).

2.2 Lagrangian K41 Phenomenology

K41 phenomenology, originally developed in the Eulerian framework, can be extended to the Lagrangian framework, by introducing the notion of temporal velocity increments along particle trajectories (which is the Lagrangian counter-part of the Eulerian spatial increments of the velocity field): $\delta_L \boldsymbol{v}(\tau) = \boldsymbol{v}(t+\tau) - \boldsymbol{v}(t)$. Here, $\boldsymbol{v}$ refers to the Lagrangian velocity, measured for each fluid particle along its trajectory. Statistics will be assumed to be stationnary, hence independent of time t, and only dependent on the time increment τ. Spanning statistical behaviours at different values of τ allows to investigate the multi-scale temporal dynamics of Lagrangian trajectories. This multiscale characterization is generally achieved by considering the dependency of the statistical moments of Lagrangian increments with τ. These define the Lagrangian structure functions: $S^L_{i,p}(\tau) = \langle \delta_L v_i(\tau)^p \rangle$ (written here for the ith component of the velocity). Note that in homogeneous isotropic turbulence $S^L_{i,p}(\tau)$ is independent of i. As for the Eulerian approach, the second order moment ($p = 2$) is of particular interest, as it is directly related to the Lagrangian correlation function $R^L_{vv}(\tau) = \sigma_v^2(1 - S^L_2(\tau)/2\sigma_v^2)$, which is itself related to the Lagrangian velocity spectrum by a simple temporal Fourier transform. The same dimensional analysis arguments as in K41 phenomenolgy allow to determine the scalings for the Lagrangian structure functions at temporal inertial scales, under the self-similar hypothesis, where ϵ is the only relevant physical parameter:

$$S^L_p(\tau) \propto (\epsilon\tau)^{p/2} \quad \text{for} \quad \tau_\eta \ll \tau \ll T_L \tag{1}$$

This predicts in particular that at inertial scales the second order Lagrangian structure function is linear in τ: $S^L_2(\tau) \propto \epsilon\tau$ (which is the Lagrangian counter-part of the Eulerian relation $S^E_2(r) \propto (\epsilon r)^{2/3}$) and equivalently the Lagrangian velocity spectrum $E^L(\omega) = C_0 \epsilon \omega^{-2}$ (which is the Lagrangian counter-part of the Eulerian spectrum $E^E(k) \propto \epsilon^{2/3} k^{-5/3}$), with C_0 some universal constant.

As for the Eulerian case, the simple K41 scaling for the Lagrangian structure function (1) is known to fail for large moments, due to intermittency effects. This results in anomalous exponents, more specifically $S^L_p(\tau) = (\epsilon\tau)^{\zeta_p}$, with $\zeta_p < p/2$ (Mordant et al. 2001; Xu et al. 2006).

2.3 Lagrangian Dispersion

One of the most classical problems of Lagrangian turbulence concerns the question of particles dispersion, with two main important aspects: (i) diffusion of single particles from a point source (also known as the *Taylor problem*) and (ii) the relative dispersion of pairs of particles (also known as the *Richardson problem*). The case of more than one or two particles has also been addressed more recently by considering triads and tetrads of particles (Chertkov et al. 1999). We will briefly recall here the main results

of the Taylor problem, by considering the dependency of the particle mean square displacement from a point source. The case of relative dispersion will be further detailed below in Sect. 4.

Consider a point source where particles are continuously released: at which rate will particles move away from the source? This question has been addressed in a seminal article by Taylor (1922), in which he proposed a solution of this problem based on the assumption that the Lagrangian correlation function is an exponential function: $R_{vv}^L(\tau) = \sigma_v^2 e^{-\tau/T_L}$, where T_L is the Lagrangian correlation time of the velocity, also known as the *Lagrangian integral time*. It can be noted that at short times ($\tau \ll T_L$) such an exponential behaviour is consistent with K41 scaling as $R_{vv}^L(\tau \ll T_L) = \sigma_v^2(1 - \tau/T_L)$ implies $S_2(\tau \ll T_L) \propto \tau$ (owing to the relation $R_{vv}^L(\tau) = \sigma_v^2(1 - S_2^L(\tau)/2\sigma_v^2)$). However, such a simple exponential correlation function cannot account for small-scale dissipative scales ($\tau \ll \tau_\eta$), where the trivial, purely kinematic scaling $S_2^L(\tau) = \sigma_a^2\tau^2$ (with σ_a^2 is the acceleration variance) is expected, as at vanishing time increment $\tau \to 0$ velocity increments are simply representative of acceleration. This is due to the fact that a simple exponential decorrelation conveys only one characteristic timescale (here the Lagrangian integral timescale T_L). Extensions to this simple approximation have been formulated since then, in the context of autoregressive stochastic models, as the two-time stochastic model by Sawford (1991), which accounts for small scales effects by introducing a double exponential correlation function. For the sake of simplicity, we will briefly present here the result by Taylor without this additional small-scale corrective term (hence assuming simply an exponential correlation function) and considering only one component (let say x) of the displacement. Let x_0 be the initial source point. The mean square displacement can then be written as $\langle (x(t) - x_0)^2 \rangle = \int_0^t \int_0^t R_{vv}(\tau' - \tau) \mathrm{d}\tau \mathrm{d}\tau'$. Assuming an exponential Lagrangian correlation function for the velocity, leads to $\langle (x(t) - x_0)^2 \rangle = 2\sigma_v^2 T_L \left(t + T_L e^{-t/T_L} - T_L\right)$, with two important asymptotic behaviours:

$$\langle (x(t) - x_0)^2 \rangle = \sigma_v^2 t^2 \quad \text{for} \quad t \ll T_L, \tag{2}$$

$$\langle (x(t) - x_0)^2 \rangle = 2\sigma_v^2 T_L t \quad \text{for} \quad t \gg T_L. \tag{3}$$

This simple result can be of interest for instance to predict the growth rate of a puff of pollutants released from a point source (for instance an industrial chimney). It shows that the mean growth rate of the puff (which can be estimated as $\langle (x(t) - x_0)^2 \rangle^{1/2}$) is directlty related to the Lagrangian correlation function (or equivalently to the Lagrangian second order structure function or Lagrangian velocity spectrum). The two asymptotic behaviours discussed above reveal that the puff will first grow ballistically (its size increasing linearly with time for timescales smaller than the Lagrangian correlation time) before transienting towards a brownian like behaviour where its size increases as $\sqrt{t}$ for larger timescales. The evolution of the fluctuations of pollutants distribution within the cloud is however related to multi-particles statistics (Falkovich et al. 2001); in particular the evolution of the variance of the pollutants distribution

is directly related to the relative dispersion problem, which will be discussed later in Sect. 4.

After this brief review of some of the main properties of Lagrangian turbulence, we discuss in the next sections two more specific questions related to Lagrangian properties of turbulence of interest for more complex flows than homogeneous isotropic turbulence, as in geophysical flows, where anisotropy and two-dimensionalisation effects can affect the way particles are transported and dispersed by the turbulence.

3 On the Validity of Kolmogorov's Local Isotropy Hypothesis

3.1 The Local Isotropy Hypothesis

Kolmogorov's original self-similar hypotheses assumed that well away from any boundaries or singularities, the statistics of turbulent flows should be universal at lengths and timescales that are small compared with the injection of energy into the flow and that averaged energy dissipation $\langle \epsilon \rangle$ should be the only relevant parameter for inertial range dynamics. As briefly discussed in the previous section, intermittency and anomalous scaling corrections reveal the limitation of considering solely the averaged dissipation $\langle \epsilon \rangle$, in particular when high order moment statistics of velocity increments are considered. Evidence of intermittency led Kolmogorov himself to reconsider, in 1962, the original formulation of self-similar hypotheses in order to account for local fluctuations of the dissipation rate ϵ. Another fundamental aspect of Kolmogorov's hypotheses concern the local-isotropy approximation which state that if the small-scale statistics are to be universal, they must be independent of the large-scale flow structure. In particular, K41 assumes that at inertial and dissipative scales the turbulence should "forget" any preferred direction of the large-scale flow and that the small-scale fluctuations should be statistically homogeneous and isotropic; this is the *local isotropy* hypothesis. Models and simulations of turbulence therefore commonly assume such isotropic conditions. Real flows, however, are never homogeneous and isotropic at large scales. Careful study of the effects of large-scale anisotropy on the small-scale turbulent fluctuations is therefore very important for understanding the behaviour of turbulent flows in real systems.

Persistent anisotropy at small scales has been noted previously in Eulerian studies of homogeneous shear flows (Pumir and Shraiman 1995; Garg and Warhaft 1998) and in the context of the SO(3) symmetry group (Biferale and Procaccia 2005). Available data is however usually limited to low or moderate Reynolds number and the trend of the persistence of small-scale anisotropy with Reynolds number remains unclear. Is small-scale isotropy somehow recovered for sufficiently large Reynolds number? This remains an open question which has been recently tackled from the Lagrangian point of view, by addressing the question of the relevance of the K41 hypothesis of local isotropy in a Von Kármán experiment (Ouellette et al. 2006), which exhibits a

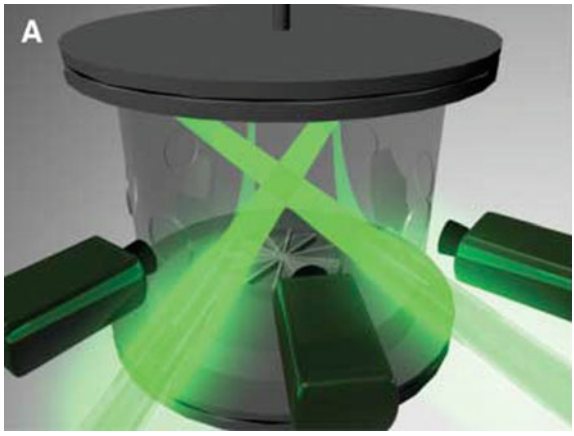

Fig. 2 Sketch of the experimental setup used by Ouellette et al. (2006). Three high-speed cameras were used to record the three-dimensional tracks of tracer particles in intense turbulence. The particles were illuminated by two high-power lasers.

strong imposed large-scale anisotropy and exploring the recovery of isotropy across scales using high resolution measurements of the second order Lagrangian velocity structure function and spectrum. The Von Kármán geometry is indeed particularly well suited for this study as it has a pronounced large-scale anisotropy (the geometry of the system imposes a large-scale axisymmetric forcing) at the same time as it produces easily very large Reynolds number turbulence (Fig. 2).

The effects of this large-scale anisotropy are investigated based on the comparison of different projections of the second order Lagrangian structure function $S^L_{2,ij}(\tau) = \langle \delta u_i(t+\tau)\delta u_j(t)\rangle$. Axisymmetric turbulence has been the subject of prior theoretical works (Batchelor 1946; Chandrasekhar 1950; Ould-Rouiss 2001), but has not yielded any experimentally verifiable prediction similar to those made by K41. Considering the second order structure function is of particular interest, since it is known not to be significantly affected by intermittent corrections, as compared to higher order structure functions. This allows to unambiguously investigate effects of anisotropy, while limiting other spurious effects. K41 phenomenology predicts that the Lagrangian structure function tensor should scale as $S^L_{2,ij}(\tau) = C_0\epsilon\tau\delta_{ij}$ in the inertial range (with i and j representing the three spatial coordinates). According to K41 universality hypotheses, the structure function should be isotropic and C_0 should have a universal value for all turbulent flows (at least in the limit of high Reynolds number). It is an important parameter in stochastic models of turbulent transport and dispersion (Rodean 1991; Sawford 1991; Weinman and Klimenko 2000) and is, remarkably, also connected to the structure functions of the fluctuations of a scalar field passively advected by the turbulence, see Sawford (2001). Previously measured values of C_0 range from 2.1 to 7.0, in part because Lagrangian experiments, where the trajectories of individual fluid particles are followed, have historically been very difficult. Hanna (1981) measured the Lagrangian spectra in the atmospheric boundary layer using neutrally buoyant balloons, but acknowledged significant (as much as 50%) uncertainty in the measurements, reporting a value of 4 ± 2 for C_0. Lien et al. (1998) measured 1D spectra using large floaters (roughly 1 m in scale) in the

oceanic boundary layer. Due to the considerable noise in their measurements, they were only able to estimate that the value of C_0 lies somewhere between 3.1 and 6.2. Mordant et al. (2001) measured the radial Lagrangian structure function in a laboratory acoustic particle tracking experiment in a counter-rotating disk device similar to ours and obtained a maximum value of 4 for C_0, which may be depressed due to the filtering effect of their relatively large tracer particles. Lien and D'Asaro (2002) have estimated a value of 5.5 from the spectral data published by Mordant et al. (2001).

3.2 *The Local Isotropy Hypothesis in Large-Scale Anisotropic Flows*

To address the question of the anisotropy of C_0, Fig. 3a, shows the full structure function tensor measured at $R_\lambda = 815$ by Ouellette et al. (2006). Two features of this tensor are particularly noteworthy. We see very short plateau regions for all three diagonal components of the structure function tensor, consistent with the K41 scaling, though without a fully developed Lagrangian inertial range. It is clear, however, that this tensor is not isotropic, contradicting the K41 hypothesis of local isotropy. The zz component, measured in the axial direction of the cylindrical flow chamber, shows a peak value roughly 25% lower than that of the xx and yy components, measured in the radial direction. The xx and yy components are identical within experimental precision, reflecting the axisymmetry of the large-scale flow. We note that the peak values of the compensated structure functions occur at very short times, less than

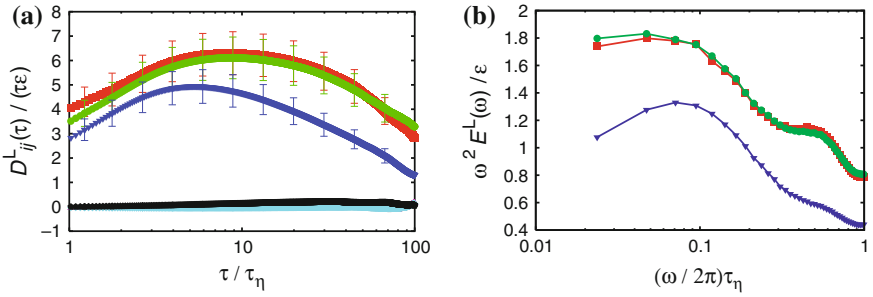

Fig. 3 **a** The xx (■), yy (●) and zz (▼) components of the compensated Lagrangian structure function at $R_\lambda = 815$. The other symbols show the off-diagonal components. The time axis has been normalized by the Kolmogorov time. The relative magnitude of the radial and axial components reflects the anisotropy of our large-scale flow. **b** Compensated Lagrangian velocity spectra at $R_\lambda = 690$ in the x-direction (■), y-direction (●) and z-direction (▼). By scaling the spectra by $\epsilon\omega^{-2}$, we expect to see a plateau in the inertial range with value B_0. The frequency axis has been scaled by the Kolmogorov frequency. As before, we note that the difference in magnitude between the radial spectra and the axial spectrum reflects the large-scale structure of our flow. The bump in the spectrum at high frequencies is due to noise in the measurements, but the inertial range behaviour is unaffected

a factor of 10 larger than the Kolmogorov time τ_η, the characteristic timescale of the fastest turbulent motion. It is also interesting to note that, although it is reduced, anisotropy remains even at the smallest scales.

The anisotropy can also be investigated via the Lagrangian velocity spectrum. Though the spectrum is essentially nothing but the Fourier space representation of the second order structure function just discussed, it can emphasize different information of the analyzed data (Davidson and Pearson 2005), in particular regarding the scale by scale anisotropy. Following K41 phenomenology, the Lagrangian spectrum should scale as $E_L(\omega) = B_0 \epsilon \omega^{-2} \delta_{ij}$ within the range of inertial time scales, and like the structure function it should be expected to become isotropic at small (inertial and dissipative) scales. The constant B_0, which is related to C_0 simply by a factor of π ($C_0 = \pi B_0$), is the Lagrangian analog of the Kolmogorov constant. The spectral representation also exhibits the same pronounced anisotropy between, the axial and the radial components.

3.3 *The Influence of Increasing Reynolds Number*

The anisotropy found between the radial and axial components of both the structure function and the spectrum persists at all the investigated Reynolds numbers. Figure 4a, shows values of C_0 determined from the plateau of the compensated

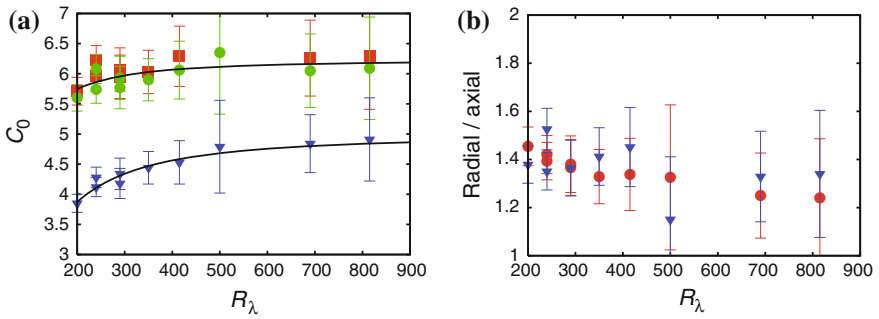

Fig. 4 **a** Measurements of C_0 from the Lagrangian structure function tensor for the xx component (■), yy component (●) and zz component (▼) as a function of Reynolds number. The zz component C_0 values are smaller than those measured for the two radial components, presumably due to the large-scale axisymmetry of our flow. C_0 is observed to increase weakly with Reynolds number. The *solid lines* are fits of Sawford's model (4) for the Reynolds number dependence of C_0 (Sawford 1991). We note that due to the time resolution in the $R_\lambda = 500$ data run, we encountered large uncertainties and were not able to measure a C_0 value from the xx component. We have therefore not included the $R_\lambda = 500$ data points in the fits of (4). **b** The ratio of the radial to the axial measurements of C_0 as a function of Reynolds number from both the structure function (●) and the spectrum (▼). While the anisotropy decreases weakly with increasing Reynolds number, the measurements remain far from isotropic even at the highest Reynolds numbers measured

structure functions as a function of the Reynolds number R_λ. For both the axial and radial structure functions, we also observe that C_0 increases weakly with Reynolds number. It is encouraging to note that Fig. 4 shows that the C_0 estimates seem to saturate as the Reynolds number increases; this result suggests that we may measure true inertial range behavior at high Reynolds number despite the very short scaling range of the structure function. To model this Reynolds number dependence of C_0 in homogeneous isotropic turbulence, Sawford (1991) has empirically fitted the trends obtained from direct numerical simulations and proposed that

$$C_0 = \frac{C_0^\infty}{1 + A R_\lambda^{-1.64}}, \tag{4}$$

where C_0^∞ is the asymptotic value of C_0 at infinite Reynolds number. From simulation data, Sawford estimated that $C_0^\infty \simeq 7$ and $A \simeq 365$. Fits of this function to the C_0 data are shown in Fig. 4a, where Sawford's fit has being applied to the different components. We find that $C_0^\infty = 6.2 \pm 0.3$ for the radial structure functions and $C_0^\infty = 5.0 \pm 0.4$ for the axial structure function (similar values for A are found in both cases).

The measurements of C_0 remain anisotropic even at the highest Reynolds number investigated. Figure 4b, shows the ratio of the radial measurements to the axial measurements. The anisotropy drops weakly with the Reynolds number, but the decrease is very slow and the anisotropy remains strong even at the highest Reynolds number investigated. Taken together, these results suggest that any symmetries (or lack thereof) present at the large scales of the flow will also be reflected in the small-scale turbulent fluctuations. Clearly, therefore, great care must be exercised when applying the results of isotropic turbulence theory to real experimental, industrial and natural flows. For instance, any climate or pollutant transport models must take the significant anisotropies present in the atmosphere into account. The significant difference between the scaling constants measured in the radial and axial directions reflects the large-scale axisymmetry in the flow. Extrapolation based on Sawford's model even predicts a persistence of small-scale anisotropy in the limit of infinite R_λ. Though such an extrapolation is highly speculative as long as the limits of validity of Sawford's fit are not well controlled, it is clear that the recovery of isotropy (if any) with increasing Reynolds number is much slower than expected. We do, however, observe K41 scaling ranges for both the Lagrangian structure function and spectrum, suggesting that while these results contradict the K41 hypothesis of local isotropy, the K41 scaling hypotheses are fulfilled for second order statistics.

To summarize, this investigation shows that the local isotropy hypothesis, generally considered in models and simulations might be more controversial than usually believed. Large-scale anisotropy appears to persist at small scales, even in the limit of large Reynolds numbers (approaching $R_\lambda \sim 10^3$).

4 Turbulent Dispersion of Tracer Particles

4.1 The Turbulent Pair Dispersion Problem

Molecules in a quiescent fluid spread due to molecular diffusion. If we consider a small spherical patch of tagged molecules, this results in an isotropic and homogeneous growth of the patch. At a microscopic level this expansion is due to random uncorrelated collisions induced by the thermal agitation of the molecules. At a macroscopic level this mechanism results in a Fickian diffusion process where the local concentration C of tagged molecules diffuses according to the simple equation $\partial C/\partial t = K\,\Delta C$, where K is the molecular diffusivity, with units $[\mathrm{m^2 s^{-1}}]$. In elementary kinetic gas theory, the connection between microscopic and macroscopic descriptions is for instance given by the relation $K \propto l v_T$ (with l a characteristic correlation length of particles trajectories, typically given by the mean free path and v_T the thermal agitation velocity of the molecules). A fundamental property of such a Fickian process concerns the linear growth with time t of the mean square separation $\langle \vec{D}^2 \rangle \propto Kt$ between any two molecules in the patch, what is generally referred to as *normal diffusion*. Normal molecular diffusion alone is very inefficient to mix and disperse usual species: for instance, molecular diffusivity of carbon dioxyde in air is $16{\cdot}10^{-6}\mathrm{m^2 s^{-1}}$, meaning that molecules separate at a rate of only a few millimeters per second.

In macroscopic flows, the slow effect of molecular diffusion is compensated by the efficiency of turbulence to mix and disperse substances and particles. At the largest scales, the uncorrelated turbulent structures act in a similar way (i.e. normally diffusive) as molecular diffusion, but with an enhanced diffusion coefficient $K_{\mathrm{turb}} \propto L\sigma$ with L the turbulence correlation length scale and σ the turbulent fluctuating velocity (standard deviation of the turbulent velocity field). In atmospheric dispersion for instance, the turbulent correlation length can be of the order of hundreds of meters (let us take 100 m as an order of magnitude) with velocity fluctuations typically of the order of meters per second in normal conditions (let us take 1 m/s as an order of magnitude), leading to a turbulent diffusivity coefficient K_{turb} of the order of $30\ \mathrm{m^2 s^{-1}}$, meaning that fluid particles separate at a rate of several meters per second, hence many orders of magnitude larger than molecular diffusion. The efficiency of turbulent diffusion therefore relies on the capacity of a substance to spread thanks to the uncorrelated motion of large-scale turbulent eddies. However, if we consider the dispersion of a patch initially much smaller than the turbulent correlation scale L (for instance a patch with an initial dimension within the inertial range of the carrier turbulence, hence much smaller than the energy injection scale L, and larger than the dissipation scale η), another mechanism is necessary to allow the patch to grow first at sufficiently large scales to eventually undergo the effect of uncorrelated turbulent diffusion. Such an inertial scale mechanism is ensured by the *super-diffusive* nature of turbulence at inertial scales. Processes where the mean square separation grows faster than in normal diffusion (i.e. $\langle \vec{D}^2 \rangle \propto t^{\alpha}$, with $\alpha > 1$) are called *super-diffusive*.

Unlike normal diffusion, *super-diffusion* is generally associated with a heterogeneous and a non-gaussian growth of the spreading patch.

4.2 Batchelor and Richardson Regimes for Pair Dispersion

Predictions for the superdiffusivity of pair dispersion in turbulence date back to 1926, when Richardson (1926) suggested that the mean square separation between two particles in the range of inertial scales should grow superdiffusively in time as t^3. By applying Kolmogorov's scaling phenomenology, Obukhov (1941) specified that in the inertial range of turbulence, where the only relevant flow parameter is the energy dissipation rate per unit mass ϵ, the mean square pair separation should grow as $\langle \Delta^2(t) \rangle = g\epsilon t^3$, with g a universal constant. An important feature of the Richardson-Obukhov superdiffusive prediction is that the separation rate is cubic in time and independent of initial separation. The absence of initial separation is however more an assumption than a consequence of Richardson-Obukhov's prediction, since the t^3 law can indeed be derived by simple dimensional analysis only if initial separation is considered as an irrelevant parameter. In this case the only relevant parameters being $\langle \Delta^2(t) \rangle$, ϵ and t, Richardson-Obukhov is a direct result of Buckingham's Pi theorem, as the only possible relation dimensionally consistent.

Batchelor (1950) refined Richardson and Obukbhov's work by considering initial separation as a possible relevant parameter of the problem. In this case, he predicted that two different dispersion regimes should exist for the dispersion of particles with initial separation at inertial range scales: for times shorter than a characteristic timescale t_0, which depends on the initial separation of the pair, the mean square separation should grow ballistically as t^2; the t^3 law being expected only for times longer than t_0. More precisely, if $\Delta(t)$ is the separation of two fluid elements at time t and defining Δ_0 as the initial separation between the fluid elements, Batchelor predicted that for Δ_0 in the inertial range

$$\langle [\vec{\Delta}(t) - \vec{\Delta}_0]^2 \rangle = \begin{cases} \frac{11}{3} C_2 \left(\epsilon \Delta_0\right)^{2/3} t^2 & \text{if} \quad t \ll t_0 = \left(\frac{\Delta_0^2}{\epsilon}\right)^{1/3} \\ g\epsilon t^3 & \text{if} \quad t_0 \ll t \ll T_L \\ Dt & \text{if} \quad T_L \ll t \end{cases} \tag{5}$$

where C_2 is the universal constant in the inertial range scaling law for the Eulerian second-order velocity structure function, which has a well-known value of approximately 2.1, see Sreenivasan (1995) (interestingly, this relation directly bridges Eulerian and Lagrangian approaches). Note that the first equation in (5) arises from a purely kinematic argument, trivially stating that at short times, a Taylor expansion of particles separation time dependency gives

$$\langle[\vec{\Delta}(t) - \vec{\Delta}_0]^2\rangle = S_2(\Delta_0)t^2 \quad \text{if} \quad t \ll t_0, \tag{6}$$

with $S_2(\Delta_0) = \langle(\delta_{\Delta_0}\vec{u})^2\rangle$ the second order Eulerian structure function estimated at a scale given by the initial separation Δ_0. In the classical cascade model of turbulence, t_0 corresponds to the eddy turnover time at the scale Δ_0 and may be interpreted as the time for which the two fluid elements "remember" their initial relative velocity as they move in the same eddy of size Δ_0. For times on the order of t_0, this eddy breaks up, and the growth of the pair separation is then expected to undergo a transition to Richardson-Obukhov scaling. According to this prediction, at short times (namely $t \ll t_0$), relative dispersion is ballistic and initial separation dependent, while it accelerates for $t_0 \ll t \ll T_L$ at the same time as it loses the memory of its initial separation. For times much larger (namely $t \gg T_L$) a Brownian-like dispersion is recovered as the two particles evolve then without any correlation. The aim of this study was to investigate this scenario by a systematic analysis of dispersion of pairs of particles in a highly turbulent flow, emphasizing the role of initial separation of the particles. In his seminal 1926 article, Richardson gave an interpretation of turbulent t^3 super-diffusion in terms of a non-Fickian process which could be locally modeled as a normal diffusion process, but with a scale dependent diffusion coefficient which depends on particles separation D, according to the celebrated Richardson's 4/3rd law: $K(D) \propto D^{4/3}$. Richardson (1926) conjectured such a scale dependent diffusive scenario from an empirical short time, scale by scale, analysis of local diffusion properties over a wide range of phenomena, from diffusion of oxygen into nitrogen, to the diffusion of cyclones in the atmosphere (Fig. 5b), such that at each scale the mean square separation could be locally written as $D^2 \propto K(D)t$. It is now accepted that his derivation of the 4/3rd law was at the same time fortuitous and the result of his unique intuition (Sawford 2001). Richardson also showed that such a non-Fickian diffusion resulted in a cubic super-diffusive growth of the mean square separation of pairs of particles according to the law $\langle D^2\rangle = g\epsilon t^3$, where ϵ is the turbulent energy dissipation rate and g a universal constant since known as the Richardson constant.

The Richardson constant g in Eq. (5) is one of the most fundamental constants in turbulence (together with the Kolmogorov constant C_K). It plays a major role in turbulent dispersion and mixing processes. However, in spite of its importance, it is only recently that estimations of its value started to converge towards a well accepted value (Sawford 2001; Salazar and Collins 2009). This is due to the difficulty to observe Richardson's superdiffusion experimentally (Sawford 2001; Bourgoin et al. 2006). Until recently, best estimates for g still spanned several orders of magnitude. Most recent high-resolution direct numerical simulations seem to point toward an estimate of $g \sim 0.5 - 0.6$ (Bitane et al. 2012; Boffetta and Sokolov 2002a), see Fig. 6a. This value is also consistent with experiments by Ott and Mann (2000) in homogeneous and isotropic turbulence at a moderate Reynolds number $R_\lambda \simeq 100$, based on Taylor micro-scale, see Fig. 6b.

Apart from this experiment, high-resolution data in well-controlled laboratory experiments is still very scarce. This is very likely due to the difficulty in obtaining sufficiently long tracks in Lagrangian measurements, allowing to unambiguously observe the long-term cubic regime *à la* Richardson. Recent experiments by Bour-

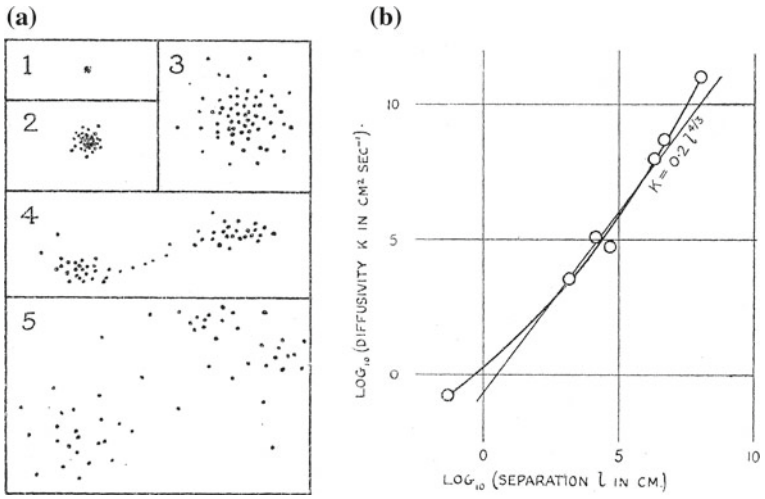

Fig. 5 **a** Qualitative illustration of the non-normal dispersion of a dense cluster of particles as proposed in Richardson's original 1926 article. **b** Original empirical derivation of the "4/3rd" law by Richardson. (Both figures are taken from Richardson's seminal article on relative dispersion (Richardson 1926)

goin et al. (2006) report highly resolved particle tracking measurements of relative dispersion at high Reynolds numbers (up to $R_\lambda \simeq 800$), although the track lengths in this experiment were too short to actually observe the t^3 Richardson regime and only the early ballistic regime was observed, see Fig. 6c.

In the next subsection, a simple phenomenology for pair dispersion is proposed which elucidates many aspects of the problem, in particular regarding the origin of the cubic super-diffusive long-term regime and its deep connection with fundamental properties of the turbulent energy cascade. We also discuss the expected consequences for the case of 2D turbulence, relevant for large-scale geophysical flows.

4.3 A Simple Ballistic Phenomenology of Turbulent Superdiffusion

Recent work by Bourgoin (2015) suggests that a scale dependent ballistic phenomenolgy, rather than a scale dependent diffusive phenomenology as originally proposed by Richardson, may be best suited to quantitatively describe turbulent superdiffusion. The idea is quite simple. Let us consider an ensemble of particles with an initial mean square separation D_0^2. In the short term, the particles will separate ballistically according to the kinematic relation (6). Let t_0 be the typical duration of the initial ballistic growth. Experimental and numerical evidence discussed in the

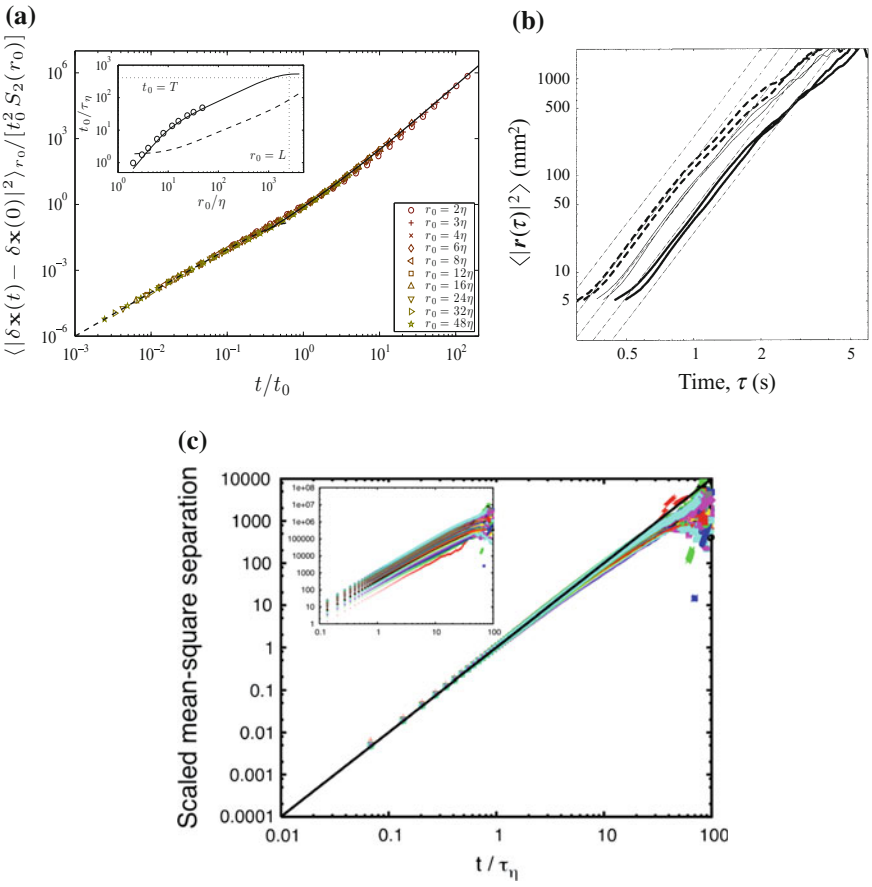

Fig. 6 Growth of the mean square separation of particle pairs in: **a** direct numericam simulations by Bitane et al. (2012) (time is non-dimensionalized by $t_0 = S_2(D_0)/2\epsilon$ which within K41 framework is proportional to $\epsilon^{-1/3} D_0^{2/3}$, different symbols correspond to different initial separations); at short time the separation follows a ballistic regime *à la* Batchelor, while at long times the separation is cubic, *à la* Richardson, with a transition occurring for times $t \simeq t_0$. **b** Experiments by Ott and Mann (2000); time in this plot has been shifted by virtual time origin T_0 to emphasize the cubic behaviour. **c** Experiments by Bourgoin et al. (2006) where the ballistic regime is robustly observed, without any adjustable parameter

previous section confirm Batchelor's suggestion that $t_0 \propto \epsilon^{-1/3} D_0^{2/3}$. Following Bitane et al. (2012) we can equivalently write $t_0' = \alpha S_2(D_0)/2\epsilon$, with α a non-dimensional parameter that we call the *persistence parameter*, as it quantifies the persistence of the ballistic regime. The main idea behind the ballistic cascade mechanism is illustrated in Fig. 7. It is based on the trivial idea that if an ensemble of particles with initial mean square separation $\vec{D}_0^2$ starts to disperse ballistically, with a separation rate $S_2(\vec{D}_0)$ over a given period t_0' after which it reaches a new mean square

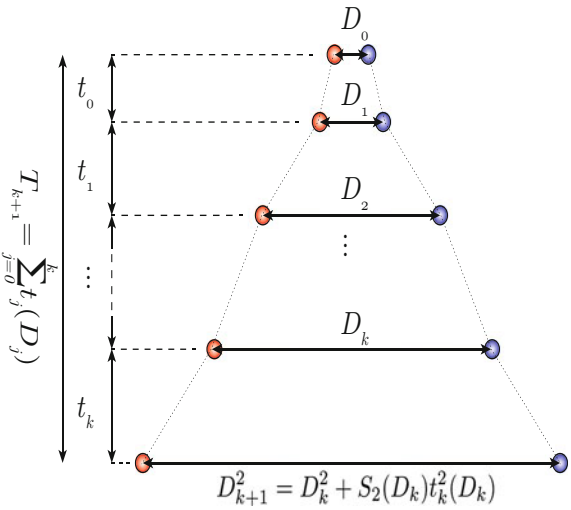

Fig. 7 Illustration of the iterative ballistic cascade for the relative separation of particles with initial mean square separation D_0^2: at each iteration step k, the mean square separation between particles grows ballistically from D_k^2 to D_{k+1}^2 with a growth rate $\sqrt{S_2(D_k)}$, during a time lag t_k'. The overall time required to reach separation D_k at the iteration number k is $T_k = \sum_{j=0}^{k-1} t_j'(D_j)$

separation $\vec{D}_1{}^2$, instead of considering a sudden transition towards an enhanced cubic dispersion regime *à la* Richardson, the ballistic process can instead be iterated starting from the new mean square separation $\vec{D}_1^2$, with a new separation rate $S_2(\vec{D}_1)$ over a period t_1' and so on. Thus, in this scenario the time evolution of the particle mean square separation is simply described by the iterative process:

$$D_{k+1}^2 = D_k^2 + S_2(D_k)t_k'^2(D_k), \tag{7}$$

where $D_k^2 = \langle|\vec{D}_k|^2\rangle$ represents the mean square separation of particle pairs after the k^{th} iteration step, $t_k'(D_k)$ is a scale dependent "time of flight" characteristic of the duration of the ballistic motion at step $k+1$. For the case of turbulent flows, $S_2(D_k)$ and $t_k'(D_k)$ will be prescribed later by imposing K41 scalings.

A concrete implementation of the iterative scheme (7) requires the expressions for the scale dependent separation rate $S_2(D_k)$ and the ballistic time of flight $t_k'(D_k)$ to be specified. For particles with separation in the inertial range of scales of the carrier turbulence in 3D turbulence and in the inverse cascade of 2D turbulence, the structure function is known to follow the K41 scaling:

$$S_2(\vec{D}_0) = C\epsilon^{2/3}D_0^{2/3}, \tag{8}$$

with $D_0 = |\vec{D}_0|$ and where C is a universal constant. For 3D-turbulence $C = C^{3D} = \frac{11}{3}C_2^{3D}$, where $C_2^{3D} \simeq 2.1$ is analytically related to the Kolmogorov constant $C_K \simeq C_2/4$, see Sreenivasan (1995), characterizing the celebrated $-5/3$ spectrum of turbulent kinetic energy ($E(k) = C_K\epsilon^{2/3}k^{-5/3}$). We shall therefore refer to C as *the* Kolmogorov constant in the sequel. The 3D-Kolmogorov constant is hence $C^{3D} \simeq \frac{11}{3} \cdot 2.1 \simeq 7.7$). The exact same phenomenology can also be applied to the

inverse cascade regime of scales of 2D-turbulence, for which S_2 also obeys K41 scalings, with $C = C^{2D} = \frac{8}{3}C_2^{2D}$, where the 2D-Kolmogorov constant is $C_2^{2D} \simeq 0.17 C_K^{2D} \simeq 13.2$ (Lindborg 1999), with $C_K^{2D} \sim 6$ (Boffetta and Ecke 2012) the spectral 2D-Kolmogorov constant (hence $C^{2D} \simeq 35.3$).

The iterative ballistic process can now be explicitly written as

$$D_{k+1}^2 = D_k^2 + S_2(D_k) t_k'^2(D_k) \quad \text{with} \quad \begin{cases} S_2(D_k) = C\epsilon^{2/3} D_k^{2/3} \\ t_k'(D_k) = \alpha t_k = \alpha S_2(D_k)/2\epsilon \end{cases}, \tag{9}$$

where the Kolmogorov constant C and the persistence parameter α are the only parameters. The Kolmogorov constant being known, α is the only adjustable parameter of the problem.

The iterative process (9) leads to a simple geometrical progression where

$$\begin{cases} D_{k+1}^2 = A D_k^2 \\ t'_{k+1} = A^{1/3} t'_k \end{cases}, \tag{10}$$

with

$$A = 1 + \frac{\alpha^2 C^3}{4}. \tag{11}$$

Simple arithmetics then lead to the following relation for the growth of the mean square separation as a function of the total time $T_k = \sum_{j=0}^{k-1} t'_j(D_j)$:

$$D_k^2 = g\epsilon \left[T_k + \left(\frac{D_0^2}{g\epsilon} \right)^{1/3} \right]^3 \tag{12}$$

with

$$g = \left[2 \frac{A^{1/3} - 1}{\alpha C} \right]^3 = \left[2 \frac{(1 + \frac{\alpha^2 C^3}{4})^{1/3} - 1}{\alpha C} \right]^3 \tag{13}$$

Several points are worth being noted at this point:

- Relation (12) shows that in the long term ($T \gg \left(D_0^2/g\epsilon\right)^{1/3}$), the iteration of elementary K41 scale dependent ballistic steps eventually builds a Richardson cubic regime where $D^2 = g\epsilon T^3$.
- It also shows that at intermediate times, the growth follows a similar cubic regime, but with a negative virtual time origin $T_{origin} = -\left(D_0^2/g\epsilon\right)^{1/3}$ such that $D^2 = g\epsilon(T - T_{origin})^3$, supports the empirical approach by Ott and Mann (2000) to extract the value of the Richardson constant from short experimental tracks.
- Finally, relation (13) relates the Richardson constant to the Kolmogorov constant C and to the persistence parameters.

4.4 Practical Implementation of the Ballistic Phenomenology

The practical implementation of the iterative ballistic phenomenology only requires the knowledge of the Kolmogorov constant C and the persistence parameter α. As discussed in the previous section, the Kolmogorov constant has well accepted values, both for the 3D turbulence case ($C^{3D} \simeq 7.7$) and for the inverse cascade of (2D turbulence ($C^{2D} \simeq 35.3$). The persistence parameter is a new quantity, which in principle is related to the correlation time of the relative velocity of pairs, which to our knowledge has never been measured yet (neither experimentally nor numerically). We will therefore extract here this parameter by comparing the prediction for the Richardson constant g from Eq. (13) to presently well accepted values of g.

Figure 8a, b show the prediction for the Richardson constant as a function of α given by Eq. (13) for the 3D and 2D turbulence cases. For the 3D case, Fig. 8a, this is obtained by fixing the value of the Kolmogorov constant to $C^{3D} \simeq 7.7$. By comparing this prediction to the well accepted value for the Richardson constant $g^{3D} \simeq 0.55$ we can retrieve the optimal value for the persistence parameter $\alpha^{3D} \simeq 0.12$. Note that $\alpha \simeq 2.8$ would be a priori another possible value of the persistence parameter also consistent with the expected value of the Richardson constant. However, as it will be discussed later, the smallest value of the persistent parameter is to be preferred in order to warrant the validity of the scale-by-scale ballistic approximation.

Figure 9 shows the result of the ballistic phenomenology with $C = C^{3D} = 7.7$ and $\alpha = \alpha^{3D} = 0.12$ for the mean square separation as a function of time as given by Eq. (12), compared to the direct numerical simulations of 3D homogeneous isotropic turbulence by Bitane et al. (2012). It can be seen that the iterative ballistic phenomenology reproduces almost perfectly the numerical data.

Figure 9 also shows the mean square separation of pairs measured in high resolution particle tracking experiments by Bourgoin et al. (2006). In those experiments, only the Batchelor ballistic regime was reported, while no hint of the Richardson regime was detected. Figure 9 emphasizes a possible reason for the failure in experiments to observe the Richardson regime: the longest experimental tracks did not exceed a few tenths of t_0 while the separation needs to be tracked for at least a few t_0 to reasonably detect the transition toward the cubic regime. A simple possible strategy to improve the chances to observe the cubic regime in experiments would simply consist in better controlling the injection of particle pairs in order to achieve sufficiently small initial separations, hence reducing the time t_0 required for the transition to occur within experimentally accessible tracking time.

For the 2D turbulence case, Eq. (13) can also be used to determine the optimal value of the persistence parameter α compatible with reported values for the forward Richardson constant g^{2D}. Values for g^{2D} in the literature still span a broad range. Experiments by Jullien et al. (1999) suggest $g^{2D} \simeq 0.55$, while numerical simulations by Boffetta and Sokolov (2002b) and by Faber and Vassilicos (2009) report $g^{2D} \simeq 3.8$ and $g^{2D} \simeq 6.9$, respectively. For the sake of the present discussion, we will consider the value proposed by Faber and Vassilicos (2009), that is $g^{2D} \simeq 6.9$, as this study also addresses explicitly and quantitatively the comparison between forward

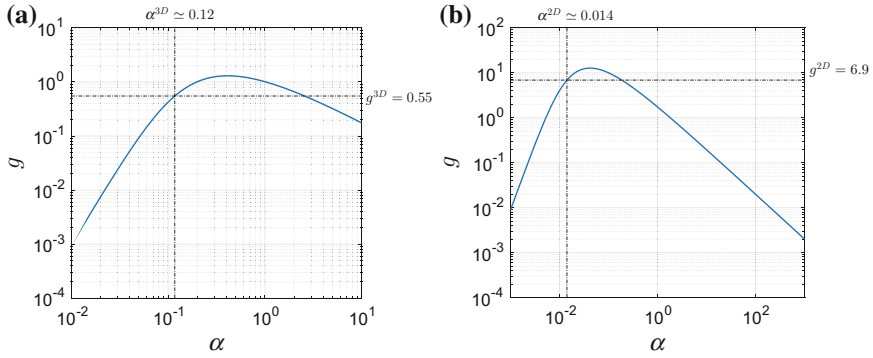

Fig. 8 Dependency of the Richardons constant as a function of the persistence parameter α as predicted by Eq. (13) for the 3D case (**a**), where the Kolmogorov constant has been fixed to $C_{3D} \simeq 7.7$, and for the 2D case (**b**), where the Kolmogorov constant has been fixed to $C_{3D} \simeq 35.3$. The *horizontal dot-dashed lines* in each plot indicate the well accepted values for the Richardson constant in both cases and the *vertical lines* indicate the optimal value of the persistence parameter leading to these values. Note that for the ballistic approximation to be valid, the smallest possible value of α is preferred (see discussion in the text)

and backward dispersion which will be discussed in Sect. 4.5. Figure 8b shows the prediction for the Richardson constant as a function of the persistence parameter α for the 2D case (i.e. from Eq. (13) with the Kolmogorov constant fixed to $C_{2D} = 35.3$), leading to an optimal value of the persistence parameter of $\alpha^{2D} \simeq 0.014$.

4.5 About the Time Irreversibility of Turbulent Relative Dispersion

One of the noticeable feature of turbulent dispersion is the temporal asymmetry, meaning that backward and forward dispersion operate at a different rate. The backward dispersion problem is analogous to the dispersion problem discussed so far, except that D_0 is now considered as a final condition rather than an initial condition: considering an ensemble of particles with a given mean square separation $\langle D_0^2 \rangle$ at $t = 0$, what was their mean square separation $\langle (\vec{D}(-t) - \vec{D}_0)^2 \rangle$ at earlier times $-t$? The concept of backward dispersion is crucial for turbulent mixing and passive scalar studies (Salazar and Collins 2009) as it determines for instance the rate at which reactants injected at two different source points will eventually get close enough to react. The temporal asymmetry of pair dispersion, was only recently pointed at by Sawford et al. (2005) who showed that backward dispersion in Lagrangian stochastic models and in three-dimensional DNS operates at a significantly faster rate compared to forward dispersion. Recent experiments and simulations by Berg et al. (2006) confirm this trend with a ratio of backward to forward Richardson constants of the order

of 2 for 3D-turbulence. Interestingly, numerical simulations of 2D-turbulence in the inverse cascade regime by Faber and Vassilicos (2009) present the opposite asymmetry, 2D forward dispersion operating faster than 2D backward dispersion. The origin of this asymmetry remained unclear and will be addressed in this section, where an extension of the ballistic phenomenology will be introduced which accounts for time asymmetry and for the differences between 2D and 3D turbulence. Sawford et al. (2005) pointed out the importance of odd moments of two points velocity statistics for the time irreversibility of relative dispersion, while Berg et al. (2006) suggested an explanation based on the strain-tensor eigenvalues, which was however shown by Faber and Vassilicos (2009) to be insufficient to explain the difference between 2D and 3D-turbulence, hence emphasizing the possible role of energy flux accross scales, which goes from large to small scales in 3D-turbulence and from small to large scale in 2D-turbulence inverse cascade.

In its present formulation, the iterative ballistic phenomenology is completely time-reversible as the elementary ballistic process in Eq. (7) at each scale is quadratic in time and hence fully reversible under the transformation $t \rightarrow -t$. An extension of the iterative ballistic phenomenology to address the question of time asymmetry can be simply introduced by the Taylor expansion extending to third order, leading to the elementary ballistic process in relation (6). When pushed to third order, the iterative scheme (9), giving the growth of pair separation at iteration between the kth and the (k+1)th iteration, becomes:

$$D_{k+1}^2 = D_k^2 + S_2(D_k)t_k'^2 + S_{au}(D_k)t_k'^3, \tag{14}$$

where $S_{au}(r) = \langle \delta_{\vec{r}}\vec{a} \cdot \delta_{\vec{r}}\vec{u} \rangle$ is the crossed velocity-acceleration structure function.

From a physical point of view, the third order term has a clear energetic interpretation. The crossed velocity-acceleration structure function $S_{au}(r) = \langle \delta_{\vec{r}}\vec{a} \cdot \delta_{\vec{r}}\vec{u} \rangle$ can indeed be analytically related to the third order Eulerian velocity structure function (and hence to the energy cascade accross scales) directly from the Navier–Stokes equation, such that under local stationarity and homogeneity assumptions (see, for instance, Mann et al. 1999; Hill 2006):

$$2\langle \delta_{\vec{r}}\vec{a} \cdot \delta_{\vec{r}}\vec{u} \rangle = \vec{\nabla} \cdot \langle \delta_{\vec{r}}\vec{u}\delta_{\vec{r}}\vec{u} \cdot \delta_{\vec{r}}\vec{u} \rangle. \tag{15}$$

In 3D turbulence, $\vec{\nabla} \cdot \langle \delta_{\vec{r}}\vec{u}\delta_{\vec{r}}\vec{u} \cdot \delta_{\vec{r}}\vec{u} \rangle = -4\epsilon$ (which is an exact relation and an alternative version of the Kármán-Howarth-Monin relation under local homogeneity and isotropy assumptions, see Frisch (1995), which leads to

$$S_{au}^{3D} = -2\epsilon. \tag{16}$$

The negative sign in this relation reflects the fact that in 3D turbulence the energy cascade at inertial scales is a *direct cascade* (energy flows from large to small scales).

Conversely, in the inverse cascade of 2D turbulence $\vec{\nabla} \cdot \langle \delta_{\vec{r}}\vec{u}\delta_{\vec{r}}\vec{u} \cdot \delta_{\vec{r}}\vec{u} \rangle = +4\epsilon$ (Lindborg 1999), leading to

$$S_{au}^{2D} = +2\epsilon, \tag{17}$$

Table 1 The different possible values for C_{au} depending on the nature of turbulence and time direction

	3D (direct cascade)	2D (inverse cascade)
Forward	-1	$+1$
Backward	$+1$	-1

the positive sign referring now to the *inverse* nature of the energy cascade.[1]

The crossed velocity-acceleration structure function therefore carries the signature of the energy flux across scales. In the present context of pair dispersion, the cubic term in Eq. (14) should therefore be seen as the Lagrangian signature of the energy flux due to the relative motion (relative velocity and relative acceleration) of particles separating from a given scale to larger scales. The negative sign in the relation $S_{au}^{3D} = -2\epsilon$ in 3D can be interpreted as the fact that in the forward dispersion process, as particles separate (from small to large scales), they climb the energy cascade "upstream", *against* the energy flux (which flows from large to small scales in the direct 3D cascade), while in the backward case separation pair separation climbs the cascade downstream, *with* the energy flux. The scenario is reversed in the inverse cascade of 2D turbulence.

The third order correction to the ballistic process in the extended iterative phenomenology therefore accounts, in the Lagrangian framework of pair dispersion, for the scale asymmetry of energy flux in the turbulent cascade and introduces the notion of Lagrangian temporal asymmetry (Table 1).

When the relation $S_{au}^{3D} = -2\epsilon$ (for 3D turbulence) is reported in the elementary short term separation process given by Eq. (14), we find that for short times the separation is still dominated by the ballistic (quadratic) contribution, with a third order temporal asymmetry such that the difference between short term forward and backward separation is $\langle D^2\rangle(-t) - \langle D^2\rangle(t) = 4\epsilon t^3$ (in 3D turbulence). This corresponds to the short term cubic in time asymmetry of relative dispersion recently investigated by Jucha et al. (2014). We will show here that the iterative propagation of this short term asymmetry also builds the long-term asymmetry, in quantitative agreement with previous studies for the Richardson regime asymmetry. Such a connection between the short term and long term asymmetry still remains to be established, as pointed by Jucha et al. (2014).

A similar iterative process as the one described previously can indeed be iterated replacing Eq. (9) with (14). Considering that $S_{au} = \pm 2\epsilon$ (the sign depending on the direction of the turbulent energy cascade), the cubic correction is written as $C_{au} 2\epsilon t^3$, where $C_{au} = \pm 1$ depending both on the nature (2D *vs* 3D) of turbulence and on the time direction (forward *vs* backward dispersion), with the rules:

[1] These relations together with Eq. (14) show that the ballistic approximation previously discussed holds as long as $t_k' \ll |S_2(D_k)/S_{au}(D_k)| = S_2(D_k)/2\epsilon$, which according to relation (9) requires $\alpha \ll 1$. This justifies the choice of the smallest relevant persistence parameter.

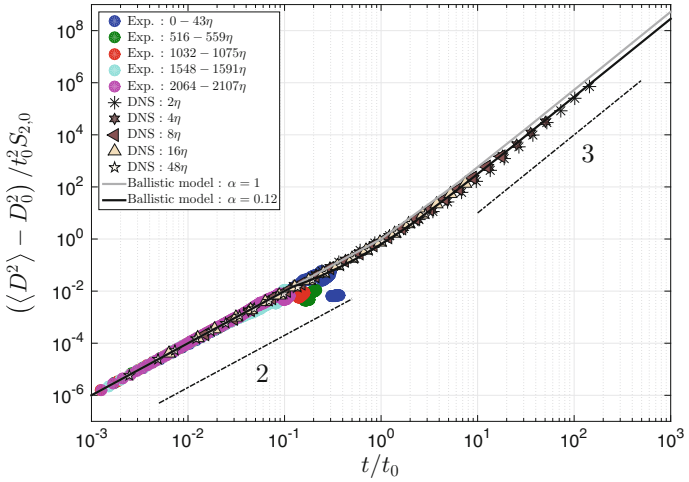

Fig. 9 Comparison of the prediction from the ballistic model for two values of the persistence parameter ($\alpha = 1$ and $\alpha = 0.12$) and for the mean square separation of particles with different initial separation D_0 (given in the inset) within inertial scales, obtained in direct numerical simulations (Bitane et al. 2012) and in high resolution particle tracking experiments (Bourgoin et al. 2006). Note that the time axis is normalized by $t_0 = S_2(D_0)/2\epsilon$ and the mean square separation is normalized by $t_0^2 S_2(D_0)$

The outcome of this calculation leads to an expression for the long term mean square separation growth identical to Eq. (12), where the only modification is in the expression for the Richardson constant, which now includes the additional coefficient C_{au} accounting for the cubic correction:

$$g = \left[2\frac{(1 + \frac{\alpha^2 C^3}{4}(1 + C_{au}\alpha))^{1/3} - 1}{\alpha C} \right]^3 \tag{18}$$

As a result, the third order corrected model behaves exactly as the purely ballistic model, except for the relation between the Richardson constant and the model parameters which now includes a corrective term, associated to the asymmetry coefficient C_{au}.

The Richardson constant can then be derived from this relation for the 2D/3D cases both in the forward/backward dispersion problem, by using the appropriate values of the Kolmogorov and persistence constants already discussed previously (we recall that $C^{3D} \simeq 7.7$, $C^{2D} \simeq 35.3$, $\alpha^{3D} \simeq 0.14$, $\alpha^{2D} \simeq 0.012$), and the appropriate values of the asymmetry constant C_{au} according to the table above. This leads to the following ratios of the forward *vs* backward Richardson constants:

$$\frac{g_{bwd}^{3D}}{g_{fwd}^{3D}} \simeq 1.9 \quad \text{and} \quad \frac{g_{bwd}^{2D}}{g_{fwd}^{2D}} \simeq 0.9\,, \tag{19}$$

which is in quantitative agreement with the experiments and simulations by Berg et al. (2006) and with the more recent simulations by Bragg et al. (2016), who all find a ratio $g_{bwd}^{3D}/g_{fwd}^{3D} \simeq 2$ for the 3D turbulence case, and with simulations by Faber and Vassilicos (2009) who report $g_{bwd}^{2D}/g_{fwd}^{2D} = 0.92$ for the inverse cascade of 2D turbulence.

5 Conclusion

Anisotropy and two-dimensionalization are two important properties of geophysical flows. The experimental results reported in Sect. 3 show that the small-scale local isotropy hypothesis, generally considered in models and simulations might be more controversial than usually believed. Large-scale anisotropy appears to persist at small scales, even in the limit of large Reynolds numbers (approaching $R_\lambda \sim 10^3$). The analysis of turbulent relative dispersion reported in Sect. 4 show that the rate at which particles separate at inertial scales (an intrinsically Lagrangian problem) can be very simply related to the usual Eulerian phenomenology of turbulence cascade, including the energy spectrum (via the second order Eulerian structure function S_2) and the energy flux (via the crossed acceleration-velocity structure function, itself related to the third order Eulerian structure function S_3). This allows to simply predict the short- and long-term time dependencies of the mean square separation by simple as well as subtle effects as temporal asymmetry. In particular, the existence of a 2D inverse cascade is responsible for a faster forward dispersion process in 2D while in a direct energy cascade scenario, as in 3D turbulence, backward dispersion operates faster than forward. It could also be noted that the ballistic iterative process is not limited to the sole case explicitly addressed here (using $S_2(r) \propto (\epsilon r)^{2/3}$), but can for instance also be applied to predict the dispersion laws for the 2D direct energy cascade by using the appropriate law $S_2(r) \propto \zeta^{2/3} r^2$, with ζ the enstrophy dissipation.

References

F. Anselmet, Y. Gagne, E.J. Hopfinger, R.A. Antonia, High-order velocity structure functions in turbulent shear flows. J. Fluid Mech. **140**, 63–89 (1984)

A. Arneodo, C. Baudet, F. Belin, R. Benzi, B. Castaing, B. Chabaud, R. Chavarria, S. Ciliberto, R. Camussi, F. Chillà, B. Dubrulle, Y. Gagne, B. Hebral, J. Herweijer, M. Marchaud, J. Maurer, J.F. Muzy, A. Naert, A. Noullez, J. peinke, F. Roux, P. Tabeling, W. van de Water, H. Willaime, Structure functions in turbulence, in various flow configurations, at Reynolds numbers between 30 and 5000, using extended self-similarity. Europhys. Lett. **34**(6), 411–416 (1996)

G.K. Batchelor, The theory of axisymmetric turbulence. Proc. R. Soc. Lond. Series A Math. Phys. Sci. **186**(1007), 480–502 (1946)

G.K. Batchelor, The application of the similarity theory of turbulence to atmospheric diffusion. Quart. J. R. Meteorol. Soc. **76**(328), 133–146 (1950)

J. Berg, B. Lüthi, J. Mann, S. Ott, Backwards and forwards relative dispersion in turbulent flow: an experimental investigation. Phys. Rev. E **74**(1), 016304 (2006)

L. Biferale, I. Procaccia, Anisotropy in turbulent flows and in turbulent transport. Phys. Rep. **414**(2–3), 43–164 (2005)
R. Bitane, H. Homann, J. Bec, Time scales of turbulent relative dispersion. Phys. Rev. E **86**(4), 045302 (2012)
G. Boffetta, I. Sokolov, Relative dispersion in fully developed turbulence: the Richardson's law and intermittency corrections. Phys. Rev. Lett. **88**(9), 094501 (2002)
G. Boffetta, I. Sokolov, Statistics of two-particle dispersion in two-dimensional turbulence. Phys. Fluids **14**(9), 3224–3232 (2002)
G. Boffetta, R.E. Ecke, Two-dimensional turbulence. Annu. Rev. Fluid Mech. **44**, 427–451 (2012)
M. Bourgoin, N.T. Ouellette, H. Xu, J. Berg, E. Bodenschatz, The role of pair dispersion in turbulent flow. Science **311**(5762), 835–838 (2006)
M. Bourgoin, J.-F. Pinton, R. Volk, Lagrangian methods in experimental fluid mechanics. in *Modeling Atmospheric and Oceanic Flows: Insights from Laboratory Experiments and Numerical Simulations*, ed. By T. von Larcher, P.D. Williams (Wiley, Inc., 2014), p. 360
M. Bourgoin, H. Xu, Focus on dynamics of particles in turbulence. New J. Phys. **16**(8), 085010 (2014)
M. Bourgoin, Turbulent pair dispersion as a ballistic cascade phenomenology. J. Fluid Mech. **772**, 678–704 (2015)
A.D. Bragg, P.J. Ireland, L.R. Collins, Forward and backward in time dispersion of fluid and inertial particles in isotropic turbulence. Phys. Fluids **28**(1), 013305 (2016)
S. Chandrasekhar, The theory of axisymmetric turbulence. Proc. R. Soc. Lond. Series A Math. Phys. Sci. **242**(855), 557–577 (1950)
S.Y. Chen, B. Dhruva, S. Kurien, K.R. Sreenivasan, M.A. Taylor, Anomalous scaling of low-order structure functions of turbulent velocity. J. Fluid Mech. **533**, 183–192 (2005)
M. Chertkov, A. Pumir, B.I. Shraiman, Lagrangian tetrad dynamics and the phenomenology of turbulence. Phys. Fluids **11**(8), 2394–2410 (1999)
P.A. Davidson, B.R. Pearson, Identifying turbulent energy distributions in real, rather than Fourier, space. Phys. Rev. Lett. **95**(21), 214501 (2005)
T. Faber, J.C. Vassilicos, Turbulent pair separation due to multiscale stagnation point structure and its time asymmetry in two-dimensional turbulence. Phys. Fluids **21**(1), 015106 (2009)
G. Falkovich, K. Gawedski, M. Vergassola, Particles and fields in fluid turbulence. Rev. Mod. Phys. **73**(4), 913–975 (2001)
U. Frisch, *Turbulence: The Legacy of A.N. Kolmogorov* (Cambridge University Press, Cambridge, England, 1995)
S. Garg, Z. Warhaft, On the small scale structure of simple shear flows. Phys. Fluids **10**(3), 662–673 (1998)
S.R. Hanna, Lagrangian and Eulerian time-scale relations in the daytime boundary-layer. J. Appl. Meteorol. **20**(3), 242–249 (1981)
R.J. Hill, Opportunities for use of exact statistical equations. J. Turbul. **7**, 43 (2006)
J. Hinze, *Turbulence* (McGraw-Hill, 1959)
J. Jucha, H. Xu, A. Pumir, E. Bodenschatz, Time-reversal-symmetry breaking in turbulence. Phys. Rev. Lett. **113**(5), 054501 (2014)
M.C. Jullien, J. Paret, P. Tabeling, Richardson pair dispersion in two-dimensional turbulence. Phys. Rev. Lett. **82**(14), 2872–2875 (1999)
A.N. Kolmogorov, The local structure of turbulence in incompressible viscous fluid for very large Reynolds numbers. Dokl. Akad. Nauk SSSR **30**, 301–305 (1941)
A.N. Kolmogorov, Refining the notions of the local structure of turbulence in an incompressible viscous fluid at high Reynolds numbers, in *Mécanique de la Turbulence* (CNRS, Paris, 1962), pp. 447–458
R.C. Lien, E.A. D'Asaro, G.T. Dairiki, Lagrangian frequency spectra of vertical velocity and vorticity in high-Reynolds-number oceanic turbulence. J. Fluid Mech. **362**, 177–198 (1998)
R.C. Lien, E.A. D'Asaro, The Kolmogorov constant for the Lagrangian velocity spectrum and structure function. Phys. Fluids **14**(12), 4456–4459 (2002)

E. Lindborg, Can the atmospheric kinetic energy spectrum be explained by two-dimensional turbulence? J. Fluid Mech. **388**, 259–288 (1999)
J. Mann, S. Ott, J.S. Andersen, Experimental study of relative, turbulent diffusion. Technical Report Riso-R-1036 (EN), Risoe National Laboratory, Roskilde, Denmark, 1999
N. Mordant, P. Metz, O. Michel, J.-F. Pinton, Measurements of Lagrangian velocity in fully developed turbulence. Phys. Rev. Lett. **87**(21), 214501 (2001)
A.M. Obukhov, On the distribution of energy in the spectrum of a turbulent flow. Izv. Akad. Nauk SSSR **5**, 453–466 (1941)
A.M. Obukhov, Some specific features of atmospheric turbulence. J. Fluid Mech. **13**, 77–81 (1962)
S. Ott, J. Mann, An experimental investigation of the relative diffusion of particle pairs in three-dimensional turbulent flow. J. Fluid Mech. **422**, 207–223 (2000)
N.T. Ouellette, H. Xu, M. Bourgoin, E. Bodenschatz, Small-scale anisotropy in Lagrangian turbulence. New J. Phys. **8**(6), 102 (2006)
M. Ould-Rouiss, The axisymmetric equivalent of Kolmogorov's equation. Eur. Phys. J. B **23**(1), 107–120 (2001)
G. Parisi, U. Frisch, A multifractal model of intermittency, in *Turbulence and Predictability in Geophysical Fluid Dynamics and Climate Dynamics*, ed. By M. Ghil, R. Benzi, G. Parisi (Amsterdam, Eds. North Holland, 1985), pp. 84–87
A. Pumir, B.I. Shraiman, Persistent small scale anisotropy in homogeneous shear flows. Phys. Rev. Lett. **75**(17), 3114–3117 (1995)
L.F. Richardson, Atmospheric diffusion shown on a distance-neighbour graph. Proc. R. Soc. Lond. Series A **110**(756), 709–737 (1926)
H.C. Rodean, The universal constant for the Lagrangian structure-function. Phys. Fluids A **3**(6), 1479–1480 (1991)
J.P.L.C. Salazar, L.R. Collins, Two-particle dispersion in isotropic turbulent flow. Annu. Rev. Fluid Mech. **41**, 405–432 (2009)
B.L. Sawford, Reynolds number effects in Lagrangian stochastic models for turbulent dispersion. Phys. Fluids A **3**(6), 1577–1586 (1991)
B. Sawford, Turbulent relative dispersion. Annu. Rev. Fluid Mech. **33**, 289–317 (2001)
B.L. Sawford, P.K. Yeung, M.S. Borgas, Comparison of backwards and forwards relative dispersion in turbulence. Phys. Fluids **17**(9), 095109 (2005)
K.R. Sreenivasan, On the universality of the Kolmogorov constant. Phys. Fluids **7**(3), 2778–2784 (1995)
G.I. Taylor, Diffusion by continuous movements. Proc. Lond. Math. Soc. **20**, 196–212 (1922)
H. Tennekes, Eulerian and Lagrangian time microscales in isotropic turbulence. J. Fluid Mech. **67**(3), 561–567 (1975)
K.A. Weinman, A.Y. Klimenko, Estimation of the Kolmogorov constant C_0 by direct numerical simulation of a continuous scalar. Phys. Fluids **12**(12), 3205–3220 (2000)
H. Xu, M. Bourgoin, N.T. Ouellette, E. Bodenschatz, High order Lagrangian velocity statistics in turbulence. Phys. Rev. Lett. **96**(2), 024503 (2006)
P.K. Yeung, Lagrangian investigations of turbulence. Annu. Rev. Fluid Mech. **34**, 115–142 (2002)

Gravity and Turbidity Currents: Numerical Simulations and Theoretical Models

Eckart Meiburg and Mohamad M. Nasr-Azadani

Abstract Part 1 of this article describes high-resolution Direct Numerical Simulations (DNS) of gravity and turbidity currents, with an emphasis on the structure, Lagrangian dynamics and energy budget of the flow. In part 2, we review a novel approach for modeling stratified flows based on vorticity, which avoids many of the empirical assumptions required by earlier modeling efforts.

1 Introduction

Gravity currents form when a heavier fluid propagates into a lighter, ambient fluid as a result of horizontal hydrostatic pressure gradients (Benjamin 1968; Huppert 1986; Simpson 1997; Borden and Meiburg 2013a). Understanding the dynamics of such currents is of general interest, as they occur frequently both in the environment and in engineering applications. Turbidity currents constitute a special class of gravity currents, in which the density difference is caused by suspended sediment. Their flow structure usually gives rise to both erosion and deposition (Kneller and McCaffrey 1999), and hence they represent an important mechanism for the transport of sediment in oceans or lakes (Meiburg and Kneller 2010). Repeated interactions of turbidity currents with the seafloor can result in the formation of a variety of topographical features, among them meandering channels, fans and lobes, gullies, levees, sediment waves and graded bedding (Kuenen and Migliorini 1950; Wynn et al. 2000; Migeon et al. 2001; Nakajima and Satoh 2001; Normark et al. 2002; Wynn and Stow 2002).

E. Meiburg (✉) · M.M. Nasr-Azadani
Department of Mechanical Engineering, University of California at Santa Barbara, Santa Barbara, CA 93106, USA
e-mail: meiburg@engineering.ucsb.edu

M.M. Nasr-Azadani
e-mail: mmnasr@engineering.ucsb.edu

H.J.H. Clercx and G.J.F. van Heijst (eds.), *Mixing and Dispersion in Flows Dominated by Rotation and Buoyancy*, CISM International Centre for Mechanical Sciences 580, https://doi.org/10.1007/978-3-319-66887-1_6

Due to the unpredictable and often catastrophic character of natural turbidity currents, many investigations aimed at obtaining insight into their dynamics have employed laboratory experiments, most often involving currents propagating over flat surfaces, e.g., Lüthi (1981), Bonnecaze et al. (1993), Gladstone et al. (1998), and de Rooij and Dalziel (2001). Currents over flat substrates are also amenable to simplified theoretical approaches, such as box models, shallow water models and linear stability analyses (Rottman and Simpson 1983; Bonnecaze et al. 1993; Dade and Huppert 1995; Hallworth et al. 1998; Hall et al. 2008; Lesshafft et al. 2011). In recent years, fully three-dimensional numerical simulations of turbidity currents propagating over flat beds have become feasible as well, e.g., Necker et al. (2002, 2005), Huang et al. (2008), and Cantero et al. (2009). Due to their numerical resolution requirements, however, these simulations to date have mostly been limited to laboratory scales.

Comparatively few investigations to date have addressed the dynamics of turbidity currents propagating over more complex seafloor topographies involving, for example, slopes or meandering submarine channels (Woods et al. 1998; Kubo and Nakajima 2002; Kubo 2004; Kassem and Imran 2004; Blanchette et al. 2005; Peakall et al. 2007; Oehy and Schleiss 2007; Kane et al. 2010; Strauss and Glinsky 2012; Janocko et al. 2013, and several references cited in Middleton 1993). From these investigations we have gained some insight into the depositional behavior of turbidity currents (Al Ja Aidi 2000), the nature of their secondary flow in channel bends, and their turbulence structure.

The present investigation aims to provide insight into the mechanisms by which turbidity currents interact with three-dimensional seafloor topography. Towards this end, we will focus on the example of a local seamount in the form of a Gaussian bump. We will explore how the topography affects such global properties as the propagation velocity of the current, its sedimentation, the resulting bottom shear stress, and runout length of the currents. In addition, we will analyze the coherent vortical structures of the flow, along with their effect on such quantities as the wall shear stress and the energy budget. Towards this end, we will employ our computational code TURBINS (Nasr-Azadani and Meiburg 2011; Nasr-Azadani 2013) to conduct high-resolution, direct numerical simulations of turbidity currents interacting with three-dimensional Gaussian bumps, cf. Fig. 1. Here, the turbidity currents are generated by the familiar lock-release process. By comparing results for several different bump heights with the flow over a flat surface, we will be able to shed light on how the current/topography interaction mechanisms depend on the bump height. We will present general results regarding the dynamics of compositional gravity currents versus turbidity currents, and concerning the critical bump height, beyond which the current is forced to go *around* the bump rather than *over* it.

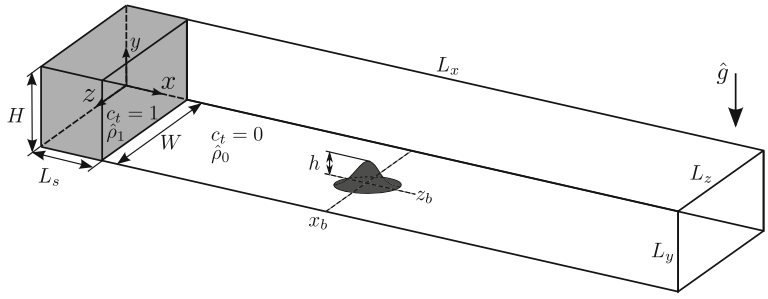

Fig. 1 Initial set-up for a lock-release turbidity current interacting with three-dimensional seafloor topography in the form of a Gaussian bump. The lock contains a bi-disperse suspension. To start the flow, the membrane separating the suspension from the ambient fluid is removed

2 Direct Numerical Simulations of Turbidity Currents

2.1 Problem Description and Modeling Approach

The modeling approach and governing equations are described in depth by Necker et al. (2002) and Nasr-Azadani and Meiburg (2011), so that a brief summary suffices here. We employ the Navier-Stokes equations in the Boussinesq approximation to model dilute suspensions with typical particle volume fractions of $O(1\%)$ or less

$$\nabla \cdot \mathbf{u} = 0\,, \tag{1}$$

$$\frac{\partial \mathbf{u}}{\partial t} + \mathbf{u} \cdot \nabla \mathbf{u} = -\nabla p + \frac{1}{Re}\nabla^2 \mathbf{u} + c_t \mathbf{e}^g\,. \tag{2}$$

In the above equations, the nondimensional quantities $\mathbf{u}$, p and c_t represent the fluid velocity, pressure and the total particle concentration (volume fraction), respectively. Moreover, $\mathbf{e}^g$ represents the unit vector in the direction of gravity. The Reynolds number Re is defined as

$$Re = \frac{\hat{u}_b \hat{H}/2}{\hat{\nu}}\,, \tag{3}$$

with $\hat{\nu}$, $\hat{H}$, and $\hat{u}_b$ representing the kinematic viscosity, lock height (see Fig. 1), and buoyancy velocity

$$\hat{u}_b = \sqrt{\frac{\hat{H}}{2}\frac{(\hat{\rho}_p - \hat{\rho}_0)C_r}{\hat{\rho}_0}\hat{g}}\,, \tag{4}$$

respectively. Here, the symbol $\hat{}$ refers to a dimensional quantity, whereas symbols without this sign indicate dimensionless quantities. C_r, $\hat{\rho}_p$, and $\hat{\rho}_0$ represent, respectively, the initial particle volume fraction within the lock, the density of the particle

material, and the ambient fluid density. In the above, the half-height of the lock $\hat{H}/2$ and the buoyancy velocity $\hat{u}_b$ serve as characteristic quantities for scaling the flow variables, i.e. $\mathbf{x} = \hat{\mathbf{x}}/(\hat{H}/2)$, $\mathbf{u} = \hat{\mathbf{u}}/\hat{u}_b$, and $p = \hat{p}/(\hat{\rho}_0 \hat{u}_b^2)$.

By assuming a dilute suspension of small particles, we can neglect particle inertia and particle-particle interactions. Hence, the particles are assumed to move with the fluid velocity plus the Stokes settling velocity

$$\hat{u}_s = \frac{\hat{d}_p^2(\hat{\rho}_p - \hat{\rho})\hat{g}}{18\hat{\mu}}\,, \tag{5}$$

acting in direction of gravity, cf. Dietrich (1982).

The suspension contains two different particle sizes with identical particle material density $\hat{\rho}_p$. For the i-th particle size ($i = 1, 2$), we define a continuum concentration field $c_i(\mathbf{x}, t)$. Each concentration field is then evolved in an Eulerian manner by

$$\frac{\partial c_i}{\partial t} + \left(\mathbf{u} + u_s^i \mathbf{e}^g\right) \cdot \nabla c_i = \frac{1}{ReSc_i} \nabla^2 c_i\,, \qquad i = 1\,,2\,. \tag{6}$$

Here, u_s^i and Sc_i denote the i-th particle settling speed and Schmidt number

$$Sc_i = \frac{\hat{\nu}}{\hat{\kappa}_i}\,, \qquad i = 1\,,2\,, \tag{7}$$

respectively. In Eq. (7), $\hat{\kappa}_i$ represents the diffusion coefficient associated with the i-th concentration field. Since for $Sc \geq O(1)$ the Schmidt number has a negligible effect on the dynamics of the flow (Härtel et al. 2000b), we set all Sc_i to unity. We assign a nondimensional particle settling speed u_s^i to each particle concentration field, respectively. These values can be translated back into dimensional settling velocities via Eq. (5). In the present investigation, we employ dimensionless settling velocities of $u_s^1 = 0.03$ (coarse particles) and $u_s^2 = 0.006$ (fine particles), and initial relative mass fractions of 50% each.

The particle concentration fields C_i are scaled with the total initial volume fraction of the particles in the lock C_r, i.e.

$$c_i = \frac{C_i}{C_r}\,, \qquad i = 1\,,2\,. \tag{8}$$

Given the above definition, the total concentration c_t (see Eq. 2) at any location can be obtained by adding all of the concentration fields c_i

$$c_t = \sum_{i=1}^{2} c_i\,. \tag{9}$$

Thus, at time $t = 0$, c_t varies between 0 in the ambient fluid and 1 in the lock region.

The computational domain size is $L_x \times L_y \times L_z = 38 \times 2 \times 3$, and the lock has dimensions $L_s \times H \times W = 1 \times 2 \times 3$ (see Fig. 1). No-slip conditions are imposed everywhere along the boundaries except for the top ($y = L_y$) and side walls ($z = 0, L_z$), where free-slip conditions are employed. To solve for the concentration fields, we implement no-flux boundary conditions at the upstream, downstream, top and side walls, respectively

$$\begin{cases} \frac{\partial c_i}{\partial x} = 0 & x = 0\,, L_x \\ \frac{\partial c_i}{\partial z} = 0 & z = 0\,, L_z \qquad i = 1\,, 2\,. \\ c_i u_s^i + \frac{1}{Sc_i\, Re} \cdot \frac{\partial c_i}{\partial y} = 0 & y = L_y \end{cases} \tag{10}$$

Along the bottom boundary, we enforce a vanishing normal derivative of the concentration field

$$\mathbf{n} \cdot \nabla c_i = 0\,, \qquad y = \Gamma(x, z) \qquad i = 1\,, 2\,. \tag{11}$$

Here, Γ and $\mathbf{n}$ denote the bottom surface height and the unit normal vector on the bottom surface pointing toward the fluid region, respectively. We remark that at the bottom, the particles leave the computational domain freely with a constant settling speed u_s^i in the direction of gravity. Moreover, we assume that the deposit layer height is small, so that it does not alter the bottom surface height throughout the simulation. In the current investigation, we do not account for any incipient motion of settled particles in the form of bedload transport and/or erosion and resuspension of particles back into the current (Garcia and Parker 1993; Blanchette et al. 2005). In all simulations, the fluid initially is at rest. The particle concentration is set to unity within the lock, and to zero outside. The interface between the suspension and ambient fluid initially is smoothed over three to four grid intervals, in order to avoid any spurious oscillations.

We conduct four main simulations. The first three have identical lock dimensions and suspension properties, but different bottom topographies. Simulation B1 includes a shallow bump, simulation B2 a tall bump, and simulation FL a flat bottom for comparison purposes. Furthermore, in order to gain insight into the difference between compositional gravity currents and turbidity currents, we carry out a fourth simulation B2-GC, which is identical to B2, except that the settling velocity is set to zero. Table 1 summarizes the parameter values employed in these simulations. Additional parametric simulations for different bump heights, Reynolds numbers and control volume widths will be referred to in more detail in the relevant sections.

The surface shapes of the bumps in simulations B1, B2 and B2-GC are given by

$$\Gamma(x, z) = h \exp\left(-\frac{(x - x_b)^2 + (z - z_b)^2}{2\epsilon^2}\right). \tag{12}$$

Table 1 Parameter sets of the four main simulations. For all simulations the Reynolds number is $Re = 2 \times 10^3$, h is the bump height, and the number of grid points is (N_x, N_y, N_z). The domain size is given by $L_x \times L_y \times L_z$ and the lock dimensions are given by (L_s, H, W)

Name	Shape	h	(N_x, N_y, N_z)	$L_x \times L_y \times L_z$	(L_s, H, W)
FL	Flat	0	(1545, 184, 250)	$38 \times 2 \times 3$	(1, 2, 3)
B1	Bump	0.25	(1645, 195, 362)	$38 \times 2 \times 3$	(1, 2, 3)
B2	Bump	0.5	(1645, 215, 362)	$38 \times 2 \times 3$	(1, 2, 3)
B2-GC	Bump	0.5	(1645, 215, 362)	$38 \times 2 \times 3$	(1, 2, 3)

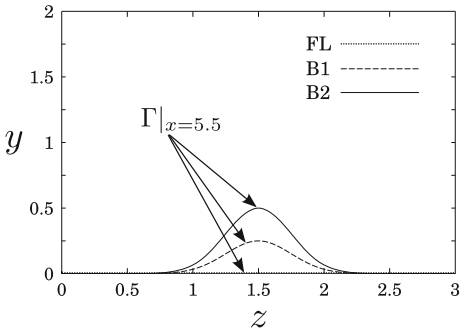

Fig. 2 Cross sections of the *bottom* topography (Γ) in simulations FL, B1, and B2, corresponding to a flat *bottom*, and bump heights equal to $h = 0.25$ and $h = 0.5$, respectively. The y, z-plane is shown at the streamwise location of the bump's peak, $x = 5.5$

The center of the Gaussian bump is located at $(x_b, z_b) = (5.5, 1.5)$ (see Fig. 1) and the width parameter ϵ of the bump is set to $\epsilon = 0.25$. The bump height h is 0.25 for B1, and 0.5 for B2 and B2-GC, cf. Fig. 2.

2.2 *Numerical Method*

Since a detailed description of the numerical method is given by Nasr-Azadani and Meiburg (2011) and Nasr-Azadani (2013), we provide only a brief summary here. The momentum equations are solved using a projection method (Chorin 1968) in conjunction with the fractional step method (Kim and Moin 1985), on a MAC-staggered grid. We employ a fully implicit central differencing method to discretize the viscous and diffusion terms in the momentum and transport equations, while the convective terms are discretized via an explicit third-order Essentially Non-Oscillatory (ENO) scheme (Harten et al. 1987). The time integration for the transport and momentum equations is performed via a second-order Total Variation Diminishing Runge-Kutta method (TVD-RK2, cf. Harten 1997). The boundary conditions along the bottom topography are implemented via an immersed boundary method with direct forcing

(Mohd-Yusof 1997; Mittal et al. 2008). Validation results, with a focus on accurate wall shear stress data, are presented in Nasr-Azadani and Meiburg (2011) and Nasr-Azadani (2013), and comparisons with experiments are described in Nasr-Azadani et al. (2013).

We employ a nonuniform structured Cartesian grid in all three directions, (Vinokur 1983). In the x-direction and in the vicinity of the bump, the grid is uniform with the spacing $\Delta x = 0.0067$. Away from the bump, the grid is smoothly stretched to values $\Delta x = 0.02$ for $0 \leq x \leq 2$, and to $\Delta x = 0.04$ for $18 \leq x$. In the y-direction, the minimal spacing $\Delta y = 0.0055$ (B1: $0 \leq y \leq 0.3$ and B2 and B2-GC: $0 \leq y \leq 0.55$) is smoothly stretched to the maximum value of $\Delta y = 0.02$ close to the top wall. In the spanwise z-direction, a minimum spacing of $\Delta z = 0.0067$ is used in the vicinity of the bump, and stretched to the maximum value of $\Delta z = 0.014$ close to the lateral boundaries.

The above grid spacing ensures that the first grid point above the bottom surface lies within the viscous sublayer. To check this, we define the dimensionless wall-normal distance of this grid point as

$$\eta_n^+ = \frac{\hat{\eta}_n \hat{u}_\tau}{\hat{\nu}} = \eta_n u_\tau Re\,, \tag{13}$$

where $\hat{u}_\tau$ and $\hat{\eta}_n$ represent the friction velocity and wall-normal distance, respectively. In all three simulations we obtain $\eta_n^+ \approx 1$.

2.3 General Current Properties

Here we compare some of the overall current features for the different bottom topographies, such as their suspended mass as a function of time, their sedimentation rates, and their respective front locations. In addition, we will contrast the dynamics of turbidity current B2 with a corresponding compositional gravity current B2-GC.

We define the suspended mass of particle size i as

$$m_s^i(t) = \int_\Omega c_i \, \mathrm{d}V \qquad i = 1, 2\,, \tag{14}$$

with Ω denoting the computational domain. Figure 3 shows the front location x_f of each current, along with the time history of the suspended mass for each particle size. To determine x_f, we average the total concentration c_t in the spanwise and vertical directions, respectively, so that we obtain a one-dimensional profile $c_f(x)$. The front location is then defined as the farthest downstream location at which c_f exceeds the threshold value of 10^{-3}.

We observe that after a brief initial transient all currents propagate with nearly the same constant velocity. During this stage of the current, which includes the well-studied slumping phase (Huppert and Simpson 1980), the front velocity of the current

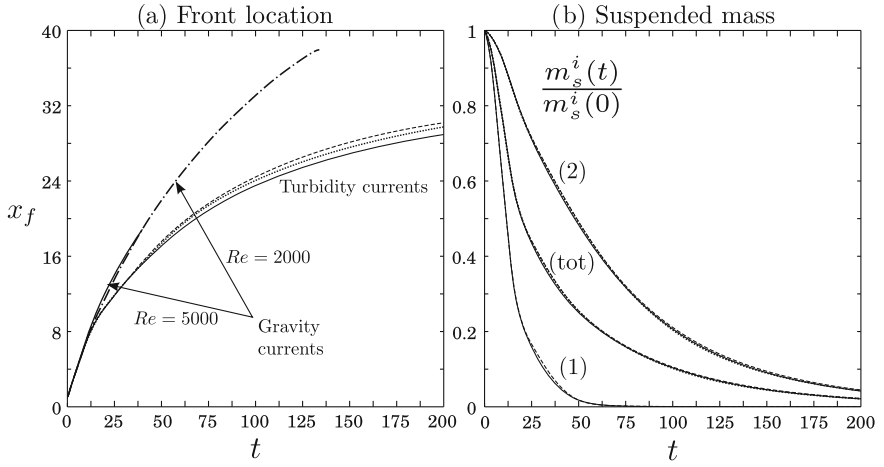

Fig. 3 Temporal evolution of the front location x_f (*left*) and the suspended mass (*right*). *Dots*, *dashed* and *solid lines* represent turbidity currents FL, B1, and B2, respectively. (1), (2), and (tot), respectively, refer to normalized suspended masses of coarse ($u_s^1 = 0.03$), fine ($u_s^2 = 0.006$), and all particles. The bump height has a non-monotonic influence on the *front* location, in that B1 advances faster than FL, whereas B2 propagates more slowly than FL and B1. The *front* location of the compositional gravity current B2-GC at $Re = 2000$ is shown for comparison (*dash-dotted line*), along with the *front* location of a simulation identical to B2-GC except that $Re = 5000$ (*solid line*). The Reynolds number has a negligible effect on the *front* velocity. The *bottom* topography is seen to have only a weak influence on the rate at which the suspended mass decreases with time

is largely independent of the settling velocity. After $t \approx 15$, all three turbidity currents gradually slow down in comparison to the compositional gravity currents, since they increasingly lose suspended particles, so that their driving force diminishes. For all of the turbidity currents, at $t = 20$ only about 50% of the particle mass is still in suspension. While the presence of the obstacles does not have a significant influence on the mass of the suspended particles, the front location of the turbidity currents displays an interesting non-monotonic behavior: current B1 over the small bump moves faster than current FL over the flat substrate; however, a further increase in the bump height to B2 results in a current that is slower than both B1 and FL. We will further explore the reasons for this non-monotonic behavior below, in the context of discussing the effective current heights and dissipation rates for each of the currents.

Figure 4 shows the time history of the sedimentation rate on the bottom surface $\dot{m}_d(t)$, defined as the time derivative of the suspended particle mass. For each particle size

$$\dot{m}_d^i = -\int_A u_s^i c_w^i \mathbf{e}^g \cdot \mathbf{n} \, \mathrm{d}A \qquad i = 1, 2\,. \tag{15}$$

Here, c_w denotes the particle concentration at the bottom wall, and A represents the bottom surface area.

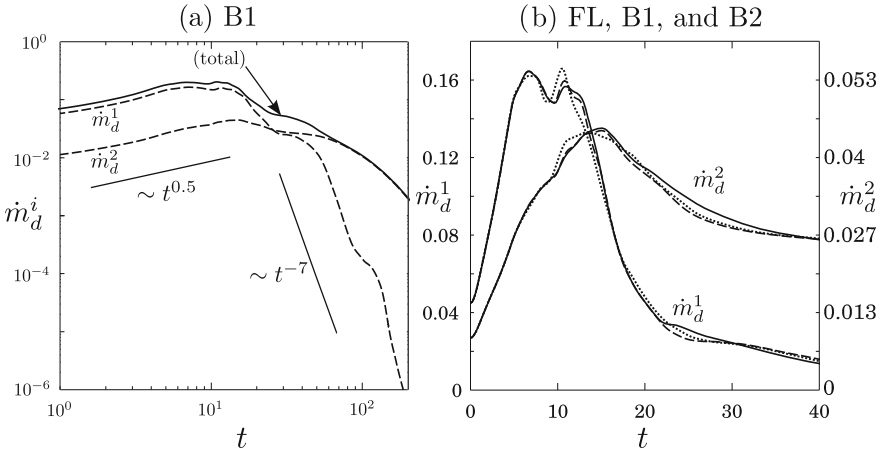

Fig. 4 Time history of particle sedimentation rate for coarse ($\dot{m}_d^1$) and fine ($\dot{m}_d^2$) particles. **a** Case B1 shown on a logarithmic scale. **b** Comparison of all cases, where *dotted*, *dashed* and *solid lines* represent cases FL, B1, and B2, respectively

Both particle sizes experience two distinctly different stages. During the first stage, the sedimentation rate can be approximated by a power law in the form of $\dot{m}_d^i(t) \sim t^{0.5}$. This is consistent with the observation by Necker et al. (2002) for a mono-disperse current with a particle settling speed of $u_s = 0.02$ propagating over a flat wall. Equation (15) indicates that, for a current with constant concentration along the bottom wall, the sedimentation rate would be proportional to the bottom surface area covered by the current. Since the front velocity is nearly constant during the early stage, this would result in a linear increase of the sedimentation rate with time. Hence, the observed exponent of 0.5 must be due to variations in the particle concentration along the bottom surface as a result of mixing, or as a result of the bore that is reflected from the back wall of the lock region.

Figure 5 verifies the above scenario for the early stages of the flow. On one hand, the particle concentration at the bottom wall is reduced in the vicinity of the nose region due to the thin layer of ambient fluid that is overrun by the current front as a result of the no-slip condition at the bottom wall. In addition, as the bore reflected from the left wall propagates forward, it reduces the particle concentration at the wall in the tail section of the current. Hence, for longer or deeply submerged locks, or for slip conditions along the bottom wall, we would expect to see a different dependence of the sedimentation rate on time (Necker et al. 2005).

After $t \approx 15$, the turbidity currents undergo the aforementioned deceleration. We note that this time corresponds approximately to the peak sedimentation rate. In addition to losing suspended particles, the currents are being diluted as ambient fluid is entrained via turbulent mixing. This phase coincides with a dramatic change in the sedimentation rate for both particle sizes. The rate at which the coarse particles sediment out decreases rapidly, following a power law exponent of approximately

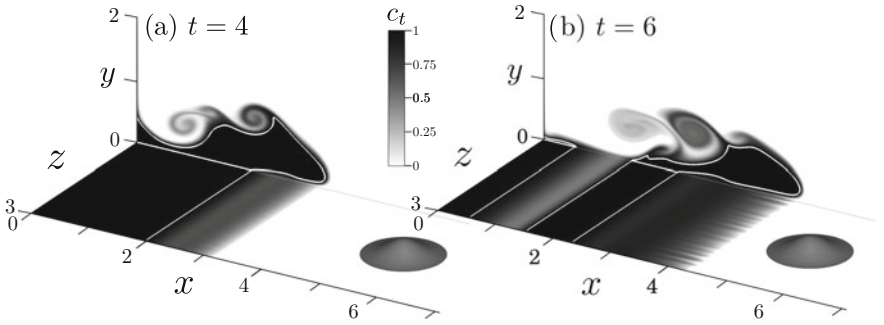

Fig. 5 Temporal evolution of the concentration (c_t) along the *bottom* wall during the initial sedimentation phase for case B1. The *vertical plane* depicts the concentration profile in the centerplane $z = 1.5$. The *white lines* represent the $c_t = 0.95$ contour. We find that the particle concentration at the *bottom* wall is reduced by the thin layer of ambient fluid overrun by the current *front*, and by the bore reflected from the *back* wall of the lock

$n = -7$. This compares with a value of $n = -2.4$ observed by Necker et al. (2002) for a monodisperse current with $u_s = 0.02$, which suggests that the sedimentation rate during the deceleration phase is a function of the particle settling speed. Furthermore, we note that the non-linear coupling between different particle sizes will also influence the temporal decay of the sedimentation rate, as discussed by Gladstone et al. (1998) and Harris et al. (2002).

For fine particles, on the other hand, the sedimentation rate does not follow a power law during this phase. Beyond $t = 50$ nearly all of the coarse particles have settled out, so that the total sedimentation rate follows that of the fine particles. Figure 4b compares the respective sedimentation rates for the FL, B1 and B2 cases. We find that the bottom topography has a very weak influence on the rate at which the particles settle out.

Figure 6 compares the current heights of flows B2 and B2-GC at different times. To compute the current height, we integrate the spanwise averaged concentration field in the y-direction. We note that a variety of current height measures have been employed in the past, such as the current moment (cf. Ellison and Turner 1959), the half height of the lock (cf. Shin et al. 2004), and the depth-integrated density profile (cf. Birman et al. 2005). Upon arrival of the current at the bump location, both cases demonstrate very similar current height profiles. Beyond this stage, however, the turbidity current experiences a more pronounced deceleration, while the frontal region of the compositional gravity current maintains a thicker profile, which accounts for its larger sustained front velocity.

In summary, we find that the influence of bottom topography on the front velocity of turbidity currents is much weaker than the influence of the particle settling velocity. The effect of the bump height on the current velocity is nonmonotonic, so that the current interacting with a bump of intermediate height advances more rapidly than its counterparts propagating over a flat bottom or interacting with a tall bump. All turbidity currents begin to decelerate appreciably sometime after having interacted

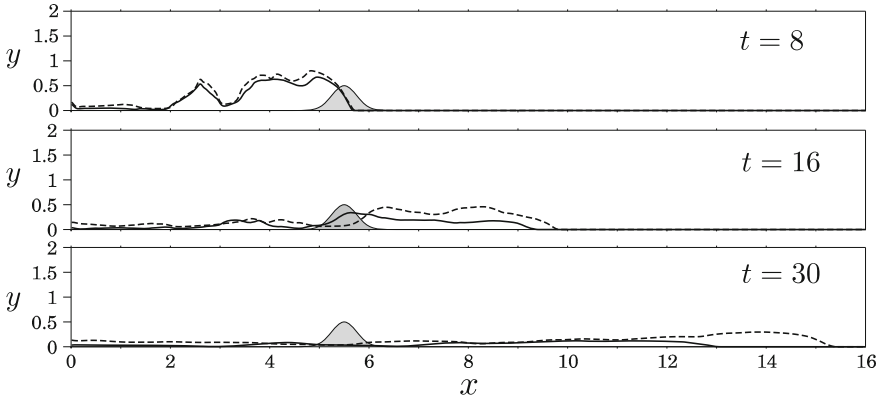

Fig. 6 Current height for cases B2 (*solid line*) and B2-GC (*dashed line*), at three different times. After interacting with the bump, the *front* of the compositional gravity current B2-GC maintains a larger height, and thus travels faster

with the bump. A corresponding compositional gravity current, on the other hand, is able to maintain a substantially higher front velocity for longer times.

2.4 Structure of the Current

The erosional and depositional nature of turbidity currents is dominated by their large-scale vortices. Hence, in this section we focus on characterizing these vortical structures, and on how their evolution is affected by the bottom topography. We furthermore compare currents propagating *over* small bumps with those flowing *around* larger bumps, and we derive scaling arguments for the critical bump height that separates these two parameter regimes. We subsequently validate this scaling law by analyzing particle path lines for currents interacting with bumps of different heights. We furthermore compare the vortical and lobe-and-cleft structures for currents of two different Reynolds numbers, and we assess the influence of the lateral domain boundaries by contrasting two simulations for different computational domain widths.

Figure 7 illustrates the temporal evolution of turbidity current B1 by visualizing the $c = 0.1$ contours of the coarse and fine particle concentration fields, respectively. During the initial phase, the flow is dominated by a pair of spanwise startup vortices (Härtel et al. 2000b), although a noticeable lobe-and-cleft instability is emerging after $t = 6$. Around $t = 8$, the current head encounters the obstacle and experiences some lateral deflection. We note that, during these early stages, the concentration fields of the coarse and fine particles are quite similar. Over long times, however, we expect the different settling velocities of the coarse and fine particles to result in major discrepancies. This is confirmed by the frames for $t = 16$, which show that

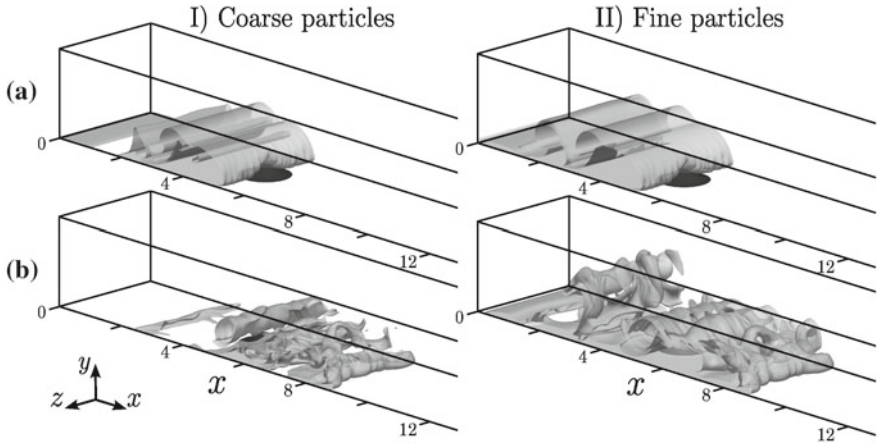

Fig. 7 Temporal evolution of the turbidity current produced by a lock release flow passing over a Gaussian bump (case B1). The $c = 0.1$ isosurfaces of the particle concentration fields are shown for the coarse (*left column*) and fine particles (*right column*), respectively. From *top* to *bottom*, times are 8 and 16

many of the coarse particles have already settled out, while most of the fine particles remain in suspension.

Figure 8 compares the structure of the B1 and B2 currents as they encounter the obstacle, with the FL current at the same time. While the front of FL is dominated by the lobe-and-cleft instability (Simpson 1972; Härtel et al. 2000a), B1 and B2 are noticeably influenced by the obstacle. However, while B1 primarily *passes over* the bump, the front of B2 is bisected by the bump, so that it mostly *flows around* it. Hence, at $t = 12$, the front of B1 resembles the FL case again, while B2 still exhibits a strong wake effect.

The different front dynamics of B1 and B2 are clearly visible in Fig. 9, which shows the concentration field in the plane $x = 5.5$, along with the v- and w-velocity components, for times 8 and 12. During the impact stage at $t = 8$, the front of B1 is seen to flow over the bump, while the taller bump in case B2 bisects the front, deflecting it laterally away from the highest point. The ambient fluid above both currents is deflected upwards at this time. Both fronts exhibit plumes of the lighter, ambient fluid from the overrun boundary layer rising upward from the bottom wall, as a result of the lobe-and-cleft instability. At $t = 12$, both currents plunge downward in the plane $x = 5.5$; however, B2 maintains a bisected front.

The above discussion raises the general question about the limiting bump height that the current is able to travel over, and beyond which it will have to go around the bump. For linearly stratified flows over obstacles, issues such as the existence of dividing streamline, the generation of internal waves and vortex shedding have been the focus of several investigations (Snyder et al. 1985; Smolarkiewicz and Rotunno 1990; Winters and Armi 2012). However, we are not aware of corresponding investigations for transient current fronts interacting with obstacles.

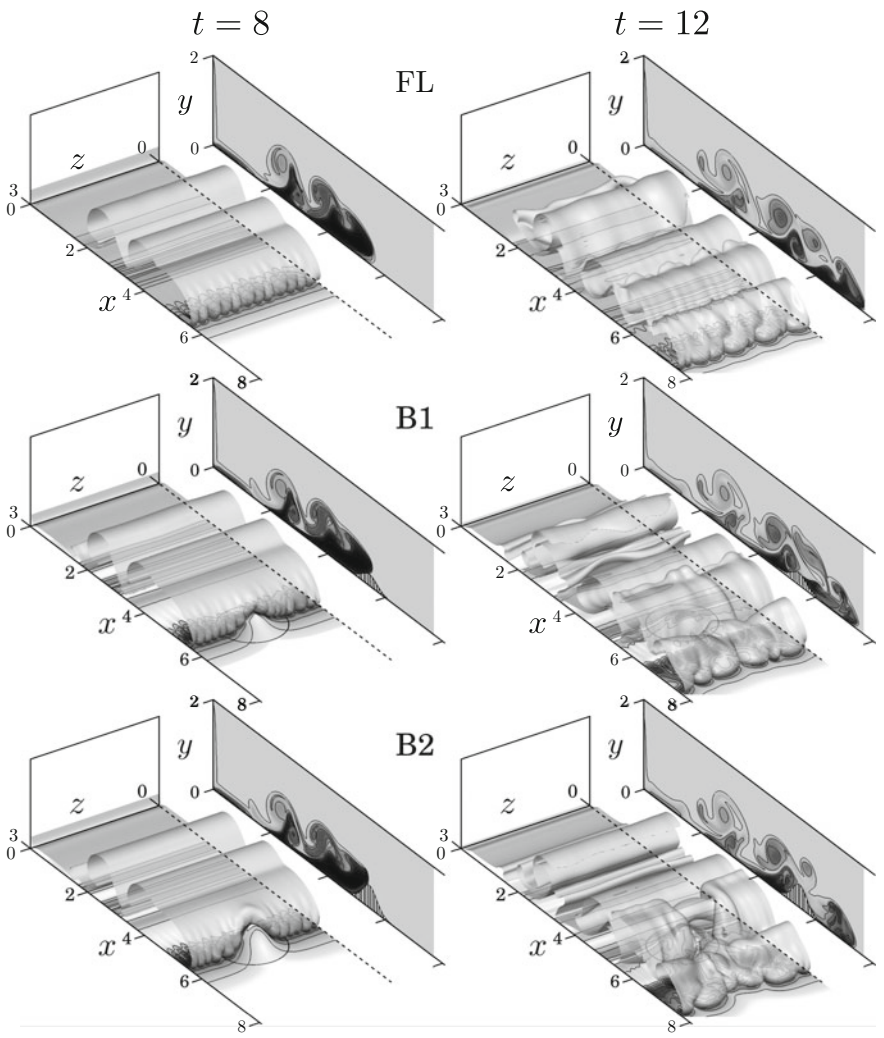

Fig. 8 Development of the current structure for cases FL, B1 and B2, visualized by the concentration contour $c_t = 0.1$. FL is dominated by the growth of lobe-and-cleft structures in the *frontal region*, whereas cases B1 and B2 show a strong influence of the bump. While current B1 primarily flows *over* the *shallow* bump, current B2 mostly flows *around* the taller bump. The shading in the *bottom plane* indicates the magnitude of the wall shear stress, and the *vertical plane* to the *right* depicts the concentration field in the symmetry plane $z = 1.5$

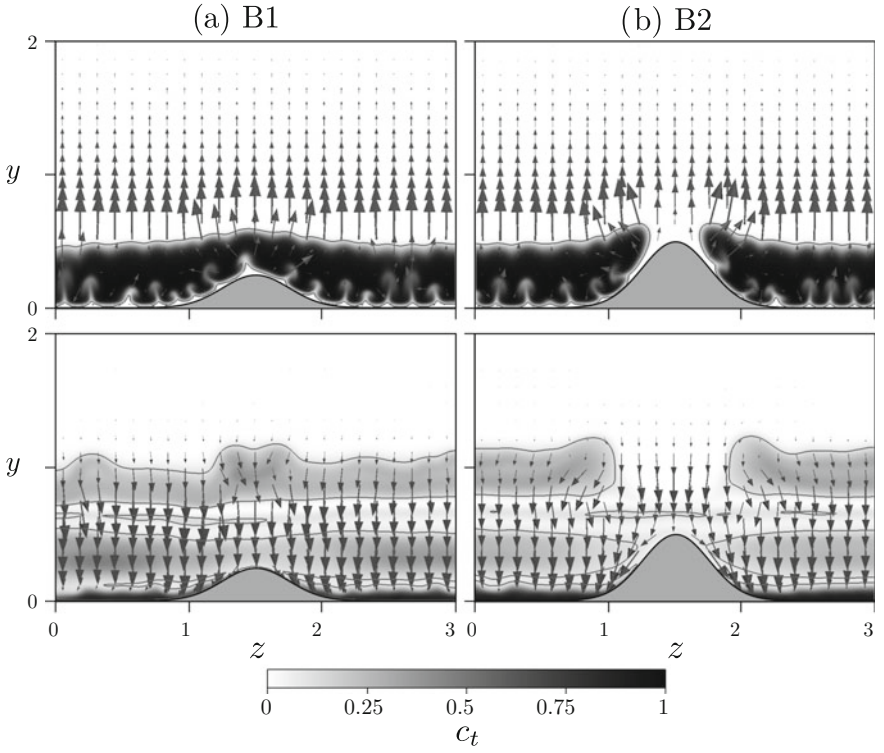

Fig. 9 Evolution of currents B1 and B2 in the plane of the peak of the bump at $x = 5.5$. The *top* row corresponds to $t = 8$, whereas the *bottom* row depicts the currents for $t = 12$. The in-plane v, w-velocity vectors are also shown. The *grey-shading* represents the total concentration field c_t, with the *line* showing the contour $c_t = 0.1$. While B1 passes over the bump, B2 mostly flows around the bump

In the following, we first consider currents with vanishing settling velocities, in order to develop scaling arguments that are independent of this quantity. Due to the relatively high Reynolds numbers and low dissipation rates of the gravity currents under investigation, we can follow the analysis by Snyder et al. (1979), and employ balance arguments for the kinetic and potential energy components in order to assess the currents' capacity to travel *over* an obstacle of a given height. Those authors argue that a heavier fluid layer of thickness $\hat{h}_c$ submerged below a lighter ambient fluid of density ρ_0 can flow over a hill of height $\hat{h}_b$ if

$$\frac{\hat{U}_\infty^2}{\hat{g}\hat{h}_c\Delta\hat{\rho}/\hat{\rho}_0} > 2\left(\frac{\hat{h}_b}{\hat{h}_c} - 1\right) \tag{16}$$

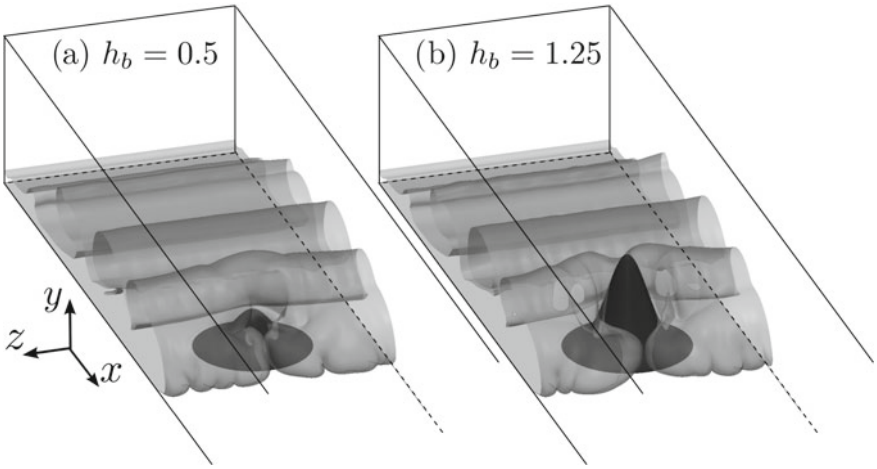

Fig. 10 Isosurface of the concentration field $c = 0.1$ shown for two different bump heights at $t = 10$. The *bottom* section of the current is not able to fully cross over the bump peak for $h_b \gtrsim 0.9$

is satisfied, where $\Delta\hat{\rho}$ denotes the density difference. Here, $\hat{U}_\infty$ represents the upstream velocity of the dense current. Employing the reference variables of the present study, Eq. (16) can be written in dimensionless form as

$$\frac{U_\infty^2}{h_c} = 2\left(\frac{h_b}{h_c} - 1\right). \tag{17}$$

Upon arrival of the current at the bump location ($t \approx 10$), the front velocity is approximately $U_\infty \approx 0.7$, with a current height $h_c \approx 0.7$. Equation (17) then suggests that the lower sections of the current, i.e. the sections above the bottom boundary layer, are able to flow over bumps of height $h_b \lesssim 0.9$.

In order to validate the above scaling law, we conducted a series of simulations for compositional gravity currents interacting with bumps of different heights h_b, cf. Fig. 10. For $h_b = 1.25$ the bump fully bisects the current front, whereas for $h_b = 0.5$ part of the current still manages to flow over the top of the bump. This is confirmed by Fig. 11, which compares the current height computed in the y, z-plane at $x = 5.5$ (corresponding to the bump's peak) for several bump heights. For increasing bump heights we note that, while the current thickness at the peak of the bump decreases, it increases away from the bump.

To further investigate the dynamics of different vertical current sections during the interaction with the obstacle, fluid path lines for passive markers are shown in Fig. 12. These markers are initially located at $y = 0.1, 0.3, 0.5$ and 0.7 upstream of the bump at $x = 4.35$ in the symmetry plane at $z = 0.5L_z$. They are released at $t = 7$, and their path lines are integrated until $t = 20$.

The observed particle path lines are seen to be consistent with the above scaling law. For bump heights $h_b \lesssim 0.9$, even particles originating in the near wall region are

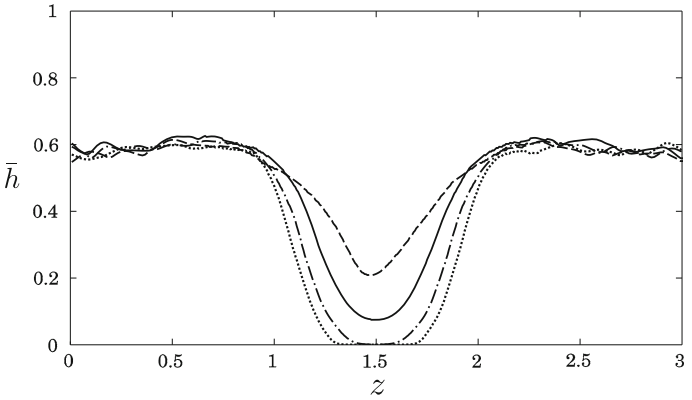

Fig. 11 Comparison of current heights in the plane of the bump peak, for gravity currents interacting with bumps of different heights. *Dashed line*, *solid line*, *dash-dots*, and *dots* correspond to bump heights of $h_b = 0.5$, 0.75, 1.0 and 1.25, respectively. The current height is averaged over the time interval from $t = 8$ to $t = 12$.

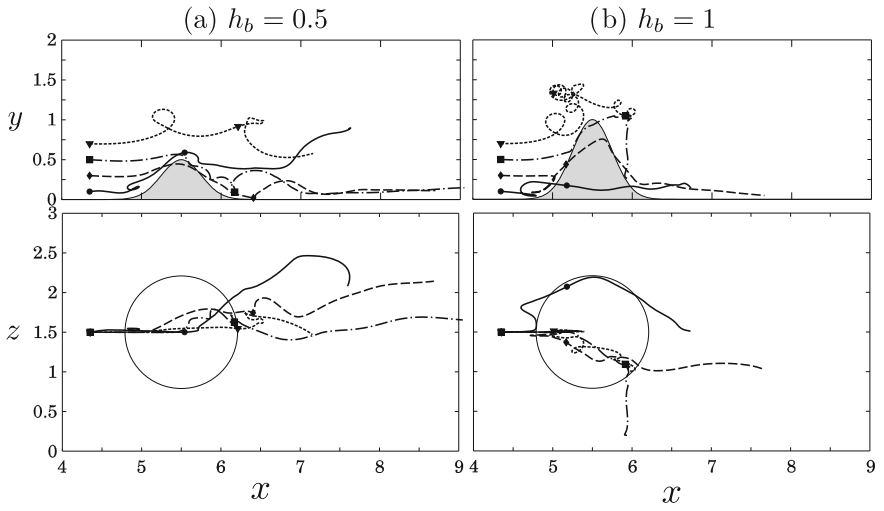

Fig. 12 Fluid path lines for gravity currents interacting with Gaussian bumps of different heights. The fluid marker particles are released at $x = 4.35$ (in the symmetry plane $z = 1.5$) and time $t = 7$, and their locations are shown for times $t = 7$, 13 and 20. For $h_b = 1$, the fluid marker particles in the lower current sections are seen to flow around the bump rather than over it, consistent with the scaling law (see Eq. (17))

seen to be lifted over the top of the bump. On the other hand, for $h_b = 1.0$ the marker released at $y = 0.1$ travels around the bump, rather than over it. We furthermore observe that fluid marker particles released near the top of the current experience strong recirculating motion, indicative of the concentrated vortical structures forming in the mixing layer between the current and the ambient.

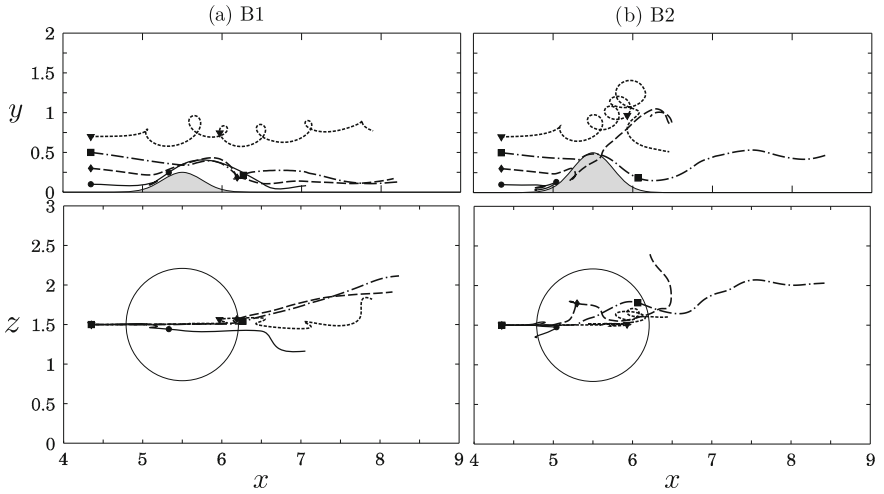

Fig. 13 Fluid path lines shown for turbidity currents B1 and B2. Four seed markers released at $t = 7$ and $x = 4.35$ (in the symmetry plane $z = 1.5$) follow the fluid velocity until $t = 20$. The markers are also shown at time $t = 13$, indicating that the lowest marker is able to flow over the peak of the bump only for case B1, but not for case B2

In order to analyze how the above observations for compositional gravity currents are modified due to the presence of a settling velocity, Fig. 13 compares fluid path lines for turbidity currents B1 and B2, for the same initial marker positions as before. Unlike for the compositional gravity current case B2-GC, the lowest marker for turbidity current B2 does not advance over the peak of the bump. This is a consequence of the lower height h_c (see Eq. (17)) of turbidity current B2 as compared to gravity current B2-GC. In addition, the energy loss of the turbidity current due to the Stokes dissipation in the small-scale flow around the particles lowers the current's capacity to travel over the obstacle. This will be analyzed in further detail below, within the context of the energy budget discussion. We conclude that, for a given current height and velocity, the scaling law (17) represents an accurate criterion for compositional gravity currents, whereas it serves as an upper limit for turbidity currents.

When comparing the uppermost fluid path lines for gravity and turbidity currents interacting with bumps of various heights in Figs. 12 and 13, we recognize a stronger recirculating motion for the turbidity currents. This suggests that the turbidity currents give rise to more vigorous mixing of interstitial and ambient fluid, as compared to the gravity currents.

Figure 14 depicts selected in-plane streamlines for case B2 within the symmetry plane $z = 1.5$, in the laboratory reference frame. These indicate that the flow separates from the rear of the bump. However, due to the highly transient nature of the flow, this separation region is very short-lived, and periodic vortex shedding does not occur. The figure furthermore shows the spanwise vorticity component. Strong clockwise vortices exist in the bottom boundary layer. We draw particular attention to the

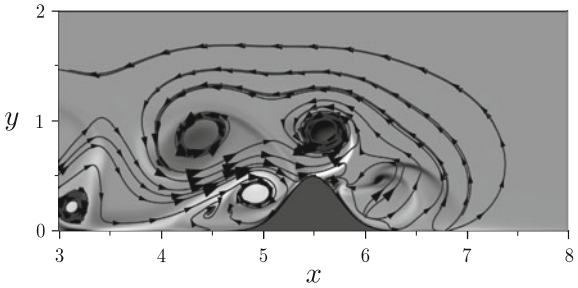

Fig. 14 In-plane streamlines plotted in the symmetry plane $z = 1.5$, at $t = 11$ for case B2. Background shading represents the out-of-plane vorticity component w_z (*black* corresponding to $+15$, *white* to -15, and *gray* to zero). The separation and re-attachment of the front are visible

boundary layer vortex located near $x = 5$, which is just upstream of the bump. As this spanwise vortex is wrapped around the sides of the bump by the flow, it will be stretched in the streamwise direction, thus taking on the familiar structure of a horseshoe vortex (cf. Baker 1980), which is characterized by a downflow region in the wake of the bump. This behavior is well-known from the flow of constant density boundary layers over obstacles (Baker 1978; Doligalski et al. 1994).

At the same time, the mixing layer separating the current from the ambient counterflow above gives rise to counterclockwise Kelvin-Helmholtz vortices (KH) in the spanwise direction. We expect the interaction of these spanwise vortices with the bump to result in the formation of streamwise vorticity as well. If the section of the KH vortex above the bump slows down compared to neighboring sections, the resulting streamwise vorticity should be opposite in sign to that of the traditional horseshoe vortex, i.e., it should lead to an upflow region in the center of the bump's wake. Conversely, if the KH vortex is accelerated above the bump, it should result in the formation of streamwise vorticity of the same sign as that of the horseshoe vortex.

This scenario is confirmed by Fig. 15, which shows the streamwise vorticity along with the v- and w-velocity components for case B2 within two different $x = const.$ planes. At $x = 5.5$ we observe two strong coherent vortical structures adjacent to the sides of the bump. Their sign, with a downwash region at the center, is consistent with that of a classical horseshoe vortex formed from the boundary layer vorticity (Doligalski et al. 1994). At $x = 5.9$, on the other hand, we find that a counterrotating streamwise vortex pair of the opposite sign dominates the near wall region, i.e., with an upwash region at the wake center. This streamwise vortex pair likely originated from the mixing layer at the top of the turbidity current.

We must keep in mind, however, that in addition to the convection, diffusion and stretching of vorticity we also have baroclinic vorticity production, as a result of the density difference between the current and the ambient. This mechanism most likely is responsible for the formation of the smaller, concentrated streamwise vortices visible at the top of the interface at $x = 5.9$.

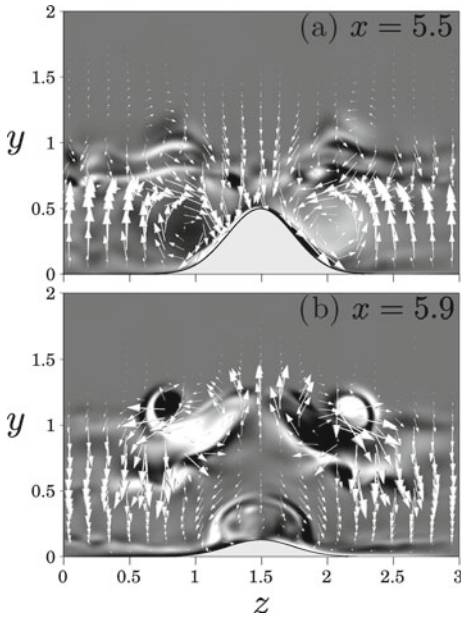

Fig. 15 Streamwise vortical structure of current B2, illustrated by in-plane velocity vectors and the out-of-plane streamwise vorticity component ω_x (*black* +8, *white* −8, and *grey* 0), at $t = 13$. The flow in the plane $x = 5.5$ is dominated by a traditional horseshoe vortex with a downwash at the *center*, whereas a streamwise vortex pair of the opposite sign dominates plane $x = 5.9$. This vortex pair is likely created by the deformation of mixing layer vorticity

2.5 Fate of Particles

In this section, we will address the fate of the particles as function of their initial location within the lock region. This will allow us to determine if particles originating near a certain location within the lock will preferentially settle out in specific regions.

Towards this end, we divide the lock into five subvolumes of equal size. Each subvolume j contains an equal number of Lagrangian markers ($M_j = 9600$) which track the fine (or coarse) sediment particles. Figure 16 shows the initial configuration. Throughout the current's evolution, we then track the $M = 48,000$ Lagrangian markers individually, in order to record their motion and, eventually, their deposit locations. For each particle size, this is accomplished by advancing the Lagrangian markers with the fluid velocity plus the corresponding particle settling velocity, i.e.

$$\frac{\mathrm{d}\mathbf{x}^k(t)}{\mathrm{d}t} = \mathbf{u} + u_s^i \mathbf{e}^g \qquad k = 1\,,\,\ldots\,,M\,. \tag{18}$$

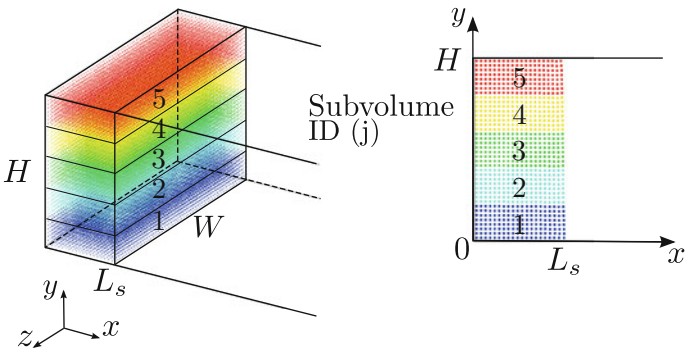

Fig. 16 Schematic of Lagrangian markers employed to represent the coarse and fine sediment particles in the FL and B2 simulations. The lock is divided into 5 equal subvolumes, each containing 9600 equally-spaced markers

The time integration for the Lagrangian marker motion is performed as a separate post-processing step via a second-order Runge-Kutta method with a time step $\Delta t = 0.2$. In order to validate the particle tracking procedure, we now compare the final deposit profiles obtained by the Lagrangian markers against the ones obtained using an Eulerian description of particles, where continuum concentration fields for both fine and coarse particles were integrated (see also Nasr-Azadani and Meiburg 2014). To conduct this comparison, we need to transform the marker particle population along the bottom surface into a continuum deposit height. This is accomplished by spreading the influence of each Lagrangian point marker particle over a finite region. In the past, several approaches along similar lines have been implemented, cf. Elghobashi and Truesdell (1993), Maxey et al. (1997), Meiburg et al. (2000), and Necker et al. (2005). Here, we adopt the method proposed by Necker et al. (2005), which defines a continuous shape function $s(r)$ for each individual marker particle k as

$$s_k(r_k) = \begin{cases} \frac{1}{\sigma_k^2 \sqrt{\pi}} \exp\left[-(r_k/\sigma_k)^2\right] & \text{if } r_k \leq 5\sigma_k\,, \\ 0 & \text{if } r_k > 5\sigma_k\,, \end{cases} \tag{19}$$

where $r_k = |\mathbf{x} - \mathbf{x}_k|$ represents the distance between the particle location and the grid location where its influence is to be evaluated. The parameter σ_k controls the domain of influence for each marker particle. In the following, we choose σ for each Lagrangian marker separately, as twice the distance between the current marker particle and its third nearest neighbor, with a minimum threshold equal to the local grid size.

The deposit height belonging to subvolume j and particle size i is then defined as

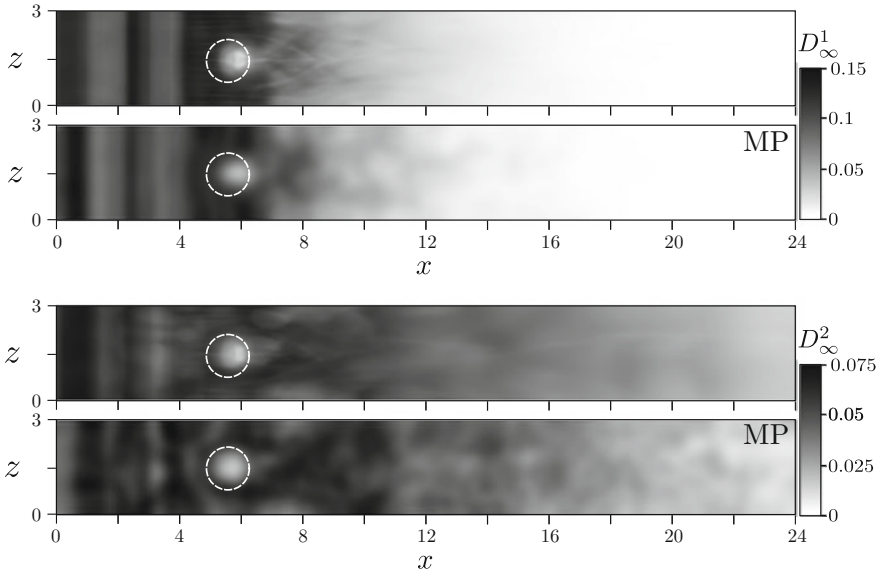

Fig. 17 Final deposit profiles for case B2, for coarse (*top*) and fine (*bottom*) particles, obtained by the continuum concentration field and the Lagrangian marker approach (MP), respectively. For the sake of comparison, the population of Lagrangian markers is translated into a continuum field, as described in the text. The runout length, maxima and minima, and various regions are reproduced to a good approximation by the Lagrangian markers deposit profiles

$$D^i_j(\mathbf{x}) = \frac{m^i_s(0)}{5}\left(\frac{1}{M}\sum_{k=1}^{M_j} s_k(r_k)\right) \qquad i = 1\,,2 \quad j = 1\,,\ \ldots\,,5\,, \tag{20}$$

With this definition, the integral of the deposit height for each subvolume, D^i_j, is equal to total initial mass of the i-th particle size within that subvolume j, i.e., $m^i_s(0)/5$, see Fig. 16.

Figure 17 compares the final Lagrangian deposit profiles for fine and coarse particles with the continuum results for case B2. The large scale features of the continuum results are reproduced to a good approximation by the Lagrangian marker approach, although differences are noticeable at the smaller scales. Figure 18 depicts the temporal evolution of the marker particles following the fine particles for case B2. During the initial stage ($t = 4$), the influence of the two-dimensional start-up vortices can be seen to dominate the motion of the particles. The marker particles originating from the top layer, i.e. subvolume 5, are trapped and advected along with the motion of these vortices (for a detailed study of these vortices, see Härtel et al. 1999). After the current arrives at the bump ($t = 8$), its nose region contains mainly marker particles originating from subvolumes 2 and 3. This is a consequence of the higher streamwise velocity within the core region of the current, away from the boundary layer at its bottom and the mixing layer at its top. After the current has passed the

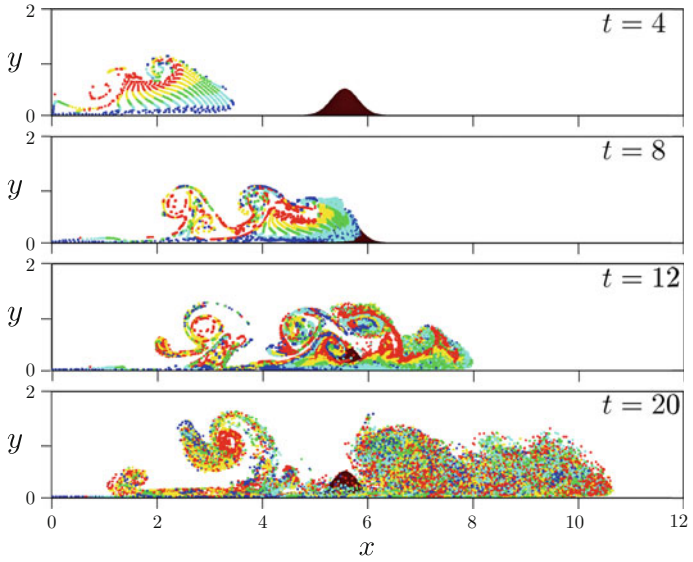

Fig. 18 Temporal evolution of the Lagrangian markers representing the fine particle ($u_s^2 = 0.006$) in case B2. The colors represent each subvolume (see Fig. 16). The fine particles are seen to be thoroughly mixed during the later stages of the current evolution

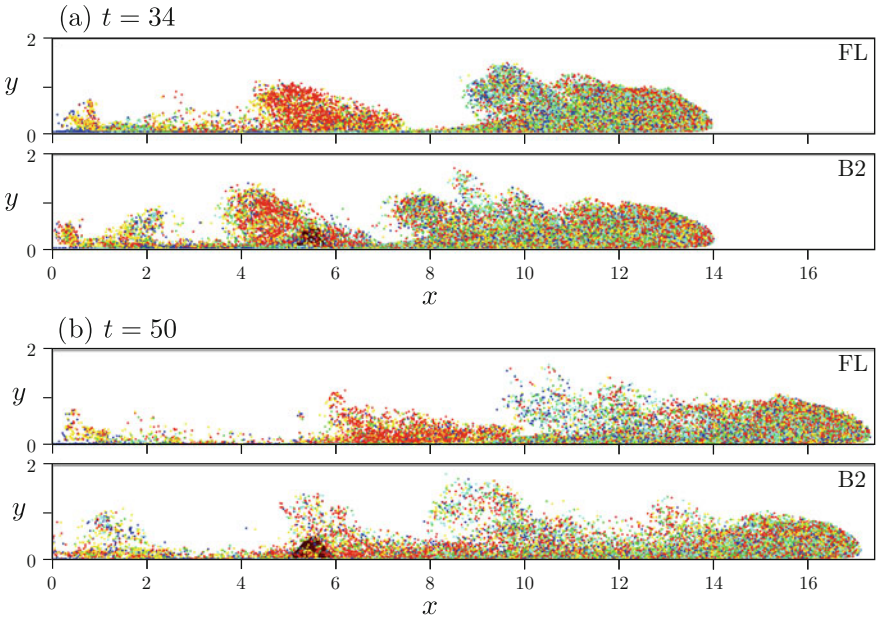

Fig. 19 Evolution of markers tracking the fine particles in cases FL and B2. During the later stages, the *red* particles from the uppermost subvolume accumulate predominantly in the tail section of the currents. The nose sections, on the other hand, are well mixed

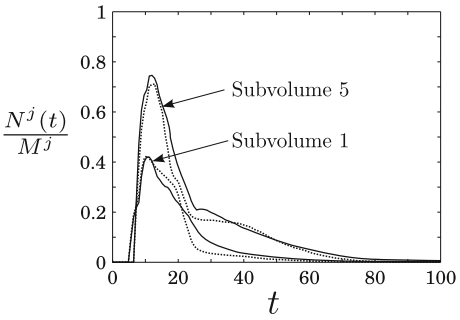

Fig. 20 Temporal history of particle population computed in the domain neighboring the obstacle, normalized by the initial number of particles belonging to the *top* ($j = 5$) and *bottom* ($j = 1$) subvolumes. *Dotted* and *solid lines* represent cases FL and B2, respectively. The obstacle in case B2 keeps the particles in suspension for longer periods due to enhanced mixing properties

obstacle ($t = 12$), the strongly three-dimensional structure of the flow results in the vigorous mixing of the particles, so that we observe a fairly uniform and well-mixed distribution in the bulk of the current at late times ($t = 20$).

Figure 19 compares the evolution of the markers following the fine particles for cases FL and B2. For both cases, we observe that fine particles in the bulk of the current and close to the nose region are well mixed. Also, in both flows the red particles originating from the uppermost subvolume tend to accumulate in the tail sections of the currents. This trend is more pronounced in case B2.

To quantify the influence of the obstacle on the population of fine particles, we count the number of fine particles in suspension, contained within the region neighboring the bump, from $x = 4$ to $x = 8$. Figure 20 compares the temporal evolution of N_j computed for the bottom and top subvolumes normalized by the initial number of particles within each subvolume M_j. The obstacle in case B2 keeps the particles belonging to top and bottom subvolumes in suspension for longer times, as compared to case FL. Furthermore, we remark that only half of the particles belonging to the bottom subvolume are in suspension in the region in the vicinity of the obstacle.

Figure 21 depicts the final deposit profiles of the coarse particles from the lowest ($j = 1$), central ($j = 3$) and uppermost ($j = 5$) subvolumes for cases FL and B2. Most of the coarse particles from the lowest subvolume are seen to settle out very early, although some are transported well past the bump. Those coarse particles initially located in the middle and top subvolumes on average travel comparable streamwise distances. Interestingly, in case B2, those coarse particles from the lowest subvolume that travel past the bump tend to be deposited closer to the lateral boundaries of the domain, whereas the coarse particles originating from the middle and top subvolumes tend to accumulate near the centerline of the bump's wake.

Figure 22 shows the final deposit profiles of the fine particles originating in subvolumes 1, 3 and 5. Again, the particles from the lowest subvolume are seen to settle out earliest, although a substantial fraction of them is carried all the way into the

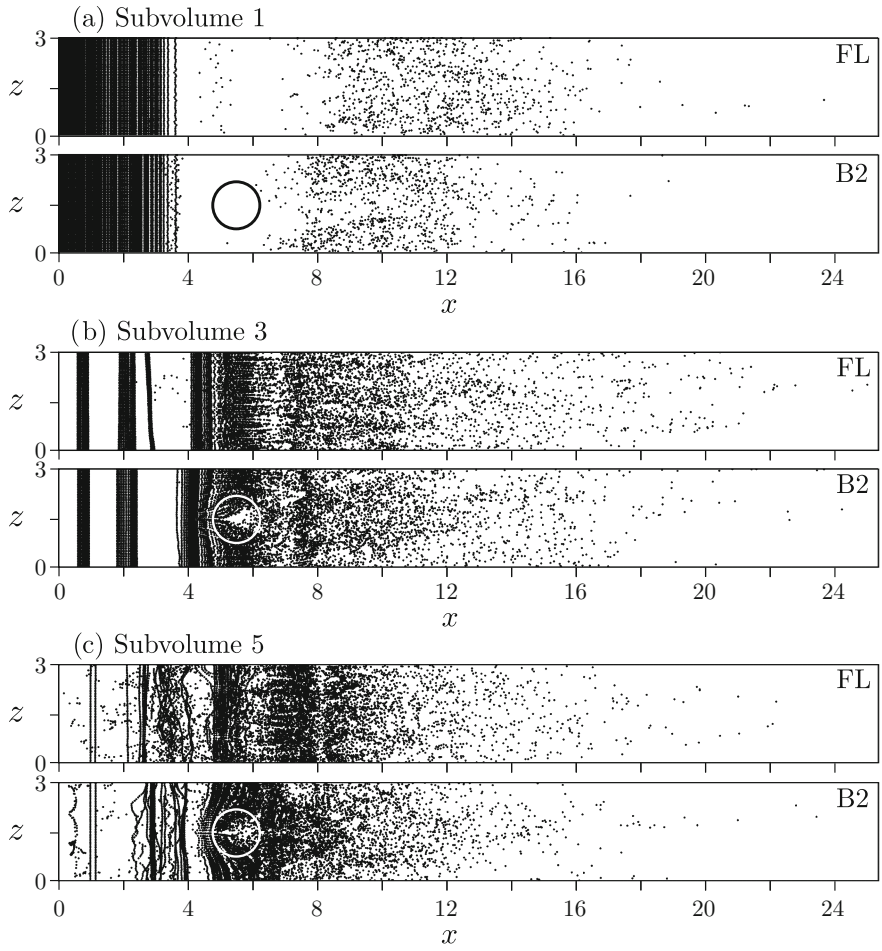

Fig. 21 Deposit profiles of the coarse particles originating in the *bottom*, *middle* and *top* subvolumes, respectively

far wake of the bump. The deposit profile corresponding to the central subvolume 3 reflects a strong influence of the bump. Immediately upstream of the bump, a pronounced deposit region partially wraps around the bump's front. Compared to the coarse particles, which were seen to be able to accumulate either near the wake centerline or away from it, the fine particles are spread fairly evenly across the spanwise direction in the wake of the bump.

In order to quantify the influence of the bump on the deposition of particles from each subvolume, we compute the mass fraction of particles of species i, originating from subvolume j, that is deposited upstream of a given streamwise location x

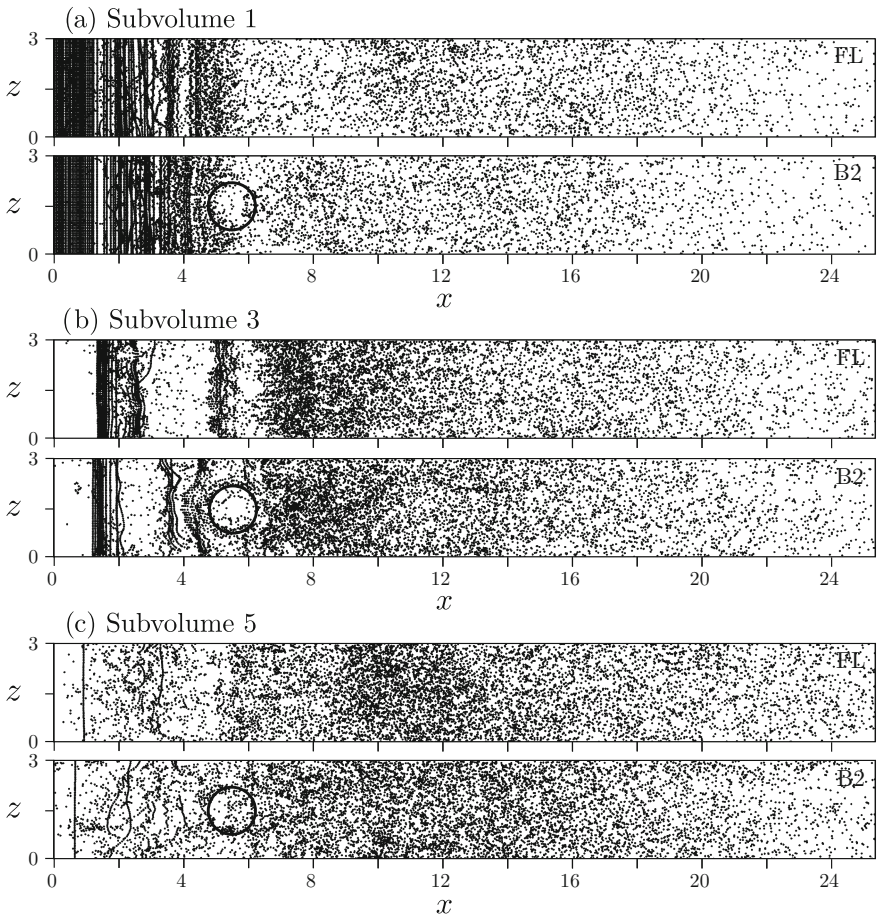

Fig. 22 Deposit profiles of the fine particles originating in the *bottom*, *middle* and *top* subvolumes, respectively

$$D_*^{j,i}(x) = \frac{\int_0^x \int_0^{L_z} D_j^i(\chi, z)\ \mathrm{d}z\mathrm{d}\chi}{m_s^i(0)/5}. \tag{21}$$

Since $D_*^{j,i}$ is scaled with the initial particle mass in the subvolume, it varies from zero at $x = 0$ to unity far downstream. Figure 23 compares the profiles of D_* corresponding to each subvolume and particle size for cases FL and B2. For the lowest subvolume 1, the deposit profiles upstream of the bump remain essentially unaffected by the bump. However, in the wake of the bump, both coarse and fine particles are seen to settle out more rapidly than for the corresponding flat bottom case. Subvolume 2 shows the overall strongest influence of the bump. Interestingly, the coarse particles are seen to be affected primarily downstream of the bump, whereas for the

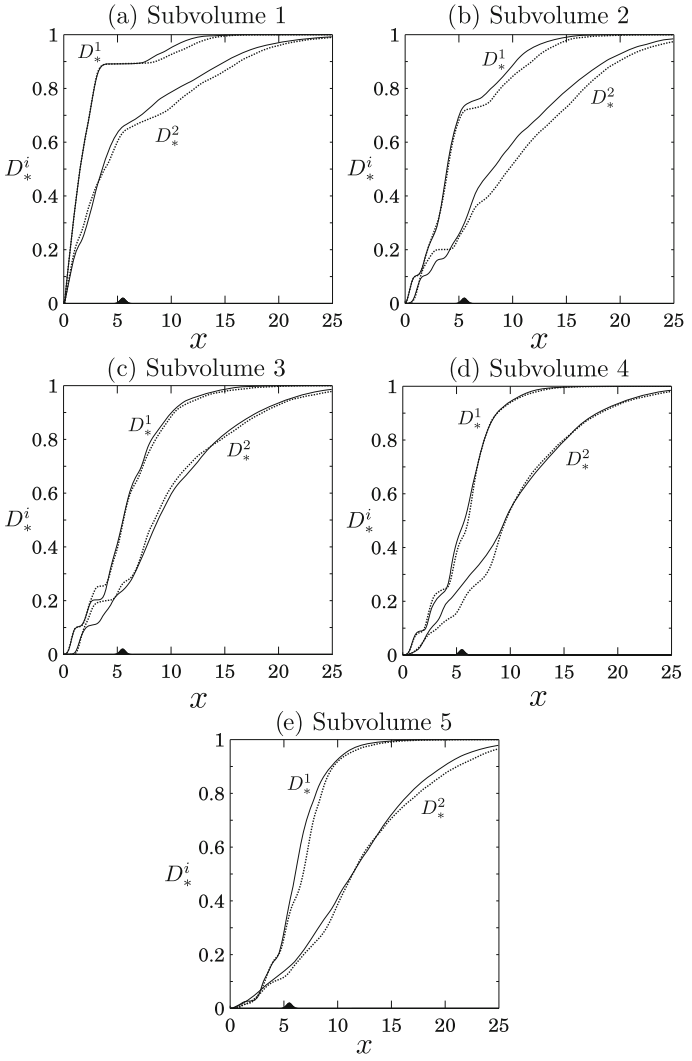

Fig. 23 Influence of the bump on the deposit profiles D_*^i for both particle sizes and all subvolumes. *Dashed lines* case FL; *solid lines* case B2

fine particles, the presence of the bump results in decreased deposition upstream of the bump, and in increased deposition downstream of it. For subvolume 3, both coarse and fine particles show reduced deposition upstream of the bump. For subvolume 4, the influence of the bump is mostly felt by the fine particles, which settle out more rapidly in the vicinity of the bump. In summary, the presence of the bump is seen to affect coarse and fine particles differently, and to influence the particles within each subvolume in different ways.

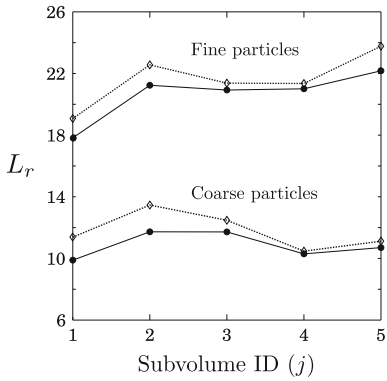

Fig. 24 Comparison of the runout lengths of particles originating in different subvolumes. For both particle sizes and all subdomains, the runout length of the turbidity current traveling over a bump (*solid lines*) is reduced, as compared to the runout length for the flat *bottom* case (*dashed lines*)

For each subvolume, we define a runout length L_r as the x-location at which the quantity $D_*^{j,i}$ reaches the value of 0.95. Figure 24 shows that the presence of the bump reduces this runout length for both particle sizes and all subdomains. Interestingly, among the fine particles those originating in the top volume travel have the largest runout length, whereas for the coarse particles, it is the interior subdomains 2 and 3 that travel farthest.

3 Vorticity-Based Models of Stratified Flows

3.1 Introduction

The development of simplified models for stratified flows with interfaces such as bores, gravity currents and intrusions has a long history, dating back to the classical works of Rayleigh (1914), Von Kármán (1940) and Benjamin (1968). Additional examples include sea breezes, thunderstorm outflows, turbidity currents, pyroclastic flows, intrusive flows or powder-snow avalanches. Traditionally, such simplified models have been based on the conservation laws for mass and streamwise momentum, e.g. Benjamin (1968). However, these conservation laws alone usually do not provide sufficiently many equations to solve for all of the unknowns, so that additional closure assumptions are required. These have typically been obtained from empirical energy-related arguments. More recently, Meiburg and coauthors have developed a new class of flow models which avoid the need for such energy-related closure assumptions by focusing on the conservation of vorticity. This approach accounts for the importance of conserving not only streamwise momentum, but also momentum in the direction normal to the main flow. In the following, we will review the basics of this new class of models.

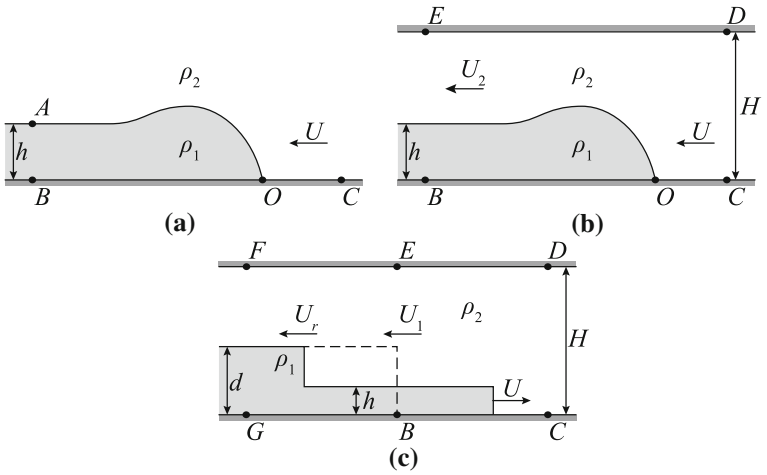

Fig. 25 Idealized gravity current in an infinitely deep ambient (**a**) and in a channel (**b**), in a reference frame moving with the current. **c** The model of Shin et al. (2004). The *dashed line* shows the setup before the current is released

3.2 Gravity Currents

Gravity currents are well suited for discussing the main features of the vorticity-based modeling approach, and for contrasting it to earlier models (Fig. 25). Dimensional analysis indicates that the quasisteady front velocity, U, of a gravity current of height h is proportional to $(g'h)^{1/2}$, where $g' = g(\rho_1 - \rho_2)/\rho_1$ is the reduced gravity, ρ_1 is the density of the current, ρ_2 the ambient, and g is the gravitational acceleration.

For more than 70 years, researchers have debated the value of the proportionality factor, called the Froude number or front condition, and how it scales on the channel depth H. Efforts to refine the relationship between the current velocity and height, denoted by the Froude number, $F_h = U/\sqrt{g'h}$, date back to Von Kármán (1940), who considered a two-dimensional gravity current in an inviscid, irrotational and infinitely deep ambient (Fig. 25a). By applying Bernoulli's equation along the streamlines C-O and O-A in the reference frame of the current front, so that the current is at rest, he obtained

$$F_h = \sqrt{\frac{2}{\sigma}}\,, \tag{22}$$

where $\sigma = \rho_2/\rho_1$ is the density ratio. For Boussinesq currents with $\sigma \approx 1$, $F_h = \sqrt{2}$. Benjamin (1968) argued that Von Kármán's assumption of energy conservation along the interface cannot be justified, and instead considered the inviscid, irrotational flow past a gravity current in a finite-depth channel (Fig. 25b). He assumed that the pressure distributions far up- and downstream of the front of the current were hydrostatic, and

applied the conservation of mass and horizontal momentum flux in the ambient as

$$U H = U_2 (H - h) \tag{23}$$

$$p_C H + \rho_2 U^2 H = p_B H + \frac{1}{2} g (\rho_1 - \rho_2) h^2 - g (\rho_1 - \rho_2) H h + \rho_2 U_2^2 (H - h) \ . \tag{24}$$

To close the problem, an additional condition is needed to determine $p_B - p_C$. Benjamin invoked Bernoulli's law, but along C-B (the bottom of the channel) rather than along C-A (the interface). Benjamin's approach produced the following Froude number formed with the channel height:

$$F_{H,b} = \frac{U}{\sqrt{g' H}} = \left[\frac{\alpha (1 - \alpha)(2 - \alpha)}{\sigma (1 + \alpha)} \right]^{1/2} , \tag{25}$$

where $\alpha = h/H$ represents the fractional current height. Similar to Von Kármán, Benjamin also calculated a Froude number scaled with the current height—the conversion is simply $F_h = F_H \alpha^{-1/2}$. This Froude number does not tend to zero in the deep channel limit, but because h is not known ahead of time (it must be measured), its value will be more uncertain when measured from experiments or simulations.

By then applying Bernoulli's equation along the top of the channel (D-E), Benjamin showed that an energy-conserving current is possible only for $\alpha = 1/2$; currents with $\alpha > 1/2$ require an input of energy to be realized.

The analyses of Von Kármán and Benjamin apply to all gravity currents, regardless of how they are generated. Shin et al. (2004) on the other hand, focused on gravity currents generated by partial-depth lock releases, (Fig. 25c, from Fig. 1.19 of Linden 2012) and considered a control volume that encompasses *both* fronts (i.e. CDFG). By conserving mass and horizontal momentum, they obtained

$$(p_D - p_F) H = (\rho_1 - \rho_2) \left[U^2 \frac{dh}{d - h} + \frac{1}{2} g d^2 \right] . \tag{26}$$

Invoking Bernoulli's law with no head loss along D-F to close the system then yields

$$F_{H,sdl} = \left\{ \frac{\beta (\beta - \alpha)(1 - \alpha)}{2\alpha \left[1 - \alpha (1 - \sigma) \right]} \right\}^{1/2} , \tag{27}$$

where $\beta = d/H$ is the non-dimensional lock height. They furthermore showed that energy-conserving flows are possible only if both fronts propagate at the same speed ($U = U_r$), and if $\alpha = \beta/2$. An alternative argument was put forward by Yih (1965), who focused on full-depth lock releases. By assuming symmetry between the light and dense fronts, and equating the rate at which potential energy is lost with the rate at which kinetic energy is gained, he arrived at

$$F_{H,y} = \left[\frac{1}{2\,(\sigma+1)}\right]^{1/2}. \tag{28}$$

Of course, full-depth lock releases are only truly symmetric in the Boussinesq limit where his Froude number reduces to 1/2.

Finally and more recently, Nokes et al. (2008) developed a model for Boussinesq intrusive gravity currents that assumes no head losses between the front stagnation point and the top of the gravity current head, but makes no assumptions about the loss of energy behind the head. The authors model the flow around the dynamic head of the gravity current and assume the flow near the front is inviscid and irrotational, and that the flow is horizontal, but not uniform, at the location of maximum height of the current head. Their model must be solved numerically, but can be approximated with the polynomial

$$F_{H,n} = \left[\alpha(0.91 - 0.80\alpha^2)\right]^{1/2} \tag{29}$$

3.3 *Circulation Based Models for Boussinesq Gravity Currents*

Consider the flow configuration in Fig. 25b. Following Benjamin, we assume the fluid within the current to be at rest far downstream of the front (along B-E), and write conservation of mass as in Eq. (23). Instead of applying the balance of streamwise momentum, however, we focus on the vorticity field in the control volume surrounding the front of the current (i.e. BCDE). For steady, two-dimensional, Boussinesq flows, the vorticity is governed by

$$\mathbf{u}\cdot\nabla\omega = -g'\frac{\partial\rho^*}{\partial x} + \nu\nabla^2\omega, \tag{30}$$

where ω is the vorticity normal to the page, ν is the kinematic viscosity, and $\rho^* = (\rho-\rho_2)/(\rho_1-\rho_2)$ is the Boussinesq density. From left to right, the terms in Eq. (30) represent the advection of vorticity, the baroclinic generation of vorticity, and the diffusion of vorticity due to fluid viscosity. Although the pressure does not explicitly appear in Eq. 30, we have not made the assumption that the flow is hydrostatic. The elimination of the dynamic pressure is purely the result of the Boussinesq approximation. Because this equation does not contain the pressure, we have one fewer unknown than do the models of Von Kármán (1940), Benjamin (1968) and Shin et al. (2004). By integrating Eq. (30) over a control volume that extends far up- and downstream of the front (BCDE), we obtain a relation governing the total circulation around the control volume:

$$\oint \omega\mathbf{u}\cdot\mathbf{n}\,\mathrm{d}S = \iint -g'\frac{\partial\rho^*}{\partial x}\,\mathrm{d}A + \oint \frac{1}{Re}\nabla\omega\cdot\mathbf{n}\,\mathrm{d}S. \tag{31}$$

The last term in Eq. (31) represents the diffusion of vorticity across the boundaries of the control volume, which requires a gradient in the vorticity normal to the boundary. For now, we, like all other gravity current models discussed above, will assume that the top and bottom boundary conditions are free-slip, which causes this term to go to zero.

With these simplifications, Eq. (31) states that changes in the convective vorticity flux should be balanced by baroclinic vorticity generation, even for flows with thin diffusive interfaces. For sharp interfaces, the area integral of the baroclinic term becomes $g'h$. As for the advective term, no vorticity enters the control volume, and vorticity flows out of the control volume confined to a thin vortex sheet between the two layers. The vorticity flux carried by the sheet is equal to the vortex sheet strength, $\gamma = U_2 - U_1$, multiplied by the sheet's principal velocity, $u_{PV} = (U_1 + U_2)/2$ (Pozrikidis 2011; Saffman 1992). Using the assumption that the velocity in the current is zero far downstream of the front (along B-E), Eq. (31) reduces to

$$\frac{1}{2}U_2^2 = g'h\ . \tag{32}$$

Combining this relationship with conservation of mass (Eq. (23)) produces

$$F_{H,c} = \sqrt{2\alpha}(1-\alpha). \tag{33}$$

Details regarding the accuracy of this model, and a comparison between the predictions by the various models and corresponding DNS simulations, can be found in Borden and Meiburg (2013a).

3.4 Two-Layer Bores

A corresponding problem arises with regard to modeling two-layer bores. Several analytical models have been proposed to relate the speed of propagation of a bore to its size, but these models usually invoke an empirical assumption about the change in energy flux across the bore. On the other hand, computational investigations of internal bores based on Navier-Stokes simulations are able to reproduce the dynamics of internal bores from mass and momentum considerations alone Borden et al. (2012), which suggests the same should be possible for an analytical model.

Existing models of two-layer internal bores, particularly those of Wood and Simpson (1984), Klemp et al. (1997), and Borden et al. (2012), consider the flow sketched in Fig. 26a to derive an expression for the bore velocity U in terms of the geometrical parameters H, h_f, and h_a. Following the approach of Rayleigh (1914) in his work on single layer hydraulic jumps, each model makes the following assumptions assumptions: that the bore propagates at a steady velocity U, that the pressure field far up- and downstream of the front is hydrostatic, and that viscous effects are negligible. In a control volume around the front of the bore, each model enforces the conser-

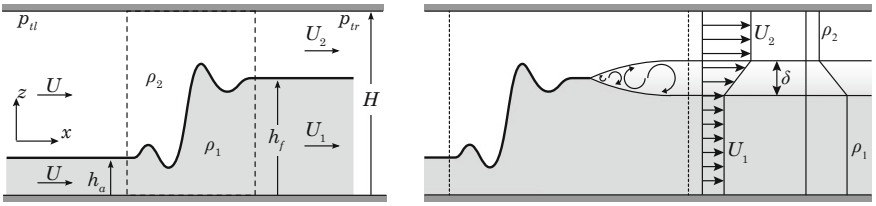

Fig. 26 **a** Simplified geometry of an internal bore used by Wood and Simpson (1984), Klemp et al. (1997), and Borden et al. (2012). **b** Same simple geometry, but with a shear layer of finite thickness separating the *upper* and *lower* layers. The velocity and density vary linearly across the layer

vation of mass within each layer, along with the conservation of overall streamwise momentum

$$U_1 h_f = U h_a \tag{34}$$

$$U_2(H - h_f) = U(H - h_a) \tag{35}$$

$$\int_0^H \left(p_l + \rho U^2\right) \mathrm{d}z = \int_0^H \left(p_r + \rho u_r^2\right) \mathrm{d}z, \tag{36}$$

where u_r represents the local velocity far downstream of the front, and p_l and p_r indicate the hydrostatic pressure plus the pressure at the top of the channel (p_{tl} and p_{tr}) at streamwise locations far up- and downstream of the front.

It would seem that we have three equations available to solve for U, U_1 and U_2 in terms of the given values of H, h_f, h_a, ρ_1 and ρ_2. However, Eq. (36) introduces an additional unknown—the pressure jump across the front along the top wall of the channel, $p_{tl} - p_{tr}$. Therefore, unlike for single layer hydraulic jumps, the conservation equations for mass and streamwise momentum alone do not provide enough information for a closed form solution. An additional equation is required.

Traditionally, this fourth equation has been obtained by making an assumption about the conservation of mechanical energy across the front of the bore. Wood and Simpson (1984) assumed that, similar to a single-layer hydraulic jump, no energy should be lost across the front of the bore in the light, upper-layer fluid. By equating the energy fluxes in and out of the control volume in the upper layer, they obtained the front velocity

$$u_{ws} = \left\{ \frac{R\,(1+R)\,(1-Rr)^2}{R^2 r - 3Rr + 2} \right\}^{1/2}, \tag{37}$$

where $R = h_f/h_a$, $r = h_a/H$, and $u = U/(g' h_a)^{1/2}$ is the non-dimensional front velocity (with $g' = g(1 - \rho_2/\rho_1)$ denoting the reduced gravity). We hereafter refer to this model as WS.

Later, Klemp et al. (1997) discovered that they obtained closer agreement with laboratory experiments of internal bores if they instead applied conservation of energy

across the front of the bore in the heavy, lower-layer fluid. This produces the front velocity

$$u_{krs} = \left\{ \frac{R^2 \left[2 - r\,(1+R)\right](1 - Rr)}{R^2 r - 3Rr + R + 1} \right\}^{1/2}, \tag{38}$$

which we refer to as the KRS model.

Based on direct numerical simulations (DNS) of internal bores, Borden et al. (2012) show that within an internal bore mechanical energy is lost due to turbulent mixing in the interfacial shear layer, cf. Fig. 26b. Furthermore, this turbulent mixing can result in a net energy transfer from the contracting to the expanding layer. By solving for the amount of energy lost in the mixing layer, the authors obtain a front velocity that is a function of the Reynolds and Schmidt numbers as well as R and r. Hereafter, we denote their front velocity as the BMC model.

3.5 Circulation-Based Model

An alternative approach for deriving an expression for the bore velocity can again be based on the vorticity variable. As explained above, in the earlier models the need for invoking an energy argument arose from the fact that the streamwise momentum Eq. (36) introduced the pressure difference along the top wall as an additional unknown. Hence, if we were able to impose the conservation of momentum in a form that does not involve the pressure, the energy equation would no longer have to enter into our considerations. This can indeed be accomplished by focusing on the well-known vorticity formulation of the momentum conservation principle, which eliminates the pressure variable by taking a linear superposition of the streamwise and vertical momentum equations.

Consider the internal bore with the simple geometry and sharp interface in Fig. 26a. Conservation of mass remains as stated in Eqs. (34) and (35). But, instead of enforcing the conservation of streamwise momentum, we examine the flux of vorticity across the control volume. For steady, two-dimensional Boussinesq flows, the vorticity is governed by

$$\boldsymbol{u} \cdot \nabla \omega = -g' \frac{\partial \rho^*}{\partial x} + \nu \nabla^2 \omega, \tag{39}$$

where $\omega = \partial w/\partial x - \partial u/\partial z$ is the vorticity normal to the page and $\rho^* = (\rho - \rho_2)/(\rho_1 - \rho_2)$ denotes the dimensionless Boussinesq density. In deriving Eq. (39), we have not made the assumption that the flow is hydrostatic. The fact that the pressure does not appear is solely the result of the Boussinesq approximation.

To obtain a control volume conservation argument, we integrate Eq. (39) over the entire control volume to produce

$$\oint \omega \boldsymbol{u} \cdot \boldsymbol{n}\, \mathrm{d}S = \iint -g' \frac{\partial \rho^*}{\partial x}\, \mathrm{d}A + \oint \nu \nabla \omega \cdot \boldsymbol{n}\, \mathrm{d}S, \tag{40}$$

where $\boldsymbol{n}$ is a unit vector normal to the surface of the control volume. By writing the first and last terms in Eq. (40) as surface integrals, we are assuming that the divergence theorem applies.

Both the in- and outflow are normal to the control volume boundaries, and vorticity is generated only along the interface, i.e., away from the walls. Especially for high Reynolds number flows, we can therefore neglect diffusive losses of vorticity across the control volume boundaries (the third term in Eq. (40)). Equation (40) then states that the change in the vorticity flux across the control volume is entirely the result of baroclinic vorticity generation within.

For sharp interfaces, the baroclinic term simplifies to the reduced gravity multiplied by the change in height of the interface: $-g'(h_f - h_a)$ in this case. Upstream of the bore, the velocity field is horizontal and uniform, cf. Fig. 26a, so no vorticity flows into the control volume. Vorticity exits the control volume as a vortex sheet along the interface between the upper and lower layers, assuming inviscid flow. The vorticity flux carried by a vortex sheet is given as the vortex sheet strength, $\gamma = U_1 - U_2$, multiplied by principle velocity of the sheet, $u_{PV} = (U_2 + U_1)/2$ (Pozrikidis, 2011; Saffman, 1992). Therefore, Eq. (40) reduces to

$$\frac{1}{2}\left(U_2^2 - U_1^2\right) = g'\left(h_f - h_a\right). \tag{41}$$

Because Eq. (41) does not contain the pressure, we no longer require a fourth equation relating the energy up- and downstream of the front. Combining Eq. (41) with the conservation of mass stated in Eqs. (34) and (35) produces a closed form solution for the front velocity of the bore

$$u_{vs} = \left\{\frac{2R^2\,(Rr-1)^2}{R - 2Rr + 1}\right\}^{1/2}, \tag{42}$$

which we hereafter refer to as the vortex sheet (VS) model.

The evolution of vorticity, as stated in Eq. (39), can be derived from a linear combination of the conservation equations for both streamwise and vertical momentum. In this way, the streamwise momentum equation does enter into the VS front velocity computation. If we desired, we could now use the conservation of streamwise momentum alone to solve for the pressure jump at the top of the channel given the VS front velocity.

To assess the validity of Eq. (41) as a jump condition, we can compare its predicted vorticity flux with the actual flux of vorticity in direct numerical simulations (DNS) of internal bores using the code of Borden et al. (2012). The density field of a representative bore generated by this code is shown in Fig. 27a. For each analytical model, we compute the predicted vorticity flux $\Omega^* = \int \omega u \, \mathrm{d}z = (U_2^2 - U_1^2)/2g'h_a$ (where $\Omega^* = \Omega/(g'h_a)$ is the dimensionless vorticity flux) as a function of the streamwise position given the local height $h(x) = \int_0^H \rho^*(x, z)\, \mathrm{d}z$. By comparing these predictions with the actual vorticity flux measured from a DNS simulation (see Fig. 27b), we observe that in the quasi-steady region close to the front of the bore, the VS model

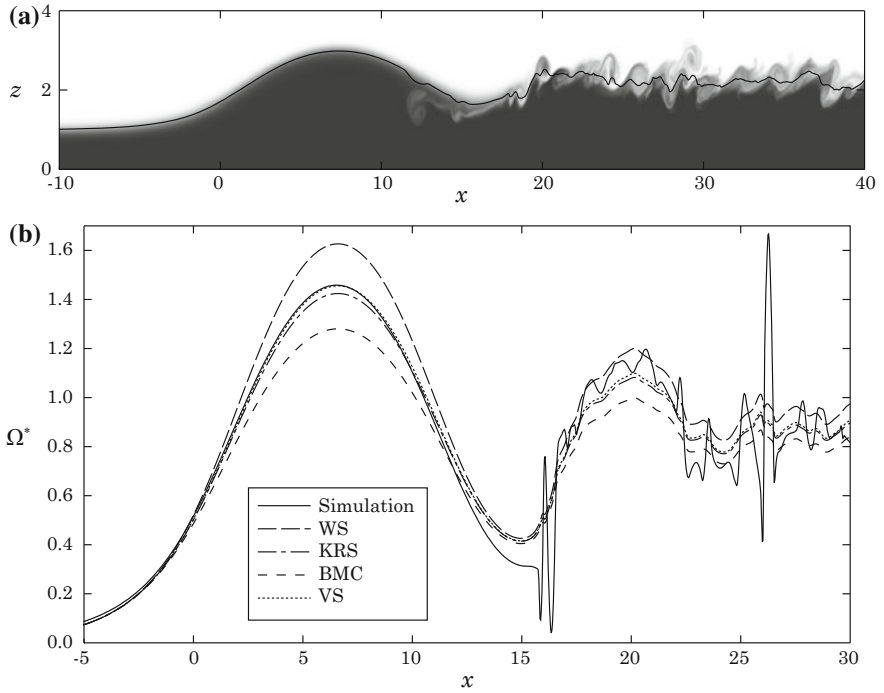

Fig. 27 **a** Density field of a DNS simulated bore at time $t = 32$ with $R = 2.22, r = 0.1$, $Re = 3500$, and $Sc = 1$. **b** Measured and predicted vorticity flux as functions of streamwise position. The *solid line* corresponds to the measured vorticity flux from a DNS with $R = 1.87, r = 0.1$, $Re = 3500$, and $Sc = 1$. The *dashed lines* represent the vorticity flux predicted by the different analytical models. Here, $x = 0$ corresponds to the *front* of the bore

predicts the correct vorticity flux more accurately than any of the earlier models. Further information can be found in Borden and Meiburg (2013b).

3.6 Gravity Currents Propagating into Shear

An interesting extension of the above models concerns the propagation of gravity currents into an ambient with shear (Nasr-Azadani and Meiburg 2015). This situation can be encountered in the atmosphere, for example, where close to the ground cold thunderstorm outflows can interact with the ambient shear in the atmosphere. In the following, we will initially consider a two-layer (TL) configuration, in which the ambient fluid consists of two constant velocity streams separated by a shear layer. Subsequently, we will focus on the related situation of a gravity current propagating into an ambient fluid of constant vorticity, the so-called single-layer (SL) configuration.

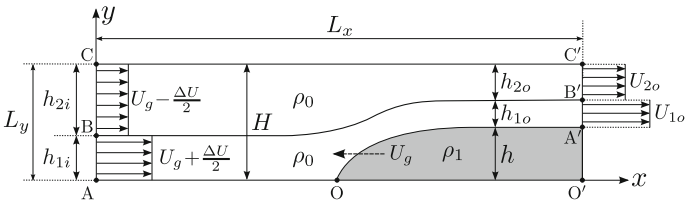

Fig. 28 The two-layer configuration: a gravity current (*gray region*) propagates into an ambient consisting of two uniform streams separated by a vortex sheet of strength ΔU

Two-layer configuration Consider a gravity current of height h and density ρ_1 propagating in a horizontal channel of height H filled with ambient fluid of density ρ_0, as shown in Fig. 28. In the laboratory reference frame, the gravity current travels from right to left with constant velocity U_g, into an environment consisting of two uniform streams whose velocities are $\Delta U/2$ and $-\Delta U/2$, respectively. This defines the laboratory reference frame. Far ahead of the current front, the inlet conditions h_{1i}, h_{2i} and ΔU are given.

To facilitate the analysis, we shift to a reference frame moving with the gravity current front, so that the flow field is steady and the fluid inside the current is at rest. The goal of our analysis is to determine the gravity current velocity U_g, as well as the conditions far downstream of the current front in terms of the layer heights (h_{1o}, h_{2o}) and velocities (U_{1o}, U_{2o}). For the steady-state configuration in the reference frame moving with the gravity current, the continuity equations for the two ambient fluid layers yield

$$(U_g + \frac{\Delta U}{2})h_{1i} = U_{1o}h_{1o}\,, \tag{43}$$

$$(U_g - \frac{\Delta U}{2})h_{2i} = U_{2o}h_{2o}\,. \tag{44}$$

In order to obtain additional equations, we now invoke the conservation of momentum. Rather than applying the x- and y-momentum equations separately, at this stage we focus on the vorticity conservation equation, i.e., a linear combination of the x- and y-momentum equations. This approach has the advantage of eliminating the pressure variable from the analysis. Note that, if information on the pressure is desired, we can solve the x-momentum equation for the pressure at a later stage, after all other flow variables have been determined. In this way, by using the vorticity equation we essentially decouple the pressure problem, cf. Borden and Meiburg (2013a, b).

For two-dimensional, steady-state Boussinesq flow, the vorticity field is governed by

$$\mathbf{u}\cdot\boldsymbol{\nabla}\boldsymbol{\omega} = -g'\frac{\partial\rho^*}{\partial x} + \nu\nabla^2\omega\,. \tag{45}$$

Here, ω, g', ρ^* and ν represent the out-of-plane vorticity component $\frac{\partial v}{\partial x} - \frac{\partial u}{\partial y}$, the reduced gravity $g(\rho_1 - \rho_0)/\rho_0$, the non-dimensional density $(\rho - \rho_0)/(\rho_1 - \rho_0)$, and the kinematic viscosity, respectively. Note that we do not make any assumptions regarding the flow being hydrostatic.

For the purpose of determining the gravity current velocity, we assume that the viscosity is sufficiently small for the vorticity to remain confined to narrow layers along the interfaces, so that there is no diffusive interaction between these vorticity layers and no diffusion of vorticity across the top and bottom boundaries. Equation (45) can then be integrated for the control volume AO′C′C in Fig. 28. Using the divergence theorem we obtain

$$\oint \omega \mathbf{u} \cdot \mathbf{n} \, \mathrm{d}\Gamma = - \iint_A g' \frac{\partial \rho^*}{\partial x} \, \mathrm{d}A \, . \tag{46}$$

Here A, Γ and $\mathbf{n}$ denote the control volume area, the control volume boundary and the unit outer normal vector, respectively. We assume the normal derivative of the shear stress along the top and bottom boundaries to vanish. At the in- and outflow boundaries, the flow is approximately unidirectional and normal to the boundaries, so that $\mathbf{n} \cdot \nabla \omega = 0$. Consequently, the diffusion of vorticity across the in- and outflow boundaries can be neglected as well. Equation (46) therefore states that the rate at which vorticity is convected out of the control volume at the downstream boundary equals the rate at which it is convected into the control volume at the upstream boundary, plus the rate at which it is generated inside the control volume as a result of baroclinic vorticity production.

We can evaluate the vorticity flux associated with a vortex sheet as the vortex sheet strength multiplied by its principal velocity, cf. Saffman (1992) and Borden and Meiburg (2013a). For the vortex sheet separating the two layers of constant density, ambient fluid, (line BB′ in Fig. 28) we obtain

$$U_g \Delta U = \frac{U_{1o} + U_{2o}}{2} (U_{1o} - U_{2o}) \, . \tag{47}$$

For the vortex sheet along the interface between the gravity current and ambient fluid, the vorticity flux is balanced by the baroclinic vorticity generation. Since the fluid inside the current is at rest, this yields

$$\frac{1}{2} U_{1o}^2 = g' h \, . \tag{48}$$

One final equation is obtained from geometrical considerations

$$h_{1o} + h_{2o} + h = H \, . \tag{49}$$

The two continuity equations for the ambient fluid layers, see Eqs. (43) and (44), along with the two vorticity equations for the interfaces, see Eqs. (47) and (48), as

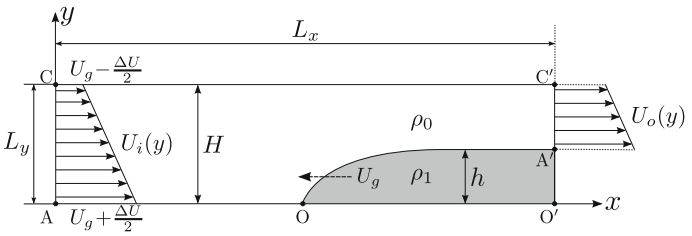

Fig. 29 The single-layer configuration: a gravity current (*gray region*) propagates into ambient fluid with constant shear

well as the geometrical constraint (49), provide five equations for the five unknowns U_g, U_{1o}, U_{2o}, h_{1o} and h_{2o}. For any given parameter set (ΔU, h, h_{1i}, h_{2i}, H, and g'), this set of nonlinear equations can be solved iteratively. Note that we did not have to invoke any assumptions regarding energy conservation along any of the streamlines in the flow, in contrast to previous studies, e.g. Benjamin (1968), Shin et al. (2004), Nokes et al. (2008). In the present investigation, we focus primarily on cases in which both ambient currents flow from left to right in the reference frame moving with the gravity current, cf. Fig. 28. Thus, the following conditions will always hold

$$U_g \pm \frac{\Delta U}{2} \geq 0\,, \tag{50}$$

$$U_{1o}, U_{2o} \geq 0\,. \tag{51}$$

Single-layer configuration Corresponding conservation arguments can now be invoked for the single layer case SL, cf. Figure 29, in which the ambient flow has constant shear across the channel height. For a given gravity current height h, reduced gravity g', and imposed shear at the inlet $\Delta U = U_i(y = 0) - U_i(y = H)$, we need to determine the gravity current velocity U_g along with the velocity profile at the outlet $U_o(y)$.

The continuity equation for the ambient takes the form

$$\int_h^H U_o(y)\,\mathrm{d}y = \int_0^H U_i(y)\,\mathrm{d}y = U_g H\,, \tag{52}$$

where $U_i(y)$ has the linear form

$$U_i(y) = U_g + \frac{\Delta U}{2} - \frac{\Delta U}{H} y\,. \tag{53}$$

Since the ambient fluid has constant density, no baroclinic vorticity is produced within the ambient stream, and the slope of the outflow velocity profile equals that of the inflow profile, i.e. $\frac{\mathrm{d}U_i}{\mathrm{d}y} = \frac{\mathrm{d}U_o}{\mathrm{d}y}$. Thus, the outflow velocity profile has the form

$$U_o(y) = U_o|_{y=h} - \frac{\Delta U}{H}(y-h) \qquad y \geq h\,. \tag{54}$$

The outflow velocity at $U_o|_{y=h}$ can be evaluated from the vorticity conservation equation along the interface (OA′ in Fig. 29)

$$\frac{1}{2}U_o^2\bigg|_{y=h} = g'h\,. \tag{55}$$

Unlike for the TL case, we can obtain explicit relations to compute the values of the two unknowns U_g and $U_o(y=h)$ for the SL configuration

$$U_o|_{y=h} = \sqrt{2g'h}\,, \tag{56}$$

$$U_g = (1-\frac{h}{H})\sqrt{2g'h} - \frac{1}{2}(1-\frac{h}{H})^2\Delta U\,. \tag{57}$$

In the following, we limit ourselves to cases where the gravity current travels from right to left in the laboratory frame, so that $U_g \geq 0$. This imposes an upper bound on the shear magnitude in the form

$$\Delta U \leq \frac{2\sqrt{2g'h}}{1-h/H}\,. \tag{58}$$

Assessment of physically feasible solutions In order to assess whether the solutions obtained for single-layer and two-layer configurations are physically feasible, we need to check whether or not they require an external energy input. Towards this end, we now perform a head loss analysis along selected streamlines.

Applying Bernoulli's equation with a head loss between the two points C and C′ along the top wall in Figs. 28 and 29 yields

$$p_{\mathrm{C}} + \frac{1}{2}\rho_0 U_{\mathrm{C}}^2 = p_{\mathrm{C}'} + \frac{1}{2}\rho_0 U_{\mathrm{C}'}^2 + \delta_{\mathrm{CC}'}\,. \tag{59}$$

For the system to be physically feasible, the head loss term $\delta_{\mathrm{CC}'}$ should be non-negative. From the analysis carried out for single-layer and two-layer configurations, we know $U_{\mathrm{C}'}$. To obtain $\delta_{\mathrm{CC}'}$, however, we also need to evaluate the pressure difference between these two points. This can be accomplished via the conservation equation for horizontal momentum

$$\int_0^H (p_i + \rho_0 U_i^2)\,\mathrm{d}y = \int_0^h p_o\,\mathrm{d}y + \int_h^H (p_o + \rho_0 U_o^2)\,\mathrm{d}y\,, \tag{60}$$

In conjunction with the hydrostatic pressure relations far up- and downstream of the gravity current front

$$p_i(y) = p_{\mathrm{C}} + \rho_0 g(H - y)\,, \tag{61}$$

$$p_o(y) = \begin{cases} p_{\mathrm{C}'} + \rho_0 g(H - y) & \text{if } y > h\,, \\ p_{\mathrm{C}'} + \rho_0 g(H - h) + \rho_1 g(h - y) & \text{if } y \le h\,, \end{cases} \tag{62}$$

we thus obtain for the pressure drop along the top wall

$$\Delta p|^{\mathrm{TL}} = p_{\mathrm{C}'} - p_{\mathrm{C}} = -\frac{1}{H}\Bigg[(\rho_1 - \rho_0) g \frac{h^2}{2} + \rho_0 h_{1o} U_{1o}^2 + \rho_0 h_{2o} U_{2o}^2 - \rho_0 h_{1i}\left(U_g + \frac{\Delta U}{2}\right)^2 - \rho_0 h_{2i}\left(U_g - \frac{\Delta U}{2}\right)^2\Bigg]\,, \tag{63}$$

$$\Delta p|^{\mathrm{SL}} = p_{\mathrm{C}'} - p_{\mathrm{C}} = -\frac{1}{H}\Bigg[(\rho_1 - \rho_0) g \frac{h^2}{2} - \rho_0 \frac{H}{12}\left(\Delta U^2 + 12 U_g^2\right) + \rho_0 (H - h)\left(\frac{1}{2} g' h + \frac{1}{3}\left\{\Delta U\left(1 - \frac{h}{H}\right) - \frac{3}{2}\sqrt{2g'h}\right\}^2\right)\Bigg]\,. \tag{64}$$

This allows us to calculate the head loss $\delta_{\mathrm{CC}'}$ along the top wall via Eq. (59).

It is straightforward to show that the head loss along any streamline in the ambient is identical to the head loss along the top wall, e.g. $\delta_{\mathrm{CC}'} = \delta_{\mathrm{AA}'}$ (for both SL and TL cases), and $\delta_{\mathrm{CC}'} = \delta_{\mathrm{BB}'}$ in the TL case. In the following, this is demonstrated for the SL case. Using Bernoulli's equation along A − A′, the head loss is obtained as

$$\delta_{\mathrm{AA}'} = p_{\mathrm{A}} - p_{\mathrm{A}'} + \frac{1}{2}\rho_0\left(U_{\mathrm{A}}^2 - U_{\mathrm{A}'}^2\right) - \rho_0 g h\,. \tag{65}$$

Using the hydrostatic pressure relations (61) and (62) far up- and downstream of the gravity current front, we obtain the pressure drop between points A and A′ as

$$p_{\mathrm{A}} - p_{\mathrm{A}'} = p_{\mathrm{C}} - p_{\mathrm{C}'} + \rho_0 g h\,. \tag{66}$$

Recall that for the SL configuration, the velocities in Eq. (65) are given as

$$U_{\mathrm{A}} = U_g + \frac{\Delta U}{2}\,, \qquad U_{\mathrm{A}'} = \sqrt{2g'h}\,, \tag{67}$$

$$U_{\mathrm{C}} = U_g - \frac{\Delta U}{2}\,, \qquad U_{\mathrm{C}'} = \sqrt{2g'h} - \left(1 - \frac{h}{H}\right)\Delta U\,, \tag{68}$$

where the gravity current velocity U_g for the SL case can be computed via Eq. (57). By substituting (66)–(68) into Eqs. (65) and (59) and simplifying, we obtain

$$\delta_{\mathrm{AA}'} = \delta_{\mathrm{CC}'}\,. \tag{69}$$

Following similar arguments, the same result can be obtained for the TL configuration.

An alternate strategy for assessing the physical feasibility of the flow is to compare the depth-integrated energy loss from the inflow to the outflow. This approach can be useful when there exists a reverse flow over a small portion of the in- or outflow boundaries. We define the net energy loss in the control volume as

$$\Delta \dot{E} = \dot{E}_i - \dot{E}_o = \int_0^H \left(p + \frac{1}{2}\rho_0 U_i^2(y) + \rho_0 g y \right) U_i(y)\, \mathrm{d}y - \int_h^H \left(p + \frac{1}{2}\rho_0 U_o^2(y) + \rho_0 g y \right) U_o(y)\, \mathrm{d}y\,. \tag{70}$$

Using the hydrostatic pressure relations at the inlet and outlet, we arrive at

$$\Delta \dot{E} = -(p_{\mathrm{C}'} - p_{\mathrm{C}}) U_g H + \frac{1}{2}\rho_0 \int_0^H U_i^3(y)\mathrm{d}y - \frac{1}{2}\rho_0 \int_h^H U_o^3(y)\, \mathrm{d}y\,. \tag{71}$$

It is then straightforward to show for the SL configuration (and similarly for the TL configuration) that the depth-integrated energy loss is related to the head loss via

$$\Delta \dot{E} = -(p_{\mathrm{C}'} - p_{\mathrm{C}}) U_g H + \frac{1}{2}\rho_0 \left(U_{\mathrm{C}}^2 - U_{\mathrm{C}'}^2 \right) U_g H = U_g H \delta_{\mathrm{CC}'}\,. \tag{72}$$

Equation (72) suggests that the head loss and depth-integrated energy loss argument yield the same result, as far as the feasibility of the solution is concerned.

Results We will now employ the above theoretical framework in order to analyze single- and two layer configurations. Subsequently, we will compare these theoretical results against DNS simulations. We will pay particular attention to the influence of the inflow conditions on the velocity and head loss of the current, and we will demonstrate the existence of current heights larger than half the channel height. Before doing so, we render the governing equations dimensionless by using as characteristic scales the channel height H, the buoyancy velocity $u_b = \sqrt{g'H}$, and the density difference $\rho_1 - \rho_0$

$$\mathbf{x}^* = \frac{\mathbf{x}}{H}\,, \tag{73}$$

$$\mathbf{u}^* = \frac{\mathbf{u}}{\sqrt{g'H}}\,, \tag{74}$$

$$t^* = \frac{t}{H/\sqrt{g'H}}\,, \tag{75}$$

$$p^* = \frac{p}{\rho_0 g' H}\,, \tag{76}$$

$$\dot{E}^* = \frac{\dot{E}}{\rho_0 g'^{3/2} H^{5/2}}\,, \tag{77}$$

$$\rho^* = \frac{\rho - \rho_0}{\rho_1 - \rho_0}\,. \tag{78}$$

In the remainder, the *-symbol is employed to indicate a dimensionless quantity.

Two-layer configuration We begin by considering case TL with $h^*_{1i} = h^*_{2i} = 0.5$, cf. Fig. 28. Figure 30 shows the gravity current velocity U^*_g and the head loss along the upper wall $\delta^*_{CC'}$ as functions of the gravity current height h^* and the inflow shear magnitude ΔU^*. Physically feasible flow conditions, i.e. those resulting in a positive head loss, are shaded gray. For vanishing shear, we recover Benjamin's classical result which states that a current occupying half the channel height has a front velocity $U^*_g = 0.5$ and conserves energy, cf. case T_0 in Fig. 30. For a detailed derivation of the energy analysis we refer to Sect. 3.7, which provides such an analysis for the single-layer configuration. In the absence of shear, as discussed by Benjamin (1968) and Borden and Meiburg (2013a), only gravity currents of less than half the channel height are physically possible. However, for positive values of ΔU^*, when the lower ambient stream moves faster than the upper one, gravity currents with significantly larger heights become feasible. Benjamin (1968) points out that such flows require external energy input into the ambient. In light of Eq. (72) it becomes clear that the presence of shear modifies the pressure jump $p_{C'} - p_C$ over the current front, which in turn affects the kinetic energy of the ambient current. If the upper stream is the faster one, on the other hand, currents with thickness greater than half the channel height cannot form. The region for which results are shown is bounded by lines determined from the condition $U_g \pm \Delta U/2 \geq 0$, so that in the moving reference frame both ambient streams flow from left to right.

To investigate the influence of the inlet properties, we also show the gravity current velocities for $h^*_{1i} = 0.25$ and $h^*_{1i} = 0.75$, cf. Fig. 31. As the thickness of the lower ambient current decreases, even thicker gravity currents become physically feasible. Conversely, the thinner the lower ambient stream, the less shear is required to obtain a given gravity current thickness $h^* > 0.5$.

The existence of a saddle-point in all of the velocity diagrams of Figs. 30a and 31 is a result of two competing effects. On one hand, for constant shear the gravity current velocity exhibits a maximum at an intermediate height h^*. For vanishing shear specifically, the analyses by Benjamin (1968) and Borden and Meiburg (2013a) place this maximum at $h^* = 0.347$ and $h^* = 0.333$, respectively (Fig. 32a). Away from this value, the gravity current velocity starts to decrease. On the other hand, for

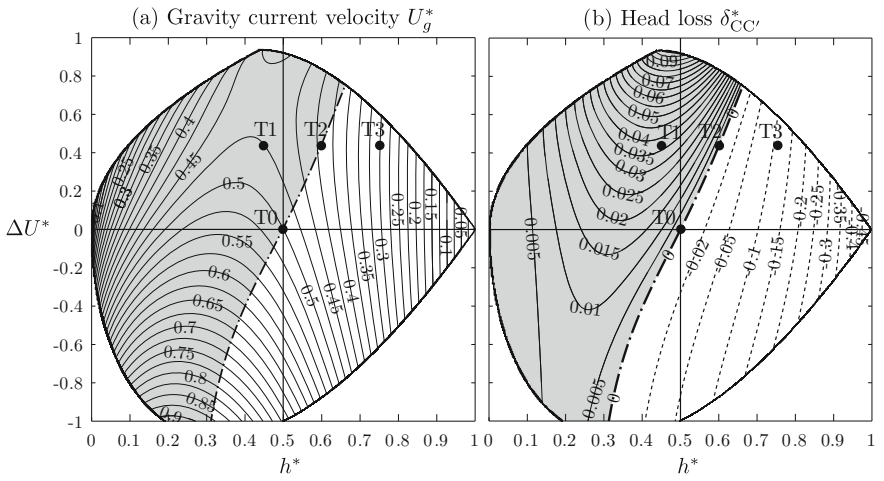

Fig. 30 Configuration TL with inlet layer heights of $h^*_{1i} = h^*_{2i} = 0.5$: Phase-space diagram for (**a**) the gravity current velocity U^*_g, and (**b**) the head loss along the *upper* wall $\delta^*_{CC'}$, as functions of ΔU^* and h^*. The *gray region* indicates physically possible solutions, i.e., solutions with a positive head loss. For positive shear, when the *lower* ambient stream moves faster than the upper one, currents with thickness larger than half the channel height can form

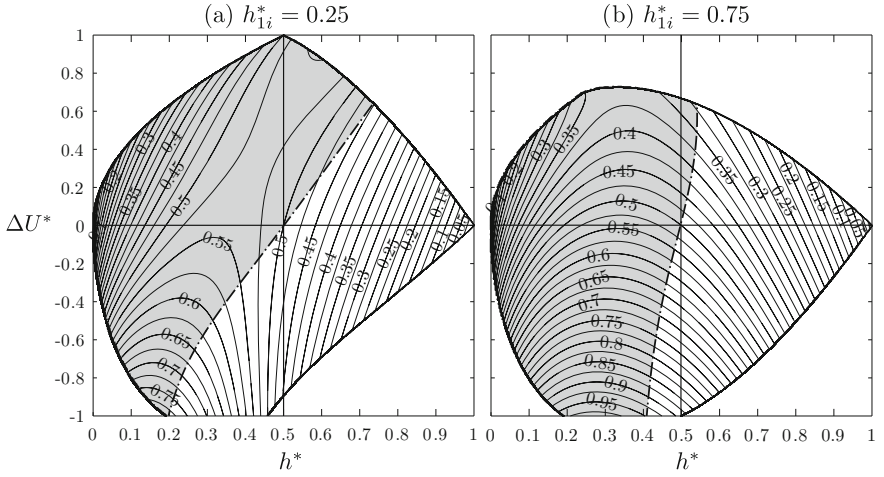

Fig. 31 Phase-space diagram for the gravity current velocity U^*_g as function of ΔU^* and h^*, for (**a**) $h^*_{1i} = 0.25$, and (**b**) $h^*_{1i} = 0.75$. Thinner *lower* ambient streams allow for a wider range of physically feasible gravity current thicknesses

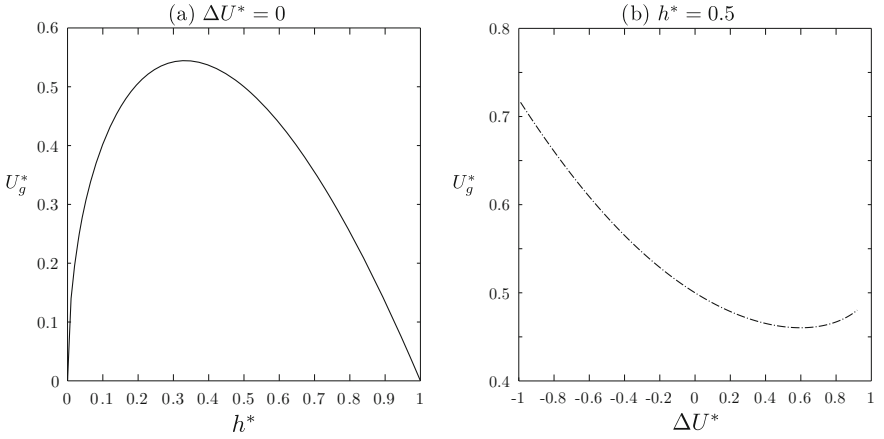

Fig. 32 Gravity current velocity for $h^*_{1i} = h^*_{2i} = 0.5$ computed for two different scenarios. **a** For a vanishing shear $\Delta U^* = 0$, the current velocity has a maximum at intermediate current heights. **b** For a fixed value of $h^* = 0.5$, the gravity current velocity reaches a minimum at an intermediate shear value. Together, these trends account for the existence of the saddle point in Fig. 30a

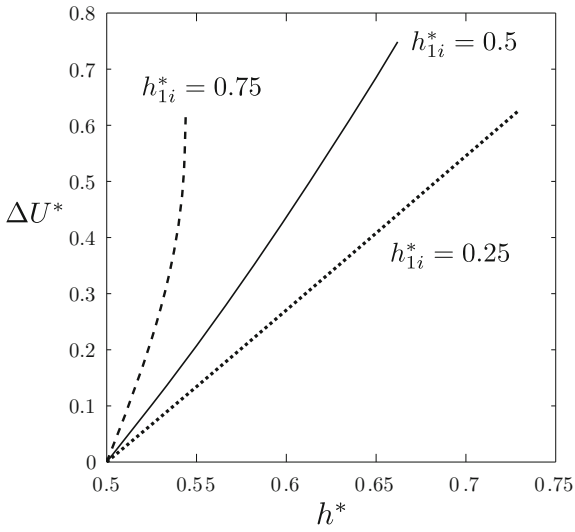

Fig. 33 The minimum shear required to produce a gravity current of a certain height larger than half the channel height, for different *lower* ambient stream thicknesses h^*_{1i}.

fixed gravity current heights the current velocity displays a minimum at intermediate shear. Away from this minimum, an increase in the shear magnitude leads to faster gravity currents (Fig. 32b). As suggested by Figs. 30a and 31, the location of the saddle point is strongly dependent on the flow parameters as well as the inlet heights.

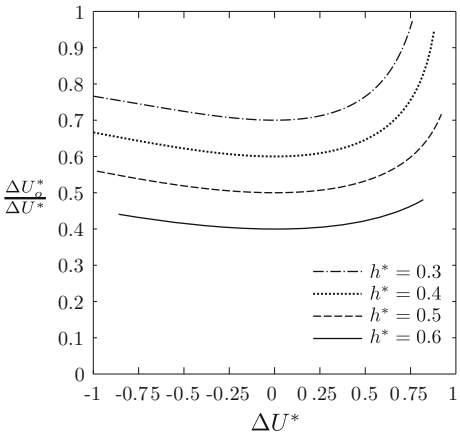

Fig. 34 Ratio of the outflow shear to the inflow shear of the ambient streams. TL configuration with $h_{1i}^* = h_{2i}^* = 0.5$

Figure 33 shows the minimum shear required for a gravity current to have a certain thickness, for different inlet height values h_{1i}^*. This minimum shear value is given by the velocity jump ΔU^* for zero head loss. We observe that the required minimum shear is a strong function of h_{1i}^*. For a given current height, a thinner lower ambient stream translates into a significantly smaller value of ΔU^*.

Figure 34 displays the ratio of outflow to inflow shear, $\Delta U_o^*/\Delta U^* = (U_{1o}^* - U_{2o}^*)/\Delta U^*$, as a function of the inflow shear ΔU^* for various gravity current heights. We observe that the outflow shear ΔU_o^* is always less than ΔU^*. This is a consequence of the higher average velocity of the ambient streams at the outflow, as compared to the inflow. Vorticity conservation dictates that the product of this average velocity and the velocity difference between the two streams remain constant, so that a larger average velocity necessarily leads to a reduced velocity difference. The continuity equation requires that the overall acceleration of the two ambient streams is stronger for larger gravity current heights, so that the reduction in shear becomes more pronounced for larger values of h^*.

Interestingly, the ratio of outflow to inflow shear is larger for a given positive shear magnitude (lower ambient stream faster) than for the same negative shear magnitude (upper ambient stream faster). This can be understood in the following way: The outflow velocity of the lower ambient stream is a function of the gravity current height only, cf. Eq. (48). Consequently, if the lower ambient stream is slower at the inflow than the upper one, it will have to be accelerated more than if it is faster at the inflow. Continuity then tells us that if the upper stream is faster at the inflow, it will have to be accelerated less than if it is slower. As a result, the velocity difference between the ambient streams decreases more strongly if the lower ambient stream is slower at the inflow than the upper one, i.e., if $\Delta U^* < 0$.

This scenario is confirmed by Fig. 35, which displays the influence of ΔU^* on the outflow height h_{1o}^* of the lower ambient stream, and on the ratio h_{2o}^*/h_{1o}^* for different gravity current heights. If the lower ambient stream is the faster one, i.e., if $\Delta U^* > 0$, it experiences weaker acceleration than if $\Delta U^* < 0$, so that it retains

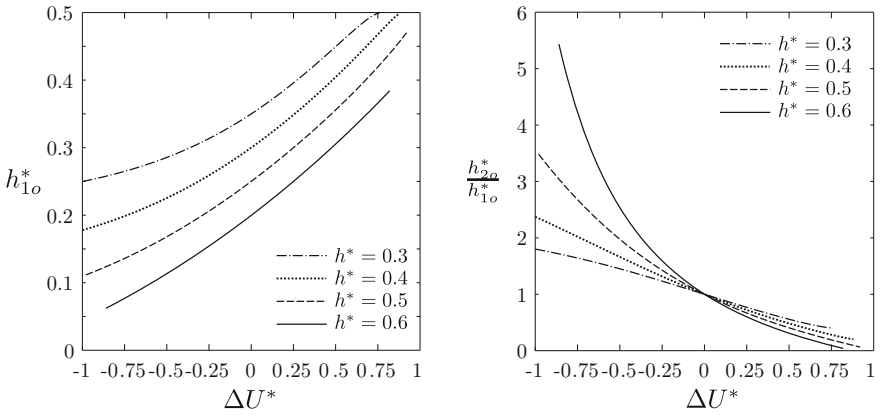

Fig. 35 Influence of inflow shear on the outflow height h^*_{1o} of the *lower* layer (*left*), and on the ratio h^*_{2o}/h^*_{1o} (*right*) for several gravity current heights. TL configuration with $h^*_{1i} = h^*_{2i} = 0.5$

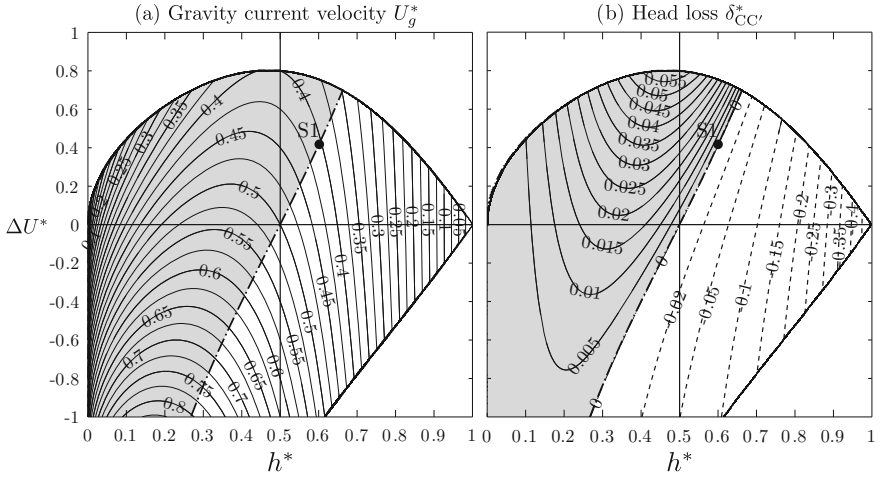

Fig. 36 Configuration SL: Phase-space diagram for: **a** the gravity current velocity U^*_g, and **b** head loss $\delta^*_{CC'}$ along the *upper* wall, as functions of shear ΔU^* and current height h^*. The *gray region* indicates the physically feasible region based on positive values of the head loss $\delta^*_{CC'}$

a larger thickness. Geometry then dictates that h^*_{2o} has to decrease, so that the ratio h^*_{2o}/h^*_{1o} also decreases.

Single-layer configuration Figure 36 displays the gravity current velocity and the head loss along the upper wall for the SL case with a linear inflow velocity profile, cf. Fig. 29. Similar to the TL configuration, we observe that with a constant shear imposed at the inlet, gravity currents exist whose thickness is more than half the channel height. For a detailed derivation of the energy analysis, we refer to Sect. 3.7 below. The range of parameters for which this occurs is quite similar to

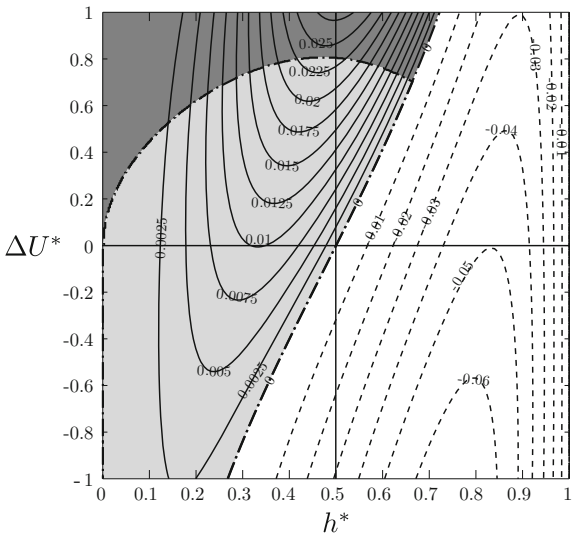

Fig. 37 Phase-space diagram for net energy loss ($\Delta \dot{E}^*$, see Eq. 71) for the SL configuration. The *light gray region* indicates the physically feasible region according to both energy difference and positive inlet/outlet velocities while the *dark gray region* indicates physically feasible solutions when one of the ambient streams flows from *right* to *left*

the corresponding TL configuration with $h^*_{1i} = h^*_{2i} = 0.5$, cf. Fig. 30. Unlike the TL configuration (Fig. 30), case SL does not exhibit a saddle point in the velocity-phase space diagram, Fig. 36a, since the gravity current velocity in the SL configuration varies monotonically with the shear magnitude ΔU in the ambient layer, cf. Eq. (57).

Figure 37 shows the depth-integrated energy loss, Eq. (72) for the SL configuration. As discussed earlier, Eq. (72) indicates that the head loss and depth-integrated energy loss arguments yield the same gray regions, as far as the feasibility of the solution is concerned. While the requirement of a $\Delta \dot{E} \geq 0$ results in the same gray region as obtained via a head loss analysis (see Fig. 36), it further identifies the parameter regime of physically feasible solutions in which ambient stream flow demonstrates mixed inflow-outflow at the inlet region (dark region in Fig. 37). This has been further discussed in Nasr-Azadani and Meiburg (2015).

3.7 Gravity Currents Thicker Than Half the Channel Height

For gravity currents propagating into quiescent ambient fluid, Benjamin (1968) discusses that without external energy input only current heights $h/H \leq \frac{1}{2}$ are possible, while currents with $h/H > \frac{1}{2}$ require external energy input. On the other hand, our theoretical predictions in Figs. 30 and 36 indicate that, for positive shear values $\Delta U > 0$, gravity currents thicker than half the channel height can form both in the TL and the SL configuration. In order to investigate this issue further, Fig. 38 compares the pressure difference $p_{C'} - p_C$, the head loss $\delta_{CC'}$, and the energy loss $\Delta \dot{E}$ for the classical case without shear to the SL case with shear. We remark that the analysis can be extended to the TL configuration in a similar fashion.

The pressure difference along the top wall for the zero shear case reads

$$\Delta p = p_{C'} - p_C = -\frac{1}{H}\left[(\rho_1 - \rho_0)g\frac{h^2}{2} + \rho_0(H-h)2g'h - \rho_0 H U_{g0}^2\right]. \tag{79}$$

Here, U_{g0} denotes the gravity current velocity given by (see Borden and Meiburg 2013a)

$$U_{g0} = (1 - \frac{h}{H})\sqrt{2g'h}\,. \tag{80}$$

For the sake of comparison, we rewrite the pressure drop obtained in the SL configuration (see Eq. 64) as

$$\begin{aligned}\Delta p\Big|^{SL} &= p_{C'} - p_C = -\frac{1}{H}\Bigg[(\rho_1 - \rho_0)g\frac{h^2}{2} + \rho_0(H-h)2g'h - \rho_0 H U_{g0}^2 \\ &+ \rho_0 H(1-\frac{h}{H})\left(-\frac{1}{2}g'h + \frac{1}{3}\left\{\Delta U(1-\frac{h}{H}) - \frac{3}{2}\sqrt{2g'h}\right\}^2\right) \\ &- \rho_0 H\frac{\Delta U^2}{12} - \rho_0 H\Delta U(1-\frac{h}{H})^3\left\{\frac{1}{4}(1-\frac{h}{H})\Delta U - \sqrt{2g'h}\right\}\Bigg].\end{aligned} \tag{81}$$

Figure 38 demonstrates that for positive shear values the pressure difference Δp increases. Recalling the definition of head loss and energy drop from Eqs. (59) and (72), we find that this modified pressure difference term allows gravity currents with heights $h/H > \frac{1}{2}$ to have a positive head loss and energy loss, suggesting a physically possible flow.

4 Concluding Remarks

The modeling of compositional gravity currents via DNS simulations has reached a certain level of maturity. However, the same cannot yet be said about about concentrated turbidity currents that give rise to significant erosion, resuspension, and bedload transport. Especially the dynamics of the near-bed region of such currents is still poorly understood, as it is governed by particlefluid and particleparticle interactions that result in strongly non-Newtonian dynamics, and by mass and momentum exchanges between the current and the sediment bed. Nevertheless, in recent years novel avenues have emerged for obtaining insight into the erosional and depositional behaviors of such currents, for example via incorporating concepts of the so-called

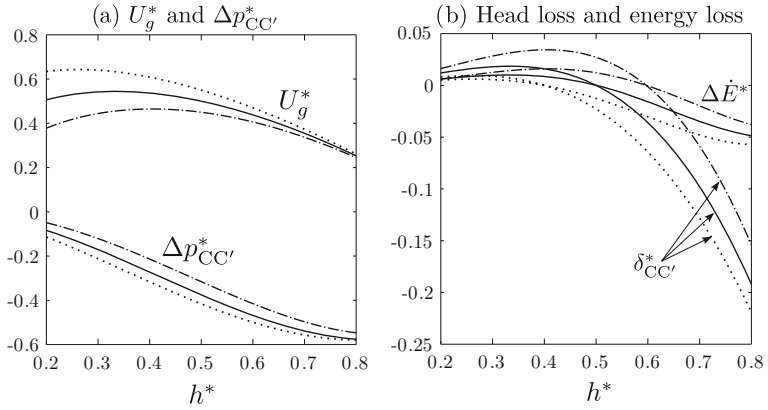

Fig. 38 **a** Gravity current velocity U_g^* and pressure difference Δp^* along the *top* wall. **b** Head loss $\delta^*_{CC'}$ and energy loss $\Delta \dot{E}^*$. The *solid*, *dotted* and *dash-dotted lines*, respectively, correspond to the cases of gravity currents without shear, with negative shear $\Delta U^* = -0.4$, and with positive shear $\Delta U^* = 0.4$ in the SL configuration. Only for positive shear can the head loss (and energy loss) be positive for $h^* > \frac{1}{2}$

$\mu(I)$-rheology. Furthermore, recently developed grain-resolving simulations appear to hold great potential in this regard as well. The application of these novel modeling approaches holds great promise for substantial progress in turbidity current research over the next decade.

References

O.S. Al Ja Aidi, The influence of topography and flow efficiency on the deposition of turbidites. Ph.D. thesis, University of Leeds, 2000

C.J. Baker, Vortex flow around the bases of obstacles. Ph.D. thesis, University of Cambridge, 1978

C.J. Baker, The turbulent horseshoe vortex. J. Wind Eng. Ind. Aerodyn. **6**(1), 9–23 (1980)

T.B. Benjamin, Gravity currents and related phenomena. J. Fluid Mech. **31**(2), 209–248 (1968)

V.K. Birman, J.E. Martin, E. Meiburg, The non-Boussinesq lock-exchange problem. Part 2. High-resolution simulations. J. Fluid Mech. **537**, 125–144 (2005)

F. Blanchette, M. Strauss, E. Meiburg, B. Kneller, M.E. Glinsky, High-resolution numerical simulations of resuspending gravity currents: conditions for self-sustainment. J. Geophys. Res. **110**(C12), C120–C122 (2005)

R.T. Bonnecaze, H.E. Huppert, J.R. Lister, Particle-driven gravity currents. J. Fluid Mech. **250**, 339–369 (1993)

Z. Borden, E. Meiburg, Circulation based models for Boussinesq gravity currents. Phys. Fluids **25**(10), 101301 (2013a)

Z. Borden, E. Meiburg, Circulation-based models for Boussinesq internal bores. J. Fluid Mech. **726**, R1 (2013b)

Z. Borden, E. Meiburg, G. Constantinescu, Internal bores: an improved model via a detailed analysis of the energy budget. J. Fluid Mech. **703**, 279–314 (2012)

M.I. Cantero, S. Balachandar, A. Cantelli, C. Pirmez, G. Parker, Turbidity current with a roof: direct numerical simulation of self-stratified turbulent channel flow driven by suspended sediment. J. Geophys. Res. **114**(C3), C03008 (2009)
A.J. Chorin, Numerical solution of the Navier-Stokes equations. Math. Comput. **22**(104), 745–762 (1968)
W. Dade, H.E. Huppert, A box model for non-entraining, suspension-driven gravity surges on horizontal surfaces. Sedimentology **42**(3), 453–470 (1995)
F. de Rooij, S.B. Dalziel, Time- and space-resolved measurements of the deposition under turbidity currents. Spec. Publ. Int. Assoc. Sedimentol. **31**, 207–215 (2001)
W.E. Dietrich, Settling velocity of natural particles. Water Resour. Res. **18**(6), 1615–1626 (1982)
T.L. Doligalski, C.R. Smith, J.D.A. Walker, Vortex interactions with walls. Annu. Rev. Fluid Mech. **26**, 573–616 (1994)
S. Elghobashi, G.C. Truesdell, On the two-way interaction between homogeneous turbulence and dispersed solid particles. 1. Turbulence modification. Phys. Fluids A **5**, 1790–1801 (1993)
T.H. Ellison, J.S. Turner, Turbulent entrainment in stratified flows. J. Fluid Mech. **6**(3), 423–448 (1959)
M. Garcia, G. Parker, Experiments on the entrainment of sediment into suspension by a dense bottom current. J. Geophys. Res. **98**(3), 4793–4807 (1993)
C. Gladstone, J.C. Phillips, R.S.J. Sparks, Experiments on bidisperse, constant-volume gravity currents: propagation and sediment deposition. Sedimentology **45**(5), 833–843 (1998)
B. Hall, E. Meiburg, B. Kneller, Channel formation by turbidity currents: Navier-Stokes-based linear stability analysis. J. Fluid Mech. **615**, 185–210 (2008)
M. Hallworth, A. Hogg, H.E. Huppert, Effects of external flow on compositional and particle gravity currents. J. Fluid Mech. **359**, 109–142 (1998)
T.C. Harris, A.J. Hogg, H.E. Huppert, Polydisperse particle-driven gravity currents. J. Fluid Mech. **472**, 333–371 (2002)
C. Härtel, E. Meiburg, F. Necker, Vorticity dynamics during the start-up phase of gravity currents. Nuovo Cimento-societa Italiana di Fisica-C **22**(6), 823–834 (1999)
C. Härtel, F. Carlsson, M. Thunblom, Analysis and direct numerical simulation of the flow at a gravity-current head. Part 2. The lobe-and-cleft instability. J. Fluid Mech. **418**, 213–229 (2000a)
C. Härtel, E. Meiburg, F. Necker, Analysis and direct numerical simulation of the flow at a gravity-current head. Part 1. Flow topology and front speed for slip and no-slip boundaries. J. Fluid Mech. **418**, 189–212 (2000b)
A. Harten, High resolution schemes for hyperbolic conservation laws. J. Comput. Phys. **135**(2), 260–278 (1997)
A. Harten, B. Engquist, S. Osher, S.R. Chakravarthy, Uniformly high order accurate essentially non-oscillatory schemes. III. J. Comput. Phys. **71**(2), 231–303 (1987)
H. Huang, J. Imran, C. Pirmez, Numerical study of turbidity currents with sudden-release and sustained-inflow mechanisms. J. Hydraul. Eng. **134**(9), 1199–1209 (2008)
H.E. Huppert, The intrusion of fluid mechanics into geology. J. Fluid Mech. **173**, 557–594 (1986)
H.E. Huppert, J.E. Simpson, The slumping of gravity currents. J. Fluid Mech. **99**(4), 785–799 (1980)
M. Janocko, M.B.J. Cartigny, W. Nemec, E.W.M. Hansen, Turbidity current hydraulics and sediment deposition in erodible sinuous channels: laboratory experiments and numerical simulations. Mar. Pet. Geol. **41**, 222–249 (2013)
I.A. Kane, W.D. McCaffrey, J. Peakall, B.C. Kneller, Submarine channel levee shape and sediment waves from physical experiments. Sediment. Geol. **223**(1), 75–85 (2010)
A. Kassem, J. Imran, Three-dimensional modeling of density current. II. Flow in sinuous confined and uncontined channels. J. Hydraul. Res. **42**(6), 591–602 (2004)
J. Kim, P. Moin, Application of a fractional-step method to incompressible Navier-Stokes equations. J. Comput. Phys. **59**(2), 308–323 (1985)
J.B. Klemp, R. Rotunno, W.C. Skamarock, On the propagation of internal bores. J. Fluid Mech. **331**, 81–106 (1997)

B. Kneller, W.D. McCaffrey, Depositional effects of flow nonuniformity and stratification within turbidity currents approaching a bounding slope; deflection, reflection, and facies variation. J. Sediment. Res. **69**(5), 980–991 (1999)
Y. Kubo, Experimental and numerical study of topographic effects on deposition from two-dimensional, particle-driven density currents. Sediment. Geol. **164**(3–4), 311–326 (2004)
Y. Kubo, T. Nakajima, Laboratory experiments and numerical simulation of sediment-wave formation by turbidity currents. Mar. Geol. **192**(1), 105–121 (2002)
P.H. Kuenen, C.I. Migliorini, Turbidity currents as a cause of graded bedding. J. Geol. **58**(2), 91–127 (1950)
L. Lesshafft, B. Hall, E. Meiburg, B. Kneller, Deep-water sediment wave formation: linear stability analysis of coupled flow/bed interaction. J. Fluid Mech. **680**, 435–458 (2011)
P. Linden, *Gravity Current-Theory and laboratory Experiments* (Cambridge University Press, Cambridge, 2012)
S. Lüthi, Experiments on non-channelized turbidity currents and their deposits. Mar. Geol. **40**(3–4), M59–M68 (1981)
M.R. Maxey, B.K. Patel, E.J. Chang, L.P. Wang, Simulations of dispersed turbulent multiphase flow. Fluid Dyn. Res. **20**(1), 143–156 (1997)
E. Meiburg, B. Kneller, Turbidity currents and their deposits. Annu. Rev. Fluid Mech. **42**, 135–156 (2010)
E. Meiburg, E. Wallner, A. Pagella, A. Riaz, C. Hartel, F. Necker, Vorticity dynamics of dilute two-way-coupled particle-laden mixing layers. J. Fluid Mech. **421**, 185–227 (2000)
G.V. Middleton, Sediment deposition from turbidity currents. Annu. Rev. Earth Planet. Sci. **21**, 89–114 (1993)
S. Migeon, B. Savoye, E. Zanella, T. Mulder, J.C. Faugères, O. Weber, Detailed seismic-reflection and sedimentary study of turbidite sediment waves on the Var Sedimentary Ridge (SE France): significance for sediment transport and deposition and for the mechanisms of sediment-wave construction. Mar. Pet. Geol. **18**(2), 179–208 (2001)
R. Mittal, H. Dong, M. Bozkurttas, F.M. Najjar, A. Vargas, A. von Loebbecke, A versatile sharp interface immersed boundary method for incompressible flows with complex boundaries. J. Comput. Phys. **227**(10), 4825–4852 (2008)
J. Mohd-Yusof, Combined immersed-boundary/B-spline methods for simulations of flow in complex geometries. CTR Annu. Res. Briefs, 317–327 (1997). NASA Ames/Stanford University
T. Nakajima, M. Satoh, The formation of large mudwaves by turbidity currents on the levees of the Toyama deep-sea channel. Japan Sea. Sedimentology **48**(2), 435–463 (2001)
M.M. Nasr-Azadani, Understanding Turbidity Currents Interacting With Complex Seafloor Topographies: A Depth-Resolved Numerical Investigation. Ph.D. thesis, University of California at Santa Barbara, 2013
M.M. Nasr-Azadani, E. Meiburg, TURBINS: An immersed boundary, Navier-Stokes code for the simulation of gravity and turbidity currents interacting with complex topographies. Comput. Fluids **45**(1), 14–28 (2011)
M.M. Nasr-Azadani, E. Meiburg, Influence of seafloor topography on the depositional behavior of bi-disperse turbidity currents: a three-dimensional, depth-resolved numerical investigation. Environ. Fluid Mech. **14**(2), 319–342 (2014)
M.M. Nasr-Azadani, E. Meiburg, Gravity currents propagating into shear. J. Fluid Mech. **778**, 552–585 (2015)
M.M. Nasr-Azadani, B. Hall, E. Meiburg, Polydisperse turbidity currents propagating over complex topography: comparison of experimental and depth-resolved simulation results. Comput. Geosci. **53**, 141–153 (2013)
F. Necker, C. Härtel, L. Kleiser, E. Meiburg, High-resolution simulations of particle-driven gravity currents. Int. J. Multiph. Flow **28**(2), 279–300 (2002)
F. Necker, C. Härtel, L. Kleiser, E. Meiburg, Mixing and dissipation in particle-driven gravity currents. J. Fluid Mech. **545**, 339–372 (2005)

R.I. Nokes, M.J. Davidson, C.A. Stepien, W.B. Veale, R.L. Oliver, The front condition for intrusive gravity currents. J. Hydraul. Res. **46**(6), 788–801 (2008)
W.R. Normark, D.J.W. Piper, H. Posamentier, C. Pirmez, S. Migeon, Variability in form and growth of sediment waves on turbidite channel levees. Mar. Geol. **192**(1), 23–58 (2002)
C.D. Oehy, A.J. Schleiss, Control of turbidity currents in reservoirs by solid and permeable obstacles. J. Hydraul. Eng. **133**(6), 637–648 (2007)
J. Peakall, K.J. Amos, G.M. Keevil, P.W. Bradbury, S. Gupta, Flow processes and sedimentation in submarine channel bends. Mar. Pet. Geol. **24**(6), 470–486 (2007)
C. Pozrikidis, *Introduction to Theoretical and Computational Fluid Dynamics* (Oxford University Press, Oxford, 2011)
L. Rayleigh, On the theory of long waves and bores. Proc. R. Soc. Lond. Ser. A Contain. Pap. Math. Phys. Character **90**(619), 324–328 (1914)
J.W. Rottman, J.E. Simpson, Gravity currents produced by instantaneous releases of a heavy fluid in a rectangular channel. J. Fluid Mech. **135**, 95–110 (1983)
P.G. Saffman, *Vortex Dynamics* (Cambridge University Press, Cambridge, 1992)
J.O. Shin, S.B. Dalziel, P.F. Linden, Gravity currents produced by lock exchange. J. Fluid Mech. **521**, 1–34 (2004)
J.E. Simpson, Effects of the lower boundary on the head of a gravity current. J. Fluid Mech. **53**(4), 759–768 (1972)
J.E. Simpson, *Gravity Currents: In the Environment and the Laboratory* (Cambridge University Press, Cambridge, 1997)
P.K. Smolarkiewicz, R. Rotunno, Low Froude number flow past three-dimensional obstacles. Part II: upwind flow reversal zone. J. Atmos. Sci. **47**(12), 1498–1511 (1990)
W. H. Snyder, R. E. Britter, and J. C. R. Hunt, A fluid modeling study of the flow structure and plume impingement on a three dimensional hill in stably stratified flow, in *Wind Engineering-Proceedings of the Fifth International Conference*, vol. 1 (Pergamon Press, 1979), pp. 319–329
W.H. Snyder, J.C.R. Hunt, J.T. Lee, I.P. Castro, R.E. Lawson, R.E. Eskridge, R.S. Thompson, Y. Ogawa, Structure of strongly stratified flow over hills: dividing-streamline concept. J. Fluid Mech. **152**, 249–288 (1985)
M. Strauss, M.E. Glinsky, Turbidity current flow over an erodible obstacle and phases of sediment wave generation. J. Geophys. Res. **117**(C6), C06007 (2012)
M. Vinokur, On one-dimensional stretching functions for finite-difference calculations. J. Comput. Phys. **50**(2), 215–234 (1983)
T. von Kármán, The engineer grapples with nonlinear problems. Bull. Am. Math. Soc. **46**(8), 615–683 (1940)
K.B. Winters, L. Armi, Hydraulic control of continuously stratified flow over an obstacle. J. Fluid Mech. **700**, 502–513 (2012)
I.R.F. Wood, J.E. Simpson, Jumps in layered miscible fluids. J. Fluid Mech. **140**, 329–342 (1984)
A.W. Woods, M.I. Bursik, A.V. Kurbatov, The interaction of ash flows with ridges. Bull. Volcanol. **60**(1), 38–51 (1998)
R.B. Wynn, D.A.V. Stow, Classification and characterisation of deep-water sediment waves. Mar. Geol. **192**(1–3), 7–22 (2002)
R.B. Wynn, G. Weaver, P.P.E. Ercilla, D.A.V. Stow, D.G. Masson, Sedimentary processes in the Selvage sediment-wave field, NE Atlantic: new insights into the formation of sediment waves by turbidity currents. Sedimentology **47**(6), 1181–1197 (2000)
C.-S. Yih, *Dynamics of Nonhomogeneous Fluids*, vol. 306 (Macmillan, New York, 1965)

Transport Phenomena in Rotating Turbulence

Herman J.H. Clercx

Abstract The role of rotation on turbulence and some of its transport properties will be reviewed with emphasis on two specific cases: statistically steady or decaying rotating turbulence and rotating thermally driven turbulence. For this purpose we briefly address a few basic concepts relevant for understanding processes in rotating (turbulent) flows such as the emergence of coherent structures, the Taylor-Proudman theorem, quasi-two-dimensional turbulence, inertial waves and Ekman boundary layers. The effect of rotation on turbulence will subsequently be illustrated with two sets of laboratory experiments: one with steadily forced rotating turbulence and another with rotating turbulent convection.

1 Introduction

The classical starting point for fundamental turbulence studies is the case where statistical homogeneity and isotropy can be assumed for the (unbounded) turbulent flow over the full range of dynamically active length scales provided these scales are sufficiently smaller than the forcing length scale. It is known to us as three-dimensional (3D) homogeneous isotropic turbulence and its fundamental description and understanding is based on ideas put forward by Kolmogorov and many others, see, for example, Frisch (1995). However, there are many ways and situations where this ideal scenario is distorted. For example, when the flow is subjected to background rotation a preferential direction will be introduced, the rotation axis, which may imply statistical anisotropy at a certain range of length scales. Similarly, buoyancy-driven turbulence also implies the presence of a preferred coordinate direction, in

H.J. Clercx (✉)
Fluid Dynamics Laboratory, Department of Applied Physics,
Eindhoven University of Technology, 513, 5600MB Eindhoven, The Netherlands
e-mail: H.J.H.Clercx@tue.nl

H.J. Clercx
J.M. Burgers Center for Fluid Dynamics, Eindhoven, The Netherlands

H.J.H. Clercx and G.J.F. van Heijst (eds.), *Mixing and Dispersion in Flows Dominated by Rotation and Buoyancy*, CISM International Centre for Mechanical Sciences 580,
https://doi.org/10.1007/978-3-319-66887-1_7

this case parallel to gravity. Although in principle both rotating turbulence and buoyancy driven turbulence can be investigated without confinement almost all examples occurring in nature and in engineering applications have some sort of confinement.

Many technological applications exist where rotation affects both bulk turbulence and boundary layer flows. For example, convective cooling in turbomachinery (Johnston 1998; Dunn 2001), mixing processes in chemical reactors, and chemical vapour deposition on heated rotating substrates, see, for example, Van Santen et al. (2000). In large-scale turbulent flows like in oceanography (see, e.g., Gascard et al. 2002; Wadhams et al. 2002), meteorology (Hartmann et al. 2001), the atmospheric boundary layer (both convective and stably stratified), and turbidity currents, density stratification and (at larger length scales) background rotation play a major role in shaping the flow dynamics and associated transport properties. A few illustrative examples are huge volcanic eruptions with a highly-turbulent particle-laden plume, see Fig. 1a, which at higher altitudes collapses and the ashes eventually are distributed over huge areas of the globe by large-scale atmospheric flows, and the dispersion of phytoplankton blooms in oceanic currents, see Fig. 1b. Transport of phytoplankton blooms is determined by flows affected by density stratification at shorter length scales and background rotation at large scales (larger than approximately 100 km). Rotating flows inside the liquid core of the Earth are responsible for stretching and twisting of the magnetic field lines of the Earth. In this way the magnetic field is prevented from being extinguished by natural decay. In astrophysical flows typical examples where rotation affects the dynamics include convection in stars (Miesch 2000) and accretion disks.

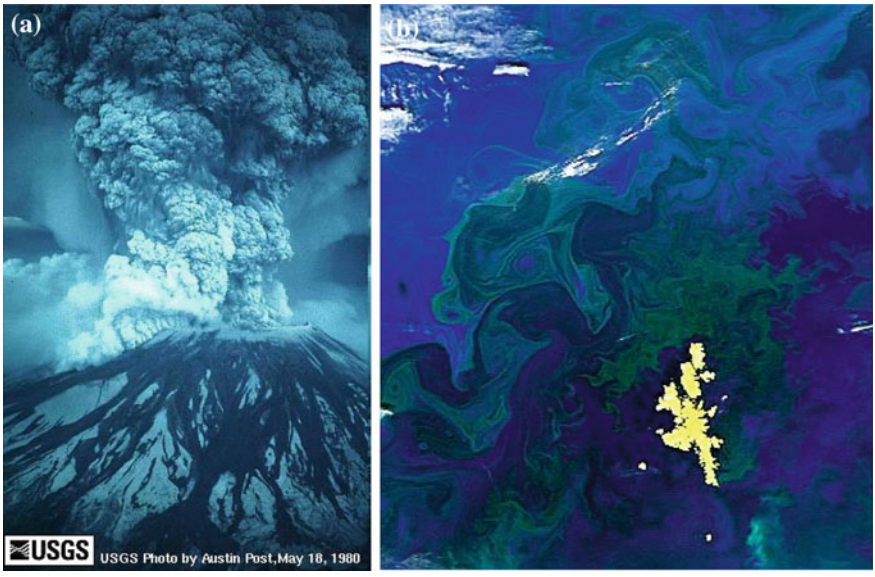

Fig. 1 **a** The eruption of Mount St. Helens, Washington, USA, on May 18, 1980 (courtesy of Austin Post, USGS). **b** Phytoplanton bloom west of the Faeroer Islands (courtesy of NASA Goddard Space Flight Center)

Having a closer look at systems like those discussed above one should be aware that in such flows turbulence and wave dynamics can be distinguished, and they often show up simultaneously. Typical waves are the internal gravity waves (when a background density gradient is available), inertial waves sustained by the Coriolis force, and, in for magnetohydrodynamics we have Alfvén waves (along the magnetic field lines in electrically conducting fluids).

1.1 Homogeneous Isotropic Turbulence

As a starting point we summarize some typical properties and quantities relevant for describing homogeneous isotropic turbulence. This will not be an exhaustive overview, such as can be found in many text books, see Frisch (1995) and Pope (2000), as the main aim here is to bring together the relevant quantities and describe the basic phenomena that will show up again when discussing rotating (thermally driven) turbulence. Our illustration will be based on a few snapshots from a numerical simulation study conducted by Kaneda and coworkers, for details see Ishihara et al. (2007), see Fig. 2. They conducted a high-resolution Direct Numerical Simulation (DNS) of the incompressible Navier-Stokes equations in a 3D periodic cube with resolution up to 4096^3 grid points. They generated statistically steady homogeneous isotropic turbulence by forcing the flow at the large scales, a scale which we can designate as the integral scale $\mathcal{L}$. The typical integral-scale Reynolds number of the flow is defined according to: $Re = \mathcal{U}\mathcal{L}/\nu$, with $\mathcal{U}$ the integral-scale velocity (here we can choose $\mathcal{U} \approx u_{rms}$, with u_{rms} the root-mean-squared velocity of the turbulent flow), and ν the kinematic viscosity of the fluid. The energy input at the large scales should eventually be dissipated at the smallest scales in order to achieve a statistically steady state. The energy input can thus be expressed in terms of the dissipation rate $\epsilon \approx \mathcal{U}^3/\mathcal{L}$. The energy injected at these large scales is transported by a process of subsequent break-ups of eddies, the so-called Kolmogorov cascade taking place in the inertial range, to the smallest dissipative scales where the kinetic energy is converted to internal energy of the fluid, see the sketch in Fig. 3. During the cascade process virtually no kinetic energy is dissipated, and formal absence of dissipation in the inertial range and the assumption of self-similarity is the basis of the famous scaling property of the kinetic energy $E(k) \propto \epsilon^{2/3}k^{-5/3}$ signifying the distribution of kinetic energy over the wave numbers k (or scales $l = 2\pi/k$) in a turbulent flow. At sufficiently high wave numbers (or small wave lengths) both the advection and diffusion time scale for momentum transport become similar. The length scale where this occurs is called the Kolmogorov length scale η and can be expressed in terms of the dissipation rate and kinematic viscosity, the only two physical quantities that play a role here, thus $\eta = (\nu^3/\epsilon)^{1/4}$. Typical velocity and time scales at the Kolmogorov scale are: $v_\eta = (\epsilon\nu)^{1/4}$ and $\tau_\eta = (\nu/\epsilon)^{1/2}$, and the Reynolds number based on the Kolmogorov scales is just $Re_\eta = v_\eta\eta/\nu = 1$. It can immediately be shown that $\eta/\mathcal{L} = Re^{-3/4}$ which indicates that a well-resolved simulation of turbulence requires $N \simeq Re^{3/4}$ grid points per coordinate direction.

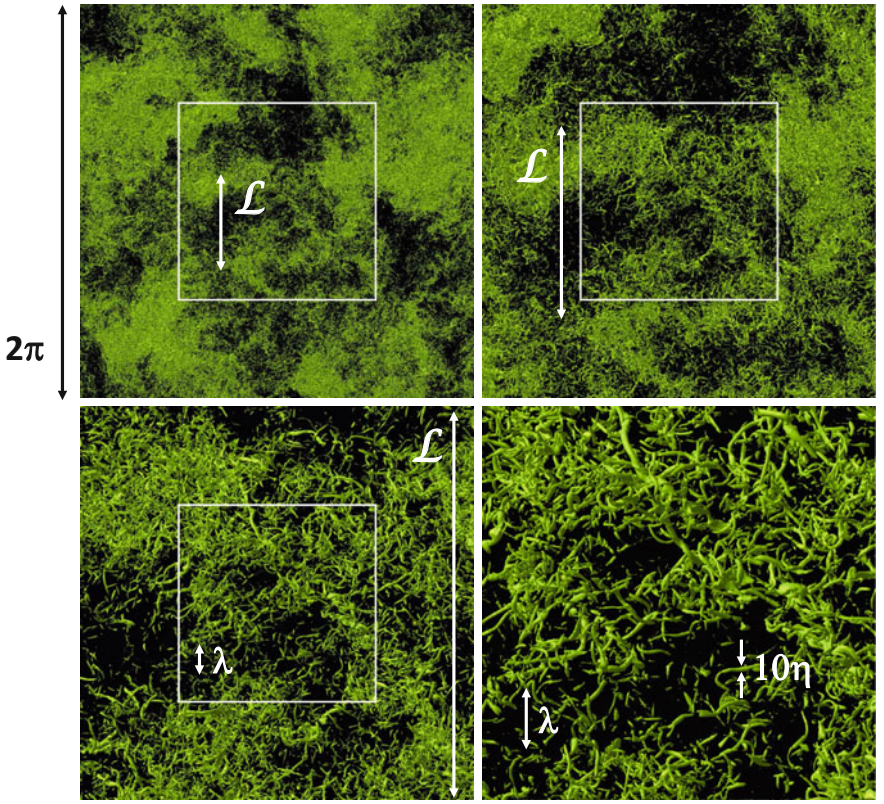

Fig. 2 A few snapshots from the simulation by Kaneda and collaborators on the Earth Simulator in Japan. Equivorticity surfaces are shown enabling visualization of intense vorticity filaments in the flow. For details we refer to the studies by Yokokawa et al. (2002); Ishihara et al. (2007). Starting with the *top-left panel* each subsequent panel (*top-right*, *bottom-left* and *bottom-right*) represent an enlargement by a factor of two (each panel shows the vorticity field from the *white box* in the preceding panel. The integral scale $\mathcal{L}$, the Taylor microscale λ, and Kolmogorov (dissipation) scale η are indicated in the *panels*, and are based on the estimates from Kaneda and Ishihara (2006)). Courtesy of Yokokawa et al. (2002)

The preceding discussion would suggest that the energy spectrum and the dissipation spectrum are strictly separated, but that is not exactly true. The high wave number range of the energy spectrum shows some overlap with the dissipation spectrum that starts to contribute significantly at these (and much higher) wave numbers. It is actually at those wave numbers or length scales, which we call the Taylor microscale λ, where production of kinetic energy balances dissipation of kinetic energy. Dissipation occurs in regions of high gradients thus: $\epsilon = \mathcal{O}(\nu \mathcal{U}^2/\lambda^2)$ from which we can show that $\lambda/\mathcal{L} = Re^{-1/2}$. An expression for the Taylor microscale in terms of basic turbulence properties is $\lambda = u_{rms}^2 \sqrt{15\nu/\epsilon}$ and the Taylor-based Reynolds number is defined as $Re_\lambda = u_{rms}\lambda/\nu$.

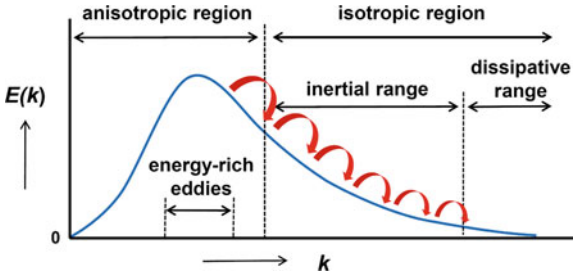

Fig. 3 A sketch of the energy spectrum as function of wave number k indicating the inertial and dissipation range and distinguishing the anisotropic from the isotropic region

1.2 What Is the Effect of Rotation on Turbulence?

Over the past four decades many laboratory experiments on rotating turbulence have been conducted with a variety of laboratory configurations. A detailed overview has recently been provided by Godeferd and Moisy (2015), see also their Table 1. Here, we will mention a few examples in order to highlight some important observations.

Decaying grid turbulence, generated by a single-grid-stroke forcing in an air flow, inside a rotating annular container, has been investigated by Ibbetson and Tritton (1975). They used hot-wire measurements and observed faster decay of turbulence under influence of increasing rotation rate and a large increase in the length scale in the axial direction (parallel to the rotation axis) and a smaller increase in the lateral direction. The first oscillating grid experiments in rotating fluids were reported by Hopfinger et al. (1982) and shortly after by Dickinson and Long (1983) using a different range of integral-scale Reynolds number (and similar grid-based Rossby numbers which represent the rotation time scale over the advection time scale). By vertically oscillating a grid near the bottom of a vertically elongated cylindrical container, mounted on a rotating table (with rotation axis parallel with the vertical), Hopfinger et al. (1982) generated statistically steady rotating turbulence with turbulence intensity decaying upwards (thus vertically inhomogeneous). The turbulent flow in the neighbourhood of the vertically oscillating grid, where the turbulence time scale is much smaller than the rotation time scale (i.e. $Ro \gg 1$), is hardly affected by the background rotation. It behaves locally like 3D homogeneous isotropic turbulence. On the other hand, far above the oscillating grid, where the turbulence intensity is substantially decreased (and the typical advection time scale is much larger than the rotation time scale, thus $Ro \lesssim 1$), vertically-aligned vortical structures (mainly cyclonic, i.e. swirling in the same direction as the background rotation) have been observed together with an overall increase of the integral length scale of the turbulent flow with rotation rate. Apparently, rotating turbulence behaves quasi-two-dimensional, statistical anisotropy is evident and its statistical properties seem more or less independent of the vertical axis. Godeferd and Lollini (1999) have mimicked some aspects of the experiment by Hopfinger et al. (1982) with numerical simulations and observed the formation of columnar vortices aligned with the rotation axis for high Reynolds number and reasonably strong background rotation. They attributed the presence of these columnar vortices also to vertical confinement. Moreover, they

observed preference for the formation of cyclones over anticyclones. Jacquin et al. (1990) studied rapidly rotating spatially decaying turbulence with hot-wire measurements and revealed that the primary effect of rotation on turbulence is the inhibition of the energy cascade and associated with that the reduction of the dissipation rate of the turbulent kinetic energy. These experiments also revealed that the velocity correlation length scales parallel with the rotation axis tend to be larger in the presence of rotation compared to the case without rotation. Numerical studies have confirmed that the faster growth of these length scales is related with the inhibition of the energy cascade, see, for example, Bardina et al. (1985), Bartello et al. (1994), and Cambon et al. (1997).

More recently, a variety of experiments have been reported on decaying rotating turbulence, generated mostly by a single grid stroke or single oscillation of a grid in water, for example, the investigations by Dalziel (1992), Morize et al. (2005), Davidson et al. (2006), Seiwert et al. (2008), Staplehurst et al. (2008), and Moisy et al. (2011). Experiments on statistically steady forced rotating turbulence have been conducted less frequently. Besides the oscillating grid experiments by Hopfinger et al. (1982) and Dickinson and Long (1983), where the effects of rotation on turbulence are measured away from the forcing region (and the turbulent flow is characterized by spatial decay away from the oscillating grid), forcing based on jets (sources) and sinks, see Baroud et al. (2002, 2003), on electromagnetic forcing of electrolyte solutions, see Van Bokhoven et al. (2009), Del Castello and Clercx (2011a, b), and on the application of several sets of flapping plates (oriented parallel with the rotation axis), see Campagne et al. (2014), have been reported where measurements have been conducted in the region of forcing. In both the decaying and forced turbulence experiments a variety of issues, such as velocity statistics, structure function scaling, characterization and visualization of coherent structures in rotating turbulence, Lagrangian velocity and acceleration statistics, geometrical statistics of the vorticity vector in rotating turbulence, etc. For details on the experimental settings (including ranges of Rossby and Reynolds numbers in each of these experiments), the particular experimental setups used, and with regard to some of the issues mentioned above the reader is referred to the recent overview paper by Godeferd and Moisy (2015).

With regard to numerical studies of homogeneous decaying turbulence we should mention, for example, Yeung and Zhou (1998), Morinishi et al. (2001), Thiele and Müller (2009), Teitelbaum and Mininni (2010), Yoshimatsu et al. (2011), Teitelbaum and Mininni (2011), and Delache et al. (2014). For forced rotating turbulence, see, for example, Smith and Waleffe (1999), Thiele and Müller (2009), and Mininni et al. (2012). Thus quite some activity has been going on in recent decades, see the discussion by Godeferd and Moisy (2015) about the specific setups and the range of Rossby and Reynolds numbers in these simulations. One of the largest simulations recently performed is a forced rotating turbulence simulation by Mininni et al. (2012) with Beltrami large-scale helical forcing. Their integral-scale Reynolds number is large $Re \simeq 27 \times 10^3$ and typical Rossby number was $Ro \sim 0.07$, thus well in the regime where rotation dominated the turbulent flow.

All these observations bring us to the question of which processes in rotating (turbulent) flows are responsible for the specific statistical properties, large-scale

anisotropic flow structuring, and scaling properties of rotating turbulence? Moreover, also inertial waves are present and play an important role. This overview will not provide answers to all these questions, but below we will provide a concise introduction into some of these aspects. This includes quasi-two-dimensionalization processes in rotating turbulence (Taylor-Proudman theorem), the role of domain boundaries (confinement) and rotating boundary layer flows, and also the origin of inertial waves and their relation with Taylor columns. Before addressing these aspects we will first introduce a regime diagram in Reynolds-Rossby space to pinpoint the different kinds of turbulence dynamics in rotating systems.

Finally, for a more detailed and rigorous analysis of rotating flows the monograph by Greenspan (1968) can be consulted. If one is particularly interested in rotating flows in a geophysical context the reader is referred to the textbook by Pedlosky (1987). For an extensive overview of the theory of rotating and stratified turbulence, including the current state of affairs, the reader is referred to the recent monograph by Davidson (2013).

1.3 Rotating Turbulence: A Regime Diagram

From the preceding Sections it is clear that statistical homogeneity and isotropy cannot be the right starting point for a basic analysis of rotating turbulent flows. Turbulent flows subjected to system rotation, thus the presence of a preferred coordinate axis, are statistically anisotropic, and as a result one distinguishes the coordinate parallel with those perpendicular to the rotation axis. The best we can get is assuming statistical homogeneity (in 3D, provided the turbulent flow is not confined) and statistical isotropy in the 2D plane perpendicular to the rotation axis.

Depending on the integral-scale Reynolds number Re and the rotation rate Ω, which is usually quantified in terms of the Rossby number, $Ro \propto \Omega^{-1}$, we can distinguish between 3D homogeneous isotropic turbulence, quasi-two-dimensional turbulence and wave turbulence. In Fig. 4 we illustrate these regimes in the so-called (Re, Ro) regime diagram. In the linear or low-Reynolds number regime applicable for very rapidly rotating flows ($Ro \ll 1$) inertial waves are observed. For similar rotation rates but with increased Reynolds number the non-linear interactions become dominant. This is the regime of wave-turbulence. Finally, for rotation-dominated turbulence ($Ro < 1$) at high Reynolds number we arrive at a kind of quasi-two-dimensional turbulence where the fluid motion predominantly takes place in planes perpendicular to the rotation axis. Here, we immediately see the challenge for laboratory experiments on rotating turbulence due to Reynolds and Rossby number constraints, $Re \gg 1$ and $Ro \lesssim 1$. These constraints can be reformulated as $\nu/\mathcal{L} \ll \mathcal{U} \lesssim 2\Omega\mathcal{L}$. Suppose we conduct a typical laboratory experiment in water with $\mathcal{L} \approx 0.1$ m, $\Omega = 1$ rad/s, and $\nu = 1 \times 10^{-6}$ m^2/s. The constraint mentioned before reformulates into: $10^{-5} \ll \mathcal{U} \lesssim 2 \times 10^{-1}$ m/s, thus the integral-scale Reynolds number is always relatively moderate in typical laboratory experiments.

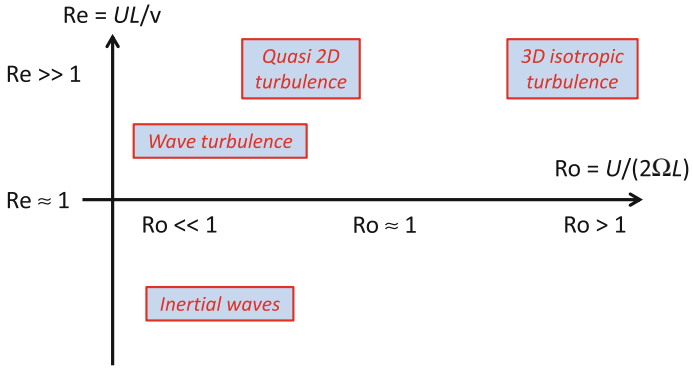

Fig. 4 A very schematic representation of the different regimes in rotating turbulence in the (Re, Ro)-plane. It serves the purpose to quickly decide what kind of turbulence is expected for the different combinations of Reynolds and Rossby numbers

2 Taylor-Proudman Theorem and Inertial Waves

As already briefly discussed and illustrated before the dynamics of geophysical and astrophysical flows and those of many industrial flows is strongly affected by system rotation. It turns out that an analysis of such flows in a co-rotating frame of reference is most suitable despite the appearance of additional terms in the Navier-Stokes equations, the so-called fictitious forces (as we are analysing the flow in a non-inertial frame of reference).

2.1 Navier-Stokes Equation in a Rotating Frame of Reference

We introduce a steadily rotating (non-inertial) frame of reference. The angular velocity with respect to the laboratory frame is Ω. For any vector $\mathbf{Q}$ a relation exists between the time-derivative of $\mathbf{Q}$ in the inertial and rotating reference frame (denoted with indices I and R, respectively):

$$\left(\frac{d\mathbf{Q}}{dt}\right)_I = \left(\frac{d\mathbf{Q}}{dt}\right)_R + \Omega \times \mathbf{Q}\,. \tag{1}$$

We then obtain for the position vector $\mathbf{r}$,

$$\left(\frac{d\mathbf{r}}{dt}\right)_I = \left(\frac{d\mathbf{r}}{dt}\right)_R + \Omega \times \mathbf{r}\,, \tag{2}$$

or $\mathbf{u}_I = \mathbf{u}_R + \Omega \times \mathbf{r}$. The relation between the acceleration of a fluid parcel in the inertial and the rotating frame is found by applying relation (1) once again, now with $\mathbf{u}_I$,

$$\left(\frac{d\mathbf{u}_I}{dt}\right)_I = \left(\frac{d\mathbf{u}_I}{dt}\right)_R + \Omega \times \mathbf{u}_I = \left(\frac{d\mathbf{u}_R}{dt}\right)_R + 2\Omega \times \mathbf{u}_R + \Omega \times (\Omega \times \mathbf{r}) \,. \quad (3)$$

Here, $2\Omega \times \mathbf{u}_R$ and $\Omega \times (\Omega \times \mathbf{r})$ are the Coriolis acceleration and the centrifugal acceleration, respectively. The latter expression can be rewritten as a gradient of a scalar: $-\nabla(\frac{1}{2}\Omega^2 r_\perp^2)$, with $r_\perp$ the distance from the rotation axis of the point $\mathbf{r}$, and $\Omega = |\Omega|$. Using (3) we can formulate the Navier-Stokes equation in the rotating frame of reference. It reads

$$\frac{\partial \mathbf{u}}{\partial t} + (\mathbf{u} \cdot \nabla)\mathbf{u} + 2\Omega \times \mathbf{u} = -\frac{1}{\rho}\nabla P + \nu \nabla^2 \mathbf{u} \,. \quad (4)$$

In this equation the reduced pressure is introduced: $P = p - \frac{1}{2}\rho\Omega^2 r_\perp^2$. Mass conservation, $\nabla \cdot \mathbf{u} = 0$, complements the momentum equation.

At this point it is convenient to introduce three dimensionless numbers which characterize the rotating flow as they are a measure for the relative importance of inertial, viscous and Coriolis forces in the Navier-Stokes equation. For this purpose we introduce the typical length and velocity scales of the flow, $\mathcal{L}$ and $\mathcal{U}$, respectively. Together with the kinematic viscosity of the fluid ν and the background rotation Ω three dimensionless numbers are defined: the Reynolds number, $Re = \mathcal{U}\mathcal{L}/\nu$, the Rossby number, representing the relative importance of inertial over Coriolis forces, is defined as $Ro = \mathcal{U}/(2\Omega\mathcal{L})$, and the Ekman number which measures the relative importance of viscous over Coriolis forces, $Ek = \nu/(\Omega\mathcal{L}^2)$. Only two of these dimensionless numbers are independent, thus also the dimensionless Navier-Stokes equation contains two dimensionless numbers only, here Ro and Ek, and read

$$\frac{\partial \mathbf{u}}{\partial t} + Ro(\mathbf{u} \cdot \nabla)\mathbf{u} + 2\mathbf{k} \times \mathbf{u} = -\nabla P + Ek \nabla^2 \mathbf{u} \,. \quad (5)$$

In this equation $\mathbf{k}$ is the unit vector in the direction of Ω, time is made dimensionless by Ω^{-1}, and the reduced pressure by $\rho\Omega\mathcal{U}\mathcal{L}$.

2.2 Taylor-Proudman Theorem

For sufficiently large Reynolds number the flow will become turbulent and viscous dissipation is almost negligible in the bulk of the fluid sufficiently far away from domain boundaries. In the boundary layers, on the other hand, viscous effects are not negligible and Coriolis and viscous forces compete (which will be discussed later on). When the background rotation is large, thus $Ro \ll 1$ (or $\mathcal{U} \ll \Omega\mathcal{L}$) we may as

a lowest order approximation ignore the advective and viscous contributions in the Navier-Stokes equation (5). Assuming also (statistical) steadiness of the (mean) flow the motion of the fluid in the rotating frame of reference is governed by

$$2\mathbf{k} \times \mathbf{u} = -\nabla P \, . \tag{6}$$

This equation shows that fluid parcel acceleration is fully determined by the balance between the pressure gradient force and the Coriolis force, which both act perpendicular to the fluid motion, in other words $\mathbf{u} \perp \nabla P$. This important relation is known as the geostrophic balance. It is of importance for explanation of basic phenomena in atmospheric and large-scale oceanic (turbulent) flows.

By taking the curl of the geostrophic balance (6) an important relation for such flows is obtained. As $\nabla \times \nabla P = \mathbf{0}$ it is readily seen that $\nabla \times (\mathbf{k} \times \mathbf{u}) = \mathbf{0}$. After applying some basic vector algebra in conjunction with flow incompressibility we obtain the following relation:

$$\frac{\partial \mathbf{u}}{\partial z} = \mathbf{0} \, . \tag{7}$$

This relation is known as the Taylor-Proudman theorem, according to Taylor (1917) and Proudman (1916) who where the first to provide experimental and theoretical evidence. In this relation we assigned the coordinate system such that the background rotation vector is aligned with the z-axis. From (7) we immediately see that the velocity components will not vary in the direction parallel with Ω, which implies two-dimensional flow behaviour in planes perpendicular to Ω. The velocity component parallel to Ω does not necessarily vanish as it can take on a constant value. Inside boundary layers the conditions leading to (7) are not valid, and the Taylor-Proudman theorem can thus not be applied there.

In carefully designed laboratory experiments Taylor (1917) provided evidence supporting this theorem. He conducted laboratory experiments by steadily towing submerged obstacles through a rotating fluid. He observed that the fluid moved around the obstacle and not over it, thus apparently the obstacle carries a stagnant column of fluid above it, now known as the Taylor column, as if the obstacle was extended over the full fluid layer. The emergence of Taylor columns are not limited to such idealized experiments with more or less laminar flows. The formation of column-like flow structures have also been observed frequently in a variety of laboratory experiments and Direct Numerical Simulations (DNS) of rotating turbulent flows, although not always very clearly visible. An example from a forced rotating turbulence experiment, is shown in Fig. 5, for experimental details see Van Bokhoven et al. (2009) and Del Castello and Clercx (2011a). In these experiments we have added small reflecting flakes to the turbulent flow that can follow the intermediate and large turbulent time scales (not the most rapid variations). By changing the rotation rate a clear change in the flow structuring becomes visible.

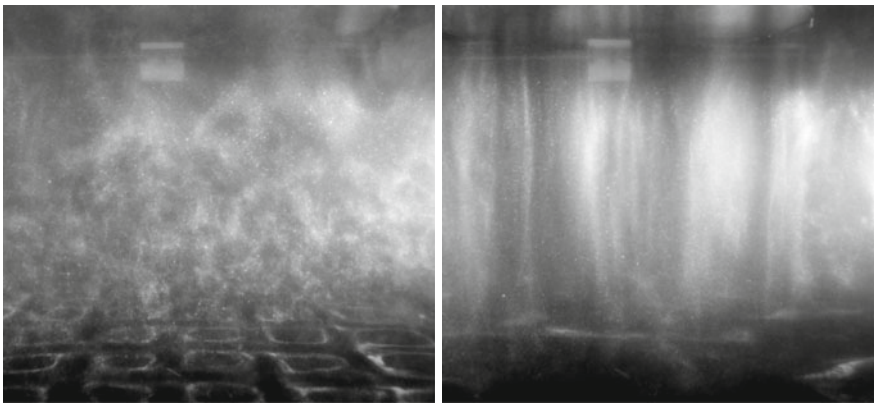

Fig. 5 The two images show instantaneous visualizations of the large-scale flow structures in statistically steady forced (rotating) turbulence by using small light-reflecting flakes. For experimental details, see Del Castello and Clercx (2011a). No background rotation is applied in the experiment shown in the left panel while $\Omega = 2$ rad/s for the experiment shown in the right panel. The presence of Taylor-Proudman columns (vertically-aligned vortical structures) are evident in the right panel. Courtesy of Del Castello

2.3 Inertial Waves

Rotating fluids support inertial waves and the propagation of these waves is due to the restoring nature of the Coriolis force. Inertial waves are found to be anisotropic and dispersive in nature. Keeping the wave character in mind it is in principle possible to describe rotating turbulence and its main features such as the formation of Taylor columns on basis of the interplay between inertial waves and turbulence.

To quantify inertial wave motion it is necessary to derive the underlying wave equation. In the limit of both $Ro \ll 1$ and $Ek \ll 1$ Eq. (4) simplifies to

$$\frac{\partial \mathbf{u}}{\partial t} = 2\mathbf{u} \times \Omega - \frac{1}{\rho}\nabla P \, . \tag{8}$$

By taking the curl of this equation the following relation is obtained

$$\frac{\partial \boldsymbol{\omega}}{\partial t} = 2(\Omega \cdot \nabla)\mathbf{u} \, , \tag{9}$$

with $\boldsymbol{\omega} = \nabla \times \mathbf{u}$ the vorticity of the flow field. To understand why this equation supports waves we first assume once again that the rotation axis is parallel to the $z-$coordinate of the reference frame (thus vertically oriented). Equation (9) simplifies to $\frac{\partial \boldsymbol{\omega}}{\partial t} = 2\Omega \frac{\partial \mathbf{u}}{\partial z}$. For steady flow the Taylor-Proudman theorem is retrieved and one can show that the flow is divergence-free in the plane perpendicular to the rotation

axis, or $\nabla_\perp \cdot \mathbf{u}_\perp = 0$, with the subscript $\perp$ denoting the horizontal components of the gradient operator and flow field. We consider now the time derivative of the vertical component of the vorticity: $\frac{\partial \omega_z}{\partial t} = 2\Omega \frac{\partial u_z}{\partial z} = -2\Omega \nabla_\perp \cdot \mathbf{u}_\perp$. Suppose we have a circular tube of fluid in the horizontal plane which is being perturbed by some (turbulent) fluctuation resulting in radial expansion of the tubular structure, thus $u_r > 0$. This implies $\nabla_\perp \cdot \mathbf{u}_\perp > 0$ and with Eq. (9) in mind ω_z should decrease. Moreover, as a result of the Coriolis force the outward radial flow induces a negative azimuthal velocity u_θ in the circular tube, $2\mathbf{u} \times \Omega = -2u_r \Omega \hat{\mathbf{e}}_\theta$. The negative azimuthal velocity component will in its turn induce a radially inward flow due to the Coriolis force, $2\mathbf{u} \times \Omega = 2u_\theta \Omega \hat{\mathbf{e}}_r$, thus $u_r < 0$ and thus contraction of the circular tube of fluid and $\nabla_\perp \cdot \mathbf{u}_\perp < 0$. This yields an increase in vertical vorticity ($\omega_z > 0$). The inward radial flow induces a positive azimuthal velocity by the Coriolis force and the process repeats itself, thus an oscillatory or wave-like motion is generated by the perturbation. Summarizing, it can be concluded that any departure from $\nabla_\perp \cdot \mathbf{u}_\perp = 0$ is opposed by the Coriolis force and results in wave-like motion to compensate for the horizontal divergence.

Differentiation of the vorticity equation, see Eq. (9), with respect to time and subsequently applying the curl operator to the resulting equation yields a wave equation, the one for inertial waves we are looking for,

$$\frac{\partial^2 (\nabla^2 \mathbf{u})}{\partial t^2} + 4(\Omega \cdot \nabla)^2 \mathbf{u} = 0 \,. \tag{10}$$

Solutions of this equation for each of the velocity components are plane waves of the form

$$\mathbf{u}(\mathbf{r}, t) = \mathcal{R}\left(\mathbf{A} \exp[i(\mathbf{l} \cdot \mathbf{r} - \tilde{\omega} t)]\right) , \tag{11}$$

with $\mathcal{R}(\cdot\cdot)$ denoting the we only consider the real part of this complex function and i is the imaginary unit. Furthermore, the wave amplitude is denoted by $\mathbf{A}$, the wave vector by $\mathbf{l} = (l_x, l_y, l_z)$, and finally $\tilde{\omega}$ is the angular frequency of Fourier mode $\mathbf{l}$. The angular frequency is described by the dispersion relation $\tilde{\omega} = \pm 2\hat{\mathbf{l}} \cdot \Omega$, with $\hat{\mathbf{l}}$ the unit vector in the direction of the wave vector $\mathbf{l}$ (with magnitude l). With the standard definitions the phase and group velocities can be derived and are, respectively,

$$\mathbf{c}_p = \frac{\tilde{\omega}}{l} \hat{\mathbf{l}} = \pm \frac{2}{l} (\hat{\mathbf{l}} \cdot \Omega) \hat{\mathbf{l}} \tag{12}$$

and

$$\mathbf{c}_g = \frac{\partial \tilde{\mathbf{l}}}{\partial \mathbf{l}} = \pm \frac{2}{l} (\hat{\mathbf{l}} \times (\Omega \times \hat{\mathbf{l}})) \; = \pm \frac{2}{l} [\Omega - (\hat{\mathbf{l}} \cdot \Omega) \hat{\mathbf{l}}] \,, \tag{13}$$

with $\frac{\partial \tilde{\mathbf{l}}}{\partial \mathbf{l}} = \left(\frac{\partial \tilde{\omega}}{\partial l_x}, \frac{\partial \tilde{\omega}}{\partial l_y}, \frac{\partial \tilde{\omega}}{\partial l_z} \right)$.

Several remarkable observations can be made. The absolute value of the wave frequency, $\tilde{\omega} = \pm 2\hat{\mathbf{l}} \cdot \Omega$, varies from zero to the maximum value of 2Ω. Furthermore, low frequency waves have wave vectors which are almost perpendicular to the

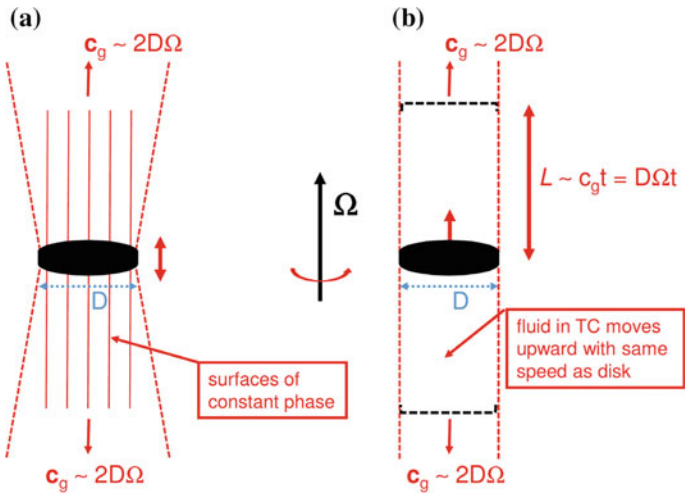

Fig. 6 **a** A sketch of inertial waves generated by a slowly (*vertically*) oscillating disk in a rapidly rotating fluid and **b** of a slowly vertically and steadily moving disk in a rapidly rotating fluid

rotation axis Ω. This means that inertial waves are thus anisotropic. Moreover, the group and phase velocities of these inertial waves, see Eqs. (12) and (13), respectively, are always perpendicular or $\mathbf{c}_p \cdot \mathbf{c}_g = 0$. A consequence of this observation is that waves travelling in a certain direction $\hat{\mathbf{l}}$ (not parallel to Ω) propagate energy in a plane that is set up by $\hat{\mathbf{l}}$ and Ω, but perpendicular to $\hat{\mathbf{l}}$. More specifically this implies that waves travelling in a direction perpendicular to the rotation axis will propagate energy parallel to the rotation axis. As a final remark, low-frequency waves (with $\hat{\mathbf{l}}$ almost perpendicular to the rotation axis) propagate energy at a speed close to $2\Omega\mathcal{L}$ (with $\mathcal{L}$ either a typical length scale of turbulent patches or the size of a disturbance) in a direction parallel to the rotation axis. High-frequency waves (which are almost parallel with Ω) hardly propagate energy in that direction.

A cartoon of two situations (a slowly oscillating disk with diameter D and $\tilde{\omega} \approx 0$, and a slowly vertically moving disk with the same diameter, in both cases with (maximum) vertical velocity V) is shown in Fig. 6. In the case of rapid system rotation such that $V \ll \Omega D$ (or $Ro \ll 1$) the group velocity, $|\mathbf{c}_g| \simeq 2D\Omega$, is much larger than the typical advection time scale of the generated flow. Information of the motion of the disk is then much more rapidly transported by the waves as $L \sim |\mathbf{c}_g|t = 2D\Omega t \gg Vt$ which connects the almost instantaneous formation of Taylor columns with inertial wave processes.

3 Quasi-Two-Dimensional Flows

In Sect. 1.1 some basic properties of 3D homogeneous isotropic turbulence have been summarized. In particular, the turbulent kinetic energy, injected in the flow at large scales, is rapidly transported without significant loss of energy by dissipation to the

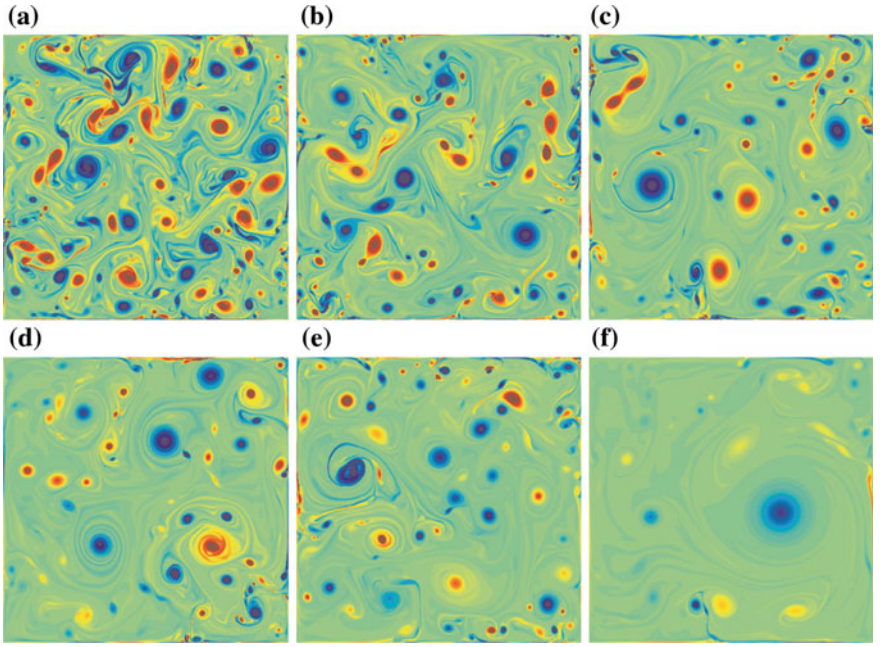

Fig. 7 Vorticity snapshots of decaying 2D turbulence on a square bounded domain. The self-organization of the flow is clearly visible by the formation of larger vortices in course of the decay process. Courtesy of Geert Keetels (TU Eindhoven)

smallest scales of the turbulent flow, a process known as the energy cascade. On the smaller scales stretching of vortex tubes is essential as a mechanism to enhance locally the velocity gradients which contribute to dissipation. Vortex stretching is also reflected in increase of the enstrophy E_ω, a measure of the amount of vorticity in the flow: $E_\omega = \int_\mathcal{V} \omega^2 dV$, with $\mathcal{V}$ the volume of fluid under consideration. Here, for $\nu \to \infty$ we should also observe unbounded growth of the enstrophy due to the continuing process of vortex stretching. As a consequence 3D turbulent flows are always strongly dissipative.

Suppose now that the flow lives in flatland, or is exactly two-dimensional (2D). We then enter into the field of 2D turbulence which is an area of research in itself. For recent reviews the reader could consult Clercx and Van Heijst (2009) and Boffetta and Ecke (2012). As an illustration a few snapshots of decaying 2D turbulence on a bounded domain (which causes also the formation of boundary layers due to the interaction of vortices with the domain walls) is shown in Fig. 7, just to appreciate the strikingly different flow dynamics compared to 3D turbulence. Here, the flow is initialized by a random vorticity field and left to decay in course of time. The large-scale Reynolds number is $Re \simeq 10^5$ and a process of self-organization of the turbulent flow is clearly visible. Also the production of vorticity filaments during the interaction of different vortices is clearly visible.

Some basic properties of 2D turbulence are the following. An important first observation is that vortex stretching and tilting is absent in 2D flows. It actually means that for inviscid 2D flows vorticity (and all higher moments of vorticity as well) is a conserved quantity, a property nicely confirmed in experiments and simulations on time scales where viscous effects can be considered as limited. This also implies conservation of enstrophy. For an inviscid 2D flow also the kinetic energy is a conserved quantity. Combining the two conserved quantities yields an interesting result by applying a similar scaling analysis as put forward by Kolmogorov for 3D homogeneous isotropic turbulence. This was done by Kraichnan (1967) for homogeneous and isotropic 2D turbulence and he found the following. Suppose we inject energy at some intermediate scale in a 2D turbulent flow. Due to conservation of kinetic energy and vorticity, an inverse cascade of energy will be set up with $E(k) \propto k^{-5/3}$. In this way energy is transported from the intermediate injection length scale towards the large scales, eventually limited by the box size of the (numerical) experiment. Together with the inverse cascade a direct enstrophy cascade will emerge, with a scaling according to $E(k) \propto k^{-3}$, transporting enstrophy from the injection scales towards the smallest scales of the flow (where it is eventually dissipated). A recent high-resolution simulation of 2D turbulence on a spatially periodic domain has been performed by Boffetta and Musacchio (2010) to explore these aspects in more detail. Both the energy spectra $E(k)$ and the energy and enstrophy fluxes have been studied for a range of resolutions (and thus a range of Re_λ) and their results are shown in Fig. 8a, b, respectively, confirming the applicability of the Kraichnan model. As the energy tends to be collected at the larger scales, 2D turbulence can be considered as weakly dissipative.

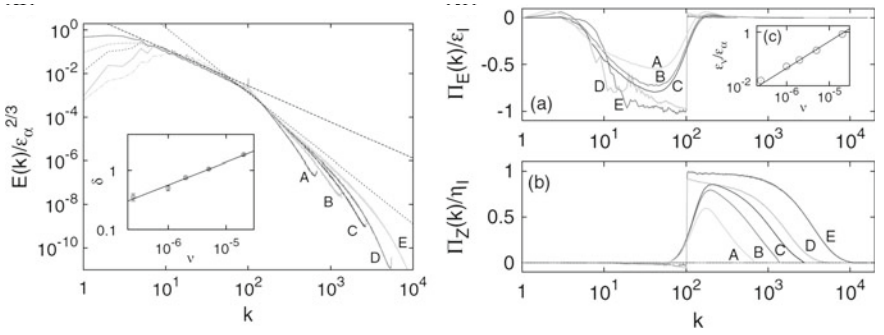

Fig. 8 (*a*) Energy spectra as obtained by Boffetta and Musacchio (2010) for increasing resolution (Re_λ increases from A to E). The *dotted lines* indicate the Kraichnan scaling for the inverse energy and direct enstrophy cascade. The inverse energy cascade is present in these runs and a quite convincing convergence to the scaling of the direct enstrophy cascade is observed for increasing Re_λ. (*b*) The energy and enstrophy fluxes in Fourier space for the runs A to E from Boffetta and Musacchio (2010) clearly showing the fluxes of energy to larger scales and fluxes of enstrophy to smaller scales. Courtesy of Boffetta and Musacchio (2010)

Rotation, stratification or shallowness of the flow domain (or some combination of them) induces strong anisotropy in the (statistical) properties of the turbulent flow. Therefore, it is already well-motivated that it does not suffice to rely on our knowledge of 3D homogeneous isotropic turbulence. Although an attractive alternative at first sight to understand the dynamics of the vortical columns emerging in rotating turbulence, the idealized case of 2D homogeneous isotropic turbulence will not suffice either. However, understanding the dynamics of 2D turbulence might provide some better understanding of rotating turbulence, in particular in the quasi-two-dimensional regime as indicated in Fig. 4. One specific tool might be useful to characterize dimensionality of the turbulent flow: the turbulence triangle or Lumley triangle introduced by Lumley and Newman (1977).

3.1 The Turbulence Triangle

Provided we have access to the three velocity components in a turbulent flow, which are available in numerical data sets and nowadays become available in experiments by employing optical measurement techniques like stereo Particle Image Velocimetry (stereo-PIV) or tomographic PIV, it is possible to calculate the components of the Reynolds stress tensor $R_{ij} = \overline{u_i u_j}$, with u_i the i-th velocity component. The overbar indicates spatial averaging here, and in what will follow. By using the Reynolds stress anisotropy tensor, with components b_{ij}, the degree of anisotropy can be quantified. This tensor is defined as the deviatoric part of the Reynolds stress tensor: $b_{ij} = \frac{R_{ij}}{R_{kk}} - \frac{1}{3}\delta_{ij}$, with δ_{ij} the components of the Kronecker tensor ($\delta_{ij} = 1$ if $i = j$ and zero otherwise). Note that with repeated indices, as in R_{kk}, the Einstein summation convention is implicitly assumed. The Reynolds stress anisotropy tensor is symmetric, has zero trace and the off-diagonal components are all zero in case of an isotropic turbulent flow. This means that the presence of nonzero off-diagonal components serves as an indicator of the presence of anisotropy. Following Lumley, better insight into the degree of anisotropy can be gained by evaluating the principal invariants of the Reynolds stress anisotropy tensor. These invariants are: $II = -\frac{1}{2}b_{ij}b_{ji}$ and $III = \frac{1}{3}b_{ij}b_{jk}b_{ki}$ and plotting them with respect to each other provides valuable information about the character of the turbulence. All realizable states are always found in a triangular-like region in this (III, $-II$) diagram, which is known as the Lumley triangle, see Fig. 9a. In this diagram we can identify a few specific situations. First of all, when $II = 0$ and $III = 0$ it specifies three-component (3C) isotropic turbulence. The two other corner points specify the limits of two-component (2C) axisymmetric turbulence (left) and one-component (1C) turbulence (right corner). The line connecting the left and right corners designates 2C turbulence, while the left curved branch from the origin is associated with pancake-like or disk-like turbulence. In the latter case two eigenvalues of the deviatoric part of the Reynolds stress are large and the third one is small, and the interpretation is that one component of the turbulent kinetic energy is significantly smaller than the other two components. The right curve from the origin represents the other situation: one component of the

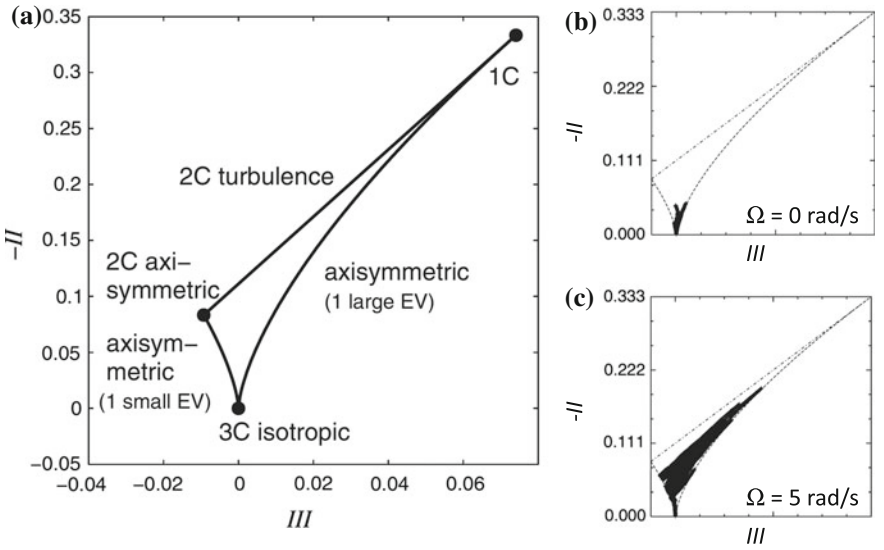

Fig. 9 **a** The Lumley turbulence triangle with an indication of the three points and three curves of the triangle. **b** Scatter plot of $(-II, III)$ for steadily forced non-rotating turbulence and **c** a similar scatter plot but now with a background rotation of $\Omega = 5$ rad/s. Courtesy of Van Bokhoven et al. (2009)

turbulent kinetic energy is substantially larger than the other two (one eigenvalue much larger than the other two). This is generally designated as cigar-shaped or rod-like turbulence. This approach should be used with substantial care and in a qualitative manner, and serves as a tool to compare similar situations, for example, rotating turbulence with varying system rotation.

The experiments by Hopfinger et al. (1982) have already provided evidence of two-dimensionalization processes in rotating turbulence in regions sufficiently far away from the generation area of turbulence. They have shown streakline photographs of the turbulent flow field. The photographs were taken in a cross section of their tank at a height of about 30 cm above the oscillating grid. They show two cases: one without rotation, showing disorderly motion of the particles indicating small-scale structures as in 3D turbulence, and another with rotation, where the streaklines of the particles clearly enable visualization of (presumably vertically-aligned) vortical structures. These phenomena, and in particular the generation of vortical structures aligned with the rotation axis, has been confirmed by numerical studies and, also in a qualitative sense in a few laboratory experiments, see discussion in Sect. 2.2, and references mentioned there. This quasi-two-dimensionalization process has been explored in a more quantitative way in a forced rotating turbulence experiment. The details of the experiment are described by Van Bokhoven et al. (2009) and the discussion here is limited to a rough sketch of the setup and two key results. The experimental setup is shown in Fig. 10 and consists of a rectangular perspex container placed on a rotating

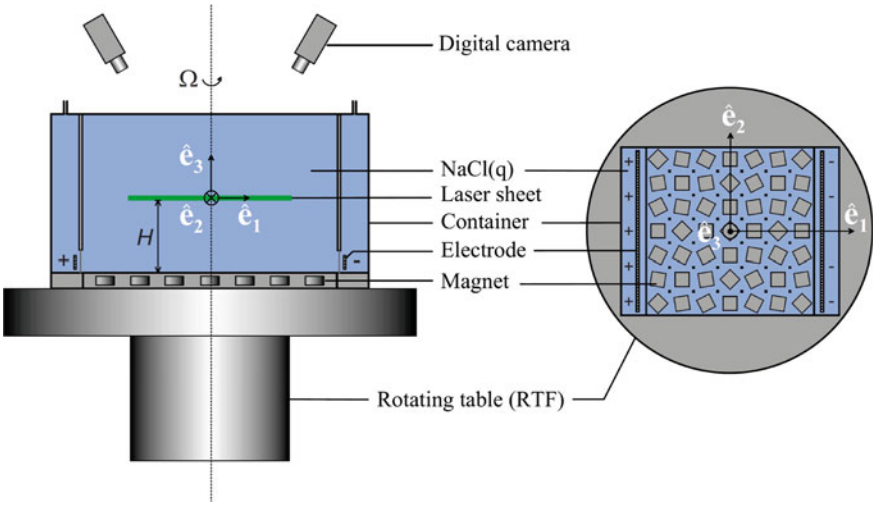

Fig. 10 Side and top view of the experimental setup. Turbulence is generated in the central part of the tank, which is filled with an electrolyte solution. Electromagnetic forcing is applied. Electrodes are placed in the compartments separated from the measurement domain in the tank. An array of magnets is placed underneath the bottom of the container. Stereo-PIV measurements are carried out for extracting flow field information. For this purpose tiny particles are added to the fluid and illuminated by a horizontal laser sheet at a certain height in the container. Courtesy to Van Bokhoven et al. (2009)

table. The rotation rate of the table is varied between 0 and 10 rad/s. An array of magnets is placed underneath the container. The container is filled with an electrolyte solution (NaCl dissolved in water) and two electrodes are placed on opposite sides of the tank. By applying an electric current in combination with the magnetic field a Lorentz force that drives the flow is generated in the fluid. Typically a moderate range of Taylor-based Reynolds numbers could be achieved, $Re_\lambda = \mathcal{O}(90 - 240)$ in the bottom part (layer of about 10 cm height) of the container. The turbulence is quantitatively investigated by applying a stereo-PIV method that allows to extract the three components of the velocity field in a horizontal layer (perpendicular to the rotation axis). These measurements have been conducted at several heights in the turbulent flow, and in four experiments: one without rotation, and three with background rotation rates of 1, 5 and 10 rad/s, respectively. The experiments without system rotation have shown that the turbulence in the measurement plane (at a height of 5 cm above the bottom) is statistically steady and isotropic, and the results turned out to be highly reproducible.

In Fig. 11 two images are shown of the velocity field at a height of 5 cm above the bottom plate, which is sufficiently far above the bottom boundary layer (for example, the Ekman boundary layer thickness for the case with $\Omega = 5$ rad/s is approximately 0.5 mm). Horizontal velocities are shown as white arrows and vertical velocities are indicated by the color bar, running from -25 mm/s (light blue) to +25 mm/s (purple).

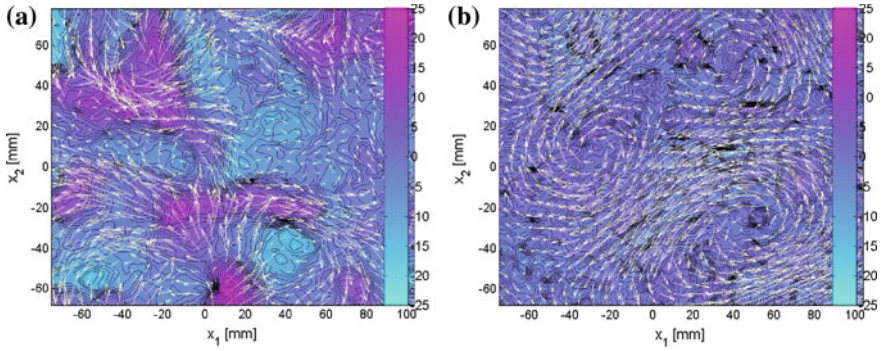

Fig. 11 Two images from stereo-PIV measurements of steadily forced (rotating) turbulence showing the horizontal flow field (*white arrows*) and contour plots of the vertical velocity. In **a** for the non-rotating case and in **b** for $\Omega = 5$ rad/s. Both the larger horizontal integral scales and the reduced vertical velocities are clearly visible in panel (**b**). Courtesy to Laurens van Bokhoven (TU/e)

The left panel (a), without background rotation, shows a rather disordered horizontal flow with vertical velocities of similar size as horizontal ones. The right panel (b), with a background rotation of $\Omega = 5$ rad/s, shows a remarkably well-organized horizontal flow field with a strongly surpressed vertical velocity, all in agreement with what we expect on the basis of the two-dimensionalization mechanism present in rotating flows. The present velocity field represents a typical example. The flow fields are also explored in a statistical sense, see Van Bokhoven et al. (2009), and one of these results concern the Lumley triangle to quantify the character of rotating turbulence in this experiment. This is possible as we have access to all three velocity components needed to determine the components of the deviatoric part of the Reynolds stress tensor. The non-rotating case clearly show that the turbulent flow can be characterized as 3C isotropic turbulence, as all data points cluster close to the point (II, III)=(0,0), see Fig. 9b. In the case of a system rotation of 5 rad/s it turns out that the data points tend to fill a part of the Lumley triangle, in particular above the left and right curved branche, see Fig. 9c. It is a strong indication that the turbulence indeed behaves as axisymmetric 2C turbulence. Here, the horizontal velocity components are on average substantially larger than the vertical components.

4 Rotating Turbulence: Eulerian and Lagrangian Approach

In this section the main results, obtained from rotating turbulence experiments conducted in the Fluid Dynamics Laboratory (TU/e, Eindhoven, The Netherlands), will briefly be reviewed addressing several of the aspects mentioned in previous Sections. Two separate sets of experiments have been carried out. In one set of experiments, which has been conducted by Van Bokhoven et al. (2009), turbulence characteristics

have been extracted by stereo-PIV measurements of the forced turbulent flow field at three different horizontal layers in the fluid. These measurements provide all three components of the turbulent flow at once and constitute an Eulerian dataset at each of the three layers and for the four different values of Ω: 0, 1, 5 and 10 rad/s. Some of these datasets have already been used in Sect. 3.1 with regard to the characterization of turbulence with the Lumley triangle. In the second set of experiments, which has been conducted by Del Castello and Clercx (2011a, b, 2013), the same setup has been used and now turbulence characteristics have been extracted by 3D PTV measurements of forced (non)rotating turbulence in a volume of typical size of $100 \times 100 \times 100$ mm^3. These measurements gave access to the three velocity components of the (rotating) turbulent flow in the 3D measurement volume and constitutes a Lagrangian dataset. The price to pay here is that the resolution in the 3D measurement volume is usually lower than the resolution of the stereo-PIV measurements in the (horizontal) plane. In the following section we will first discuss some results from the Eulerian dataset.

4.1 Eulerian Velocity Measurements in Rotating Turbulence

In the experiments by Van Bokhoven et al. (2009) statistically steady turbulence is produced in a non-intrusive way using electromagnetic forcing. Depending on the rotation rate it is found that the Taylor-based Reynolds number is in the range $90 \lesssim Re_\lambda \lesssim 240$. Applying stereo-PIV it allows instantaneous measurement of all three velocity components in horizontal planes at three distances from the bottom. The root-mean-square turbulent velocity decreases inversely with height in the non-rotating experiments while it is approximately constant when background rotation is applied, see Table III of Van Bokhoven et al. (2009). Based on the behavior of the principal invariants of the Reynolds stress anisotropy tensor, see Sect. 3.1, rotating turbulence can be characterized as a 3D-2C flow. This is also confirmed by an analysis of the contribution to the turbulent kinetic energy of each of the velocity components which are computed according to $\langle e_i \rangle_{TA}$ with $e_i(t) = \frac{1}{2}\langle u_i^2 \rangle_{SA}$ (here i denotes each of the three coordinate directions, TA denotes a time average, and SA denotes a surface average over the measurement plane). It turns out that $\langle e_x \rangle_{TA} \approx \langle e_y \rangle_{TA}$ and $\langle e_i \rangle_{TA} \gg \langle e_z \rangle_{TA}$ for i is x or y, see Table VII of Van Bokhoven et al. (2009). Furthermore, these stereo-PIV measurements provide supporting evidence for the reduction of the dissipation rate when background rotation is applied. The dissipation rate is formally computed as $\epsilon(t) = 2\nu\langle s_{ij} s_{ij} \rangle_{SA}$, with s_{ij} the components of the strain rate tensor. As gradients perpendicular to the measurement plane are inaccessible with stereo-PIV measurements the dissipation rate is approximated by the surrogate $15\nu\langle(\partial u_x/\partial x)^2\rangle_{SA}$. In Table III of Van Bokhoven et al. (2009) values for the dissipation rate are given and they show values about an order of magnitude smaller than for the nonrotating case (at the same height), and this is clearly a sign that the turbulent flow becomes more quasi-two-dimensional. This is further supported by measurement of the spatially and time averaged vertical vorticity $\langle \omega_z' \rangle_{TA}$ with $\omega_z' = \sqrt{\langle \omega_z^2 \rangle_{SA}}$.

It is found that $\langle \omega_z' \rangle_{TA}$ is basically constant over the full fluid layer depth for each of the three rotation rates considered in the experiments (confirming the presence of Taylor-Proudman like coherent structures), while it is strongly decaying with height for the nonrotating case.

Both temporal and spatial velocity (auto)correlations have been computed based on the stereo-PIV dataset. Stronger background rotation results in stronger time correlation, although the temporal autocorrelation of the vertical velocity components is weaker than for the two horizontal velocity autocorrelations. The spatial velocity autocorrelations are strongly enhanced compared to such autocorrelations from the nonrotating experiments. It is found that the behaviour of the longitudinal correlations is consistent with earlier reported numerical findings by Yeung and Zhou (1998) and by Godeferd and Lollini (1999). For an extensive discussion, see van Bokhoven (2009).

Finally, the linear (anomalous) scaling of the longitudinal spatial structure function exponents in the presence of rotation will be discussed briefly. As already touched upon in Sect. 1.1 self-similarity is an important concept for understanding the behaviour of 3D homogeneous isotropic turbulence. An important question is thus to investigate whether or not the statistics of a turbulent flow are self-similar for a wide range of spatial scales. This is usually done by exploring the scaling behaviour of the longitudinal spatial velocity structure function,

$$S_i^p(l) = \langle |u_i(\mathbf{r} + l\hat{\mathbf{e}}_i, t) - u_i(\mathbf{r}, t)|^p \rangle \,. \tag{14}$$

Here, p is the order of the structure function and l is the separation distance between the two measurement points. The separation vector $\mathbf{l} = l\hat{\mathbf{e}}_i$ is parallel with the velocity component under consideration. In case of self-similar statistics we have $S_i^p(l) \sim l^{\zeta_p}$, with $\zeta_p \propto p$. For self-similar 3D homogeneous isotropic turbulence we have $\zeta_p = p/3$. In forced rotating turbulence experiments in the low Rossby number regime, see Baroud et al. (2002), a self-similar flow with anomalous scaling of the structure functions was observed: $\zeta_p = p/2$. This implies $\zeta_2 = 1$ and thus the 1D spectrum based on the horizontal velocity components has the form $E(k) \sim k^{-2}$, with k the wave number in a plane perpendicular to the rotation axis. DNS of rotating turbulence, isotropically forced on the large scales, yielded similar results, $\zeta_2 \approx 1$ (thus $E(k) \approx k^{-2}$), see Müller and Thiele (2007). The higher-order exponents ζ_p have been found intermediate between $p/2$ and values usually found for (intermittent) 3D turbulence. In decaying rotating turbulence yet a slightly different scaling was observed: $\zeta_p \approx 0.7p$, see Seiwert et al. (2008), which would suggest a spectral scaling $E(k) \sim k^{-2.4}$. The stereo-PIV data from the experiments by van Bokhoven (2009), including also experiments with twice as strong forcing of the flow, have been used to compute the scaling exponent. It turns out that $p \approx 0.75$, see Fig. 12, which would suggest $E(k) \propto k^{-2.5}$, with k the wave number in the plane perpendicular to the rotation vector. Quite remarkably, also many theoretical and numerical approaches predict spectral scaling in the range $E(k) \approx k^{-2}$ to $k^{-2.5}$ (or $k_\perp^{-2.5} k_{||}^{-0.5}$, with $k_\perp$ and $k_{||}$ perpendicular and parallel with the rotation axis, respectively), but the information is

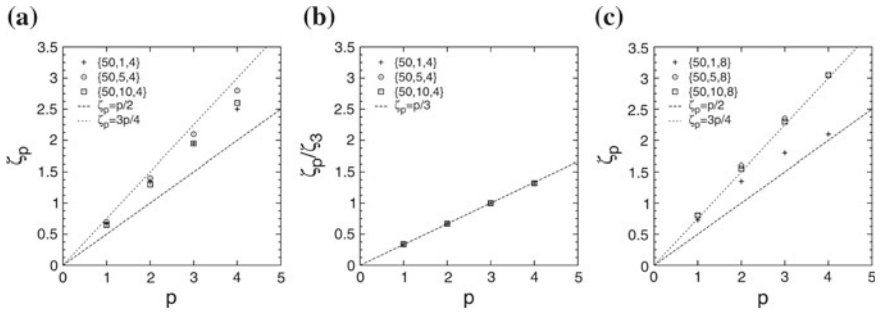

Fig. 12 **a** Scaling of the structure function exponents ζ_p with order p for the rotating experiments. **b** Same as **a** but now the ζ_p is scaled by ζ_3 (extended self-similarity). **c** Same as **a** but now with the flow forcing twice as strong. Courtesy of Van Bokhoven et al. (2009)

still too scattered and the experiments and simulation settings too diverse to come to more definitive conclusions. For further discussion, see Godeferd and Moisy (2015).

4.2 Lagrangian Velocity Measurements in Rotating Turbulence

Lagrangian statistics of passive tracers in steadily forced confined rotating turbulence have for the first time been acquired and investigated by Del Castello and Clercx (2011a) who applied 3D Particle Tracking Velocimetry (3D-PTV). The experimental setup to generate the turbulent flow is basically the same as the one shown in Fig. 10. The optical arrangement (light source and acquisition system) is different, see Fig. 13. Four digital cameras are placed above the tank and have access to the flow via the top lid and acquire images of the central-bottom region of the flow domain (where the flow is fully turbulent). The (passive) particles in the flow domain are illuminated by means of an LED array, see Del Castello and Clercx (2011a) for technical details. Besides the non-rotating case they have subjected the turbulent flow to five different rotation rates, $\Omega = 0.2, 0.5, 1.0, 2.0$ and 5.0 rad/s, partially overlapping with the settings used by Van Bokhoven et al. (2009) (for benchmarking purposes). The Ekman boundary-layer thickness is typically between 2.5 and 0.5 mm (from $\Omega = 0.2$ to 5.0 rad/s, respectively).

Full analysis of the flow field in the measurement volume has shown that under the same forcing conditions for the nonrotating experiment the turbulent flow is statistically homogeneous in the horizontal plane and the vertical decay of the total root-mean-square velocity is consistent with evaluation of this quantity at three heights obtained in the stereo-PIV measurements (note that we can interpolate the Lagrangian velocity data to an Eulerian grid and execute the full comparison). Moreover, and quite encouraging, the Eulerian longitudinal integral length scales in the horizontal directions, derived from our Lagrangian dataset, agree extremely well with those obtained by Van Bokhoven et al. (2009) for the rotation rates of $\Omega = 0$, 1.0 and 5.0 rad/s.

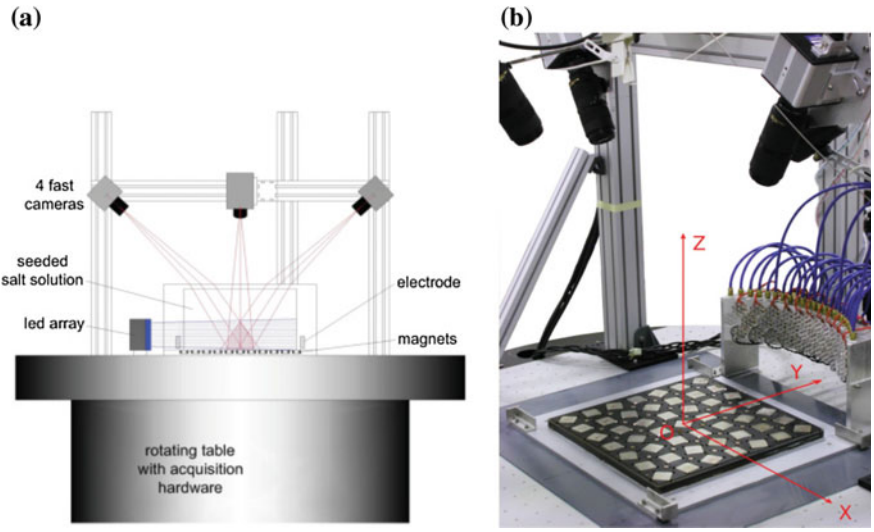

Fig. 13 **a** Schematic drawing of the setup which is similar as shown in Fig. 10. An aluminium frame holds the four cameras (only three shown) in a stable position. The common field-of-view is indicated. A powerful LED array is used for illumination. **b** Picture of the partially mounted setup showing the magnet array consisting of large and small magnets

An analysis of the height dependence of the Rossby number, defined as $Ro = u_{rms}/(2\Omega\mathcal{L})$, and the Taylor-based Reynolds number, $Re_\lambda = u_{rms}\lambda/\nu$ (with λ computed as mentioned before), shows that for rotation rates $\Omega \gtrsim 1.0$ rad/s both Ro and Re_λ are approximately constant in the full measurement domain, except just above the bottom plate. Within a distance of about 10 mm just above the bottom plate they grow to the bulk values. For $\Omega = 1.0$, 2.0 and 5.0 rad/s we found $Re_\lambda \approx 70$, 90 and 170, respectively, and $Ro \approx 0.11$, 0.07 and 0.04, respectively. Kolmogorov length and time scales are in the range $0.6 < \eta < 0.8$ mm and $0.2 < \tau_\eta < 0.5$ s.

In Fig. 14 we show the horizontal and vertical Lagrangian velocity probability distribution functions (PDFs). The horizontal Lagrangian velocity PDFs are based on 8×10^6 data points from both the x- and y-components of the velocity (based on the assumption of horizontal homogeneity and isotropy). The PDFs for the vertical Lagrangian velocity is based on 4×10^6 data points. With regard to the horizontal PDF for $\Omega = 2$ rad/s some asymmetry is observed (see Del Castello (2010) for more details), but furthermore the horizontal Lagrangian velocity PDFs are quite close to their Eulerian counterparts. The velocity component parallel to the (vertical) rotation axis gets strongly reduced (compared to the horizontal ones) with increasing system rotation, in particular for $\Omega = 5.0$ rad/s. It reflects the well-known effect of suppresion of fluid motion in the direction parallel to the rotation axis. It thus induces strong quasi-two-dimensionalization of the flow field.

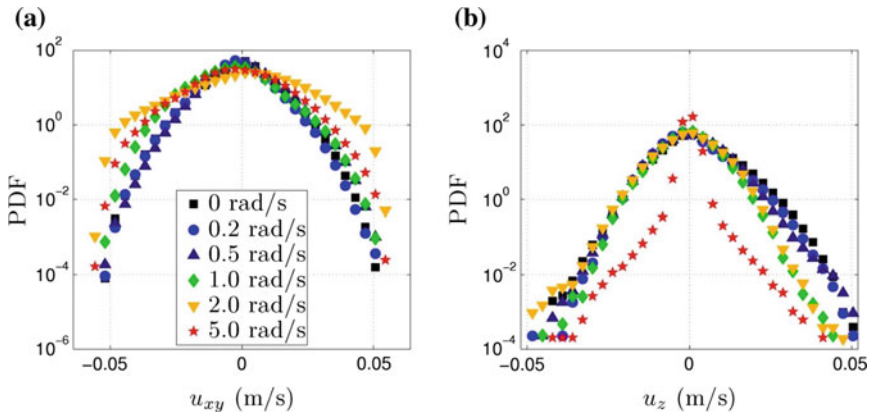

Fig. 14 PDFs of the velocity components in a linear-logarithmic scale for all experiments. **a** PDFs of the horizontal velocity component (both the x- and y-components) and **b** PDFs of the vertical velocity component

4.3 Lagrangian Acceleration Statistics in Rotating Turbulence

Extracting information about the fluid parcel acceleration is best done with the 3D PTV dataset. No counterpart is available from our stereo-PIV measurements. In Fig. 15 the horizontal and vertical Lagrangian acceleration PDFs are shown as reported by Del Castello and Clercx (2011b). They are based on the same data set as discussed in the previous section. First observation is that these PDFs are highly non-

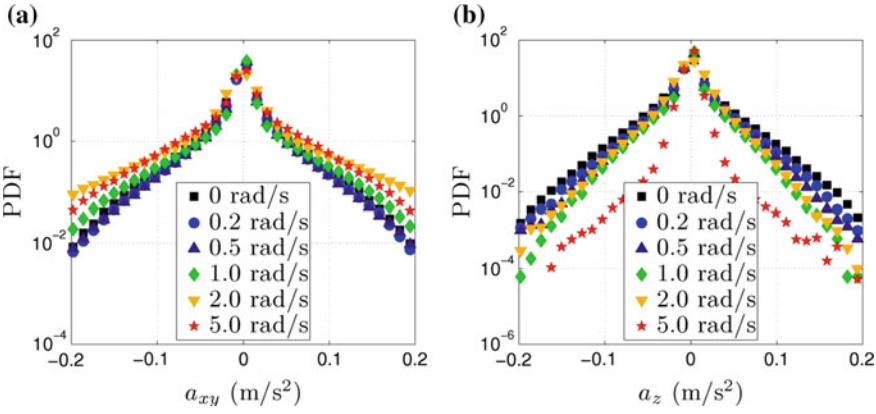

Fig. 15 PDFs of the acceleration components in linear-logarithmic scale graphs for all experiments: **a** PDFs of the horizontal acceleration component (both the x- and y-components) and **b** PDFs of the vertical acceleration component. Courtesy of Del Castello and Clercx (2011b)

Gaussian (like those found in homogeneous isotropic turbulence), but clear effects of background rotation on the PDFs are visible. Direct effects of background rotation on these acceleration PDFs are twofold. The high-acceleration events parallel to the (vertical) rotation axis are strongly suppressed for the experiment with $\Omega = 5.0$ rad/s and a gradual and monotonous (with rotation rate) decrease of the tails is seen for the other rotation rates. This is an indicator for the importance of the quasi-two-dimensionalization process induced by rotation and affecting the accelerations of passive fluid elements, despite the fact that in all experiments and rotation rates the same statistically steady 3D forcing is applied to the fluid.

The high-acceleration events grow in number for the horizontal Lagrangian acceleration, see left panel Fig. 15, but this process is not monotonic with rotation rate. The tails of the PDFs for the experiments with $\Omega = 0.2$ and 0.5 rad/s are slightly lower than for the non-rotating case. They get higher and even significantly higher for $\Omega = 1.0$ and 2.0 rad/s, respectively, before the tails diminish for the highest rotation rate. The PDFs are not skewed, as the skewness remains approximately zero for all experiments. The kurtosis ($K = \langle a^4 \rangle / \langle a^2 \rangle^2$) reaches highest values for intermediate rotation rates ($\Omega = 0.5$ and 1.0 rad/s), although for the vertical Lagrangian acceleration PDF it reaches large values for $\Omega = 5.0$ rad/s (due to strong quasi-two-dimensionalization).

5 Rotating Turbulent Convection

In order to illustrate the effect of rotation on Rayleigh-Bénard (RB) convection, which is the flow driven by buoyancy when the fluid is heated from below and cooled from above, we will discuss and partly explain some basic rotation-induced phenomena in RB convection by concepts like the Taylor-Proudman theorem, its version applicable in the presence of density gradients (the thermal wind balance) and Ekman boundary layers. Rayleigh-Bénard convection is the well-known classical system used to study thermally driven turbulence in a confined space, see the recent reviews by Ahlers et al. (2009) and by Lohse and Xia (2010). Turbulent convection in geophysical and astrophysical flows and in several engineering applications is dramatically affected by system rotation. Although (turbulent) rotating convection has received considerable attention during the last decades, it is since about 10 years ago that there is a revival of interest in this topic and activities have increased strongly again. This is partly due to the observation of new phenomena such as transitions between turbulent states, as discussed by Stevens et al. (2009), and associated sudden heat transport enhancement by passing a critical system rotation rate, see Kunnen et al. (2008a) and Zhong et al. (2009). Also the development of advanced optical diagnostics to explore turbulence, including Lagrangian methods, and the huge increase in computing power for simulations contributed to this revival.

Since the experiments by Rossby (1969) almost fifty years ago it is quite well-known that rotation may enhance heat transport. Rossby observed that the heat transport first increases with respect to the value for non-rotating RB convection when

the rotation rate is increased. At first sight this increase seems rather counterintuitive as the stability analysis of Chandrasekhar (1961) has shown that rotation stabilizes convection and from this one would expect that the heat transport should decrease. However, it turns out that Ekman pumping in the boundary layers near the top and bottom plate may be responsible for this increase in heat transport, see Stevens et al. (2013) and references therein. For a substantially larger rotation rate it is observed that the heat transport is indeed strongly reduced. After Rossby (1969) many experiments and direct numerical simulation (DNS) studies have been conducted. For a review on turbulent rotating Rayleigh-Bénard convection, including references to many of the experimental and numerical studies, Stevens et al. (2013) can be consulted.

5.1 The Boussinesq Equations in a Rotating Frame of Reference

The analysis of turbulent rotating convection requires some additional ingredients compared to those already discussed in Sect. 2 with regard to rotating turbulence: we need to consider the Boussinesq equations of motion in a rotating frame of reference and we need to understand the basic flow profile in the Ekman boundary layer near the top or bottom plate, to be discussed in the next section.

We start from Eq. (4), add the buoyancy term in the momentum equations and provide an additional equation for the transport of heat, all made dimensionless,

$$\frac{\partial \mathbf{u}}{\partial t} + (\mathbf{u}\cdot\boldsymbol{\nabla})\mathbf{u} + \frac{1}{Ro}\hat{\mathbf{z}}\times\mathbf{u} = -\boldsymbol{\nabla}P + T\hat{\mathbf{z}} + \sqrt{\frac{Pr}{Ra}}\nabla^2\mathbf{u}\,, \tag{15}$$

and

$$\frac{\partial T}{\partial t} + (\mathbf{u}\cdot\boldsymbol{\nabla})\mathbf{u} = \frac{1}{\sqrt{Pr\,Ra}}\nabla^2 T\,. \tag{16}$$

On top of that the flow is assumed incompressible ($\boldsymbol{\nabla}\cdot\mathbf{u} = 0$). Here, T is the temperature and $Ra = g\alpha\Delta T H^3/(\nu\kappa)$ is the Rayleigh number and $Pr = \nu/\kappa$ is the Prandtl number. The height of the fluid layer is H, the temperature difference between bottom and top plate is ΔT, and ν, κ and α are the kinematic viscosity, thermal diffusivity and thermal expansion coefficient of the fluid, respectively. The typical velocity scale is the so-called free-fall velocity $\mathcal{U} = \sqrt{g\alpha\Delta T H}$, and the Rossby number translates then into $Ro = \mathcal{U}/(2\Omega H) = \sqrt{Ra/(PrTa)}$, with $Ta = (2\Omega H^2/\nu)^2$ the Taylor number. Finally, temperature has been non-dimensionalized by $T = (T^* - T_0)/\Delta T$, where T^* is the actual temperature and T_0 the temperature of the top plate.

The temperature at the top and bottom plate is constant and the cylindrical sidewall is thermally insulating thus no normal heat flux at the sidewall. The velocity at all boundaries satisfies the no-slip condition.

Let us now consider the same limiting situation as discussed with regard to the Taylor-Proudman theorem. We assume that $Ro \ll 1$, the flow can be approximated as statistically steady and inertial and viscous effects are of minor importance. Then we end up with a modified version of the geostrophic balance:

$$\frac{1}{Ro}\hat{\mathbf{z}} \times \mathbf{u} = -\boldsymbol{\nabla} P + T\hat{\mathbf{z}}\,, \tag{17}$$

known as the thermal wind balance in the atmospheric boundary layer community. Taking the curl of this equation gives, for later use formulated in cylindrical coordinates $\mathbf{r} = (r, \theta, z)$,

$$\begin{aligned} \frac{1}{Ro}\frac{\partial u_r}{\partial z} &= -\frac{1}{r}\frac{\partial T}{\partial \theta}\,, \\ \frac{1}{Ro}\frac{\partial u_\theta}{\partial z} &= \frac{\partial T}{\partial r}\,, \\ \frac{1}{Ro}\frac{\partial u_z}{\partial z} &= 0\,, \end{aligned} \tag{18}$$

with $\mathbf{u} = (u_r, u_\theta, u_z)$ the velocity components in the cylindrical frame of reference. Equation (18) reveals that the vertical velocity component is still constant over height (parallel with the rotation axis) as is the case in the classical Taylor-Proudman theorem. However, in the presence of a horizontal temperature gradient a vertical shear in the horizontal velocity field is induced: the thermal wind.

5.2 Ekman Boundary Layers

It is often reasonable to assume that the bulk flow is (almost) inviscid. Near domain boundaries (also in rotating flows) viscous effects will become important. Ekman (1905) was the first who analysed the boundary-layer structure of rotating flows. For practical purposes we align the system rotation with the (vertical) z-axis. The geostrophic balance dictates the (mean) flow in the bulk of rapidly rotating turbulence. The bulk can be populated with (on average) vertically-aligned cyclones and anticyclones and will have low pressure regions in cyclones and high pressure regions in anticyclones. We assume that the pressure fields in these vortical structures are approximately independent of the vertical coordinate ($\partial p/\partial z \approx 0$) and determine the pressure distribution in the boundary layers. The magnitude of the (mean) large-scale horizontal velocity components, and thus also the Coriolis contribution, will be reduced in the boundary layers. As a consequence the Coriolis force and pressure gradient are not in balance anymore and inward swirl in cyclones and outward swirl in anticyclones is set up inside the Ekman boundary layer. Mass conservation then dictates a flow from the boundary layer into the bulk (pumping) in cyclones and a flow from bulk into boundary layer (suction) in anticyclones: the Ekman boundary

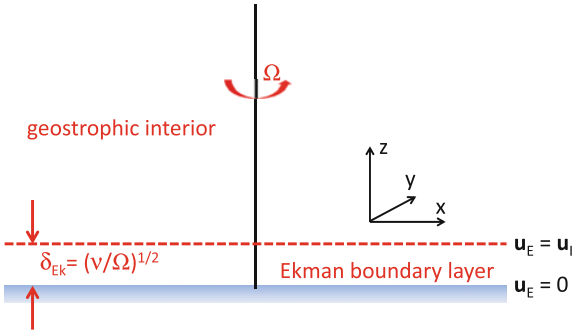

Fig. 16 A schematic representation of the Ekman boundary layer just above a horizontal plate. The angular velocity vector is pointing upwards (perpendicular to the bottom plate)

layer actively influences the flow deep in the fluid bulk. For further analysis, see, for example, Kundu (2016) and Greenspan (1968).

The bottom plate (infinitely extended) is defined in the horizontal xy-plane, see Fig. 16, and any (statistical) flow properties near the bottom plate are horizontally homogeneous and vertically inhomogeneous. In the boundary layer only the z-derivative needs to be retained as gradients in the velocity profile are largest in the direction perpendicular to the boundary. Starting once again with Eq. (15) with the assumption of (statistically) quasi-stationary flow, in the rapid rotation limit, thus $Ro \ll 1$, and by retaining the z-derivative of the viscous contribution we arrive at the following relation:

$$2\mathbf{k} \times \mathbf{u} = -\nabla P + Ek \frac{\partial^2 \mathbf{u}}{\partial z^2} , \tag{19}$$

with $Ek \ll 1$. In laboratory experiments we find typically $Ek \approx 10^{-5}$. The general solution for the horizontal velocity field, satisfying the no-slip boundary conditions at the wall, is:

$$u_E = u_I - [u_I \cos(z/\delta) + v_I \sin(z/\delta)] \exp(-z/\delta) , \tag{20}$$

$$v_E = v_I + [u_I \sin(z/\delta) - v_I \cos(z/\delta)] \exp(-z/\delta) . \tag{21}$$

Here, (u_I, v_I) and (u_E, v_E) are the horizontal velocity components (parallel to the boundary) of the bulk flow and boundary layer flow, respectively, and $\delta = \sqrt{Ek}$ is the dimensionless boundary layer thickness of the Ekman layer. The physical thickness is $\delta_{Ek} = \sqrt{\nu/\Omega}$, implying that the Ekman boundary layer thickness is thus independent of the particular flow configuration and only depends on the system rotation (and fluid viscosity). The Ekman boundary layers play an active role and they strongly influence the bulk properties of rotating (thermally driven) turbulence, for example by pumping and suction of fluid into and out of the bulk of the fluid, respectively.

5.3 Transition Between Turbulent States at Critical Rossby

In this Section we briefly review the most remarkable changes with regard to flow structuring and heat transfer properties in thermally driven convection by increasing the background rotation rate. We restrict the discussion on RRB to experiments and simulations with flows in cylindrical convection cells with equal diameter and height (aspect-ratio one cells).

Thermally driven turbulence in convection cells possesses a remarkable feature: the flow organises itself into a domain-filling Large-Scale Circulation (LSC), see Krishnamurti and Howard (1981). On one side of the container warm plumes rise while on the opposite side cold plumes sink, forming a kind of 'flywheel' structure, see Kadanoff (2001). The existence of the LSC is the starting point of the scaling theory of heat transfer as proposed by Grossmann and Lohse (2000).

Figure 17 shows the velocity field in a horizontal plane at some distance below the top lid. In each panel the velocity field as obtained with stereo-PIV measurements is displayed (the horizontal velocity is shown with the arrows while the vertical velocity is indicated by the colors). The left picture for the non-rotating case ($Ro = \infty$) has the signature of the Large Scale Circulation (LSC) as the right part of panel (a) shows rising fluid (red) and the left part shows sinking fluid (blue). In between a reasonably uniform velocity field is observed. A similar velocity field snapshot for the case with $Ro = 2.9$ (weak background rotation), not shown here, shows the break-up of the LSC: several large patches of rising and sinking fluid and a rather irregular horizontal flow. The transition point is indicated by the rotation rate where the LSC is destroyed. This occurs at a critical Rossby number ($Ro_c \approx 2.5$). In Fig. 17b for $Ro = 0.72$ the small-scale structures indicate the presence of vortical structures although they cannot yet be recognized as vertically-aligned vortices. The latter is more clearly visible in the right panel ($Ro = 0.09$).

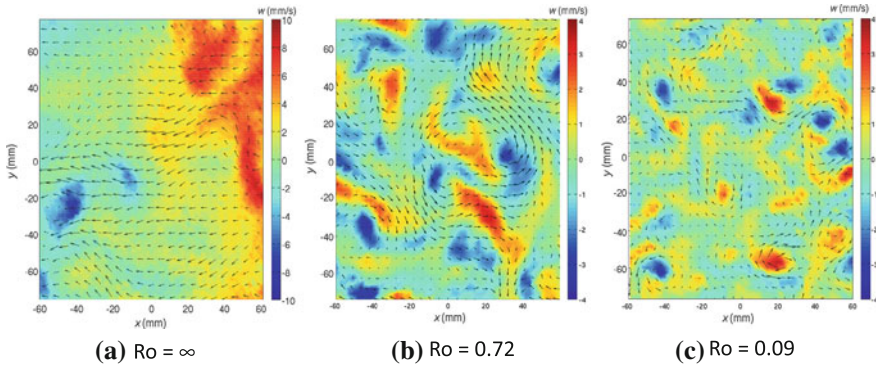

Fig. 17 Snapshots of the velocity field, obtained with stereo-PIV, in a horizontal plane near the top lid of the convection cell. *Colors* represent vertical velocity and *arrows* the horizontal velocity components. **a** no background rotation, **b** intermediate background rotation, and **c** rapid background rotation. Courtesy of Kunnen, TU/e

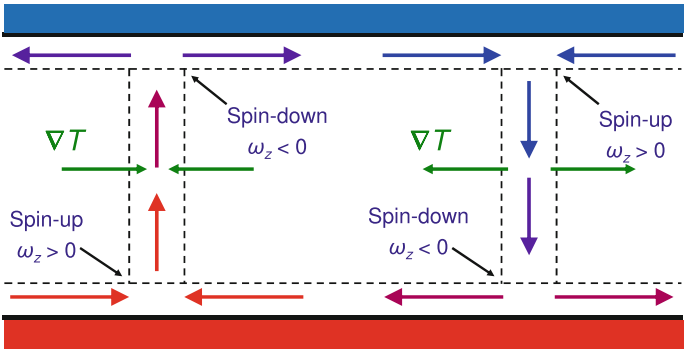

Fig. 18 A schematic representation of the role of the thermal wind in modifying the vorticity in the vertically-aligned plumes when departing from the plate and moving to the opposite wall

The blue patches in Fig. 17c indicate sinking fluid. They contain cyclonic vorticity (counter-clockwise vorticity), which means that the relative rotation of fluid parcels has the same sign as the background rotation. The upwelling fluid (red patches) are vortical structures originating from the bottom plate. They should also have cyclonic vorticity but in the snapshot the vorticity is anticyclonic. The origin of the change to anticyclonic vorticity can be understood by invoking the thermal wind balance. When a plume with cyclonic vorticity is rising from the bottom plate, see the sketch in Fig. 18, it contains hot fluid in an environment with lower temperature. On average the vortex sees a negative radial temperature gradient together with a cyclonic azimuthal velocity. The thermal wind balance states that the azimuthal velocity of the vortex should decrease (thus the cyclonic vorticity decreases) and the vorticity can even change sign and becomes anticyclonic. This process is further supported by widening of the vortex tube when approaching the opposite wall.

The destruction of the LSC can be quantified by measuring the temperature profile at the cylindrical sidewall at half height of the convection cell. This approach can be implemented in experiments with a large number of temperature sensors in the sidewall very close to the interior surface. Numerically, this can be implemented by putting temperature probes just at the inner surface of the cylindrical cavity (also at half height). After averaging the signal and applying a Fourier decomposition one is in principle able to identify the larger structures. For the LSC one has warm rising fluid at one side of the cylinder and sinking cold fluid at the opposite side and the temperature signal can be identified with the $n = 1$ Fourier mode of the harmonic temperature signal. For rapidly rotating thermal convection it turns out that the temperature signal at the sidewall is more or less random and a Fourier decomposition of the temperature signal suggests that it consists mostly of Fourier modes with $n \geq 4$, and the inset in Fig. 19 shows the typical flow structure consisting of these vertically-aligned vortices. The sudden drop of the $n = 1$ contribution in Fig. 19 is a clear indication of the collapse of the LSC. It occurs at the critical Rossby number $Ro_c \approx 2.5$, in agreement with our observations in Fig. 17. In the right panel

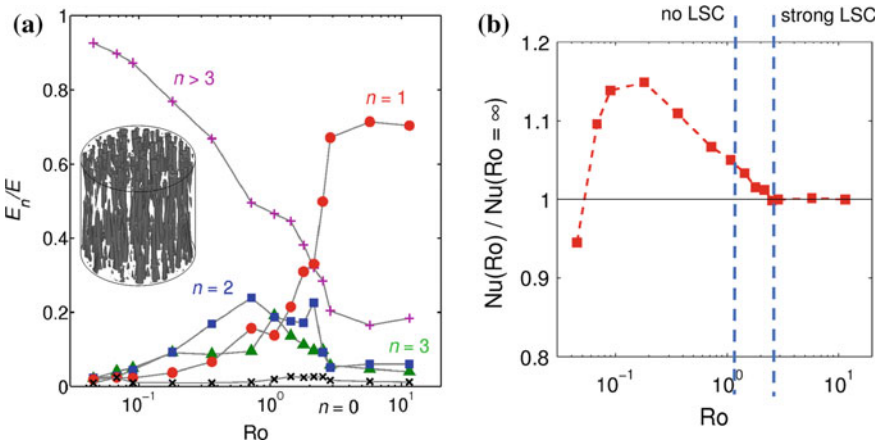

Fig. 19 **a** Normalized average energy content of different Fourier modes. The $n = 1$ mode represent the LSC and the $n > 3$ modes are basically an indirect indication of the presence of many vertical vortex tubes, see *inset*. **b** The normalized Nusselt number representing heat transfer relatively to heat transfer in the nonrotating case (with the same Ra, Pr). A clear transition is visible at $Ro_c \approx 2.5$. For detailed discussion, see Kunnen et al. (2008a)

of Fig. 19 the Nusselt number (the non-dimensional heat flux, $Nu = QH/(\lambda\Delta)$ with Q the heat-current density and λ the thermal conductivity), normalized by the Nusselt number for the non-rotating case (with same Ra), is shown. We see that up to the transition the normalized Nusselt number is constant (and has the non-rotating value), and when the critical Rossby number is passed the normalized Nusselt number increases sharply until a maximum is obtained. The decrease for higher rotation rates reflects the stabilizing role of background rotation as eventually, for very high background rotation, it is expected that the conductive regime will be reached, where $Nu(Ro \to 0)$ should approach the value one.

Summarizing we have the following situation, sketched in Fig. 20, with regard to thermal transport in Rayleigh-Bénard convection without (left panel) and with background rotation (right panel). The basic processes involving the role of system rotation can be understood by invoking Ekman boundary-layer dynamics and the role of the thermal wind. The transition between the two regimes at Ro_c can be understood by the fact that the Ekman boundary-layer dynamics has a strong impact on the LSC when rotation is increased and can eventually destroy the standard flat plate (Prandtl-Blasius) boundary layer induced by the LSC. By exploring the anisotropy in the bulk of rotating RB convection we can see a continual progression of the effect of rotation on the turbulent velocity and acceleration statistics towards the centre of the flow domain. This topic will briefly be touched upon in the next section.

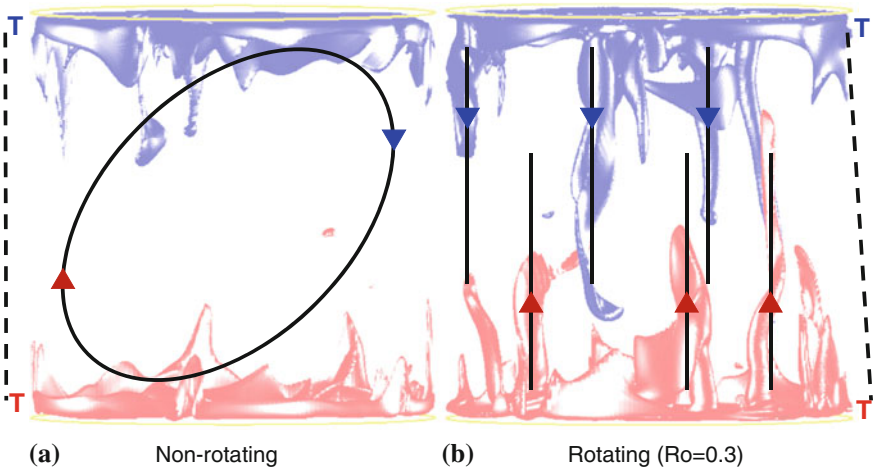

Fig. 20 Schematic of the transport processes (indicated by the *arrows*) in non-rotating RB convection (*left*) and rotating RB convection (*right*). Also note the difference in the mean temperature gradient in the bulk for the two cases. Courtesy of Stevens

5.4 Eulerian and Lagrangian Statistics in (R)RB Turbulence

In a similar way as discussed in Sect. 3.1 the velocity fields measured at two heights in the convection cell by stereo-PIV can be used to compute the second and third invariants of the deviatoric part of the Reynolds stress tensor. These data points, collected at the heights $z = 0.5H$ (central part of the domain, and in the bulk of the turbulent flow) and at $z = 0.8H$ (below and outside the top boundary layer), have been plotted in the Lumley-triangle. The results are shown in Fig. 21, the left panel (a) shows the time-dependent distribution and in the right panel (b) the average value of $(-II, III)$ has been displayed for each rotation rate. Two main observations can be made here. For the non-rotating case, which show quite strong variations (large cloud of data points) some anisotropy is present and has similar character at $z = 0.5H$ and $z = 0.8H$, although the data for $z = 0.8H$ tend to cluster closer to the right branch (indicating elongated structures as it is the region where plumes are abundant). Applying a sequence of background rotation rates clearly show that near the top plate statistical 3D isotropy seems to be restored, but the data in the bulk ($z = 0.5H$) show the presence of axisymmetric (rod-like) turbulence which seems in good agreement with the presence of vertically-aligned vortical structures in the bulk of the flow. This is also confirmed by the "trajectories" of the average value of $(-II, III)$ in Fig. 21b. These structures are also present at $z = 0.8H$ but vertical velocity fluctuations are damped and due to Ekman dynamics in the boundary layers larger horizontal velocity fluctuations are present.

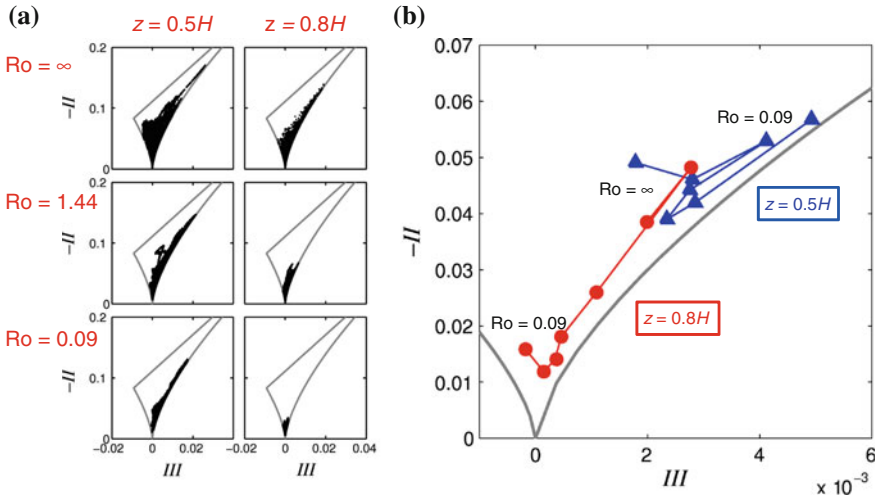

Fig. 21 The Lumley turbulence triangle for (rotating) RB convection. **a** Scatter plot of $(-II, III)$ for three different values of Ro (both in the bulk and near the top lid), and **b** the time-averaged values of $(-II, III)$ for all experiments. Courtesy of Kunnen et al. (2008b)

The anisotropy has also been explored by the Lagrangian velocity and acceleration statistics of passive tracers in (rotating) turbulent convection, see Rajaei et al. (2016). The Rayleigh and Prandtl numbers in these particular experiments were $Ra = 1.3 \times 10^9$ and $Pr = 6.4$ (water). Eight different rotation rates have been explored, corresponding to Rossby numbers in the range ∞ to 0.1. The measurements have been performed in the centre of the convection cell and at two locations near the top plate. The measurement volumes are located with their centre on the axis of the convection cell and at the heights of $z = 0.5H$, $0.8H$ and $0.975H$, respectively. The measurement volume is $50 \times 50 \times 50$ mm^3 in the centre and at $z = 0.8H$ and $50 \times 50 \times 10$ mm^3, thus substantially thinner near the top plate. In these measurement volumes approximately 1000 particles could be tracked in each time step. The duration of an experiment was about 400 min and the camera frame rate is 30 Hz. From the larger measurement volumes the number of data points for the velocity and acceleration statistics is about 60-80 $\times 10^6$ and for the smaller volume it is about 30×10^6.

The measured Lagrangian velocity and acceleration PDFs have been compared with laboratory experiments and numerical simulations for the non-rotating case, see Ni et al. (2012) and Kaczorowski et al. (2014), and turn out to be comparable to each other. In Fig. 22a the Lagrangian root-mean-square velocity fluctuations are plotted as function of Ro. For the measurements at $z = 0.5H$ and $z = 0.8H$ we see an increase in turbulent velocity fluctuations while crossing Ro_c and after that (for higher rotation rates) a decrease. This decrease is consistent with the scaling observed with Eulerian velocity fluctuations (measured with stereo-PIV, see Kunnen et al. 2010). Near the top plate the behaviour is somewhat different. Considering the ratio

of vertical and horizontal Lagrangian velocity fluctuations, see Fig. 22b, we observe anisotropy with increasing rotation rate for measurements at the centre and a tendency to restore isotropy at $z = 0.8H$. Both are consistent with the Eulerian datasets used for the Lumley triangle, see discussion about measurements by Kunnen et al. (2008b) above. We cannot claim full isotropy at $z = 0.8H$ as we are considering a volume with a vertical range of $0.675H \leq z \leq 0.925H$ while the stereo-PIV measurements are based on data from the plane at $z = 0.8H$. Very close to the top plate the root mean square velocity fluctuations are once again indicating strong anisotropy. This is attributed to the strong horizontally spiralling flows in the region where Ekman boundary layers are active.

The Lagrangian root mean square accelerations show a slightly different picture, see Fig. 22c, d. In the bulk horizontal and vertical accelerations have similar values for all rotation rates considered, suggesting isotropy with regard to accelerations (while velocity fluctuations show anisotropic behaviour). Near the top plate strong anisotropy is observed with substantially larger horizontal accelerations than vertical accelerations, which is probably due to the Ekman boundary-layer dynamics, as this

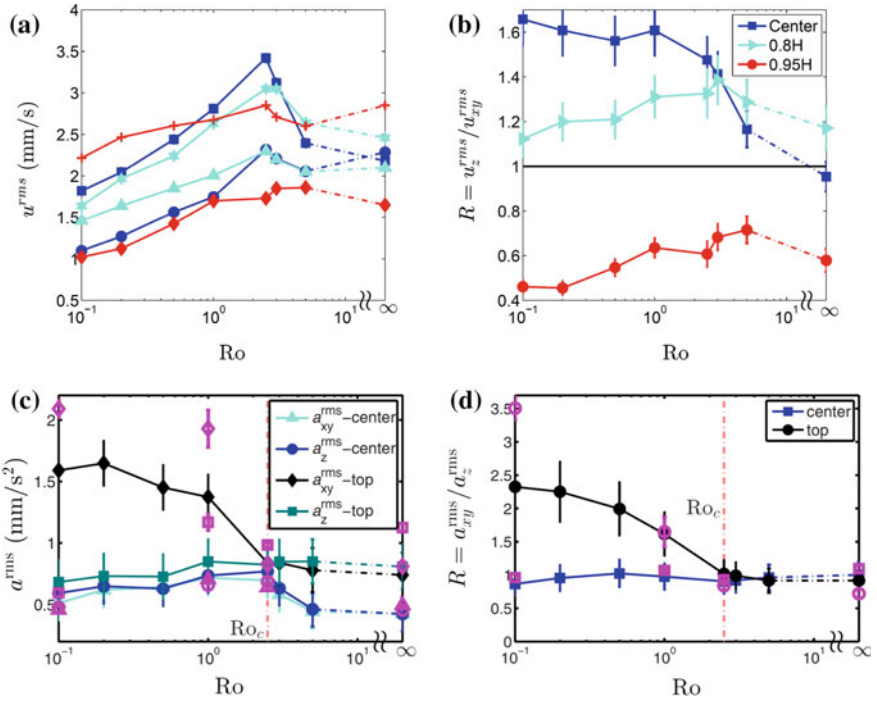

Fig. 22 **a** Horizontal (u_{xy}) and vertical (u_z) velocity fluctuations from experiments as function of *Ro*. *Blue circles* and *squares* are the *horizontal* and *vertical* components at the cell centre, respectively. *Cyan triangles* and stars at $z = 0.8H$ and *red* pluses and *diamonds* at $z = 0.975H$. **b** The anisotropy ratio $R = u_z/u_{xy}$ at each of the heights. **c** Acceleration rms values and **d** the ratio $R = a_{xy}/a_z$ as function of *Ro*. Purple open symbols from DNS. Courtesy to Rajaei et al. (2016)

difference starts to build up beyond the critical rotation rate associated with the collapse of the LSC and emergence of vertically-aligned vortices.

6 Concluding Remarks

After a general introduction to illustrate the role of rotation on the dynamics of turbulent flows and a brief summary of the some aspects of homogeneous isotropic turbulence we have introduced an overview on some of the most remarkable effects of rotation on turbulence and provided a regime diagram of the (Ro, Re) plane (including quasi-2D turbulence, homogeneous isotropic turbulence, inertial-wave dominated regime and wave turbulence). The Taylor-Proudman theorem and inertial waves have been discussed and illustrated, including their relation. A specific and important part of the (Ro, Re) regime diagram is characterized by quasi-2D turbulence, thus the characteristics have been explored in somewhat more detail. Its features are also reflected in the Lumley turbulence triangle which allows one to characterize the anisotropy of the turbulent flow (2D turbulence, 3D homogeneous turbulence, rod-like and disk-like turbulence). This characterization turns out to be helpful with regard to experimental datasets for the flow field. These tools allowed us to explore in more detail both (isothermal) rotating turbulence and rotating thermally driven turbulence and explore the Lagrangian statistics of these turbulent flows and the transport properties, in particular heat, in rotating Rayleigh-Bénard convection and some interesting observations have been reported.

References

G. Ahlers, S. Grossmann, D. Lohse, Heat transfer and large scale dynamics in turbulent Rayleigh-Bénard convection. Rev. Modern Phys. **81**, 503–537 (2009)

J. Bardina, J.H. Ferziger, R.S. Rogallo, Effect of rotation on isotropic turbulence: computation and modelling. J. Fluid Mech. **154**, 321–336 (1985)

C.N. Baroud, B.B. Plapp, Z.-S. She, H.L. Swinney, Anomalous self-similarity in a turbulent rapidly rotating fluid. Phys. Rev. Lett. **88**(11), 114501 (2002)

C.N. Baroud, B.B. Plapp, H.L. Swinney, Z.-S. She, Scaling in three-dimensional and quasi-two-dimensional rotating turbulent flows. Phys. Fluids **15**(8), 2091–2104 (2003)

P. Bartello, O. Métais, M. Lesieur, Coherent structures in rotating three-dimensional turbulence. J. Fluid Mech. **273**, 1–29 (1994)

G. Boffetta, R.E. Ecke, Two-dimensional turbulence. Ann. Rev. Fluid Mech. **44**, 427–451 (2012)

G. Boffetta, S. Musacchio, Evidence for the double cascade scenario in two-dimensional turbulence. Phys. Rev. E **82**(1), 016307 (2010)

C. Cambon, N.N. Mansour, F.S. Godeferd, Energy transfer in rotating turbulence. J. Fluid Mech. **337**, 303–332 (1997)

A. Campagne, B. Gallet, F. Moisy, P.-P. Cortet, Direct and inverse energy cascades in a forced rotating turbulence experiment. Phys. Fluids **26**(12), 125112 (2014)

S. Chandrasekhar, *Hydrodynamic and Hydromagnetic Stability* (Oxford University Press, Oxford, 1961)

H.J.H. Clercx, G.J.F. van Heijst, Two-dimensional Navier-Stokes turbulence in bounded domains. Appl. Mech. Rev. **62**, 020802 (2009)
S.B. Dalziel, Decay of rotating turbulence: Some particle tracking experiments. Appl. Sci. Res. **49**(3), 217–244 (1992)
S.B. Dalziel, The twists and turns of rotating turbulence. J. Fluid Mech. **666**, 1–4 (2011)
P.A. Davidson, *Turbulence in Rotating*. Stratified and Electrically Conducting Fluids (Cambridge University Press, 2013)
P.A. Davidson, P.J. Staplehurst, S.B. Dalziel, On the evolution of eddies in a rapidly rotating system. J. Fluid Mech. **557**, 135–144 (2006)
L. Del Castello, *Table-Top Rotating Turbulence: An Experimental Insight Through Particle Tracking.* PhD Thesis, Eindhoven University of Technology, 2010
L. Del Castello, H.J.H. Clercx, Lagrangian velocity autocorrelations in statistically steady rotating turbulence. Phys. Rev. E **83**(5), 056316 (2011a)
L. Del Castello, H.J.H. Clercx, Lagrangian acceleration of passive tracers in statistically steady rotating turbulence. Phys. Rev. Lett. **107**(21), 214502 (2011b)
L. Del Castello, H.J.H. Clercx, Geometrical statistics of the vorticity vector and the strain rate tensor in rotating turbulence. J. Turbul. **14**(10), 19–36 (2013)
A. Delache, C. Cambon, F. Godeferd, Scale by scale anisotropy in freely decaying rotating turbulence. Phys. Fluids **26**(2), 025104 (2014)
S.C. Dickinson, R.R. Long, Oscillating-grid turbulence including effects of rotation. J. Fluid Mech. **126**, 315–333 (1983)
M.G. Dunn, Convective heat transfer and aerodynamics in axial flow turbines. J. Turbomach. **123**(4), 637–686 (2001)
V.W. Ekman, On the influence of the Earth's rotation on ocean currents. Arkiv för Matematik, Astronomi och Fysik **2**(11), 1–52 (1905)
U. Frisch, *Turbulence: The Legacy of A.N. Kolmogorov* (Cambridge University Press, 1995)
J. Gascard, A.J. Watson, M.J. Messias, K.A. Olsen, T. Johannesen, K. Simonsen, Long-lived vortices as a mode of deep ventilation in the Greenland Sea. Nature **416**, 525–527 (2002)
F.S. Godeferd, L. Lollini, Direct Numerical simulations of turbulence with confinement and rotation. J. Fluid Mech. **393**, 257–308 (1999)
F.S. Godeferd, F. Moisy, Structure and dynamics of rotating turbulence: a review of recent experimental and numerical results. Appl. Mech. Rev. **67**, 030802 (2015)
H.P. Greenspan, *The Theory of Rotating Fluids* (Cambridge University Press, 1968)
S. Grossmann, D. Lohse, Scaling in thermal convection: a unifying theory. J. Fluid Mech. **407**, 27–56 (2000)
D.L. Hartmann, L.A. Moy, Q. Fu, Tropical convection and the energy balance at the top of the atmosphere. J. Climate **14**(24), 4495–4511 (2001)
E. Hopfinger, P. Browand, Y. Gagne, Turbulence and waves in a rotating tank. J. Fluid Mech. **125**, 505–534 (1982)
A. Ibbetson, D.J. Tritton, Experiments on turbulence in a rotating fluid. J. Fluid Mech. **68**, 639–672 (1975)
T. Ishihara, Y. Kaneda, M. Yokokawa, K. Itakura, A. Uno, Small-scale statistics in high-resolution direct numerical simulations of turbulence: Reynolds number dependence of one-point velocity gradient statistics. J. Fluid Mech. **592**, 335–366 (2007)
L. Jacquin, O. Leuchter, C. Cambon, J. Mathieu, Homogeneous turbulence in the presence of rotation. J. Fluid Mech. **220**, 1–52 (1990)
J.P. Johnston, Effects of system rotation on turbulence structure: a review to turbomachinery flows. Int. J. Rotat. Mach. **4**(2), 97–112 (1998)
M. Kaczorowski, K.-L. Chong, K.-Q. Xia, Turbulent flow in the bulk of Rayleigh-Bénard convection: aspect-ratio dependence of the small-scale properties. J. Fluid Mech. **747**, 73–102 (2014)
L.P. Kadanoff, Turbulent heat flow: structures and scaling. Phys. Today **54**(8), 34–39 (2001)
Y. Kaneda, T. Ishihara, High-resolution direct numerical simulation of turbulence. J. Turbul. **7**, N20 (2006)

R.H. Kraichnan, Inertial ranges in two-dimensional turbulence. Phys. Fluids **10**(7), 1417–1423 (1967)
R. Krishnamurti, L.N. Howard, Large-scale flow generation in turbulent convection. Proc. Natl. Acad. Sci. USA **78**, 1981–1985 (1981)
P.K. Kundu, I.M. Cohen, D.R. Dowling, *Fluid Mechanics* (Academic Press, 2016)
R.P.J. Kunnen, H.J.H. Clercx, B.J. Geurts, Breakdown of large-scale circulation in turbulent rotating convection. Europhys. Lett. **84**(2), 24001 (2008a)
R.P.J. Kunnen, H.J.H. Clercx, B.J. Geurts, Enhanced vertical inhomogeneity in turbulent rotating convection. Phys. Rev. Lett. **101**(17), 174501 (2008b)
R.P.J. Kunnen, B.J. Geurts, H.J.H. Clercx, Experimental and numerical investigation of turbulent convection in a rotating cylinder. J. Fluid Mech. **642**, 445–476 (2010)
D. Lohse, K.-Q. Xia, Small-scale properties of turbulent Rayleigh-Bénard convection. Ann. Rev. Fluid Mech. **42**, 335–364 (2010)
J.L. Lumley, G.R. Newman, The return to isotropy of homogeneous turbulence. J. Fluid Mech. **82**, 161–178 (1977)
M.S. Miesch, The coupling of solar convection and rotation. Solar Phys. **192**(1), 59–89 (2000)
P. Mininni, D. Rosenberg, A. Pouquet, Isotropisation at small scales of rotating helically driven turbulence. J. Fluid Mech. **699**, 263–279 (2012)
F. Moisy, C. Morize, M. Rabaud, J. Sommeria, Decay laws, anisotropy and cyclone-anticyclone asymmetry in decaying rotating turbulence. J. Fluid Mech. **666**, 5–35 (2011)
Y. Morinishi, K. Nakabayashi, S. Ren, A new DNS algorithm for rotating homogeneous decaying turbulence. Int. J. Heat Fluid Flow **22**(1), 30–38 (2001)
C. Morize, F. Moisy, M. Rabaud, Decaying grid-generated turbulence in a rotating tank. Phys. Fluids **17**(9), 095105 (2005)
W.-C. Müller, M. Thiele, Scaling and energy transfer in rotating turbulence. Europhys. Lett. **77**(3), 34003 (2007)
R. Ni, S.D. Huang, K.-Q. Xia, Lagrangian acceleration measurements in convective thermal turbulence. J. Fluid Mech. **692**, 395–419 (2012)
J. Pedlosky, *Geophysical Fluid Dynamics* (Springer, 1987)
S.B. Pope, *Turbulent Flows* (Cambridge University Press, 2000)
J. Proudman, On the motion of solids in a liquid possessing vorticity. Proc. R. Soc. A: Math. Phys. Eng. Sci. **92**(642), 408–424 (1916)
H. Rajaei, P. Joshi, K.M.J. Alards, R.P.J. Kunnen, F. Toschi, H.J.H. Clercx, Transitions in turbulent rotating convection: a Lagrangian perspective. Phys. Rev. E **93**(4), 043129 (2016)
H.T. Rossby, A study of Bénard convection with and without rotation. J. Fluid Mech. **36**(2), 309–335 (1969)
J. Seiwert, C. Morize, F. Moisy, On the decrease of intermittency in decaying rotating turbulence. Phys. Fluids **20**(7), 071702 (2008)
L.M. Smith, F. Waleffe, Transfer of energy to two-dimensional large scales in forced, rotating three-dimensional turbulence. Phys. Fluids **11**(6), 1608–1622 (1999)
P.J. Staplehurst, P.A. Davidson, S.B. Dalziel, Structure formation in homogeneous freely decaying rotating turbulence. J. Fluid Mech. **598**, 81–106 (2008)
R.J.A.M. Stevens, J.-Q. Zhong, H.J.H. Clercx, G. Ahlers, D. Lohse, Transitions between turbulent states in rotating Rayleigh-Bénard convection. Phys. Rev. Lett. **103**(2), 024503 (2009)
R.J.A.M. Stevens, H.J.H. Clercx, D. Lohse, Heat transport and flow structure in rotating Rayleigh-Bénard convection. Eur. J. Fluid Mech. B/Fluids **40**, 41–49 (2013)
G.I. Taylor, Motions of solids in fluids when the flow is not irrotational. Proce. R. Soc. A: Math. Phys. Eng. Sci. **93**(648), 99–113 (1917)
T. Teitelbaum, P.D. Mininni, Large-scale effects on the decay of rotating helical and non-helical turbulence. Physica Scripta **2010**, 014003 (2010)
T. Teitelbaum, P.D. Mininni, The decay of turbulence in rotating flows. Phys. Fluids **23**(6), 065105 (2011)

M. Thiele, W.-C. Müller, Structure and decay of rotating homogeneous turbulence. J. Fluid Mech. **637**, 425–442 (2009)

L.J.A. van Bokhoven, H.J.H. Clercx, G.J.F. van Heijst, R.R. Trieling, Experiments on rapidly rotating turbulent flows. Phys. Fluids **21**(9), 096601 (2009)

H. van Santen, C.R. Kleijn, H.E.A. van den Akker, On turbulent flows in cold-wall CVD reactors. J. Crystal Growth **212**(1–2), 299–310 (2000)

P. Wadhams, J. Holfort, E. Hansen, J.P. Wilkinson, A deep convective chimney in the winter Greenland Sea. Geophys. Res. Lett. **29**(10), 1434–1437 (2002)

P.K. Yeung, Y. Zhou, Numerical study of rotating turbulence with external forcing. Phys. Fluids **10**(11), 2895–2909 (1998)

M. Yokokawa, K. Itakura, A. Uno, T. Ishihara, Y. Kaneda, 16.4-Tflops direct numerical simulation of turbulence by a Fourier spectral method on the Earth simulator, in *Proceedings IEEE/ACM SC2002 Conference, Baltimore, 2002*, http://www.supercomputing.org/sc2002/paperpdfs/pap.pap273.pdf

K. Yoshimatsu, M. Midorikawa, Y. Kaneda, Columnar eddy formation in freely decaying homogeneous rotating turbulence. J. Fluid Mech. **677**, 154–178 (2011)

J.-Q. Zhong, R.J.A.M. Stevens, H.J.H. Clercx, R. Verzicco, D. Lohse, G. Ahlers, Prandtl-, Rayleigh-, and Rossby-number dependence of heat transport in turbulent rotating Rayleigh-Bénard convection. Phys. Rev. Lett. **102**(4), 044502 (2009)